VNIVERSITAT DE VALÈNCIA

Departament de Física Atòmica, Molècular i Nuclear

Search for CP violation in single top quark events with the ATLAS detector at LHC

PhD THESIS

María Moreno Llácer

Supervised by:
Dra. M^a José Costa Mezquita
Prof. Dr. José Bernabéu Alberola

Valencia, 2014

A todas aquellas personas que me han acompañado durante estos años y que me han ayudado a llegar hasta aquí. A todos os dedico este trabajo con todo mi amor y cariño. Gracias.

VNIVERSITAT DE VALÈNCIA

Departament de Física Atòmica, Molècular i Nuclear

Search for CP violation in single top quark events with the ATLAS detector at LHC

PhD THESIS

María Moreno Llácer

Supervised by:
Dra. M^a José Costa Mezquita
Prof. Dr. José Bernabéu Alberola

Valencia, 2014

La **Dra. M^a José Costa Mezquita** y el **Prof. Dr. José Bernabéu Alberola**, Científica Titular del Consejo Superior de Investigactiones Científicas y Catedrático de la Universidad de Valencia, respectivamente,

CERTIFICAN:

Que la presente memoria, "***Search for CP violation in single top quark events with the ATLAS detector at LHC***", ha sido realizada bajo nuestra dirección en el *Departament de Física Atòmica, Molecular i Nuclear* de la *Universitat de València* por María Moreno Llácer y constituye su tesis para optar al grado de doctor en Física por la *Universitat de València*.

Y para que conste, en cumplimiento de la legislación vigente, firmamos el presente Certificado en Burjasot a 14 de Abril de 2014.

Dra. M^a José Costa Mezquita

Prof. Dr. José Bernabéu Alberola

Declaration

This dissertation is the result of my own work, except where explicit reference is made to the work of others, and has not been submitted for another qualification to this or any other university.

María Moreno Llácer

Contents

Preface

This thesis documents an exciting period in the timeline of the ATLAS experiment where several milestones were achieved. The studies presented summarise part of the ATLAS research program between 2008 and 2013. The first part of this thesis presents some performance studies obtained with the first ATLAS data: global cosmic-ray runs recorded during the commissioning period and first proton-proton collisions runs. The second and main part is dedicated to the measurement of a new observable which is sensitive to $\mathcal{CP}$ violation in single top quark decays. This genuine observable is a forward-backward asymmetry $A_{\mathrm{FB}}^{\mathrm{N}}$ which is expected to be zero in the Standard Model (SM) and non-zero values would imply complex phases in the Wtb vertex Lagrangian. All the results presented here have been published in ATLAS papers, led to public notes within the ATLAS collaboration or as supporting documents for a paper.

Prior to collisions, cosmic-ray data taking periods allowed to exercise the whole data-flow chain, from the hardware and data acquisition system to the reconstruction and analysis software. At the same time that different parts of the detector were being installed, cosmic-ray data were recorded in the so-called Milestone weeks. The work leading to this thesis started in March 2008 in the Milestone-6 where, for the first time, the SemiConductor Tracker (SCT) took part of these combined runs. The installation of the detector ended up by Summer 2008 and the full ATLAS detector operated for the first time in the cavern. Several global cosmic-ray runs were taken with different magnet and detector configurations. A large sample of cosmic-ray muons was recorded and several studies were carried out with that dataset. Most of them were focused on understanding the performance of individual subdetectors, while in this thesis the performance of the combined muon reconstruction using information of all ATLAS subdetectors (inner tracker, calorimeters and muon chambers) is presented. No relative alignment between the two ATLAS tracking systems (inner detector and muon spectrometer) was applied at that time. Therefore, before attempting to do a combined fit, it was necessary to verify that the relative alignment of the two tracking systems was adequate. Checks were performed by comparing the track parameters for standalone tracks reconstructed in both subsystems, separately in the top and bottom hemispheres of ATLAS. The results obtained with 2008 dataset became public, being the first ATLAS combined results with cosmic-rays data. A comparison with predictions from Monte Carlo simulation allowed to validate and even improve the latter. In 2009, several improvements were made in the detector in terms of calibration, coverage and trigger. Therefore, the previous studies were repeated and extended. The performance of the combined tracking was evaluated by comparing the two reconstructed tracks left by a single cosmic-ray muon passing through the upper and then the lower half of the detector. In addition, the track parameter resolutions were derived using information only from data. The results obtained with 2009 data were included in the ATLAS combined cosmic-ray paper [1], published in 2010 and presented in this thesis.

Once the LHC delivered the first collisions, the performance studies continued. During 2010 ATLAS recorded an integrated luminosity of around 45 pb^{-1} of proton-proton collisions at 7 TeV and the first cross sections measurements were carried out. In this respect, the work presented in this thesis focuses on a performance study of the reconstruction of jets, in particular the data/simulation comparison of the jet shapes in both the region inside and outside the jet cone size. For these studies a sample of dijet events was used. The aim was to compare in both data and Monte Carlo simulations the fraction of jet momentum left out of the jet cone, since a disagreement in such quantity could lead to biases in some physics measurements. The results showed that the relative difference was below 3% and these studies were documented in an ATLAS internal note [2].

The main part of this work is dedicated to a search for $\mathcal{CP}$ violation in single top quark decays. The focus is on the measurement of an asymmetry which allows to probe the Wtb vertex in polarized top quark events. The SM provides a purely left-handed vector coupling (V_{L}) in the Wtb vertex, while a more general Lagrangian (an extension of the SM) allows also right-handed vector and left- and right-handed tensor couplings (V_{R}, g_{L} and g_{R} respectively). The W helicity fractions measured in $t\bar{t}$ events have allowed to set limits to the real part of the anomalous couplings V_{R}, g_{L} and g_{R}. However, they are not sensitive to their complex phases which would imply that the top quark decay has a $\mathcal{CP}$-violating component. As shown in Ref. [3], the W polarisation fractions with respect to a new direction (later defined as $\vec{N}$) are very sensitive to the imaginary part of one of these couplings, g_{R}. The proposed observable is a forward-backward asymmetry A_{FB}^{N} extracted from the angular distribution $\cos\theta^{\text{N}}$ where θ^{N} is the angle between the lepton from the W boson decay and the direction normal ($\vec{N}$) to the plane formed by the W boson momentum direction and the top quark spin direction. This axis can only be defined for polarized top quarks produced via electroweak interaction, as it is the case of single top quark production. The measurement of this asymmetry using the full 7 TeV dataset collected by the ATLAS detector in 2011, which corresponds to an integrated luminosity of $4.66\,\text{fb}^{-1}$, is the main contribution of this thesis. The measurement involves understanding the process at generator level, the full reconstruction of the top quark, a precise determination of the background processes, applying an unfolding procedure and estimating several systematic uncertainties. The final result is $A_{\text{FB}}^{\text{N}} = 0.031 \pm 0.065\,(\text{stat.})\,^{+0.029}_{-0.031}\,(\text{syst.})$, consistent with the SM prediction given the uncertainty. Assuming a value for the top quark polarisation of $P = 0.9$ [4, 5], which is the prediction for the t-channel single top production, the first experimental limits on $Im(g_{\text{R}})$ are found to be $[-0.20, 0.30]$ at 95% confidence level. These results led to a conference note of the ATLAS collaboration [6] (further details are documented in Ref. [7] and presented in this thesis).

1
Theoretical framework

The elementary particles, their properties and their interactions are described by the SM, which is the theoretical framework for the study of the strong interactions of quarks and gluons and the unified electroweak force and that is based on local gauge invariance. The SM is very successful in giving account of most of the observed phenomena at the microscopic frontier of physics, having been verified and tested in many experiments in the last decades. The SM has also induced the search of novel observable phenomena, the last one the discovery of the Higgs boson by the ATLAS (A Toroidal LHC ApparatuS) [8] and CMS (Compact Muon Solenoid) [9] experiments at the LHC (Large Hadron Collider) [10] facility at CERN (Conseil Européen pour la Recherche Nucléaire[1], in Geneva, Switzerland) [11]. Despite these spectacular successes, we have evidences that the theory cannot be complete since, besides some possible theoretical diseases (the hierarchy problem), it is unable to explain some observed phenomena in nature. First of all, it does not include gravity and explains less than 5% of the energy-matter content of our universe. No SM constituents can be candidates to describe dark matter. Furthermore, the observation of neutrino oscillations with atmospheric, solar, reactor and accelerator sources implies neutrino mass and mixing, incompatible with the minimal version of the SM. And, in addition, the standard flavour physics framework for $\mathcal{CP}$ (charge conjugation - parity symmetry) violation, the mismatch between weak interaction and mass eigenstates of quarks by means of the Cabibbo-Kobayashi-Maskawa (CKM) mixing matrix, is unable to explain the baryon asymmetry of the universe by many orders of magnitude. Although precision experiments in the K and B meson facilities agree with the predictions of the SM, **new physics sources of $\mathcal{CP}$ violation are unavoidable**.

In this chapter, a brief introduction to the SM of particle physics is presented with emphasis in $\mathcal{CP}$ violation. A review of $\mathcal{CP}$ violating observations and how they are explained within the SM

[1]The name in English is 'European Council for Nuclear Research'. At present the CERN facility is also called 'European Council for Particle Physics'.

as a phase in the mixing matrix that describes the charged current weak interactions of quarks (the CKM matrix) are discussed.

1.1 The Standard Model of particle physics

Aggregate matter is composed of atoms. A neutral atom consists of a nucleus (~ 1/20,000 the size of the atom) made up of protons and neutrons (both composed by quarks) and of an outer part with electrons (equal number to the number of protons in the nucleus). Quarks and electrons are elementary particles interacting via four fundamental forces in nature: the electromagnetic, the strong, the weak and the gravitational[2] force.

The SM of particle physics describes the fundamental particles and how they interact. The SM includes the unified electroweak and the strong interactions[3] and it is based on quantum field theory. According to the SM (see Figure 1.1), particles are classified in fermions (matter constituents) and vector bosons (force carriers).

1.1.1 Matter constituents: fermions

In the SM, elementary particles of spin $s = \frac{1}{2}$, called fermions, are the building blocks of matter. They obey Fermi-Dirac statistics and the Pauli exclusion principle, which implies that two identical fermions cannot share the same quantum state. The SM contains twelve of these elementary fermions, six quarks and six leptons, which can be arranged in three generations, as shown in Table 1.1. Each generation consists of an up-type quark (up (u), charm (c), top (t)) and a down-type quark (down (d), strange (s), bottom (b)), a charged lepton (electron (e), muon (μ), tau (τ)) and the corresponding neutrino (electron-neutrino (ν_e), muon-neutrino (ν_μ), tau-neutrino (ν_τ)).

Quarks, unlike leptons, carry fractional electric charge, which can be either $Q = +\frac{2}{3}$ or $Q = -\frac{1}{3}$. Leptons can be either electrically charged with a charge of -1 or electrically neutral, neutrinos. Neutrinos are assumed to be strictly mass-less in the SM. However, experiments with solar, atmospheric, reactor and accelerator neutrinos [12–14] have provided evidences for neutrino oscillations[4] (whereby a neutrino of a specific lepton flavour can later be measured to have a different flavour) which indicate that neutrinos have non-vanishing masses. In order to explain these results, an extension of the SM is required.

Fermions with negative chirality[5] (called left-handed fermions) have weak isospin $T = \frac{1}{2}$ and can be grouped into doublets with $T_3 = \pm\frac{1}{2}$ that behave the same way under the weak inter-

[2]Gravity plays an important role on large scales, e.g. for galaxies and stars, but can be neglected on subnuclear scales.

[3]The electromagnetic, the weak and the strong force are the dominating forces in elementary particle reactions.

[4]Neutrino oscillation is a quantum mechanical phenomenon predicted by Bruno Pontecorvo [15, 16] in which a neutrino created with a specific lepton flavour (electron, muon or tau) can later be measured to have a different flavour. This arises from a mixture between the flavour and mass eigenstates of neutrinos.

[5]Something is chiral, if it cannot be mapped to its mirror image by simple rotations and translations alone. An example of chiral objects are human hands: the left hand is a non-superposed mirror image of the right hand and vice versa. The two possible chiral states are named left- and right-handed after this example.

action. With this, up-type quarks and neutrinos have $T_3 = +\frac{1}{2}$ while down-type quarks and charged leptons have $T_3 = -\frac{1}{2}$. There are no transitions between two quarks with the same T_3, known as natural flavour conserving neutral current interactions. Fermions with positive chirality (also called right-handed fermions) have $T = 0$ and form singlets that do not undergo weak interactions. The electric charge Q is related to weak isospin T_3 and weak hypercharge Y_W: $Q = T_3 + \frac{Y_W}{2}$. Right-handed neutrinos would have all numbers vanishing and they do not exist in the SM. Their possible existence is under experimental search, mainly by the mixing in neutrino oscillations.

Quarks carry an additional quantum number, the colour charge. There are three different types: red, green or blue. Free coloured particles have not been observed in nature, quarks are confined into colour-less composite particles. These bound states of quarks are called hadrons and there are two types: baryons (consisting of three quarks with different colour charge) or mesons (consisting of a quark and an antiquark).

Additionally, every particle has an associated antiparticle, which has the same mass, but carries the opposite charge to its corresponding particle.

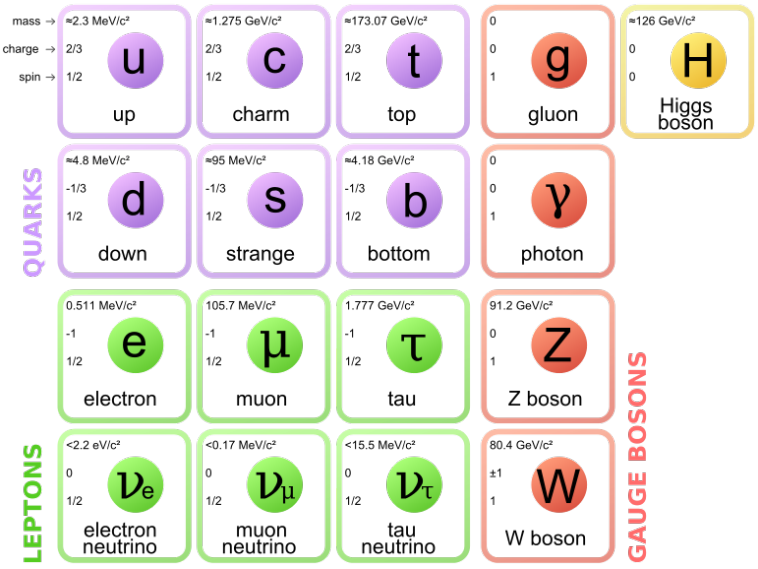

Figure 1.1: *Fundamental particles of the Standard Model.*

Each family differs from the other ones in the flavour, i.e. the fermion type and the mass of the particles, while the other corresponding quantum numbers are the same (see Tables 1.1-1.2[6]). All ordinary matter of our present expanded and cold universe is composed of particles

[6]One can notice that the top quark is distinguished by its large mass, about 35 times larger than the mass of the next heavy quark. This unique property raises a number of interesting questions and makes top quark physics of special

	Generations			Properties		
	1	2	3	Electric charge Q (e)	Weak isospin T_3	Colour
Quarks	u	c	t	2/3	1/2	rgb
	d	s	b	-1/3	-1/2	rgb
Leptons	ν_e	ν_μ	ν_τ	0	1/2	-
	e	μ	τ	-1	-1/2	-

Table 1.1: *The three families of leptons and quarks of the SM. Q denotes the electric charge, T_3 the weak isospin and rgb the colour charges (red, green and blue).*

Generations	Quarks	Mass (MeV/c^2)	Charged leptons	Mass (MeV/c^2)
1	u	$2.3^{+0.7}_{0.5}$	e	0.511 (prec.$\sim 10^{-9}$)
	d	$4.8^{+0.5}_{0.3}$		
2	c	$(1.275 \pm 0.025) \times 10^3$	μ	105.658 (prec.$\sim 10^{-7}$)
	s	95 ± 5		
3	t	$(173.34 \pm 0.27 \pm 0.71) \times 10^3$	τ	1776.82 ± 0.16
	b	$(4.18 \pm 0.03) \times 10^3$		

Table 1.2: *Masses of the three generations of fermions (values from PDG 2012 report [17]). Unlike the leptons, quarks are confined inside hadrons and are not observed as physical particles. Therefore, their masses cannot be measured directly, but can be determined indirectly through their influence on hadronic properties. Any quantitative statement about the value of a quark mass must refer to the particular theoretical framework and scheme dependence that is used to define it. The masses of the light quarks (up, down and strange) are given in a mass independent subtraction scheme such as the $\overline{MS}$ at a scale $\mu \sim 2$ GeV. The charm and bottom quark masses are the 'running' masses in the $\overline{MS}$ scheme. The top quark mass value is obtained from direct observations of top quark events. The quoted value is the most precise combination of CDF and D0 published measurements [18].*

of the first family. The higher generations appear only in high energy interactions, such as collisions of cosmic rays with molecules of the atmosphere or in the laboratory environment of collider experiments. Once produced, these massive fermions decay subsequently into the lighter fermions of the first generation. The measurement of the invisible Z boson decay width at the Large Electron-Positron Collider (LEP) [19] showed that there are three families of light neutrinos. Up to now, there is no evidence for a fourth generation of fermions.

1.1.2 Force mediators: vector bosons

In quantum field theory, the dynamics of a physical system is described by Lagrangians. This dynamics of the interaction is induced by a local gauge symmetry which is not fulfilled by the free Lagrangian. To ensure the invariance, additional vector fields have to be introduced to the Lagrangian to compensate for the effects raised by the transformations. In quantum field theory, these fields represent particles transmitting the forces which are called gauge bosons, they have spin $s = 1$ and therefore obey Bose-Einstein statistics. A compilation of these force mediators

interest, being the main topic of this thesis.

and some of their properties is shown in Table 1.3. They are directly connected to the fields of the three fundamental interactions: the strong force (described by $SU(3)_C$ transformation group) and the unified electromagnetic and weak interaction (the electroweak force, described by the $SU(2)_L x U(1)_Y$ group). The interaction strength is determined by the coupling constant.

The electromagnetic force is the interaction responsible for almost all the daily phenomena, with the exception of gravity. All electrically charged particles interact via this force. It is described by the abelian theory of Quantum Electro-Dynamics (QED) [20] at energies below the electroweak unification scale and the mediating gauge boson is the photon (γ), which is a mass-less particle with no electric charge. The infinite range of the electromagnetic force is a direct consequence of the zero-mass of the photon.

The strong force between colour charged particles is described by a non-abelian theory, Quantum Chromo-Dynamics (QCD) [21]. The gauge bosons of this force are the gluons (g), which are mass-less particles and electrically neutral. Unlike the electrically neutral photon, gluons themselves carry colour charge and therefore they not only interact with coloured particles, i.e. quarks, if not also among themselves (gluon self-coupling). The gluons are colour octets while the quarks are colour triplets. By the exchange of a gluon, a quark with one colour can interact with another quark of any other colour. The strength of the strong interaction is determined by the coupling which runs with the energy of the interacting particles. At very high energy (short distances), the coupling becomes small which makes perturbative calculations possible, named asymptotic freedom; while at very low energy (large distances), the increase in the strength forces quarks to create colour-less bound states called hadrons.

Force	Couples to	Rel. Strength	Range (m)	Bosons	Q (e)	Mass (GeV/c^2)
EM	electric ch.	1/137$\sim 10^{-2}$	∞	photon (γ)	0	0
Strong	colour	1	10^{-15}	8 gluons (g)	0	0
Weak	isospin	10^{-5}-10^{-2}	10^{-18}	W$^{\pm}$	$\pm$1, 0	80.4
				Z	0	91.2

Table 1.3: *The three fundamental interactions explained by the SM and the gauge bosons. EM refers to the electromagnetic force.*

The weak force is unified with the electromagnetic force in the SM. In contrast to the mass-less photon and gluons, the mediators of the weak force are massive gauge bosons: the charged W bosons and the electrically neutral Z boson. The large mass (80.4 and 91.2 GeV/c^2, respectively) limits the range of the weak force to subnuclear scales. Weak gauge bosons couple to fermions through weak isospin ($SU(2)_L$) and hypercharge ($U(1)_Y$). The weak force is the only force in the SM that affects neutrinos, since they have weak isospin and hypercharge, but they do not carry electric or colour charge.

1.1.3 The Standard Model Lagrangian and the Higgs boson

The Lagrangian[7] of the SM, $\mathcal{L}_{SM}$, is Lorentz invariant, which limits the speed of interactions to the speed of light, and is also invariant under the gauge transformation $SU(3)_C x SU(2)_L x U(1)_Y$. It consists of different parts:

$$\mathcal{L}_{SM} = \mathcal{L}_{\text{gauge}} + \mathcal{L}_{\text{matter}} + \mathcal{L}_{\text{int}} \tag{1.1}$$

The $\mathcal{L}_{\text{gauge}}$ and $\mathcal{L}_{\text{matter}}$ terms describe the gauge fields and fermions (matter) respectively, and $\mathcal{L}_{\text{int}}$ represents their interactions. These matter fields, associated to quarks and leptons of spin $s = \frac{1}{2}$, are multiplets of $SU(2)_L$ classified according to their chirality state, left-handed doublets and right-handed singlets:

$$\psi_i = \begin{pmatrix} u_i \\ d_i \end{pmatrix}_L \quad u_{iR}, \quad d_{iR} \quad \text{(for quarks)} \tag{1.2}$$

and

$$\psi_i = \begin{pmatrix} \nu_i \\ l_i \end{pmatrix}_L \quad l_{iR} \quad \text{(for leptons)}, \tag{1.3}$$

where u_i (d_i) stands for the up-type (down-type) quark, ν_i for the neutrino and l_i for the charged lepton. The index i runs over the number of fermion families and the R (L) stands for the right (left) fermions. These parts of the Lagrangian are invariant under $\mathcal{CP}$ symmetry.

With the terms above, the description of the SM is incomplete. Invariance under $SU_L(2)xU_Y(1)$ implies that all the fermions as well as the gauge bosons have to be mass-less. This is in clear contradiction with the experimental observations, therefore it is necessary to introduce particle masses in a way which preserves the original gauge invariance of the Lagrangian. The mechanism of spontaneous symmetry breaking [22] provides an elegant way to generate the masses of the gauge fields by introducing an extra scalar field in the Lagrangian, $\mathcal{L}_{\text{Higgs}}$, in form of a complex isospin doublet of $SU_L(2)$ with weak hypercharge $Y_W = +1$ [23–26]:

$$\mathcal{L}_{\text{gauge}} \quad \Longrightarrow \quad \mathcal{L}'_{\text{gauge}} = \mathcal{L}_{\text{gauge}} + \mathcal{L}_{\text{Higgs}} \tag{1.4}$$

This field triggers the spontaneous symmetry breaking of the electroweak group to the electromagnetic subgroup ($SU_C(3)xSU_L(2)xU_Y(1) \rightarrow SU_C(3)xU_{EM}(1)$) that induces a non-zero vacuum expectation value leading to effective masses for the gauge bosons and a remnant massive scalar is left. This is the *Brout-Englert-Higgs mechanism*, in which the weak gauge bosons acquire mass while the photon, being associated to the residual symmetry $U_{EM}(1)$, does not acquire any mass, and in which the remnant is a new elementary particle called Higgs boson (H) with spin $s = 0$. This term of the Lagrangian is also $\mathcal{CP}$ conserving.

To finalise the theory, the fermion masses, which are forbidden explicitly, are also generated through the spontaneous symmetry breaking and are introduced via gauge invariant interaction terms between the fermions and the scalar fields leading to the Yukawa term $\mathcal{L}_{\text{Yukawa}}$:

$$\mathcal{L}_{\text{matter}} \quad \Longrightarrow \quad \mathcal{L}'_{\text{matter}} = \mathcal{L}_{\text{matter}} + \mathcal{L}_{\text{Yukawa}} \tag{1.5}$$

[7] The Lagrangian $\mathcal{L}$ of a dynamical system is a function that summarizes the dynamics of the system.

These lead to massive quarks and charged leptons (the strength with which these fermions couple to the Higgs boson is proportional to their mass) but mass-less neutrinos. Since 1998, measurements of the fluxes of atmospheric, solar, reactor and accelerator neutrinos provide an evidence for neutrino oscillations, which indicate that neutrinos are massive (see Ref. [12] for a review). That means that $\mathcal{L}_{\mathrm{SM}}$, as it is now, cannot give a complete description of nature and it must be extended. One way to accommodate massive neutrinos is to introduce right-handed neutrinos and allow to write the Yukawa coupling like other charged fermions. This extension of the SM is allowed by the gauge symmetry and leads to Dirac masses for neutrinos at very high energy scales. Other possibility beyond the SM is the see-saw model leading to Majorana masses. With masses and mixing for fermions, the door is open to $\mathcal{CP}$ violation for three families (or more).

Within the SM, the Higgs boson is unique since it is the only physical scalar in the theory. A free parameter of the model is the mass of the Higgs boson itself. Theoretically it must be below the TeV range, as required by partial wave unitarity in gauge boson scattering. Its self-couplings and the couplings to the massive particles (weak gauge bosons, quarks and charged leptons) are expressed in terms of the masses of the interacting particles.

One of the main aims of the LHC at CERN is to elucidate whether the mechanism of symmetry breaking postulated by the SM is actually realised in nature. On July 4^{th} 2012 its two main experiments, ATLAS [27] and CMS [28], announced that they had found a new particle with a mass of about 125 GeV/c^2, and some months later it was confirmed the particle was "consistent with the Higgs boson". The experimental study of the Higgs boson at the LHC is undoubtedly one of the most exciting areas in contemporary particle physics. Now that it has been discovered, the emphasis is on a more precise measurement of its mass and properties. Establishing the properties of the Higgs boson such as its spin, parity and branching ratios is essential to understand whether the observed particle is the SM Higgs boson or something more exotic. Other goals of the LHC physics program are searches of new particles and new physics beyond the SM, since, as it will be now discussed, there are several phenomena that this theory is not able to explain and therefore it needs to be extended.

1.1.4 Problems of the Standard Model

The SM, as it now stands[8], explains successfully most of the present experimental results to precise level and gives predictions that are in perfect agreement with experimental observations. However, there are evidences that this theory is not complete: it does not describe gravity, neutrino masses, matter-antimatter asymmetry (baryogenesis), dark energy and dark matter. In the following these unexplained phenomena are reviewed:

- **Gravity:** The SM does not include gravity. Although a theoretical particle known as "graviton" (not observed yet but predicted to be mass-less and with spin $s = 2$) could help to explain it, so far there is no way of describing gravity in terms of a quantum field theory. Attempts to extend the SM by adding gravitons run into serious theoretical difficulties at high energies (close to and above the Planck scale) because of non-renormalizable infinities arising due to quantum effects.

[8]The current SM requires 19 parameters whose values are unrelated and arbitrary.

- **Neutrino masses:** As already discussed, the SM predicts that neutrinos are mass-less particles. This is in clear contradiction with the evidence for neutrino oscillations which imply that their mass is non-zero. Neutrinos are able to oscillate among the three available flavours while they propagate through space because the neutrino flavour eigenstates are not the same as the neutrino mass eigenstates. These mass terms can not be as those of the other fermions, i.e. via interactions with the scalars in $\mathcal{L}_{\text{Yukawa}}$, because these interactions involve both left- and right-handed fermions and only left-handed neutrinos have been observed so far. Another point is that the mass terms need to be extraordinarily small so that it is not clear if they arise in the same way as the masses of other fundamental particles in the SM.

- **Matter-antimatter asymmetry of the universe:** The universe today contains mostly matter over antimatter for its baryonic component. The SM predicts that matter and antimatter should have been created in almost equal amounts and so far there is no mechanism able to explain the observed predominance of matter over antimatter ($\mathcal{CP}$ violation). In the SM, the only place where $\mathcal{CP}$ violating effects can be accommodated is in the weak interactions of quarks and leptons, but its prediction is many orders of magnitude below the observed value and new sources of $\mathcal{CP}$ violation are needed.

- **Dark matter and dark energy:** Cosmological observations from different sources, including the temperature fluctuations of the cosmic microwave background radiation, show that ordinary matter can only account for 5% of the observed energy and matter in the universe, and the rest is assumed to be dark matter (about 27%) and dark energy (about 68%). The dark matter is assumed to behave as other matter but only interacts via weak force. It cannot be seen directly since it does not emit nor absorb light but its existence is inferred from its gravitational effects on visible matter and radiation. The SM cannot explain the observed amount of cold dark matter. The rest should be dark energy, a constant energy density for the vacuum. Attempts to explain dark energy in terms of vacuum energy in quantum field theory lead to a mismatch of 120 orders of magnitude.

Although there have been (and are) several attempts to extend the SM, both from the theoretical and the experimental side, currently no proposed theory is able to explain all current observations. Theories beyond the SM include various extensions through supersymmetry, such as the Minimal Supersymmetric Standard Model (called MSSM), or entirely new explanations, such as string theory and extra dimensions. These theories should reproduce all the phenomena observed in nature and even combine, or unify, gravity and the SM.

1.2 $\mathcal{CP}$ violation and weak hadronic interactions

$\mathcal{CP}$ is a discrete symmetry of nature given by the product of two components: charge conjugation C, which transforms a particle into its antiparticle (i.e. maps matter into antimatter), and parity inversion $\mathcal{P}$, which creates the mirror image of a physical system (i.e. is the transformation that inverts the space coordinates). The combined operation of C and $\mathcal{P}$ relates the rates of particle transitions to antiparticle transitions. If $\mathcal{CP}$ symmetry is conserved, then the rate for a particular particle decay would be the same as that for the related antiparticle decay. If $\mathcal{CP}$ symmetry is violated, these transition rates would differ. The symmetries C, $\mathcal{P}$ and $\mathcal{CP}$ hold for

strong and electromagnetic interactions, but not in the weak ones.

$\mathcal{CP}$ violation is required to explain the observed dominance of mater over antimatter in the universe. The SM provides the possibility of $\mathcal{CP}$ violation in the weak interactions of quarks and leptons. To date, $\mathcal{CP}$ violation has only been observed in the quark sector, where many precise measurements have been made in the K^0-$\bar{K}^0$ and B^0-$\bar{B}^0$ systems. Despite the observation of $\mathcal{CP}$ violating effects in the weak interactions of quarks, in good agreement with SM predictions, this is not sufficient to explain the observed matter-antimatter asymmetry of the universe and other sources need to be identified.

1.2.1 $\mathcal{CP}$ violation in the early universe

In the early universe, there were an equal number of baryons and antibaryons since they were in thermal equilibrium with the mixture of energetic photons that pervaded all the space. As the universe expanded, its temperature decreased and the density of baryons and antibaryons also decreased until a point in which the numbers of baryons and antibaryons was fixed. This process is known as "Big Bang baryogenesis" theory. The calculations of thermal freeze predict equal number densities for baryons and antibaryons and a baryon to photon density ratio of

$$n_B = n_{\overline{B}} \sim 10^{-18} n_\gamma \,. \tag{1.6}$$

However, this prediction is in contradiction with the observed asymmetry Y_B[9]

$$Y_B = \frac{n_B - n_{\overline{B}}}{n_\gamma} \sim 10^{-9}, \tag{1.7}$$

which can be deduced from the cosmic microwave background and "Big Bang nucleosynthesis". This means that in the early universe there were 10^9+1 baryons for every 10^9 antibaryons, which annihilated to give the observed 10^9 photons for every baryon in today's universe.

To explain this, three conditions originally formulated by A. Sakharov in 1967 must be satisfied:

- baryon number violation such that $n_B - n_{\overline{B}}$ is not constant,
- C and $\mathcal{CP}$ violation, because if these asymmetries are conserved, for each reaction that creates a net number of baryons over antibaryons there would be a $\mathcal{CP}$ conjugate reaction that generates a net number of antibaryons over baryons, and
- departure from thermal equilibrium to allow for baryon number violation.

1.2.2 First observation of $\mathcal{P}$, C and $\mathcal{CP}$ violation in weak interactions

Until 1956, parity conservation was believed to be one of the fundamental conservation laws. That year, the theoretical physicists T. D. Lee and C. N. Yang [29] reviewed the existing experimental data and revealed that while parity conservation had been verified in decays by the strong or electromagnetic interactions, it was untested in the weak interaction. They proposed some

[9] The baryon asymmetry of the universe Y_B is characterized by the ratio of the baryon number density to the photon entropy density.

direct experimental tests. Few months later, in 1957, a group led by C. S. Wu carried out a first test based on β-decay[10] of Cobalt-60 nuclei ($^{60}_{27}\text{Co} \rightarrow {}^{60}_{28}\text{Ni}\ e^-\bar{\nu}_e$) [30]. They observed that some reactions did not occur as often as their mirror image and probed that weak interactions violate parity symmetry. In the same year R. Garwin's group studied the pion decay ($\pi^-(\bar{u}d) \rightarrow \mu^-\bar{\nu_\mu}$). The comparison with π^+ decay implied that charge conjugation symmetry is also violated in weak interactions. However, the combined symmetry $\mathcal{CP}$ seemed to be preserved.

With the discovery of parity violation, Fermi's theory, developed in the 1933 to explain β - decay by introducing the neutrino, was revised to incorporate the new phenomena. Fermi described the β-decay as a four-fermion local interaction between a leptonic current associated to the electron and neutrino and a hadronic current for the neutron and the proton. In 1957 R. Feynman and M. Gell-Mann [31] and others, presented a new theory where these currents where described by a linear combination of a vector and an axial operator, V-A. These two operators have opposite parities and allow parity violation to take place (and also ensures that mass-less right-handed fermions do not interact weakly). According to this theory, the muon and the neutron β-decay decay involve different particles and also have different decay times but its coupling constants are very similar, and therefore they were governed by the same interaction. Several experiments were conducted after this idea of universality of the weak interaction, including new mesons, pion ($\pi^-(\bar{u}d)$) and kaon ($k^-(\bar{u}s)$) decays. In those, the strength of the coupling in the muon and in the nuclear β-decay was found to be different. Furthermore, different coupling strengths were found for non-strange and strange particles. These observations were originally explained by Cabibbo in 1963 [32]: the weak interactions of quarks have the same strength as the leptons, but the weak eigenstates of quarks differ from the mass eigenstates (u, d and s). He proposed a theory to explain the weak interactions of quarks (see next section).

Within this theory, $\mathcal{CP}$ symmetry was assumed to hold in weak interactions. Thus, the discovery of $\mathcal{CP}$ violation was completely unexpected when, in 1964, V. Fitch, J. Cronin and collaborators observed this phenomenon for the first time in the study of the decays of neutral kaons, particles formed by a strange quark and a down antiquark [33]. The observed effect was small (one part in a thousand), but was extremely important because it proved that matter and antimatter are intrinsically different. It took almost ten years to explain this phenomenon in the context of the SM of particle physics.

In 2001, direct $\mathcal{CP}$ violation was observed in a different system, $B(\bar{u}b)$ mesons [34,35]. Due to the $\mathcal{CPT}$ theorem, which states that local quantum field theories satisfying Lorentz invariance and Hermiticity must be symmetric under a combined transformation of $\mathcal{C}$, $\mathcal{P}$ and $\mathcal{T}$ (time reversal), $\mathcal{CP}$ violation implies violation of the time-reversal symmetry. However it was not until 2012 that time reversal violation was observed in the B^0-$\bar{B}^0$ system [36] through the exchange of initial and final states in transitions that can only be connected by a $\mathcal{T}$-symmetry transformation. The problem of unstability of the particles is bypassed using 'entanglement' [37] in the B factory.

[10] The strength of the weak interaction for quarks can be determined from the study of nuclear β-decay.

1.2.3 The weak interactions of quarks

Both the slightly different values of the strength of the coupling in the muon G_F^μ and in the nuclear β-decay G_F^β and the observed suppression of kaon decay rates compared to the expectation assuming a universal weak interaction for quarks were explained by Cabibbo hypothesis (1963): the weak eigenstates of quarks differ from the mass eigenstates, i.e. weak interactions of quarks have the same strength as for leptons but a u quark couples to d', a linear combination of d and s quarks. He proposed the theory of weak interactions written in terms of the quark u with charge +2/3 and the quarks d and s with charge -1/3, forming the doublet

$$\begin{pmatrix} u \\ d' \end{pmatrix} = \begin{pmatrix} u \\ d\ cos\ \theta_c\ +\ s\ sin\ \theta_c \end{pmatrix}$$

where θ_c is known as the Cabibbo angle. The observed different values in G_F^μ and G_F^β and the kaon decay $K^-(\bar{u}s) \rightarrow \mu^-\bar{\nu}_\mu$ rate relative to the pion decay rate were explained with this hypothesis for $\theta_c \sim 13^\circ$ [33]:

$$G_F^\beta\ =\ G_F^\mu\ cos\ \theta_c \quad \text{and} \quad \frac{\Gamma(K^-(\bar{u}s) \rightarrow \mu^-\bar{\nu}_\mu)}{\Gamma(\pi^-(\bar{u}d) \rightarrow \mu^-\bar{\nu}_\mu)}\ =\ tan^2\theta_c\ . \tag{1.8}$$

When the Cabibbo mechanism was proposed, the charm quark (c) had not been discovered. Since this mechanism allows for ud and us couplings, the flavour changing neutral current (FCNC) decay of the neutral kaon $K_L \rightarrow \mu^+\mu-$ can occur via the exchange of a virtual u. Computing the neutral current one obtains:

$$u\bar{u}\ +\ d\bar{d}\ cos^2\theta_c\ +\ (s\bar{d} + d\bar{s})\ cos\ \theta_c\ sin\ \theta_c\ , \tag{1.9}$$

i.e. the doublet of quarks formed by the quark u and d' generates a neutral current carrying strangeness. However, the observed branching ratio of $K_L \rightarrow \mu^+\mu-$ is much smaller than the expected. This observation was explained in 1970 by the GIM mechanism [38] proposed by S. Glashow, J. Iliopoulos and L. Maiani that postulated the existence of an extra (fourth) quark (before discovery of the charm quark in 1974) and introduced a new doublet of quarks formed by the quark c and s', a linear combination of s and d orthogonal to d',

$$\begin{pmatrix} c \\ s' \end{pmatrix} = \begin{pmatrix} c \\ s\ cos\ \theta_c\ -\ d\ sin\ \theta_c \end{pmatrix}.$$

In this way the term $(s\bar{d} + d\bar{s})$ is cancelled naturally and it explains the smallness of the observed $K_L \rightarrow \mu^+\mu-$ branching ratio. Flavour changing neutral current interactions are only induced in higher order weak interaction with different masses for equal charge quarks. With this mechanism, the charged current in the mass eigenstate basis can be written as

$$-i\frac{g_W}{\sqrt{2}}(\bar{u},\quad \bar{c})\ \gamma^\mu\ V\ \tfrac{1}{2}(1-\gamma_5)\ \begin{pmatrix} d \\ s \end{pmatrix},$$

where the matrix V is defined as

$$V = \begin{pmatrix} cos\ \theta_c & sin\ \theta_c \\ -\ sin\ \theta_c & cos\ \theta_c \end{pmatrix}.$$

In 1973, M. Kobayashi and T. Maskawa [39] extended this matrix to account for $\mathcal{CP}$ violating effects observed in the kaon system [33] nine years before. A third quark family was needed and, even though there was no experimental evidence at that time, two new quarks were predicted, the bottom quark (b) and the top quark (t). Some years later, in 1978 [40,41] and in 1995 [42,43] respectively, they were observed at Fermilab.

1.2.4 The CKM matrix and $\mathcal{CP}$ violation in the Standard Model

The Cabibbo mechanism is naturally extended to the three generations in the SM and the weak interaction of quarks is described in terms of the unitary CKM matrix [32, 39], V_{CKM}, which is a 3×3 unitary matrix that operates on the mass eigenstates of the down-type quarks (d, s, b) resulting in the corresponding weak eigenstates (d', s', b'):

$$\begin{pmatrix} d' \\ s' \\ b' \end{pmatrix} = V_{CKM} \begin{pmatrix} d \\ s \\ b \end{pmatrix} \quad \text{with} \quad V_{CKM} = \begin{pmatrix} V_{ud} & V_{us} & V_{ub} \\ V_{cd} & V_{cs} & V_{cb} \\ V_{td} & V_{ts} & V_{tb} \end{pmatrix}$$

Consequently, in the SM, the weak charged-current vertices involving quarks are given by

$$-i\frac{g_W}{\sqrt{2}}(\bar{u}, \quad \bar{c}, \quad \bar{t})\,\gamma^\mu \begin{pmatrix} V_{ud} & V_{us} & V_{ub} \\ V_{cd} & V_{cs} & V_{cb} \\ V_{td} & V_{ts} & V_{tb} \end{pmatrix} \frac{1}{2}(1-\gamma_5) \begin{pmatrix} d \\ s \\ b \end{pmatrix}.$$

For example the weak partner of the top quark is b', which is a linear combination of the mass eigenstates of the three down-type quarks d, s and b. In general, the coupling of two quarks q_1 and q_2 to a W boson is proportional to the corresponding CKM matrix element $V_{q_1q_2}$. These matrix elements are complex constants which values are free parameters of the SM and thus are derived from experiments. As shown in Table 1.4, diagonal elements have by far the largest values, so transitions of quarks within a generation are favoured over transitions into quarks of others. For the given example this implies that the top quark can in principle decay into any of the three down-type quarks, but the decay into a b quark is the most probable one.

Within the SM, the charged weak interaction provides the only way to change flavour and to change from one generation of quarks to another. These charged current interactions are not invariant under $\mathcal{CP}$ transformations. In the following, it will be shown that $\mathcal{CP}$ violation is allowed in the SM if a complex phase appears in the CKM matrix in the quark sector.

A general n×n complex matrix has n^2 complex elements, and thus $2n^2$ real parameters. Unitary ($V^\dagger V = VV^\dagger = 1$) implies n^2 constraints: n unitary conditions (unity of the diagonal elements) and n^2-n orthogonality relations (vanishing off-diagonal elements). The phases of the quarks can be rotated freely: $u_{Li} \rightarrow e^{i\phi_i^u} u_{Li}$ and $d_{Lj} \rightarrow e^{i\phi_i^d} d_{Lj}$. Since the overall phase is irrelevant, $2n$-1 relative quark phases can be removed. Summarizing, a n×n matrix is described by $2n^2$-n^2-(2n-1) =(n-1)^2 free parameters. Subsequently, one can divide these free parameters of an orthogonal matrix into Euler angles and phases: $\frac{1}{2}n(n-1)$ angles describing the rotations among the n dimensions and the remaining $(n\text{-}1)^2\text{-}\frac{1}{2}n(n-1) = \frac{1}{2}(n-1)(n-2)$ free parameters are the

phases. In the case of the SM, where n=3, there are three Euler angles and one complex phase[11].

The property of unitarity of the CKM matrix sets constraints on the possible values of its elements. These are usually expressed in terms of unitarity triangles, as for example:

$$V_{td}V_{ud}^{*} \; + \; V_{ts}V_{us}^{*} \; + \; V_{tb}V_{ub}^{*} \; = \; 0$$

In addition, the following unitary relations express the so-called *weak universality* since they show that the squared sum of the coupling strengths of the quark u to the d, s and b quarks is equal to the overall charged coupling of the quark c or the quark t:

$$\begin{aligned} V_{ud}V_{ud}^{*} \; + \; V_{us}V_{us}^{*} \; + \; V_{ub}V_{ub}^{*} \; &= \; 1 \\ V_{cd}V_{cd}^{*} \; + \; V_{cs}V_{cs}^{*} \; + \; V_{cb}V_{cb}^{*} \; &= \; 1 \\ V_{td}V_{td}^{*} \; + \; V_{ts}V_{ts}^{*} \; + \; V_{tb}V_{tb}^{*} \; &= \; 1 \end{aligned} \tag{1.10}$$

Furthermore, these sums add up to 1, meaning that 'there is no probability remaining' to couple to a 4^{th} down-type quark.

In the literature there are many different parametrizations of the CKM matrix. A standard representation[12] uses three Euler angles (θ_{12} -the original Cabibbo angle-, θ_{23} and θ_{13}) and one $\mathcal{CP}$ violating phase δ_{13}. Couplings between quark generations i and j vanish if $\theta_{ij} = 0$. With the notation $c_{ij} \; = \; cos\,\theta_{ij}$ and $s_{ij} \; = \; sin\,\theta_{ij}$ one finds:

$$V_{CKM} = \begin{pmatrix} c_{12} & s_{12} & 0 \\ -s_{12} & c_{12} & 0 \\ 0 & 0 & 1 \end{pmatrix} \begin{pmatrix} c_{13} & 0 & s_{13}e^{-i\delta_{13}} \\ 0 & 1 & 0 \\ -s_{13}e^{i\delta_{13}} & 0 & c_{13} \end{pmatrix} \begin{pmatrix} 1 & 0 & 0 \\ 0 & c_{23} & s_{23} \\ 0 & -s_{23} & c_{23} \end{pmatrix}$$

$$= \begin{pmatrix} c_{12}c_{13} & s_{12}c_{13} & s_{13}e^{-i\delta_{13}} \\ -s_{12}c_{23} - c_{12} - s_{23}s_{13}e^{i\delta_{13}} & c_{12}c_{23} - s_{12}s_{23}s_{13}e^{i\delta_{13}} & s_{23}c_{13} \\ s_{12}s_{23} - c_{12} - c_{23}s_{13}e^{i\delta_{13}} & -c_{12}s_{23} - s_{12}c_{23}s_{13}e^{i\delta_{13}} & c_{23}c_{13} \end{pmatrix}.$$

Quarks do not propagate as free particles, but hadronise on a length scale of 10^{-15} m, except the top quark that decays before hadronising. Consequently, the final states of weak interactions involving quarks have to be described in terms of mesons or baryons, such as the neutral kaon system or neutral D- or B-mesons systems. The observed hadronic states are composed of particular quark flavours and, therefore, the quark mass (flavour) eigenstates are the ones that form the observable quantities in hadronic weak interactions. With this, the studies of such hadrons and their oscillations performed in experiments such as Babar [44], Belle [45], Tevatron and LHC provide constraints on the nine individual elements of the CKM matrix separately. The present values are shown in Table 1.4.

[11] To allow for $\mathcal{CP}$ violation the mixing matrix has to contain complex elements satisfying $V_{ij} \neq V_{ij}^{*}$, and this requires at least three families.

[12] This parametrization was introduced by L. L. Chau and W.-Y. Keung in 1984, and has been adopted by the Particle Data Group.

CKM element	Source	Value
$\|V_{ud}\|$	nuclear β-decays	0.97425±0.00022
$\|V_{us}\|$	semi-leptonic K decays	0.2252±0.0009
$\|V_{ub}\|$	semi-leptonic B decays to u-particle ($B \to X_u l^+ \nu$)	0.00415±0.00049
$\|V_{cd}\|$	ν and $\bar{\nu}$ induced c-particle production	0.230±0.011
$\|V_{cs}\|$	semi-leptonic D or leptonic D_s decays	1.006±0.023
$\|V_{cb}\|$	semi-leptonic B decays to c-particle ($B \to \bar{D}^* l^+ \nu$)	0.0409±0.0011
$\|V_{td}\|$ $\|V_{ts}\|$	loop-mediated and box diagrams with top quarks	0.0084±0.0006 0.0429±0.0026
$\|V_{tb}\|$	$R = \frac{B(t\to Wb)}{B(t\to Wq)} = \frac{\|V_{tb}\|^2}{\sum_q \|V_{tq}\|^2} = \|V_{tb}\|^2$, where $q = b, s, d$	0.89±0.07

Table 1.4: *Direct determinations of the CKM matrix elements V_{ij} (values from PDG 2012 report [17]).*

Taking all these individual measurements and exploiting unitarity, further constrains can be placed on the less precisely determined elements by performing a global fit [17]. This leads to:

$$V_{CKM} \approx \begin{pmatrix} 0.974 & 0.227 & 0.004 \\ 0.227 & 0.973 & 0.042 \\ 0.008 & 0.042 & 0.999 \end{pmatrix}$$

It is important to highlight the strong hierarchy in the size of the matrix elements of the quark mixing matrix. There is no doubt that this is intriguing but its origin is not (yet) understood. The origin of the quark mixing matrix lies in the Yukawa couplings between the Higgs field and the quark fields. At the same time, these Yukawa couplings are responsible for the generation of the quark masses which values also show a striking hierarchy. This leads to think on possible underlying connection between the quark masses and the charged current quark couplings.

1.2.5 New sources of $\mathcal{CP}$ violation beyond the Standard Model

The Kobayashi-Maskawa mechanism provides an elegant and simple explanation of $\mathcal{CP}$ violation in the weak interaction for quarks. The model has only one free parameter that governs $\mathcal{CP}$ violation, and it manages to explain all the $\mathcal{CP}$ violating measurements obtained in particle physics experiments to date. Nevertheless, this is not sufficient to explain the observed matter-antimatter asymmetry in the universe -our original question-. This shortcoming has profound implications: the SM is not complete and other sources of $\mathcal{CP}$ violation must exist. There are suggestions (not yet experimentally confirmed) that $\mathcal{CP}$ violation in the lepton sector during the early evolution of the universe might account for the observed asymmetry. However, it is also possible that there are new (yet undiscovered) $\mathcal{CP}$ violating processes beyond the SM. In this direction, many extensions of the SM have been proposed. If any one of these theories is correct, the first glimpse of new physics beyond the SM may come from studies of $\mathcal{CP}$ violation.

In this thesis, an extension of the SM with additional sources of $\mathcal{CP}$ violation in the top quark sector is proposed. It is generally believed that the top quark, because of its large mass, allows to probe new physics beyond the SM. For this reason, top quark physics constitutes one of the main programs for hadron colliders such as the current LHC. The top quark decays almost exclusively

into a b quark and a W boson via the weak interaction, thus it allows to probe the chiral structure of the $W - t - b$ interaction (so-called Wtb vertex).

2

Observables sensitive to $\mathcal{CP}$ violation in a modified Lagrangian for the Wtb vertex

In this chapter an extension of the SM with additional sources of $\mathcal{CP}$ violation in the top quark sector is presented. Among the different top quark couplings to the gauge and Higgs bosons, the Wtb vertex deserves a special attention, precisely because the top quark decays almost exclusively through the $t \to bW^+$ mode. If this vertex were somehow modified by new physics to have a different magnitude, it would affect the top quark's intrinsic width and thus the angular distribution of its decay products. A modified Lagrangian ($\mathcal{L}_{\text{int}} \implies \mathcal{L}'_{\text{int}}$) with an effective Wtb vertex with additional non-SM couplings is proposed and an observable sensitive to $\mathcal{CP}$ violation in the top quark sector is derived.

The top quark was discovered by the Fermilab experiments CDF and D0 in 1995 [42, 43] around the mass predicted by the electroweak fit of LEP data at CERN. This discovery completed the three family structure of fundamental particles in the SM. The top quark differs from the other SM quarks not only by its large mass, being the most massive elementary particle, but also due to the fact that it decays before hadronisation can take place. Thus, the quark spin information can be studied through its decay products. This makes the top quark a very interesting object and offers some unique possibilities to test the SM predictions and possible new physics beyond the SM. Top quarks are produced via two types of mechanisms: strong and electroweak processes. At hadron colliders like the Tevatron or the LHC, top quarks are predominantly produced via strong interaction in pairs together with their antiquarks. In addition, top quarks are produced through electroweak interaction in which the single top quarks produced are highly polarized and the weak coupling of the top quark to the W boson and the b quark appears both in the production and the decay vertices. Probing the couplings of the Wtb vertex offers an interesting window to new physics. The large sample of top quark events at the LHC allows for such precision measurements.

2.1 Effective Wtb vertex with additional non-SM couplings

One can immediately write down the Wtb vertex as

$$\mathcal{L}_{Wtb}^{SM} = -\frac{g}{\sqrt{2}}\overline{u}_b\gamma^\mu V_{tb}\frac{1}{2}\left(1-\gamma^5\right)\overline{u}_t W_\mu + \text{h.c.}\,, \tag{2.1}$$

where γ^μ denotes the Dirac matrices, γ^5 the chirality matrix and g the coupling constant of the electroweak interaction. This expression reflects the vector ($\bar{\psi}\gamma^\mu\psi$) minus axial ($\bar{\psi}\gamma^\mu\gamma^5\psi$) structure, abbreviated V-A structure, of the weak interaction in the SM. The V+A structure is not implemented in the SM. This explains why this force only couples to left-handed fermions and right-handed antifermions (parity violation).

For a model-independent analysis of the structure of the Wtb vertex, a more general Lagrangian [3, 46] can be considered. The amplitude of the decay $t(p) \to b(k)W^+(q)$, where all particles are on-shell can be written as:

$$\mathcal{L}_{W^+tb} = -\frac{g}{\sqrt{2}}\overline{u}_b\gamma^\mu\left(V_L P_L + V_R P_R\right)u_t W_\mu^+ - \frac{g}{\sqrt{2}}\overline{u}_b\frac{i\sigma^{\mu\nu}}{M_W}q_\nu\left(g_L P_L + g_R P_R\right)u_t W_\mu^+ \tag{2.2}$$

where V_L, V_R, g_L and g_R are left- and right-handed vector and tensor couplings (also called form factors), respectively, and are in general complex. At tree level in the SM, the coupling V_L is given by the CKM matrix element V_{tb} and is therefore almost equal to one, while the other three couplings (so-called anomalous couplings) V_R, g_R and g_L vanish, leading to the pure V-A structure of the SM. Although non-vanishing values of the right-handed coupling V_R and of the tensor couplings g_R and g_L are not forbidden, several constraints on these anomalous couplings exist from both indirect observations and direct measurements (see review in Ref. [47]). Deviations from the expected values can be probed by measuring W polarisation fractions (helicity fractions) or angular asymmetries in the decay products of the top quark decay.

The amplitude of the charge-conjugate decay $\bar{t}(p) \to \bar{b}(k)W^-(q)$ has the general structure:

$$\mathcal{L}_{W^-\bar{t}\bar{b}} = -\frac{g}{\sqrt{2}}\overline{v}_t\gamma^\mu\left(V_L' P_L + V_R' P_R\right)v_b W_\mu^- - \frac{g}{\sqrt{2}}\overline{v}_t\frac{i\sigma^{\mu\nu}}{M_W}q_\nu\left(g_L' P_L + g_R' P_R\right)v_b W_\mu^- \tag{2.3}$$

$\mathcal{CP}$ invariance requires, apart from V_L being real, that the couplings in Eqs.6.1-2.3 satisfy [48, 49]:

$$V_i' = V_i \quad g_i' = g_i \quad (i = L, R). \tag{2.4}$$

Assuming that absorptive parts, i.e. final-state interactions, of the form factors can be neglected, $\mathcal{CPT}$ invariance implies:

$$V_i' = V_i^* \quad g_i' = g_i^* \quad (i = L, R). \tag{2.5}$$

These relations show that, if absorptive parts can be neglected[1], $\mathcal{CPT}$ invariance enforces the

[1]This Lagrangian is assumed to be Hermitian in order to preserve unitarity, as it is demanded for a fundamental theory of elementary particle interactions. This implies that all complex phases in this effective Lagrangian are $\mathcal{CP}$ violating.

real parts of the form factors to be equal, even if $\mathcal{CP}$ is violated:

$$Re(V_i') = Re(V_i) \quad Re(g_i') = Re(g_i) \quad (i = L, R). \tag{2.6}$$

In this case $\mathcal{CP}$ violation induces non-zero imaginary parts which are equal in magnitude but differ in sign, namely,

$$Im(V_i') = -Im(V_i) \quad Im(g_i') = -Im(g_i) \quad (i = L, R). \tag{2.7}$$

Non-zero absorptive parts of the decay amplitude (non-Hermitian Lagrangian) also lead to imaginary parts of the form factors. If $\mathcal{CP}$ is conserved they are equal in magnitude and sign. If $\mathcal{CP}$ is broken then $\mathcal{CP}$ violating absorptive parts of the decay amplitude can contribute to the real parts of the form factors and violate Equation 2.6.

2.2 The top quark production and decay

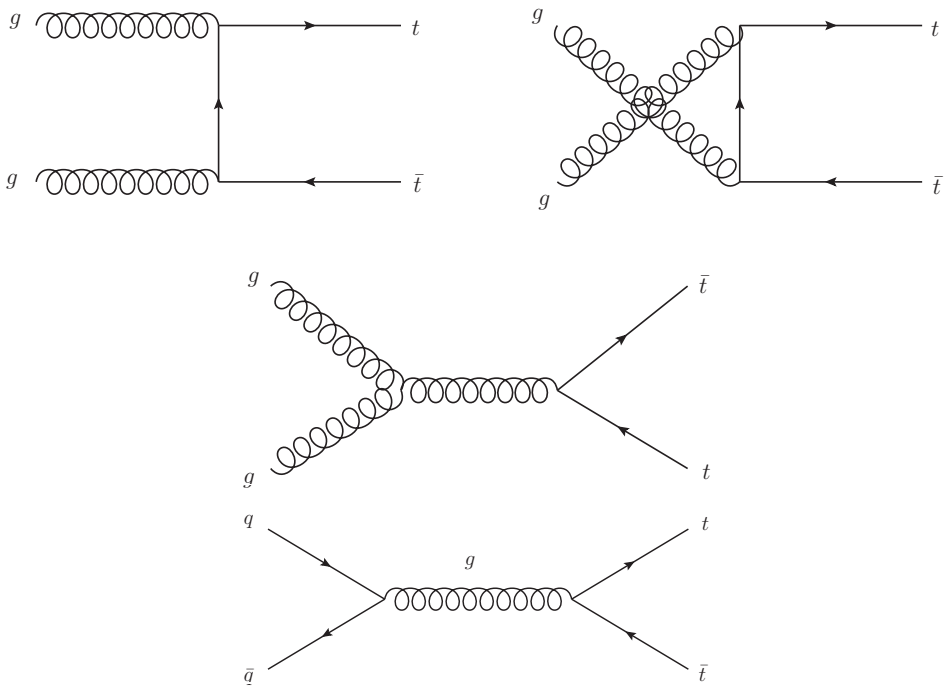

Figure 2.1: *$t\bar{t}$ pair production through gluon fusion (top and middle) and quark and antiquark annihilation (bottom).*

As anticipated, in the SM, the top quark can be produced in top and antitop quark pairs (called $t\bar{t}$ production) or as a single top quark associated with other particles. In hadron colliders, the top quark is predominantly produced in pairs via the strong interaction, through gluon

fusion or quark and antiquark annihilation (see Figure 2.1). At the LHC (unlike the Tevatron) the former mechanism dominates, contributing by a factor ∼80% to the total top quark pair production cross section. The $t\bar{t}$ production cross section is predicted at next-to-next-to-leading order and include soft gluon re-summation at next-to-next-to-leading logarithmic order (NNLO+NNLL). The most precise predictions for the LHC are $\sigma_{t\bar{t}} = 177.3^{+10.1}_{-10.8}$ pb at 7 TeV and $\sigma_{t\bar{t}} = 252.9^{+13.3}_{-14.5}$ pb at 8 TeV for a top quark mass of $m_{top} = 172.5$ GeV/c^2 [50].

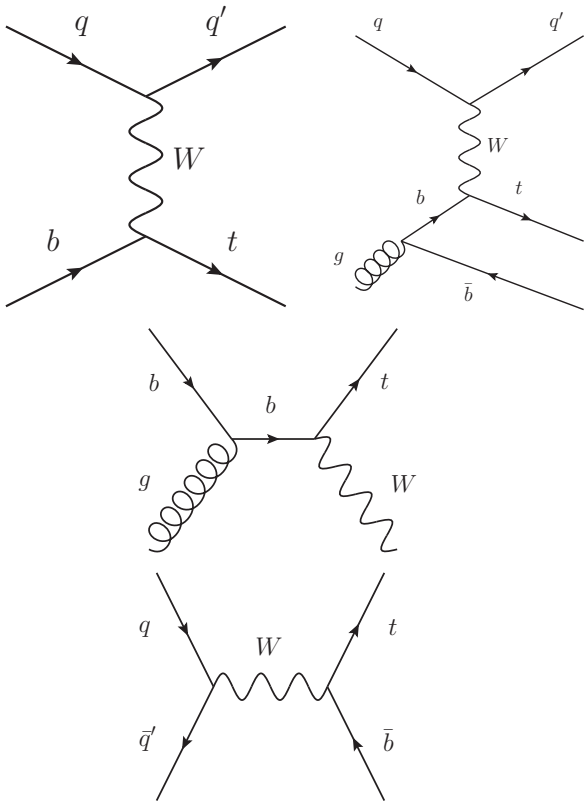

Figure 2.2: *Single top quark production mechanisms: t-channel (top), Wt associated production (middle) and s-channel (bottom).*

In the case of single top quarks, they are produced through electroweak interactions via three different mechanisms: t-channel, Wt associated production and s-channel (see Figure 2.2). The cross section values are calculated at next-to-leading order QCD with resummed next-to-next-to-leading logarithmic accuracy, called approximate next-to-next-to-leading order ($\text{NNLO}_{\text{approx}}$). The predictions for the LHC for a top quark mass of $m_{top} = 172.5$ GeV are: $64.6^{+2.7}_{-2.0}$ pb at 7 TeV and $87.8^{+3.4}_{-1.9}$ pb at 8 TeV for the t-channel [51], 15.7 ± 1.1 pb at 7 TeV and 22.4 ± 1.5 pb at 8 TeV for the Wt associated production [52] and 4.6 ± 0.2 pb at 7 TeV and 5.6 ± 0.2 pb at 8 TeV

for the s-channel [53].

The $t\bar{t}$ and single top quark production cross sections have been measured at the LHC. Figure 2.3 shows the ATLAS cross section measurements compared to their theoretical predictions. The inclusive $t\bar{t}$ production cross section is measured to be 177^{+11}_{-9} pb at 7 TeV [54] and 241 ± 32 pb at 8 TeV in the lepton+jets channel [55]. The single top quark t-channel and Wt associated production cross sections have been also measured in ATLAS at both 7 and 8 TeV [56–59], while for the s-channel an upper limit is set at 7 TeV [60]. Using the ratio of the measured t-channel cross-section to the predicted cross-section and assuming that the CKM matrix elements obey the relation $|V_{tb}| >> |V_{ts}|, |V_{td}|$, the coupling strength at the Wtb vertex is determined to be $|V_{tb}| = 0.97^{+0.09}_{-0.10}$. Assuming that $|V_{tb}| \leq 1$, a lower limit of $|V_{tb}| > 0.78$ is obtained at the 95% confidence level [57].

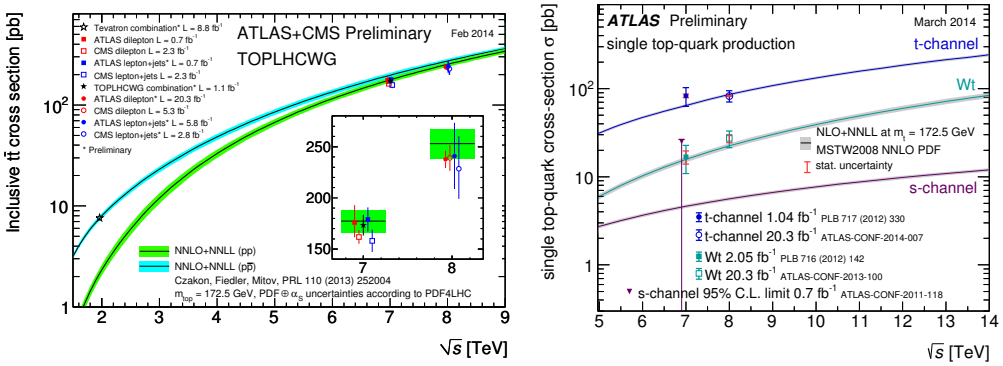

Figure 2.3: *Left: Summary of LHC and Tevatron measurements of the $t\bar{t}$ production cross section as a function of the centre of mass energy compared to the NNLO+NNLL calculation. The theory band represents uncertainties due to renormalisation and factorisation scale, parton density functions and the strong coupling. The measurements and the theory calculation is quoted at m_{top} = 172.5 GeV. Right: Summary of measurements of the single top production cross sections in various channels as a function of the center of mass energy compared to a theoretical calculation based on approximate NLO. For the s-channel only an upper limit is shown.*

In the SM, the top quark decays weakly into any down-type quark d, s or b and an on-shell W boson. The branching ratio for the different modes can be calculated using the CKM matrix elements. From them, one can see that top quark decays almost 100% via $t \rightarrow Wb$. The top quark decay is classified in different channels according to the decay of the W boson. The latter can decay either hadronically into two quarks (ud or cs) or leptonically into a lepton and the corresponding antineutrino. The relative branching rations are:

$$\frac{\text{hadronically}}{\text{leptonically}} = \frac{\{cs, ud\} \times colour}{\{e, \mu, \tau\}} = 6/3 \tag{2.8}$$

This leads to the following topologies for events with two W bosons in the final state such as $t\bar{t}$ and Wt events: all-hadronic (36/81), lepton+jets (36/81) and dileptonic (9/81) events, as it can

be seen in Figure 2.4. In the case of the t- and s-channels, where there is only one W in the event, one can classify them in hadronic (6/9) or leptonic (3/9) final state topologies. An important point is that the τ lepton is not identified by itself in the detector, but its decay products. The lepton τ decays dominantly to a pair of jets (64.8%) or to an electron (17.8%) or muon (17.4%) plus two corresponding neutrinos. Taking this into account, these two single top quark channels can be classified in another way: hadronic sample including hadronic τ decays (74.7%) and leptonic sample with electrons or muons (25.3%). In the analysis presented in this thesis, t-channel single top quark events with leptonic W boson decay with an electron or muon in the final state are considered.

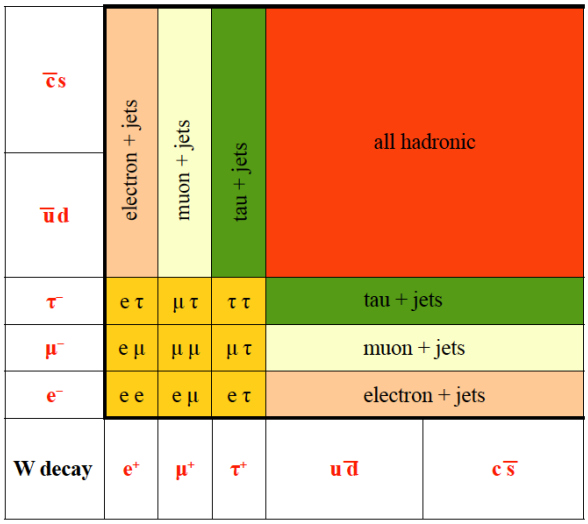

Figure 2.4: *The top quark decay channels.*

The CKM matrix element $|V_{tb}|$ does not only play an important role for the decay mode of the top quark but also for its decay width. The theoretical prediction of the decay width is:

$$\Gamma(t \rightarrow Wb) = \frac{G_F m_t^3}{8\pi\sqrt{2}} |V_{tb}| \left(1 + \vartheta(\frac{m_W^4}{m_t^4})\right) \approx 1.5\ GeV. \tag{2.9}$$

This can be translated into a lifetime of $\tau_t \approx 4.3 \times 10^{-25}$ s and $c\tau \approx 0.12$ fm. D0 experiment extracts the total width of the top quark from the measured t-channel cross section and from the branching ratio $\mathcal{BR}(t \rightarrow Wb)$ which is extracted from a measurement of the ratio $R = \mathcal{BR}(t \rightarrow Wb)/\mathcal{BR}(t \rightarrow Wq)$ in the $t\bar{t}$ lepton+jets channel. The result is $\Gamma = 2.00^{+0.47}_{-0.43}$ GeV which translates to a top-quark lifetime of $\tau_t = (3.29^{+0.90}_{-0.63}) \times 10^{-25}$ s [61]. Compared to the hadronisation scale $\tau_{had} \approx 28 \times 10^{-25}$ s this means that the top quark decays before hadronisation can take place. Therefore, as already mentioned, the spin[2] information of this quark is transferred to the decay products.

[2] As for the other fundamental fermions the spin of the top quark is expected to be 1/2.

2.3 The helicity of W bosons from top quark decays

In the top quark decay, the emitted W boson (s=1) is polarised with negative, zero or positive helicity[3], as shown in Figure 2.5. Each polarisation state has a corresponding partial decay width (Γ_L, Γ_0 and Γ_R) defined in relation to the total decay width $\Gamma(t \rightarrow Wb) = \Gamma_L + \Gamma_0 + \Gamma_R$. The W boson only couples to b quarks of left-handed chirality, which translates into left-handed helicity, assuming the b quark is mass-less. This assumption is justified by the small b quark mass compared to the masses of the top quark and the W boson. In the top quark rest frame the W boson and the b quark are emitted back-to-back and therefore, due to angular momentum conservation[4], the W boson can then only either be longitudinally polarised or left-handed, depending on the orientation of the top quark spin.

Negative helicity				Zero helicity				Positive helicity			
	Spin		Fraction		Spin		Fraction		Spin		Fraction
	b t W	$-\frac{1}{2}$ $+\frac{1}{2}$ +1	0.30	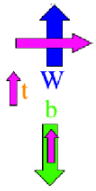	W t b	0 $+\frac{1}{2}$ $+\frac{1}{2}$	0.70	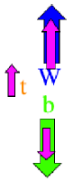	W t b	+1 $+\frac{1}{2}$ $-\frac{1}{2}$	3.6×10^{-4}

Figure 2.5: *Schematic representation of the top quark decay (for convenience in its rest frame) into a b quark and a W boson with negative (left-handed), zero and positive (right-handed) helicity. The big arrows represent the W boson and b quark momentum directions and the small ones the spin of the particles.*

The different polarisation states of the W boson determine the angular distribution of its decay products. In the leptonic decay, the helicity information is visible through angle θ^*, which is defined as the angle between the momentum of the charged lepton in the W rest frame and the W momentum in the top quark rest frame (see Figure 2.6). The normalised differential decay rate can be written as:

$$\frac{1}{\Gamma}\frac{d\Gamma}{d\cos\theta^*} = \frac{3}{8}(1-\cos\theta^*)^2 F_{\mathrm{L}} + \frac{3}{4}\sin^2\theta^* F_0 + \frac{3}{8}(1+\cos\theta^*)^2 F_{\mathrm{R}}\,, \tag{2.10}$$

with $F_i \equiv \Gamma_i/\Gamma$ being the W boson helicity fractions. The resulting $\cos\theta^*$ distribution is shown in Figure 2.10. At NNLO in QCD, the prediction is $F_L = 0.311 \pm 0.005$, $F_0 = 0.687 \pm 0.005$

[3]Helicity is the projection of the spin $\vec{s}$ of a particle along its momentum direction $\hat{p}$: $\mathrm{h} = \vec{s}\cdot\hat{p}$. A particle is of positive helicity, if the spin is projected parallel to its momentum, and of negative helicity, if the projection is antiparallel to the direction of motion.

[4]The sum of the b quark spin and the W boson spin has to be the top quark spin angular momentum (± 1/2).

and $F_R = 0.0017 \pm 0.0001$ [62] for $m_t = 172.8 \pm 1.3$ GeV/c^2 and m_b=4.8 GeV/c^2.

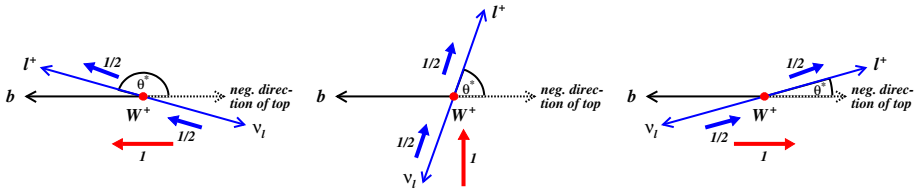

(a) left-handed (b) longitudinal (c) right-handed

Figure 2.6: *Illustration of the decay of a polarised W boson into a charged lepton and a neutrino in the W boson rest frame. The W boson can be left-handed (a), longitudinally polarised (b) or right-handed (c). The dotted black arrow represents the direction of the W boson momentum in the rest frame of the top quark.*

A common method to extract information about the Wtb vertex from the angular distribution $\cos\theta^*$ is through asymmetries [46]. For any fixed value of z in the interval [-1,+1], one can define an asymmetry as:

$$A_z = \frac{N(\cos\theta^* > z) - N(\cos\theta^* < z)}{N(\cos\theta^* > z) + N(\cos\theta^* < z)} \tag{2.11}$$

where $N(\cos\theta^* > z)$ (or $N(\cos\theta^* < z)$) is the number of events where $\cos\theta^*$ is below (or above) z. The most obvious choice is $z = 0$, giving the forward-backward (FB) asymmetry A_{FB}, which is proportional to the difference between F_{R} and F_{L}. For $z = \mp(2^{2/3} - 1)$, the asymmetries depend only on F_{R} and F_0, or F_0 and F_{L}:

$$\begin{aligned} z = 0 \quad &\rightarrow \quad A_{\mathrm{FB}} = \frac{3}{4}(F_{\mathrm{R}} - F_{\mathrm{L}}) \\ z = -(2^{2/3} - 1) \quad &\rightarrow \quad A_+ = 3\beta[F_0 + (1+\beta)F_{\mathrm{R}}] \\ z = (2^{2/3} - 1) \quad &\rightarrow \quad A_- = -3\beta[F_0 + (1+\beta)F_{\mathrm{L}}]\,, \end{aligned} \tag{2.12}$$

where $\beta = 2^{1/3} - 1$. At LO in the SM the values of these angular asymmetries are $A_{\mathrm{FB}} = -0.227$, $A_+ = 0.544$ and $A_- = -0.841$. From the A_+ and A_- asymmetries and using $F_{\mathrm{R}} + F_{\mathrm{L}} + F_0 = 1$, the W boson helicity fractions can be obtained:

$$F_{\mathrm{L}} = \frac{1}{1-\beta} - \frac{A_+ - \beta A_-}{3\beta(1-\beta^2)}\,,\quad F_0 = -\frac{1+\beta}{1-\beta} + \frac{A_+ - A_-}{3\beta(1-\beta)}\,,\quad F_{\mathrm{R}} = \frac{1}{1-\beta} + \frac{A_- - \beta A_+}{3\beta(1-\beta^2)}\,. \tag{2.13}$$

The W boson helicity fractions or asymmetries in the $\cos\theta^*$ distribution have been measured both at Tevatron and LHC in $t\bar{t}$ events. A recent combination of the current helicity fractions measurements [63] at LHC gives:

$$\begin{aligned} F_{\mathrm{L}} &= 0.359 \pm 0.021\ (\mathrm{stat.}) \pm 0.028\ (\mathrm{syst.}) \\ F_0 &= 0.626 \pm 0.034\ (\mathrm{stat.}) \pm 0.048\ (\mathrm{syst.}) \\ F_{\mathrm{R}} &= 0.015 \pm 0.034\ (\mathrm{stat.} \oplus \mathrm{syst.})\,. \end{aligned} \tag{2.14}$$

These measurements are in agreement with NNLO QCD predictions and have allowed to set limits to the real part of the anomalous couplings V_R, g_L and g_R (see Figure 2.7). However, these observables are not sensitive to all anomalous couplings, especially to their complex phases that would imply that the top quark decay has a $\mathcal{CP}$ violating component.

2.4 W boson polarisation beyond helicity fractions

For unpolarised top quark production the only meaningful reference direction in the top quark rest frame is the momentum $\vec{q}$ of the W boson (or $-\vec{q}$ of the b quark). However for polarised top quarks, such as those produced via electroweak interactions, one can also exploit the direction given by $\vec{s}_t$. From these two directions, further references can be defined normal and transverse to the formed plane:

$$\begin{aligned} \vec{N} &= \vec{s}_t \times \vec{q}\,, \\ \vec{T} &= \vec{q} \times \vec{N}\,, \end{aligned} \tag{2.15}$$

where $\vec{N}$ is the normal and $\vec{T}$ the transverse direction, as can be seen in Figure 2.8. In a similar way that θ^* is defined between the lepton in the W boson rest frame and the momentum $\vec{q}$ of the W boson, the angles θ^{N} and θ^{T} are defined between the lepton from the W boson and these new directions.

Defining the positive $\hat{z}$ axis in the direction $\vec{q}$ of the W boson momentum in the top quark rest frame, the top spin direction is parametrised as:

$$\vec{s}_t = (\sin\theta\ \cos\phi, \sin\theta\ \sin\phi, \cos\theta) \tag{2.16}$$

Following the formalism in Ref. [3], the spin density matrix elements for the W boson helicity components $i, j = 0, \pm 1$ are:

$$\mathcal{A}(t \to W_i b) \cdot \mathcal{A}^*(t \to W_j b) = \frac{g^2}{4} m_t^2 M_{ij}, \tag{2.17}$$

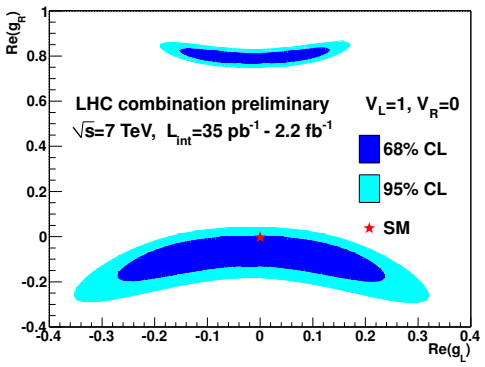

Figure 2.7: *Allowed regions for the Wtb anomalous couplings obtained from the LHC combination of the helicity fractions and assuming V_L=1 and V_R=0, at 68% and 95% confidence level.*

being

$$
\begin{aligned}
M_{00} &= A_0 + 2\frac{|\vec{q}|}{m_t}A_1\cos\theta\,,\\
M_{++} &= B_0(1+\cos\theta) + 2\frac{|\vec{q}|}{m_t}B_1(1+\cos\theta)\,,\\
M_{--} &= B_0(1-\cos\theta) - 2\frac{|\vec{q}|}{m_t}B_1(1-\cos\theta)\,,\\
M_{0+} &= M^*_{+0} = \left[\frac{m_t}{\sqrt{2}M_W}(C_0 - iD_0) - \frac{|\vec{q}|}{\sqrt{2}M_W}(C_1 - iD_1)\right]\sin\theta e^{i\phi}\,,\\
M_{0-} &= M^*_{-0} = \left[\frac{m_t}{\sqrt{2}M_W}(C_0 - iD_0) + \frac{|\vec{q}|}{\sqrt{2}M_W}(C_1 - iD_1)\right]\sin\theta e^{-i\phi}\,,\\
M_{+-} &= M_{-+} = 0.
\end{aligned}
\tag{2.18}
$$

The spin density matrix elements $\tilde{M}_{ij}$ for the decay of antitop quarks are:

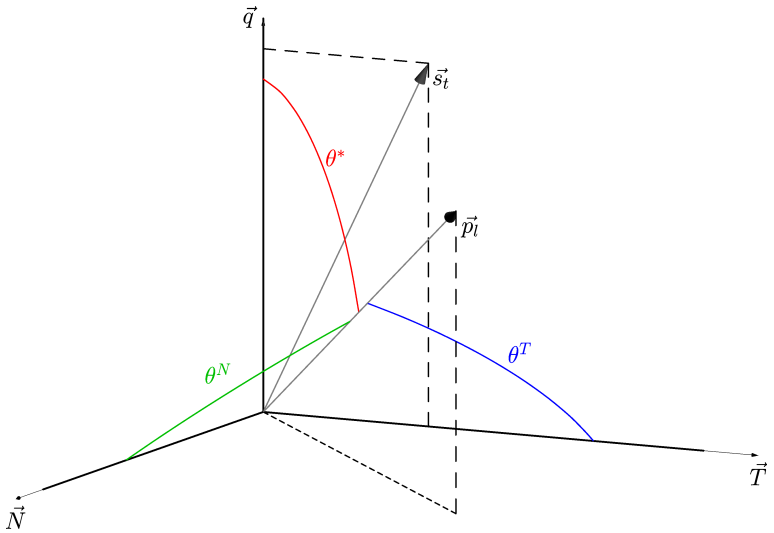

Figure 2.8: *Definition of the two directions $\vec{N}$ and $\vec{T}$ given the direction of polarisation of the top quark, $\vec{s}_t$, and the momentum of the W boson in the top quark rest frame, $\vec{q}$. The angles θ^*, θ^N and θ^T are defined between the three reference directions ($\vec{q}$, $\vec{N}$ and $\vec{T}$, respectively) and the momentum direction of the charged lepton, $\vec{p}_l$.*

$$
\begin{aligned}
\tilde{M}_{00} &= A_0 - 2\frac{|\vec{q}|}{m_t}A_1 \cos\theta\,, \\
\tilde{M}_{++} &= B_0(1+\cos\theta) - 2\frac{|\vec{q}|}{m_t}B_1(1+\cos\theta)\,, \\
\tilde{M}_{--} &= B_0(1-\cos\theta) + 2\frac{|\vec{q}|}{m_t}B_1(1-\cos\theta)\,, \\
\tilde{M}_{0+} &= \tilde{M}^*_{+0} = \left[\frac{m_t}{\sqrt{2}M_W}\,(C_0+iD_0) - \frac{|\vec{q}|}{\sqrt{2}M_W}(C_1+iD_1)\right]\sin\theta e^{i\phi}\,, \\
\tilde{M}_{0-} &= \tilde{M}^*_{-0} = \left[\frac{m_t}{\sqrt{2}M_W}\,(C_0+iD_0) + \frac{|\vec{q}|}{\sqrt{2}M_W}(C_1+iD_1)\right]\sin\theta e^{-i\phi}\,, \\
\tilde{M}_{+-} &= \tilde{M}_{-+} = 0.
\end{aligned}
\tag{2.19}
$$

The dependence on the Wtb couplings is encoded in eight dimensionless form factors:

$$
\begin{aligned}
A_0 &= \frac{m_t^2}{M_W^2}[|V_{\rm L}|^2+|V_{\rm R}|^2](1-x_W^2) \;+\; [|g_{\rm L}|^2+|g_{\rm R}|^2](1-x_W^2) \\
&\quad -\; 4x_b Re[V_{\rm L}V_{\rm R}^* + g_{\rm L}g_{\rm R}^*] \;-\; 2\frac{m_t}{M_W}Re[V_{\rm L}g_{\rm R}^* + V_{\rm R}g_{\rm L}^*](1-x_W^2) \\
&\quad +\; 2\frac{m_t}{M_W}x_b Re[V_{\rm L}g_{\rm L}^* + V_{\rm R}g_{\rm R}^*](1+x_W^2)\,, \\
A_1 &= \frac{m_t^2}{M_W^2}[|V_{\rm L}|^2-|V_{\rm R}|^2] \;-\; [|g_{\rm L}|^2-|g_{\rm R}|^2] \;-\; 2\frac{m_t}{M_W}Re[V_{\rm L}g_{\rm R}^* - V_{\rm R}g_{\rm L}^*] \\
&\quad +\; 2\frac{m_t}{M_W}x_b Re[V_{\rm L}g_{\rm L}^* - V_{\rm R}g_{\rm R}^*]\,, \\
B_0 &= [|V_{\rm L}|^2+|V_{\rm R}|^2](1-x_W^2) \;+\; \frac{m_t^2}{M_W^2}[|g_{\rm L}|^2+|g_{\rm R}|^2](1-x_W^2) \\
&\quad -\; 4x_b Re[V_{\rm L}V_{\rm R}^* + g_{\rm L}g_{\rm R}^*] \;-\; 2\frac{m_t}{M_W}Re[V_{\rm L}g_{\rm R}^* + V_{\rm R}g_{\rm L}^*](1-x_W^2) \\
&\quad +\; 2\frac{m_t}{M_W}x_b Re[V_{\rm L}g_{\rm L}^* + V_{\rm R}g_{\rm R}^*](1+x_W^2)\,, \\
B_1 &= -[|V_{\rm L}|^2-|V_{\rm R}|^2] \;+\; \frac{m_t^2}{M_W^2}[|g_{\rm L}|^2-|g_{\rm R}|^2] \;+\; 2\frac{m_t}{M_W}Re[V_{\rm L}g_{\rm R}^* - V_{\rm R}g_{\rm L}^*] \\
&\quad +\; 2\frac{m_t}{M_W}x_b Re[V_{\rm L}g_{\rm L}^* - V_{\rm R}g_{\rm R}^*]\,, \\
C_0 &= [|V_{\rm L}|^2+|V_{\rm R}|^2+|g_{\rm L}|^2+|g_{\rm R}|^2](1-x_W^2) \;-2x_b Re[V_{\rm L}V_{\rm R}^* + g_{\rm L}g_{\rm R}^*](1+x_W^2) \\
&\quad -\; \frac{m_t}{M_W}Re[V_{\rm L}g_{\rm R}^* + V_{\rm R}g_{\rm L}^*](1-x_W^4) \;+4x_W x_b Re[V_{\rm L}g_{\rm L}^* + V_{\rm R}g_{\rm R}^*]\,, \\
C_1 &= 2[-|V_{\rm L}|^2+|V_{\rm R}|^2+|g_{\rm L}|^2-|g_{\rm R}|^2] \;-2\frac{m_t}{M_W}Re[V_{\rm L}g_{\rm R}^* - V_{\rm R}g_{\rm L}^*](1+x_W^2)\,, \\
D_0 &= \frac{m_t}{M_W}Im[V_{\rm L}g_{\rm R}^* + V_{\rm R}g_{\rm L}^*](1-2x_W^2+x_W^4)\,, \\
D_1 &= -4x_b Im[V_{\rm L}V_{\rm R}^* + g_{\rm L}g_{\rm R}^*] \;-\; 2\frac{m_t}{M_W}Im[V_{\rm L}g_{\rm R}^* - V_{\rm R}g_{\rm L}^*](1-x_W^2)\,,
\end{aligned}
\tag{2.20}
$$

being $x_W = M_W/m_t$ and $x_b = m_b/m_t$. The W boson momentum in the top quark rest frame can be written as: $|\vec{q}| = \frac{m_t}{2}(1-x_W^2)$. One can check that, in the x_b=0 limit, the linear terms with new couplings interfering with V_L (non-zero in the SM) are $Re(g_{\rm R})$ and $Im(g_{\rm R})$. Thus, top quark decays are most sensitive to the presence of $g_{\rm R}$ coupling.

Using the form factors defined above, the partial widths for the top decay into a W boson with helicity 0 or ±1 and the total decay width can be written as [3, 46]:

$$
\Gamma_0 = \frac{g^2|\vec{q}|}{32\pi}A_0\,, \qquad \Gamma_\pm = \frac{g^2|\vec{q}|}{32\pi}\left(B_0 \pm 2\frac{|\vec{q}|}{m_t}B_1\right), \qquad \text{and } \Gamma = \Gamma_R+\Gamma_0+\Gamma_L = A_0+2B_0\,. \tag{2.21}
$$

For the new directions, two further sets of W boson polarisation fractions can be defined, Γ_-^N, Γ_0^N and Γ_+^N (normal) and Γ_-^T, Γ_0^T and Γ_+^T (transverse):

$$\Gamma_0^N = \frac{g^2|\vec{q}|}{32\pi} B_0 \qquad \Gamma_\pm^N = \frac{g^2|\vec{q}|}{32\pi}\left(\frac{A_0 + B_0}{2} \pm \frac{\pi}{4}\frac{m_t}{M_W} D_1\right) \tag{2.22}$$

$$\Gamma_0^T = \Gamma_0^N \qquad \Gamma_\pm^T = \frac{g^2|\vec{q}|}{32\pi}\left(\frac{A_0 + B_0}{2} \pm \frac{\pi}{4}\frac{m_t}{M_W} C_0\right). \tag{2.23}$$

At tree level in the SM, the values of these W boson polarisation fractions are $F_{\rm L}^N = 0.4256$, $F_0^N = 0.1487$, $F_{\rm R}^N = 0.4256$ and $F_{\rm L}^T = 0.1718$, $F_0^T = 0.1487$, $F_{\rm R}^T = 0.6794$ for m_t=175 GeV/c^2, m_W=80.4 GeV/c^2 and m_b=4.8 GeV/c^2. These quantities are very useful to access some of the off-diagonal terms in the spin density matrix, namely C_0 and D_1. It is worth to remark that D_1 depends on the imaginary part of the anomalous couplings; so observables depending on the normal set of polarisation fractions will deserve special attention.

If $\mathcal{CP}$ is conserved in the Wtb vertex, i.e. if all anomalous couplings are real, then $\Gamma_+^N = \Gamma_-^N$. A net normal W polarisation ($\Gamma_+^N \neq \Gamma_-^N$) can be produced if $\mathcal{CP}$ is violated in the $t \to bW^+$ decay[5]. This property is unique of the normal direction and is here explored in the decay of polarised top quarks.

2.4.1 Sensitive observable to $\mathcal{CP}$ violation: $A_{\rm FB}^{\rm N}$

In the single top quark t-channel (see Figure 2.9), the top quarks are produced highly polarised along the direction of the spectator quark (q') with a degree of polarisation of $P \approx 0.9$ at $\sqrt{s}$= 7 TeV, as stated in Ref. [4, 5]. Therefore, the normal $\vec{N}$ and transverse $\vec{T}$ directions can be defined. The introduction of the angular distributions $\cos\theta^{\rm N}$ and $\cos\theta^{\rm T}$ allows to define new asymmetries in polarised top quark decays, in analogy to the ones obtained for the $\cos\theta^*$ distribution (see Figure 2.10), called $A_{\rm FB}^{\rm N}$ and $A_{\rm FB}^{\rm T}$ respectively.

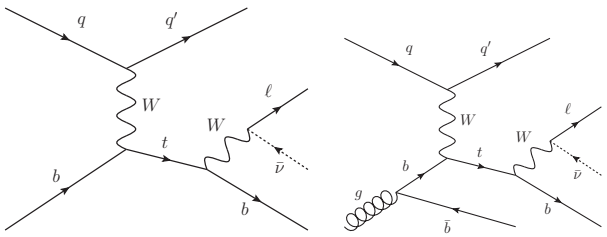

Figure 2.9: *Feynman diagram for the t-channel single top quark where the W boson decays leptonically. The spin direction of the top quark $\vec{s}_t$ in the single top quark t-channel is assumed to be in the direction of the momentum of the spectator quark (q').*

[5]It is important to point out that a net normal polarisation ($\Gamma_+^N \neq \Gamma_-^N$) is T-odd but not a genuine $\mathcal{CP}$ violating observable, if absorptive parts were present in the decay amplitude.

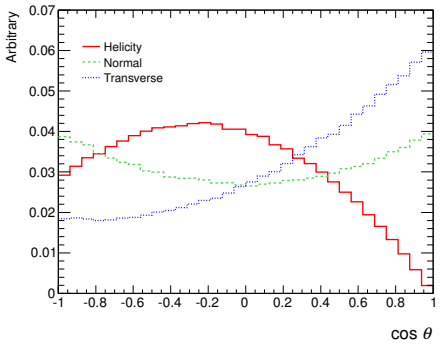

Basis	Angular dist.	A_{FB}
Helicity	$\cos\theta^*$	-0.22
Normal	$\cos\theta^N$	0.00
Transverse	$\cos\theta^T$	+0.34

Figure 2.10: *Angular distributions in* $\cos\theta^*$, $\cos\theta^N$ *and* $\cos\theta^T$ *and the corresponding forward-backward asymmetries in the SM.*

$$\begin{aligned} A_{\rm FB} &= \tfrac{3}{4}(F_{\rm R}-F_{\rm L}) = \tfrac{3}{4}\,\frac{\frac{4|\vec{q}|}{m_t}B_1}{A_0+2B_0} \\ A_{\rm FB}^{\rm N} &= \tfrac{3}{4}\,P\,(F_{\rm R}^N-F_{\rm L}^N) = \tfrac{3}{4}\,P\left[\frac{\frac{\pi}{2}\frac{|\vec{q}|}{M_W}D_1}{A_0+2B_0}\right] \\ A_{\rm FB}^{\rm T} &= \tfrac{3}{4}\,P\,(F_{\rm R}^T-F_{\rm L}^T) = \tfrac{3}{4}\,P\left[\frac{\frac{\pi}{2}\frac{m_t}{M_W}C_0}{A_0+2B_0}\right] \end{aligned} \tag{2.24}$$

The forward-backward asymmetry in the $\cos\theta^*$ distribution $A_{\rm FB}$ does not depend on the top quark polarisation, while the other ones are proportional to P. Taking into account the dependence of the form-factors with the anomalous couplings (Equation 2.20), the forward-backward asymmetries for each angular distribution can be written in terms of the couplings.

As pointed in Ref. [3], the polarisation fractions with respect to the normal direction, and therefore the asymmetry $A_{\rm FB}^{\rm N}$, are very sensitive to the imaginary part of the anomalous coupling $g_{\rm R}$. Although we will focus on this direction, for completeness, the dependence of the three asymmetries with $g_{\rm R}$ coupling is studied. It is assumed that all other anomalous couplings are zero: $Re(V_{\rm L}) \geq 0$, $|Re(g_{\rm R})| \geq 0$, $|Im(g_{\rm R})| \geq 0$ and $V_{\rm R} = g_{\rm L} = 0$. The total decay width can be written in terms of $V_{\rm L}$ and $g_{\rm R}$ as:

$$\begin{aligned} \Gamma &\approx \frac{g^2|\vec{q}|}{32\pi}\left[(2+\frac{m_t^2}{M_W^2})\,|V_{\rm L}|^2 + (1+\frac{2m_t^2}{M_W^2})\,|g_{\rm R}|^2 - \frac{6m_t^2}{M_W^2}\,Re(V_{\rm L}g_{\rm R}^*)\right] \\ &= 0.23\,[6.65\,|V_{\rm L}|^2 + 10.30\,|g_{\rm R}|^2 - 12.94\,Re(V_{\rm L}g_{\rm R}^*)] \end{aligned} \tag{2.25}$$

Assuming a top quark decay width similar to its SM value, the $V_{\rm L}$ coupling is slightly changed when changing $g_{\rm R}$:

$$\Gamma = \Gamma_{SM} \Rightarrow V_{\rm L} = +0.97\,Re(g_{\rm R}) \pm \sqrt{1-1.55\,|g_{\rm R}|^2+0.95\,Re(g_{\rm R})^2} \tag{2.26}$$

$$A_{\mathrm{FB}} \approx \frac{3}{2}\,\frac{-|V_{\mathrm{L}}|^2 - \frac{m_t^2}{M_W^2}\,|g_{\mathrm{R}}|^2 + \frac{2m_t^2}{M_W^2}\,Re(V_{\mathrm{L}}g_{\mathrm{R}}^*)}{(2+\frac{m_t^2}{M_W^2})\,|V_{\mathrm{L}}|^2 + (1+\frac{2m_t^2}{M_W^2})\,|g_{\mathrm{R}}|^2 - \frac{6m_t^2}{M_W^2}\,Re(V_{\mathrm{L}}g_{\mathrm{R}}^*)}$$
$$= -\frac{3}{2}\,\frac{|V_{\mathrm{L}}|^2 + 4.65\,|g_{\mathrm{R}}|^2 - 4.31\,Re(V_{\mathrm{L}}g_{\mathrm{R}}^*)}{6.65\,|V_{\mathrm{L}}|^2 + 10.30\,|g_{\mathrm{R}}|^2 - 12.94\,Re(V_{\mathrm{L}}g_{\mathrm{R}}^*)} \tag{2.27}$$

$$A_{\mathrm{FB}}^{\mathrm{N}} \approx \frac{3}{4}P\frac{\pi}{2}\frac{|\vec{q}|}{M_W}\,\frac{\frac{-2m_t}{M_W}Im(V_{\mathrm{L}}g_{\mathrm{R}}^*)}{(2+\frac{m_t^2}{M_W^2})\,|V_{\mathrm{L}}|^2 + (1+\frac{2m_t^2}{M_W^2})\,|g_{\mathrm{R}}|^2 - \frac{6m_t^2}{M_W^2}\,Re(V_{\mathrm{L}}g_{\mathrm{R}}^*)}$$
$$= -4.30\,P\,\frac{Im(V_{\mathrm{L}}g_{\mathrm{R}}^*)}{6.65\,|V_{\mathrm{L}}|^2 + 10.30\,|g_{\mathrm{R}}|^2 - 12.94\,Re(V_{\mathrm{L}}g_{\mathrm{R}}^*)} \tag{2.28}$$

$$A_{\mathrm{FB}}^{\mathrm{T}} \approx \frac{3}{4}P\frac{\pi}{2}\frac{m_t}{M_W}\,\frac{|V_{\mathrm{L}}|^2 + |g_{\mathrm{R}}|^2 - \frac{m_t}{M_W}(1+x_W^2)Re(V_{\mathrm{L}}g_{\mathrm{R}}^*)}{(2+\frac{m_t^2}{M_W^2})\,|V_{\mathrm{L}}|^2 + (1+\frac{2m_t^2}{M_W^2})\,|g_{\mathrm{R}}|^2 - \frac{6m_t^2}{M_W^2}\,Re(V_{\mathrm{L}}g_{\mathrm{R}}^*)}$$
$$= 2.54\,P\,\frac{|V_{\mathrm{L}}|^2 + |g_{\mathrm{R}}|^2 - 2.62\,Re(V_{\mathrm{L}}g_{\mathrm{R}}^*)}{6.65\,|V_{\mathrm{L}}|^2 + 10.30\,|g_{\mathrm{R}}|^2 - 12.94\,Re(V_{\mathrm{L}}g_{\mathrm{R}}^*)} \tag{2.29}$$

The dependence of these asymmetries on the real and imaginary part of the anomalous coupling g_{R} is shown in Figure 2.11. It is important to notice that the asymmetries A_{FB} and $A_{\mathrm{FB}}^{\mathrm{T}}$ (or helicity and transverse polarisation fractions) are sensitive to the real part of g_{R} while the asymmetry $A_{\mathrm{FB}}^{\mathrm{N}}$ (or normal polarisation fractions) is very sensitive to its imaginary part. Therefore non-zero values of $A_{\mathrm{FB}}^{\mathrm{N}}$ would imply non-vanishing $Im(g_{\mathrm{R}})$ coupling[6]. The relation in Equation 2.28 can be simplified: $A_{\mathrm{FB}}^{\mathrm{N}} \approx 0.64\,P\,Im(g_{\mathrm{R}})$. $A_{\mathrm{FB}}^{\mathrm{N}}$ not only vanishes at tree level in the SM but also for real coupling g_{R}. The one loop electroweak correction predicts g_{R} = -(7.85+1.23i) $\times 10^{-3}$ [47]. This absorptive part, which is $\mathcal{CP}$ conserving, can be disentangled from a genuine $\mathcal{CP}$ violating new coupling by comparing top and antitop quark decays.

2.5 Top quark polarisation

In t-channel single top quark production, top quarks are ~90% polarized through the V-A coupling structure of the involved electroweak interactions. New physics models may alter the coupling structure effectively which consequently affects the top quark polarization. The spin polarisation of the top quark can be analyzed through the angular distribution of its decay particles, which act as spin analyzers. The general form of the angular distribution of a spin analyzer with respect to the spin direction $\hat{z}$ is given by:

$$\frac{1}{\Gamma}\frac{d\Gamma}{dcos\theta_X} = \frac{1}{2}(1 + P_z\,\alpha_X\,\cos\,\theta_X) \tag{2.30}$$

[6] Although the $A_{\mathrm{FB}}^{\mathrm{N}}$ asymmetry is sensitive to $\mathcal{CP}$ violating phases in the top quark decay vertex, it is not genuinely $\mathcal{CP}$ violating and could be faked by unitarity phases. The sum of asymmetries for top and antitop quark decays, $A_{FB}^{CP} = A_{FB}^{N}(t) + A_{FB}^{N}(\bar{t})$ is unambiguously $\mathcal{CP}$ violating.

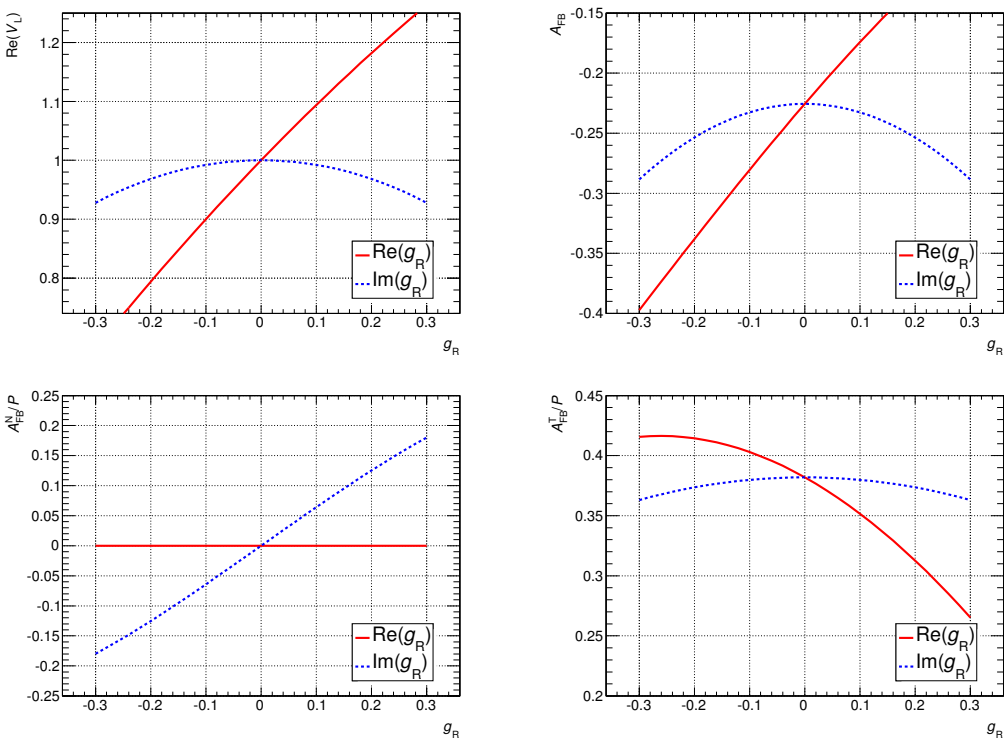

Figure 2.11: *From top left to bottom right: Dependence of V_L coupling and forward-backward asymmetries A_{FB}, A_{FB}^N/P and A_{FB}^T/P with the real and imaginary part of g_R assuming that the top quark decay width is equal to its SM value.*

being θ_X the angle between the momentum of the decay particle[7] $X = W, b, l, \nu$ in the top quark rest frame and the arbitrary direction $\hat{z}$ chosen to quantize the top spin. P_z is the top quark polarisation along this direction and the α_X is the spin analyzer power that depends on the particle type and which can be affected by anomalous couplings.

As pointed before, in the t-channel the spin direction of the top quark is given by the spectator quark (q' in Figure 2.9). Using the lepton as spin analyser and assuming again $Re(V_L) \geq 0$, $|Re(g_R)| \geq 0$, $|Im(g_R)| \geq 0$ and $V_R = g_L = 0$, one can write:

[7] It has to be noted that the analyzer X is not limited to the direct daughters (W boson and b quark), the W boson decay products (lepton and neutrino) are possible as well.

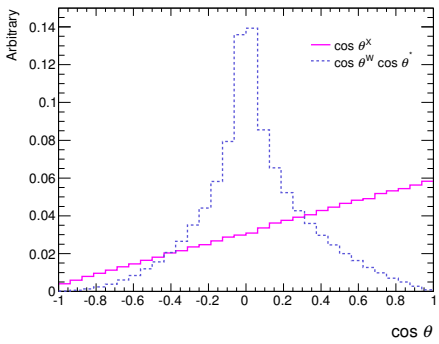

Angular dist.	A_{FB}	P
$\cos\theta^X$	0.45	0.89
$\cos\theta^W \times \cos\theta^*$	0.10	0.89

Figure 2.12: *Angular distributions in* $\cos\theta^X$ *and* $\cos\theta^* \cdot \cos\theta^W$ *and the corresponding forward-backward asymmetries in the SM.*

$$
\begin{aligned}
\alpha_l &= \frac{a_l}{a_0} \\
&= \frac{\left(1 + x_W^2 - 2x_W^4\right)|V_{\rm L}|^2 \; + \; \left(-2 - 11x_W^2 + x_W^4 + \; 6\frac{M_W}{q}x_W log(\frac{E_W+q}{E_W-q})\right)|g_{\rm R}|^2 + 6x_W(1-x_W^2)Re(V_{\rm L}g_{\rm R}^*)}{(1 + x_W^2 - 2x_W^4)\,|V_{\rm L}|^2 \; + \; (2 - x_W^2 - x_W^4)\,|g_{\rm R}|^2 + 6x_W(1-x_W^2)\,Re(V_{\rm L}g_{\rm R}^*)} \\
&= 1 + \frac{\left(-4 - 10x_W^2 + 2x_W^4 + 6\frac{M_W}{q}x_W log(\frac{E_W+q}{E_W-q})\right)\,|g_{\rm R}|^2}{(1 + x_W^2 - 2x_W^4)\,|V_{\rm R}|^2 + (2 - x_W^2 - x_W^4)\,|g_{\rm R}|^2 + 6x_W(1-x_W^2)\,Re(V_{\rm L}g_{\rm R}^*)} \\
&= 1 - \frac{0.95\,|g_{\rm R}|^2}{1.12\,|V_{\rm L}|^2 + 1.74\,|g_{\rm R}|^2 - 2.19\,Re(V_{\rm L}g_{\rm R}^*)}
\end{aligned}
\tag{2.31}
$$

A more general dependence is presented in Ref. [46]. One may notice that α_l has no linear terms in $g_{\rm R}$, so the spin analyzer is less sensitive to new physics.

The angular distribution $\cos\theta^{\rm X}$ using the lepton as spin analyser is shown in Figure 2.12. From here one can measure a forward-backward asymmetry $A_{\rm FB}^X$ which is proportional to P:

$$A_{\rm FB}^X = +\frac{1}{2}\,P_z\,\alpha_X \tag{2.32}$$

The measurable product $P_z\,\alpha_X$ shows the production-decay interplay in this angular distribution. An important issue is to disentangle new physics in production and decay. This, of course, would become crucial in case that deviations from the SM predictions were found.

With this aim, in Ref. [64], a new asymmetry sensitive to the polarisation of the top quark along a chosen axis in the decay of polarised top quark is defined. It consists in a *double forward-backward* asymmetry in the decay of polarised top quark, $A_{\rm FB}^{\rm tW}$:

$$A_{\rm FB}^{\rm tW} = \frac{\cos\theta^{\rm W}\cdot\cos\theta^* > 0 - \cos\theta^{\rm W}\cdot\cos\theta^* < 0}{\cos\theta^{\rm W}\cdot\cos\theta^* > 0 + \cos\theta^{\rm W}\cdot\cos\theta^* < 0} \tag{2.33}$$

being θ^{W} the angle between the W boson momentum in the top quark rest frame $\vec{q}$ and the direction $\hat{z}$ chosen to quantize the top spin $\vec{s}_t$, and θ^* as defined before (see Figure 2.8). The angular distribution is also shown in Figure 2.12. This new asymmetry is related to the top quark polarisation along the chosen direction and the W helicity fractions:

$$A_{\mathrm{FB}}^{\mathrm{tW}} = \frac{3}{8}\, P\,(F_{\mathrm{R}} + F_{\mathrm{L}}) \;=\; \frac{3}{8}\, P \left[\frac{2B_0}{A_0 + 2B_0}\right]. \tag{2.34}$$

As before, assuming that the only non-vanishing anomalous coupling is g_{R}, one can derive the dependence of $A_{\mathrm{FB}}^{\mathrm{tW}}$ (see also Figure 2.13):

$$\begin{aligned} A_{\mathrm{FB}}^{\mathrm{tW}} &\approx \frac{3}{4}\, P\, \frac{|V_{\mathrm{L}}|^2 + \frac{m_t^2}{M_W^2}\,|g_{\mathrm{R}}|^2 - \frac{2m_t^2}{M_W^2}\, Re(V_{\mathrm{L}} g_{\mathrm{R}}^*)}{(2 + \frac{m_t^2}{M_W^2})\,|V_{\mathrm{L}}|^2 + (1 + \frac{2m_t^2}{M_W^2})\,|g_{\mathrm{R}}|^2 - \frac{6m_t^2}{M_W^2}\, Re(V_{\mathrm{L}} g_{\mathrm{R}}^*)} \\ &= \frac{3}{4}\, P\, \frac{|V_{\mathrm{L}}|^2 + 4.65\,|g_{\mathrm{R}}|^2 - 4.31\, Re(V_{\mathrm{L}} g_{\mathrm{R}}^*)}{6.65\,|V_{\mathrm{L}}|^2 + 10.30\,|g_{\mathrm{R}}|^2 - 12.94\, Re(V_{\mathrm{L}} g_{\mathrm{R}}^*)} \\ &= -\frac{1}{2} A_{\mathrm{FB}}\, P \end{aligned} \tag{2.35}$$

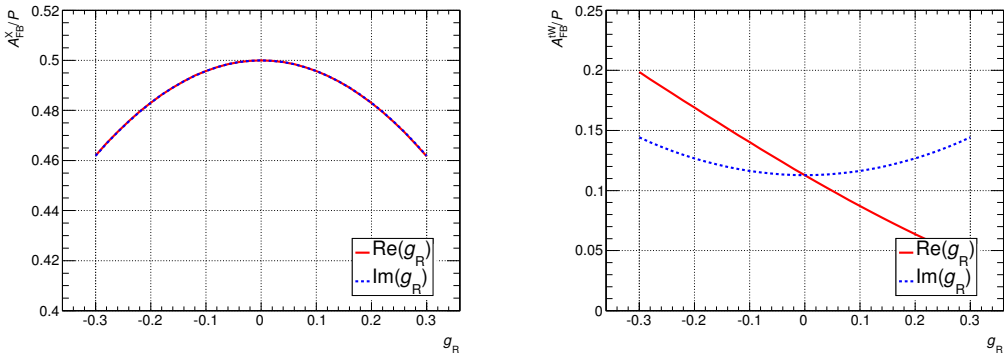

Figure 2.13: *Forward-backward asymmetries A_{FB}^{X} and A_{FB}^{tW}.*

2.6 Scope of this thesis

The large number of top quark events produced in the LHC - which has been colliding protons from 2010 to 2012 and reaching a center of mass energy of 7 and 8 TeV - allows very precise measurements of the properties of this quark and to study the structure of the Wtb vertex. In this thesis an extension of the SM in terms of possible complex anomalous couplings associated to the Wtb vertex and allowing for $\mathcal{CP}$ violation is proposed. The main part of this work describes the measurement of the $A_{\mathrm{FB}}^{\mathrm{N}}$ asymmetry in the ATLAS detector using t-channel single top quark events from proton-proton collisions. In addition, the first experimental limit on the imaginary part of g_{R} is set.

3
LHC and ATLAS

In order to study physics processes involving top quarks, data from high energy experiments are required since the top quark is very massive and its production requires a large amount of energy. With this aim, collider experiments are built. In those, beams of particles are accelerated to very high speeds in the so-called accelerator machine usually placed in an underground tunnel and they collide in different points of the ring. In such points, particle detectors are built to collect information about the particles produced such as their momentum and energy. At present, the most powerful collider is the LHC at CERN where protons have been colliding from 2010 to 2012 at a centre-of-mass energy of 7 and 8 TeV.

This chapter provides a basic introduction to the LHC collider and the ATLAS detector. Section 3.1 describes the CERN laboratory and its facilities, the layout of the LHC collider and its particle detectors (LHC experiments) and the computing model (Grid). Some general remarks concerning proton-proton collisions are given in Section 3.2. Later, Section 3.3 describes the ATLAS detector (the one in which this thesis is developed), giving an overview of its different subsystems (tracker, calorimeters, muon chambers and trigger system) and of the recorded datasets. Finally, in Section 3.4 the algorithms used in ATLAS to reconstruct final state objects such as electrons, photons, muon and jets are briefly described.

3.1 The Large Hadron Collider

3.1.1 CERN and its facilities

One of the largest international scientific project in the world nowadays is the LHC which includes a hadron accelerator, four huge detectors at its four collision points and a computing Grid project to store and process the recorded data. The LHC is a proton-proton collider located

at CERN, on the border of Switzerland and France, near Geneva. It is the most powerful accelerator ever built and allows to explore new frontiers of knowledge.

The CERN facility was established in July 1953, as a council formed by 12 founding member states: Belgium, Denmark, France, the Federal Republic of Germany, Greece, Italy, the Netherlands, Norway, Sweden, Switzerland, the United Kingdom and Yugoslavia. It was one of the first European projects after the World War II. In 1954, this council became a laboratory which was placed in Switzerland. After its establishment, the studies done went beyond the atomic nucleus into higher energy physics. Today it is the world's largest particle physics laboratory with 20 European member states and many other countries which are involved in different ways such as Japan, United States, Russia, India and others; and where physicists, engineers and technicians from different cultures work together in a highly cooperative environment. Spain first joined CERN in 1961, left in 1969 and rejoined in 1983.

The first accelerator built at CERN was a 600 MeV SynchroCyclotron (SC) in 1957. Since then, a large list of accelerators and facilities have been built. The Proton Synchrotron (PS) accelerated protons for the first time in 1959, being for a brief period the world's highest energy particle accelerator. In 1964, the SC started to concentrate on nuclear physics alone, leaving particle physics to the PS. When CERN built new accelerators in the 1970s, the role of the PS became to supply particles to the new machines. Since the PS started up in 1959, the intensity of its proton beam has increased a thousandfold.

The first proton-proton collider in the world, the Intersecting Storage Rings, came into operation in 1971. Ten years later, the Super Proton Synchrotron (SPS) was built and produced the massive W and Z bosons confirming the unification of electromagnetic and weak theories. At the end of 1989, LEP collider became the largest machine of its kind, housed in a 27 km long circular tunnel which nowadays houses the LHC. During its 11 years of research, LEP performed very precise measurements of the SM which allowed a detailed study of the electroweak interaction. In addition, it also proved that there are three - and only three - generations of particles of matter. At the end of 2000, LEP was shut down in order to build the LHC in the same tunnel.

The LHC is the world's most powerful particle accelerator at this moment which produces two proton beams in opposite directions with a design energy of 7 TeV each (i.e. centre-of-mass collision energies of 14 TeV) and a design instantaneous luminosity $\mathcal{L}$ of 10^{34} cm^{-2} s^{-1} (see Table 3.1). On September 9^{th} 2008, the first proton beams circulated inside the LHC, starting a new era of discovery at the high energy frontier. The first proton-proton collisions took place in March 2010 at lower energy than the design value. Since then and until the end of 2012, the LHC has been running with 3.5 or 4 TeV per beam (centre-of-mass energy of 7 and 8 TeV, respectively) and the total integrated luminosity delivered is of around 5 fb^{-1} and 20 fb^{-1}, respectively (see Table 3.2). In order to achieve the design energy, some technical issues need to be solved during 2013 and 2014, and later on the LHC will be running at the nominal conditions. Compared to the previous world hadron accelerator, Tevatron [65], the LHC is designed to be seven times more energetic and thirty times more intense. This has been possible thanks to the new technologies developed in the latest decades.

3.1.2 The LHC accelerator

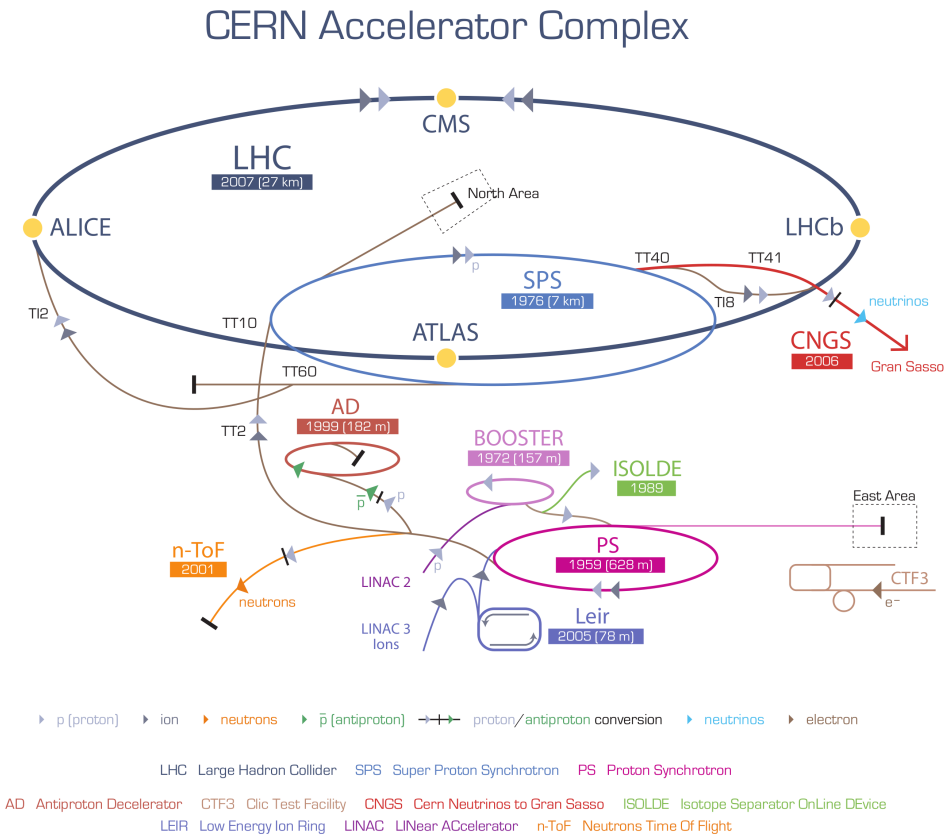

Figure 3.1: *CERN accelerator complex.*

The whole CERN accelerator complex is shown schematically in Figure 3.1. It consists of several machines interconnected with higher and higher capabilities, i.e. particle beams are injected from one to the next, bringing them to higher energies successively. The protons, which are obtained by removing electrons from hydrogen atoms, pass through a LINear ACceletator (called LINAC 2) and are injected into the booster with an energy of 50 MeV. Then, circular accelerators are used to increase the protons energy. The maximum energy that can be transferred to the beams is proportional to the radius of the accelerator ($p_T = 0.3 \cdot q \cdot B \cdot r$ being p_T the transverse momentum of the particles, B the strength of the magnetic field and r the radius of the circular accelerator). In the first circular accelerator, called Booster, the protons are accelerated up to 1.4 GeV before they are directed to the PS from where they leave with 26 GeV for the SPS. Via two injection lines (TI 2 and TI 8) the two proton beams are injected with 450 GeV energy into the LHC accelerator, where they finally reach few TeVs.

LHC parameter	**proton-proton collisions**
Beam energy	7 TeV (up to now: 3.5-4 TeV)
centre-of-mass energy ($\sqrt{s}$)	14 TeV (up to now: 7-8 TeV)
Injection energy	450 GeV
Luminosity ($\mathcal{L}$)	10^{34} cm^{-2} s^{-1}
Frequency (f)	40 MHz
Bunch separation	25 ns
Number of particles per bunch (N_b)	$1.15 \cdot 10^{11}$
Average radius of a beam	16 μm
Beam current	0.58 A
Circumference length	26.66 km
Radius	4.24 km
Number of dipole magnets	1232
Length of the dipole magnets	14.3 m
Number of quadrupole magnets	392
Nominal magnetic field (B)	8.33 T
Total mass	27.5 tons

Table 3.1: *Design accelerator parameters of the LHC collider.*

To keep the two circulating proton beams in their orbits a total of 1232 superconducting dipole magnets are needed. These are twin bore magnets which consist of two sets of coils and beam channels within the same mechanical structure and cryostat. This design is required by the fact that the magnets at the LHC have to accelerate two beams of particles with the same charge but in opposite directions, and there are obvious room constraints (not enough room for two separate magnets in the LHC tunnel). To reach the required field strength of 8.33 T the magnets are cooled down to 1.9 K using super-fluid helium (He). The coils are made of niobium-titanium (NbTi) which is a material that allows to reach the superconducting regime when it is at 1.9 K. In addition, there are 392 quadrupole magnets for beam focusing and beam corrections; and also sextupole, octupole and decapole magnets mainly for compensating the systematic non-linearities.

Each beam has an internal structure as they are arranged in bunches separated in space. At design luminosity the protons are accelerated in bunches of $1.15 \cdot 10^{11}$ protons each, with 25 ns bunch spacing (rate of 40 MHz). Only 2808 bunches are filled out of the 3564 possible bunches in each beam direction. This corresponds to a total beam current of 0.58 A, equivalent to a stored energy of 362 MJ per beam. The main LHC design parameters are summarized in Table 3.1. The conditions of 2010-2012 proton runs are presented in Table 3.2.

The LHC physics program is mainly based on proton-proton collisions. However, shorter running periods, typically one month per year, with heavy-ion collisions are included in the program. The collisions of high energetic beams at the LHC produces tones of particles. They are recorded by particle detectors, the so-called LHC experiments, which are placed just at the collision points. A brief description of them is given in the next section.

3.1.3 The LHC experiments

There are six experiments at the LHC, all of them run by international collaborations bringing together scientists from all over the world. The four largest experiments, namely ATLAS, CMS, LHCb (Large Hadron Collider beauty) and ALICE (A Large Ion Collider Experiment), are located each of them in an interaction point around the LHC where the two beams are brought to collision. Figure 3.2 shows the location of the LHC and of its experiments. ATLAS and CMS are general-purpose experiments, designed to cover the widest possible range of physics at the LHC, from SM precision measurements to new physics searches. The ALICE [66] experiment focuses on studying strongly interacting matter at the extreme energy densities in heavy-ion collisions and performing measurements of the phase transition between hadronic matter and the quark-gluon plasma. This is a state of matter where quarks and gluons, under conditions of very high temperatures and densities, are no longer confined inside the hadrons. Such state of matter probably existed just after the Big Bang, before particles such as protons or neutrons were formed. LHCb [67] is the LHC experiment dedicated to the physics of the b quark and to study $\mathcal{CP}$-violating processes and rare decays. Apart from these experiments installed in four huge underground caverns built around the collision points, there are two smaller experiments at the LHC, TOTEM (TOTal Elastic and diffractive cross section Measurement experiment) and LHCf (Large Hadron Collider forward) experiments. The aim of the TOTEM [68] experiment is to perform simultaneous measurements of the total proton-proton collisions cross section and the luminosity. It covers the very forward region in the pseudo-rapidity (see Section 3.3.1) range. It consists of Roman pots placed several hundred meters on either side of the CMS interaction point, as well as detectors integrated in the CMS apparatus at about ten meters from the interaction point. LHCf [69] is another very forward experiment, located 140 meters on either side of the ATLAS experiment interaction point, and its aim is to measure the neutral particles emitted in this forward region in order to provide data for calibrating the hadron interaction models that are used in the study of extremely high energy cosmic-rays.

3.1.4 Worldwide LHC Computing Grid

The LHC produces roughly 15 petabytes (15 million gigabytes) of data every year. In addition, thousands of scientists around the world need to access and analyse these data. Therefore, a distributed computing and data storage infrastructure has been developed to deal with these needs: the Worldwide LHC Computing Grid [70]. This project is split in three Grid flavours: LHC Computing Grid (LCG) [71] in Europe, NorduGrid/ARC also in Europe (Nordic countries only) and Open Science Grid in the United States of America.

Data from the LHC experiments are distributed around the globe, with a primary copy recorded on tape at CERN (*Tier-0* center). After initial processing, the data are distributed to eleven large computer centers - in Canada, France, Germany, Italy, the Netherlands, the Nordic countries, Spain, Taipei, the United Kingdom and two sites in the United States of America - with sufficient storage capacity for a large fraction of the data, and with round-the-clock support for the computing grid. These centers are called *Tiers-1* and make the data available to over 160 *Tiers-2* centers for specific analysis tasks. Individual scientists can then access the LHC data from their home country, using local computer clusters or even individual PCs. The Spanish cloud, which belongs to the LCG flavour, has a multiexperiment *Tier-1* placed at PIC (Barcelona) and

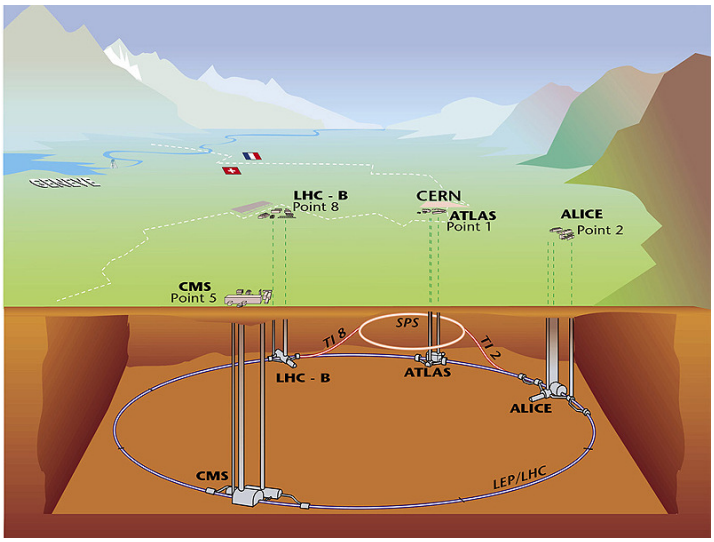

Figure 3.2: *View and location of the LHC and the four experiments ATLAS, CMS, LHCb and ALICE.*

seven distributed *Tiers-2*: CIEMAT (Madrid) and IFCA (Santander) for CMS, IFIC (Valencia), IFAE (Barcelona) and UAM (Madrid) for ATLAS and UB (Barcelona) and USC (Santiago de Compostela) for LHCb.

3.2 Phenomenology of proton-proton collisions

In the this section, some characteristics of proton-proton collisions are described. The total proton-proton cross section at 7 TeV is approximately 110 mb[1]. This cross section can be broken down into three contributions: inelastic (60 mb), elastic (40 mb) and single diffractive (12 mb). Only the inelastic scattering gives rise to particles at sufficient high angles with respect to the beam axis such that can be seen in the detectors. Elastic scattering of the protons and diffractive events are not seen by the detectors.

Scattering processes at hadron colliders such as the LHC and Tevatron are classified as either *soft* or *hard*. QCD is the underlying theory for all such processes, but the approach (and the level of understanding) is very different for the two cases. A crucial property of strong interactions is asymptotic freedom, whereby the interaction strength decreases with energy. This implies that in high energy collisions, quarks and gluons may be treated as effectively free particles, allowing for perturbative QCD calculations. Conversely, at low energies quarks and gluons interact strongly, forming hadrons such as the proton. A fundamental parameter of QCD is the strong coupling constant α_s which indicates the effective strength of the strong interaction in the

[1] A barn (symbol b) is a unit of area. Within high energy physics, it is used to express the cross sections of scattering processes and is understood as the probability of interaction between particles. A barn is defined as 10^{28} m^2 (100 fm^2) and is approximately the cross sectional area of a uranium nucleus.

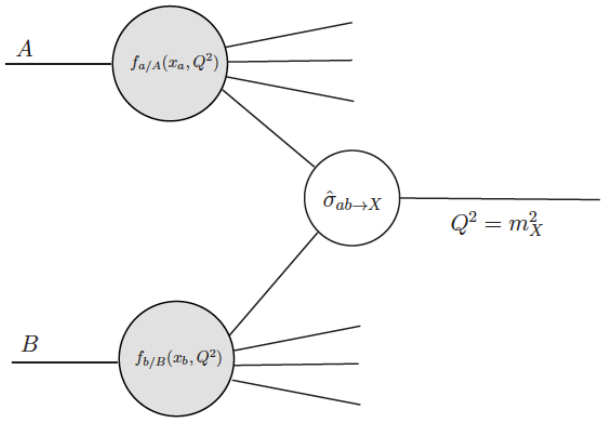

Figure 3.3: *Schematic diagram for particle production in proton-proton collisions.*

process and that depends on the energy scale Q, typically the momentum transfer in the given process. Most of the interactions are soft, i.e. long distance collisions between the two protons, in which the transverse momentum exchanged between both is so small that most of the energy escapes along the beam pipe. The rates and properties of these soft interactions are dominated by non-perturbative QCD effects. The most interesting events are hard interactions, in which the inelastic scattering between the two protons can be treated as direct *parton-parton scattering*. In this case, the rates and event properties can be predicted with precision using perturbation theory.

3.2.1 The proton structure

At hadron colliders, the composite nature of the hadrons has to be considered. Protons are a bound state of partons (quarks and gluons). In addition to its constituent quarks (*valence quarks*), which are *uud*, the proton has also the so-called *sea quarks* (coming from gluon splitting into quark and antiquark pairs). The momentum of the proton is shared among all these constituents and its structure depends on the energy scale at which it is probed. At lower energies ($Q \sim$1 GeV), the momentum of the proton is primarily distributed among the three valence quarks. As energy increases (1$<$ Q $\leq$100 GeV), the emission of gluons is more probable and these gluons carry some of the initial momentum of the quarks. The proton dynamics can be understood in terms of the fraction of the proton momentum distributed among its constituent partons. Formally, it is expressed as a probability distribution, called a *parton distribution function* (PDF). The interacting partons carry only a fraction x_1 and x_2 of this momentum; therefore, the centre-of-mass energy of the interaction is only a fraction of the total energy:

$$\hat{s} = x_1 x_2 s.$$

3.2.2 The cross section for processes in hadron-hadron collisions

The space-time picture of a proton-proton collision is shown in Figure 3.3 and suggests the possibility of separating long (non-perturbative QCD) and short (hard parton level interactions, perturbative QCD) distance physics. The *factorization* theorem, first proposed by Drell and Yan [72], postulates that, in hadronic collisions, the cross section of a *hard scattering process* can be separated into a partonic cross section (short distance), which is process-dependent and calculable in pertubative QCD, and a universal part corresponding to the distribution of partons inside the colliding hadrons (long distance), given by the PDFs.

The PDFs give the probability that the parton a carries a fraction of the hadron's momentum x_a,

$$f_a(x_a, \mu_F^2), \tag{3.1}$$

and depends on the *factorization scale* μ_F^2 which separates long and short distance physics, i.e. above that scale one can rely on perturbative calculations.

The total cross sections for X production in proton-proton collisions, $\sigma_{pp\to X}$, can be determined from the convolution of the cross section of the incoming partons a and b, $\hat{\sigma}_{ab\to X}$, and the PDFs for the partons a and b inside the two protons, f_a and f_b:

$$\sigma_{pp\to X} = \sum_{ab} \int dx_a\, dx_b\, f_a(x_a, \mu_F^2) f_b(x_b, \mu_F^2) d\hat{\sigma}_{ab\to X}(x_a, x_b, \mu_F^2)\,, \qquad \text{with}$$

$$\hat{\sigma}_{ab\to X} = [\hat{\sigma}_{LO}(x_a, x_b, \mu_F^2) + \alpha_s(\mu_R)\hat{\sigma}_{NLO}(x_a, x_b, \mu_F^2) + \alpha_s^2(\mu_R)\hat{\sigma}_{NNLO}(x_a, x_b, \mu_F^2) + ...]_{ab\to X} \tag{3.2}$$

The partonic cross section $\hat{\sigma}_{ab\to X}$ can be calculated in perturbative QCD and written in terms of leading order (LO), next-to-leading order (NLO), next-to-next-to-leading order (NNLO) and so on processes. Two scales enter the formula: the already defined *factorization scale* μ_F and the *renormalisation scale* μ_R. The higher orders terms give rise to logarithmic divergences due to soft and collinear gluon emissions [73]. The purpose of renormalisation is to replace these divergent integrals such that large logarithms vanish; more precisely, they are resummed into power series expansion in the running coupling constants α_s being therefore the choice of μ_R arbitrary. The physical cross section is independent of μ_F and μ_R. However, the truncation of the infinite perturbative series at finite order typically results in a non-negligible scale dependence. In order to obtain a reliable prediction, higher order corrections are calculated until this dependence is reduced. Often, both scales are assumed to be equal and are chosen at the order of magnitude of momentum scales of the hard process.

3.2.3 Parton distribution functions

As mentioned above, the PDFs describe the parton content of the hadrons. A PDF is defined as the probability density for finding a parton a in the hadron h with a certain longitudinal momentum fraction x_a at a scale μ_F^2. This probability is parametrized as a function of the momentum fraction x_a of a parton in a proton. They cannot be derived from calculations, because of the non-perturbative nature of QCD. Instead, they are extracted from global fits to data: deep-inelastic

scattering, Drell-Yan production and jet measurements. The main experimental inputs come from deep-inelastic lepton-hadron scattering experiments such as HERA [74] ep collider (experiments H1 and ZEUS) and from various fixed target experiments in which neutron-nucleon scattering is measured. Further data come from various pp and pd scattering experiments at Fermilab, $\bar{p}p$ data at the Tevatron and now also from the LHC. The most widely used sets of PDFs are provided by the CTEQ [75] and MSTW [76] (previously MRST) groups. Figure 3.4 shows the PDF distributions for u, d, c and s quarks and the corresponding antiquarks and gluons at μ_F^2 =10 GeV^2 and μ_F^2 =10^4 GeV^2 for MSTW, including the associated one-sigma (68%) confidence level uncertainty bands.

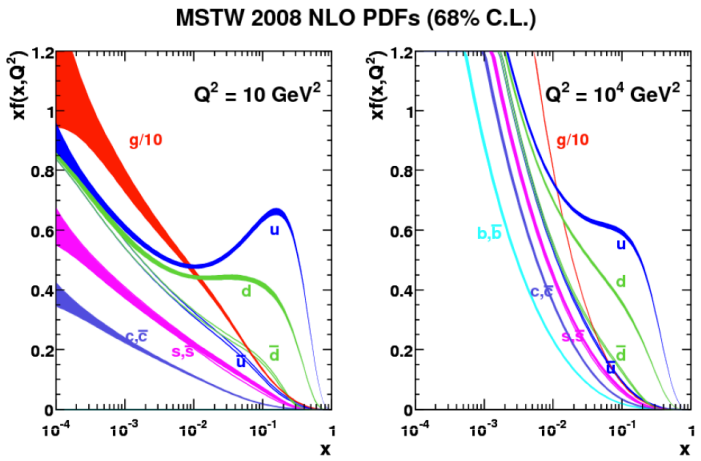

Figure 3.4: *Parton distribution functions of a proton at two different values of Q^2 using the MSTW 2008 NLO [76] PDF set. The gluon gives the dominant contribution to a proton. With increasing Q^2 the number of quarks carrying small momentum fraction grows.*

3.2.4 Expected cross sections

Figure 3.5 shows the predicted cross section of different processes at hadron colliders such as the Tevatron (proton-antiproton) and the LHC (proton-proton) for different centre-of-mass energies. Figure 3.6 shows the measured cross sections in ATLAS for different processes both at 7 and 8 TeV and how they compare to theory predictions.

3.2.5 Underlying event

The *underlying event* [78] is an important element of the hadronic environment at the LHC. After the hard parton-parton interaction, a coloured/beam remnant that did not take part of the hard process itself is left over. Therefore, multiple parton interactions may occur within one collision. The underlying event is the collection of all the soft processes that accompany the high-p_T interaction of interest, except the hard process itself (see Figure 3.7). It consists of the initial and final state radiation (ISR and FSR) plus beam-beam remnants that are left over after

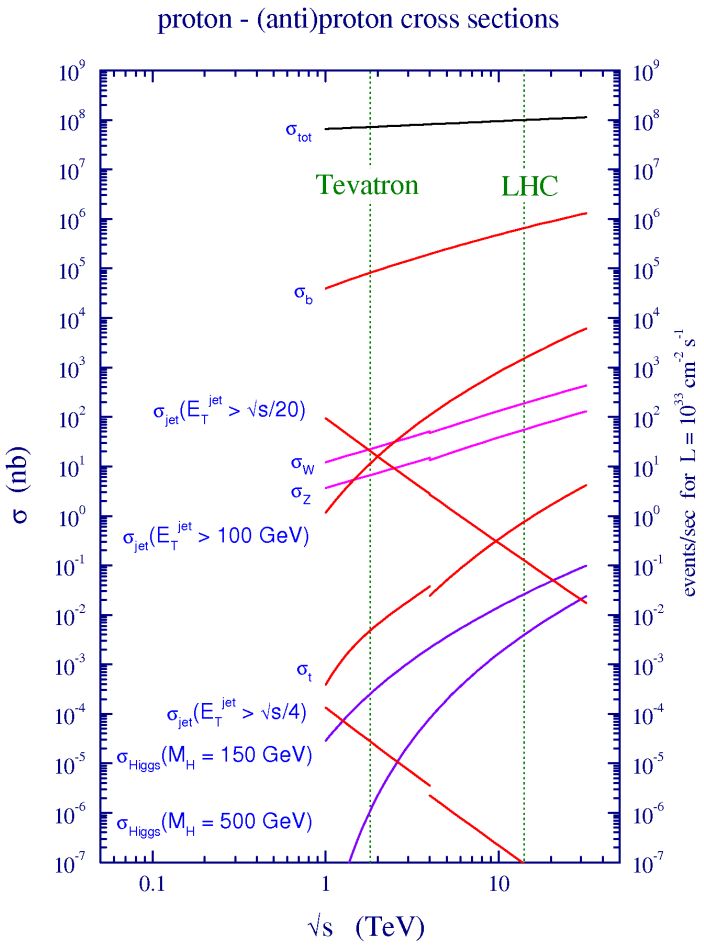

Figure 3.5: *Predicted cross sections and event rates for some characteristic proton-proton processes as function of the centre-of-mass energy. The vertical lines indicate the proton-antiproton collider Tevatron at 1.96 TeV and the proton-proton collider LHC at a design energy 14 TeV (value not yet reached). Source: [77].*

a parton is knocked out of each of the initial two beam hadrons.

The modelling of these soft interactions is important because they may impact other high p_T measurements and also affect the detector resolution. However, these low p_T scattering processes are difficult to predict using perturbative methods only. For this reason, predictions of the models are compared to LHC data and later improved/tuned. Several phenomenological models are available. One of these models, implemented in PYTHIA and described in Ref. [79], assumes that multiple interactions take place in a substantially independent way (except for the effect of momentum conservation), so that Poisson statistics can be used, and that they can be

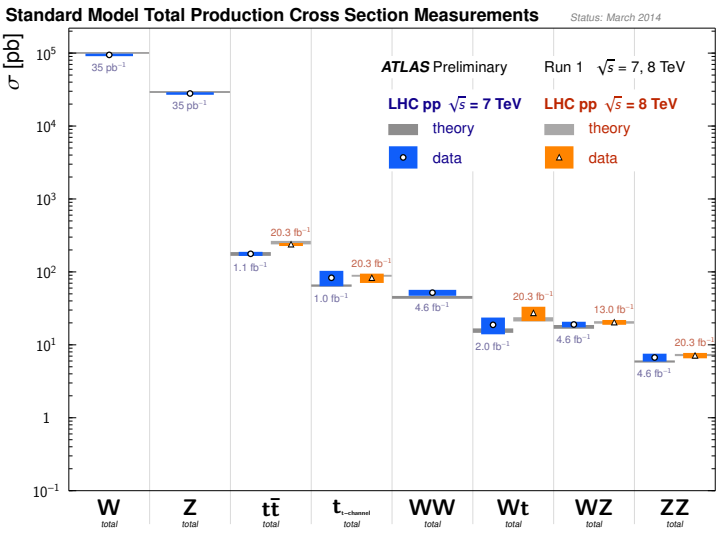

Figure 3.6: *Summary of several proton-proton total production cross section measurements, corrected for leptonic branching fractions, compared to the corresponding theoretical expectations. All theoretical expectations were calculated at NLO or higher. The W and Z vector boson inclusive cross sections were measured with 35 pb^{-1} of integrated luminosity from the 2010 dataset at 7 TeV. All other measurements were performed using the 2011 dataset at 7 TeV or the 2012 dataset 8 TeV. The luminosity used for each measurement is indicated close to the data point. Uncertainties for the theoretical predictions are quoted from the original ATLAS papers. They were not always evaluated using the same prescriptions for PDFs and scales.*

described by perturbative QCD above a certain scale p_T^{min} (since the perturbative cross section will diverge if $p_T \rightarrow 0$). The chosen scale p_T^{min} is one of the main parameters of the model. A dependence on the proton-proton impact parameter is also introduced (as an option), since a low value would increase the amount of multiple parton interactions. An alternative model is implemented in the JIMMY Monte Carlo program and is described in Ref. [80].

3.2.6 Luminosity in a particle collider

Besides the high energy required, the other important parameter in a particle collider is the rate of interactions, commonly called *events*. The quantity that defines the ability of a collider to produce a flux of events per unit of transverse area and time is called the *instantaneous luminosity* $\mathcal{L}$:

$$R_{\text{inel}} = \mathcal{L} \times \sigma_{\text{inel}} \rightarrow \mathcal{L} = \frac{\mathcal{R}_{\text{inel}}}{\sigma_{\text{inel}}} \tag{3.3}$$

where R_{inel} is the number of inelastic proton-proton collisions per second and σ_{inel} is the proton-proton inelastic cross section.

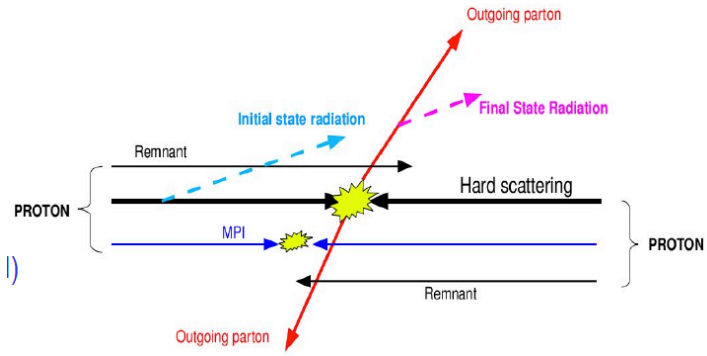

Figure 3.7: *An illustrative event in hadronic collisions: hard parton-parton scattering. The resulting event contains particles that originate from the two outgoing partons and from the initial and final state radiation and particles that come from the break-up of the protons (*beam-beam remnants*). The* underlying event *is everything except the two outgoing hard scattered 'jets', i.e. consists of the* beam-beam remnants *plus initial and final state radiation.*

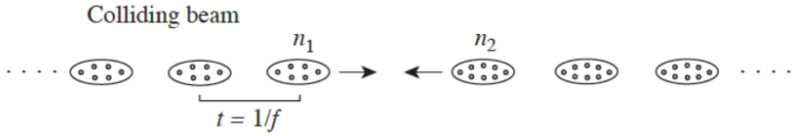

Figure 3.8: *Colliding beams with a bunch crossing frequency f.*

The particle beams usually come in bunches, as illustrated in Figure 3.8. Therefore, the instantaneous luminosity[2] can be written as:

$$\mathcal{L} = \frac{\mu f}{\sigma_{\text{inel}}} = \frac{\mu n_{\text{b}} f_{\text{rev}}}{\sigma_{\text{inel}}} \tag{3.4}$$

where μ is the average number of inelastic interactions per bunch crossing and f the bunch crossing frequency which can be written in terms of the number of bunch pairs colliding per revolution n_{b} and the revolution frequency f_{rev} ($f = n_{\text{b}} f_{\text{rev}}$).

In terms of the accelerator parameters, the instantaneous luminosity $\mathcal{L}$ can also be written in terms of the number of particles per bunch in the two colliding beams, n_1 and n_2, the bunch crossing frequency and the bunch transverse area. Thus, assuming a Gaussian transverse particle bunch profile, the instantaneous luminosity is defined as:

$$\mathcal{L} = \frac{n_1 n_2}{4\pi\sigma_x\sigma_y} n_b f_{rev}$$

[2]The instantaneous luminosity is usually given in units of $\text{cm}^{-2}s^{-1}$ or $\text{fb}^{-1}s^{-1}$.

where σ_x and σ_y are the Gaussian widths in the horizontal and vertical plane of the bunch respectively. The revolution frequency in a collider is accurately known and the number of particles or beam intensity is continuously measured with beam current transformers. The effective transverse area $A_{eff} = \frac{1}{4\pi\sigma_x\sigma_y}$ in which the collisions take place is measured with the Van Der Meer method [81].

In practice, the single particle transverse motion is modulated by an amplitude function β and the beam optics are configured such that the beams are focused at the interaction point in order to maximize the number of collisions. The value of the amplitude at the interaction point is called β^*. Another important parameter to characterize the beam performance is the emittance ϵ, corresponding to the space and momentum phase space occupied by the particles in the beam. In terms of these beam parameters, the instantaneous luminosity can be rewritten as:

$$\mathcal{L} = \frac{n_1 n_2}{4\pi\epsilon_n\beta^*} n_b f_{rev} \gamma_r F \tag{3.5}$$

where the factor F accounts for the impact of the crossing angle θ_c and other characteristics of the beam configuration:

$$F = \left(1 + \left(\frac{\theta_c\sigma_z}{2\sigma^*}\right)\right)^{-1/2} \tag{3.6}$$

being σ_z and σ^* the root mean square of the bunch length and of the transverse beam size at the interaction point. From this, one can conclude, that in order to achieve high luminosity, the beam should collide bunches with large numbers of particles with low emittance at high frequency in a region where the amplitude function is as low as possible.

Integrating the instantaneous luminosity over time, one can define the *integrated luminosity* $\mathcal{L}_{\text{int}}$[3]. The design LHC parameters and those from 2010-2012 runs are shown in Table 3.2.

Parameter	**2010**	**2011**	**2012**	**Nominal**
Beam energy (TeV)	3.5	3.5	4.0	7.0
centre-of-mass energy ($\sqrt{s}$) (TeV)	7	7	8	14
Maximum bunch pairs colliding	368	1380	1380	2808
Bunch separation (ns)	150	75/50	50/25	25
Maximum bunch intensity (10^{11} protons/bunch)	1.2	1.45	1.7	1.15
β^* (m)	3.5	1.5/1.0	0.6	0.55
ϵ_n (μm rad)	2.0	2.4	2.5	3.75
Peak luminosity (10^{33} cm^{-2} s^{-1})	0.2	3.7	7.7	10.0
Mean interactions per crossing	8	17	38	$\sim$ 23
Total integrated luminosity delivered	48 pb^{-1}	5.6 fb^{-1}	23.3 fb^{-1}	

Table 3.2: *LHC parameters for proton-proton collisions for nominal design and for 2010 and 2011 runs at 7 TeV and 2012 runs at 8 TeV. Source: [82].*

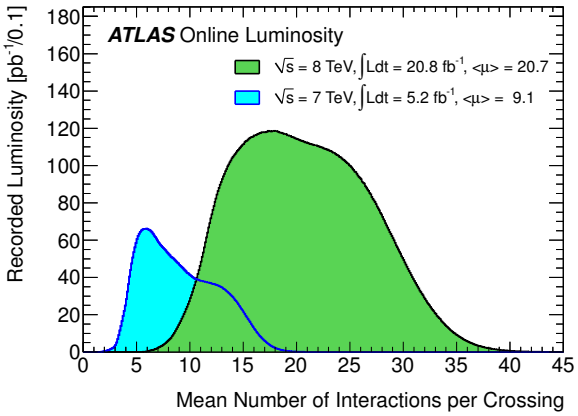

Figure 3.9: *Number of interactions per crossing shown is the luminosity-weighted distribution of the mean number of interactions per crossing from 2011 and 2012 data at 7 and 8 TeV, respectively.*

3.2.7 Pile-up

Pile-up is a challenge for the detectors and for the acquisition and analysis of the data. In particle physics, *pile-up* is called to the situation where the detector is being affected by several events at the same time. Pile-up is a major challenge to many of the physics studies. Due to the large number of protons in colliding bunches at the LHC, it is not unlikely that multiple independent hard interactions occur during one bunch crossing, called *in time pile-up*. This is equivalent to the above defined μ and it increases with increasing instantaneous luminosity:

$$\mu = \frac{n_1 n_2}{4\pi\sigma_x\sigma_y}\sigma_{\text{inel}} \tag{3.7}$$

The mean number of interactions per crossing corresponds the mean of the Poisson distribution on the number of interactions per crossing calculated for each bunch. In design running conditions, about 23 inelastic collisions are expected to accompany each high energy event. In addition, the spacing between the bunches is shorter than the response time of the detectors, so additional collisions from different bunches are recorded simultaneously, referred to as *out of time pile-up*. In Figure 3.9, one can see the mean number of interactions per crossing in the ATLAS detector from 2011 and 2012 LHC proton-proton collisions at 7 and 8 TeV respectively. Figure 3.10 shows the average number of interactions per bunch crossing and number of colliding bunches in ATLAS versus time during the proton-proton runs of 2010, 2011 and 2012.

After this short review of the LHC project and the characteristics of proton-proton collisions, a brief description of the ATLAS detector is presented in the next section.

[3]The integrated luminosity is usually given in units of fb^{-1}.

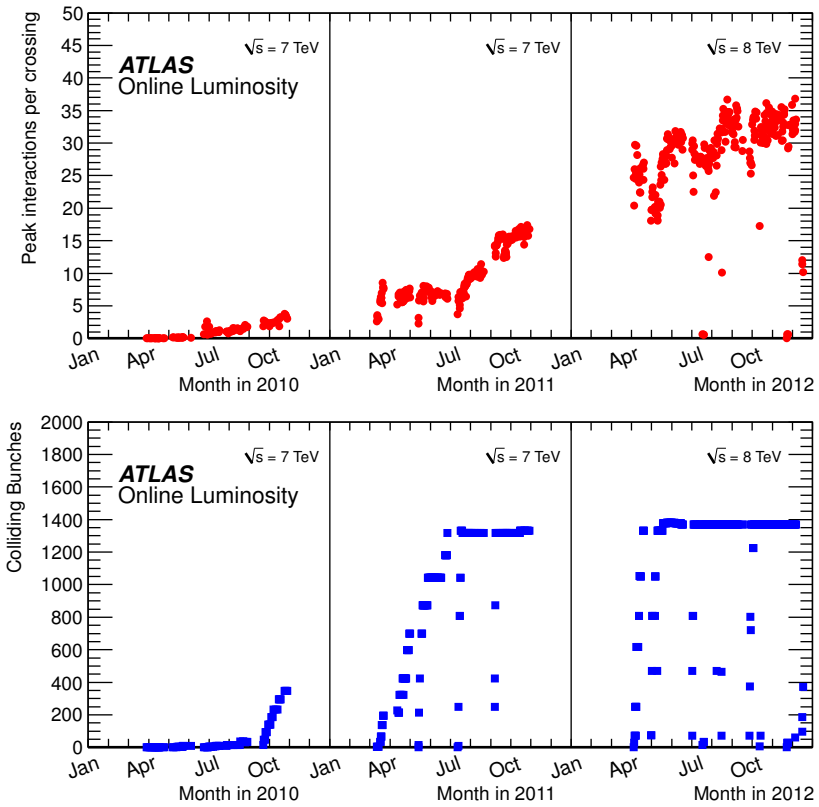

Figure 3.10: *Average number of interactions per bunch crossing and number of colliding bunches in ATLAS versus time during the proton-proton runs of 2010, 2011 and 2012. The product of these two quantities is proportional to the peak luminosity at the start of each LHC fill.*

3.3 The ATLAS detector

ATLAS is a general-purpose experiment, designed to cover the widest possible range of physics at the LHC. The formal proposal for ATLAS was introduced in 1994 [83] and 10 years later the detector installation in the cavern began [84]- [77]. Around 3000 scientists from 177 institutes in 38 countries work on the ATLAS experiment.

The particles created in LHC collisions are recorded in ATLAS through different detecting subsystems that allow to identify particles and measure their momentum and energy. In general, these include b quarks, light quarks, electrons, muons, taus and photons. The quarks hadronise (except the top quark which decays before hadronisation) and form *jets* of particles which are the ones reconstructed in the detector. The ATLAS layout is similar to other general purpose high energy collider detector, with cylindrical shape (4π coverage) and layers of subdetectors. A cut-away view of the ATLAS detector, which has a length of 44 m and a diameter of 25 m, is

shown in Figure 3.11. Driven by the physics requirements, the detecting technologies are a precision tracking system (for measuring the momentum of charged particles), calorimeters (for the determination of the energy of the electromagnetic and strongly interacting particles) and muon chambers (for measuring the momentum of muons). Therefore, ATLAS consists of three main subsystems: the tracking system, the electromagnetic and hadronic calorimeters and the muon chambers, and the main performance goals for each subdetector are listed in Table 3.3. The values achieved so far are summarized in Section 3.4. In addition, the experiment counts with a huge magnet system that bends the paths of charged particles in order to measure their momentum. The central part around the beam line is called the barrel and the wheels perpendicular to the beam axis in the forward parts are called end-caps. The interactions in the ATLAS detectors will create large amount of data. In order to deal with these, ATLAS needs an advanced trigger and data acquisition system and a large computing system.

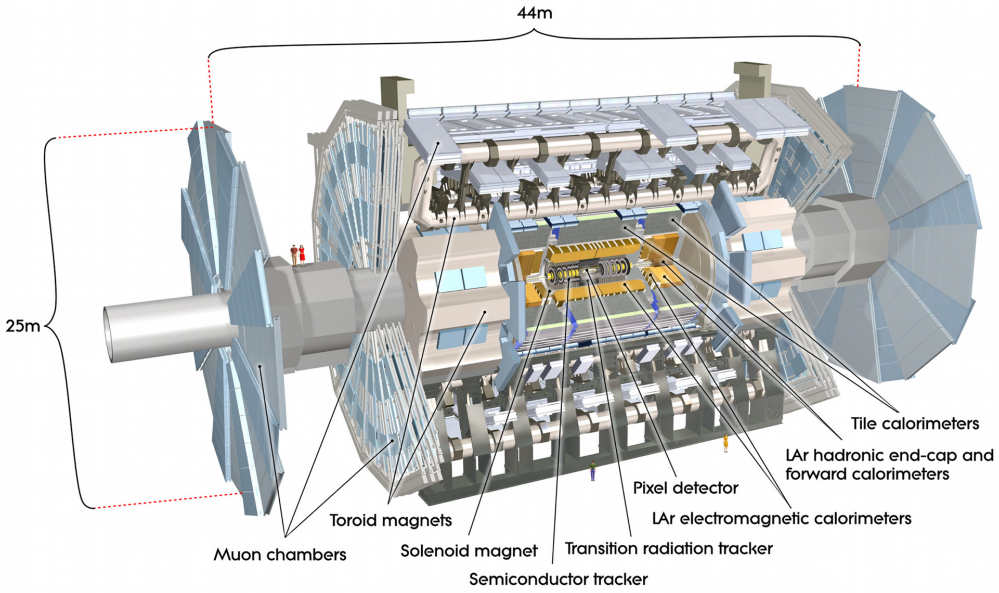

Figure 3.11: *Schematic view of the ATLAS detector.*

In the following, an overview of the detector geometry is presented and later the different subdetectors are described.

3.3.1 Detector geometry

The coordinate system used in the ATLAS detector is shown in Figure 3.12. The beam direction defines the z-axis and the x-y plane is transverse to the beam direction. The positive x-axis is defined pointing to the centre of the LHC ring and the positive y-axis is defined pointing upwards. The transverse energy E_T and momentum p_T are defined in the x-y plane. The azimuthal

subdetector	Resolution	$\|\eta\|$ coverage
Tracking	$\sigma_{p_T}/p_T = 0.05\% \times p_T \oplus 1\%$	±2.5
ECAL	$\sigma_E/E = 10\%/\sqrt{E} \oplus 0.7\%$	±3.2
HCAL		
barrel and end-cap	$\sigma_E/E = 50\%/\sqrt{E} \oplus 3\%$	±3.2
forward	$\sigma_E/E = 100\%/\sqrt{E} \oplus 10\%$	3.1 < $\|\eta\|$ <4.9
Muon spectrometer	$\sigma_{p_T}/p_T = 10\%$ at $p_T = 1\ TeV$	±2.7

Table 3.3: *ATLAS performance goals in terms of resolutions and pseudo-rapidity coverage for the different ATLAS subdetectors [85].*

angle ϕ is measured around the beam axis and the polar angle θ is the angle with respect to the beam axis. The angle θ is generally not used as such but transformed into a quantity called pseudo-rapidity that is defined as η = -ln [tan(θ/2)]. This quantity is 0 if the particle is emitted perpendicular to the beam ($\theta = 90°$) and is about 4.5 close to the beamline ($\theta = 1°$), at the limit of the detector. It is also common to define the ΔR quantity as a measure of the separation between two particles: $\Delta R^2 = \Delta\eta^2 + \Delta\phi^2$.

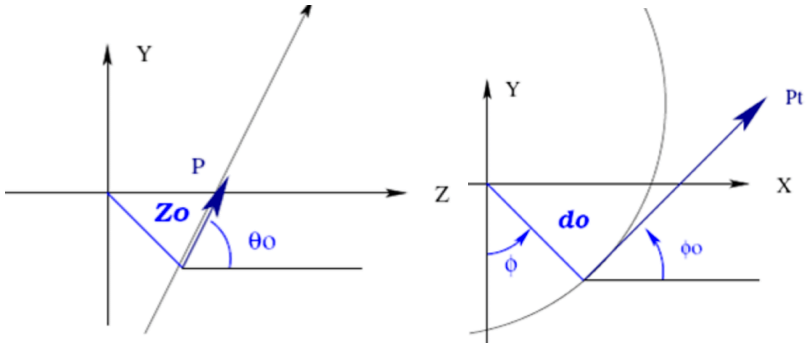

Figure 3.12: *ATLAS coordinate system. The beam direction defines the z-axis and the x-y plane is transverse to the beam direction. The positive x-axis is defined pointing to the centre of the LHC ring and the positive y-axis is defined pointing upwards.*

3.3.2 Inner Detector

The Inner Detector (ID) [86] is the ATLAS tracker which provides an efficient detection of charged particles with high spatial and momentum resolutions and is capable of identifying primary and secondary vertices. Its high granularity allows to perform the pattern recognition, vertex and momentum measurements in the pseudo-rapidity range $|\eta| < 2.5$. These capabilities are achieved with a combination of three different subdetectors: semiconductor pixel and strip detectors and a straw tube tracking detector. It operates embedded in a 2 T axial magnetic field generated by a solenoid [87]. This magnetic field bends the charged particles and therefore their

charge and momentum can be measured. A schematic view of the ID is shown in Figure 3.13. The total size of the ID is 6.2 m long and 2.1 m width. Typically for each track the pixel detector contributes with 3 hits, the strip detector with 4 space-points[4] and the straw tube tracker with around 36 tracking points.

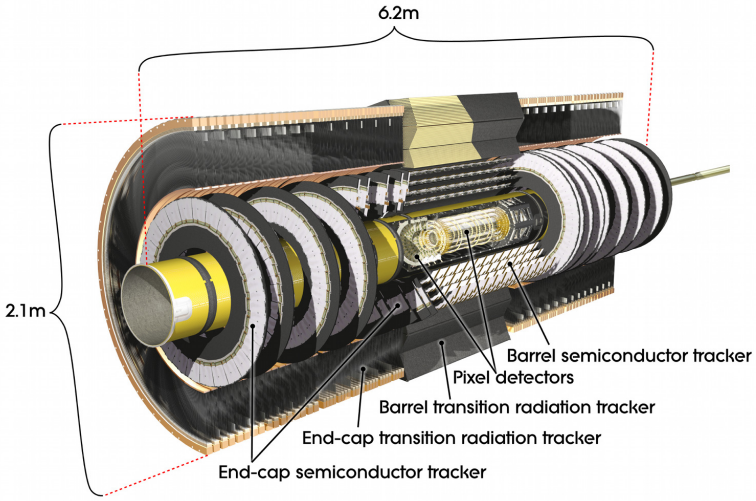

Figure 3.13: *A view of the ATLAS inner detector. The pixel detector has three barrel layers and three end-cap disks on each side. The SCT has four barrel layers and nine end-cap disks each. The TRT has three barrel layers and two end-cap wheels on each side.*

Around 1500 charged particles will cross the ATLAS ID every 25 ns at the LHC design luminosity (10^{34} cm^{-2} s^{-1}). To deal with such density of tracks and vertices a very fine granularity is needed. For this purpose the ID has 5832 individual silicon modules (with about 86 million readout channels). In addition, the ID electronics and all the sensor elements must be fast and radiation hard. To keep an adequate noise performance in the high-radiation environment the heat from the silicon modules is removed via a cooling system. The cooling loops must keep the temperature at around -7°C for the strips and 0°C for the pixels, while introducing a minimal amount of extra material into the detector volume in order to minimize the production of secondary particles.

From inside to outside, the three ID subdetectors are:

- **Pixel detector:** The Pixel detector [88] is the component closest to the beam pipe and it therefore has to cope with a higher particle flux than any other detector in ATLAS. This requires a high granularity to disentangle tracks from individual charged particles and to identify primary and secondary vertices. It consists of 1744 modules that are grouped in three cylindrical layers in the barrel and three disks in each of the end-caps, resulting in a

[4]The space-points are 3D spatial coordinates obtained from the combination of 2D or 1D spacial measurements in the pixels or SCT clusters.

total active area of silicon of approximately 1.7 m^2 and 80.4 million readout channels. The area of each module is ~2x6 cm^2, the thickness is ~250 μm and they contain thousands of pixels with a size of ~50×400 μm^2. They have an intrinsic resolution of 10 μm in the transverse direction and 115 μm in the z direction in the barrel region.

- **Semi-Conductor Tracker (SCT):** The SCT is a silicon microstrip detector located just after the Pixel detector and its main purpose is to contribute to a precise and efficient identification of charged particles. The SCT consists of four concentric layers in the barrel [89] and nine disks in each of the end-caps [90]. In this way, four precision measurements per track can be obtained in the barrel and nine in each end-cap. A SCT detector module consists of two sensors glued back-to-back under a small stereo angle of 40 mrad to provide a two-dimensional measurement (R and ϕ). The same design is used for the modules in the barrel cylinders, whereas different types varying in external dimensions (trapezoidal shape) and strip pitch are used in the end-caps. In the barrel region, each module has a size of 6.36×6.40 cm^2 with 768 strips and 80 μm pitch. Therefore, the spatial resolution achieved is about 17 μm in $r\phi$ and 580 μm in z. In the end-caps, the modules are arranged in (up to three) rings within a disk, therefore there are three types of modules (inner, middle and outer) and the strip pitch varies from 57 to 90 μm. In total, the SCT has 4088 modules (2112 barrel and 1976 end-cap modules) which means 61 m^2 of silicon sensors with 6.3 million channels.

- **Transition Radiation Tracker (TRT):** Finally, the TRT [91] consists of straw detectors arranged parallel to the beam axis in the barrel and radially in wheels in the end-caps. It provides a large number of measurements (typically 36). There are about 300,000 gaseous straw tubes that have a diameter of 4 mm and are filled with a xenon-based gas mixture (70% Xe, 27% CO_2, 3% O_2). Between them, the subdetector is filled of another material (polypropylen) where transition radiation photons are produced when a particle traverses it. The emission of these photons depends on the type of particle and allows to identify electrons in the TRT. For the xenon-based gas the resolution is 130 μm. As this gas is very expensive, an argon-based gas mixture (which resolution decreases to about 190 μm) was used during the commissioning period.

Particles that traverse the ID will interact with the material (sensors, cables, support structures, etc.). The most important effects are: multiple Coulomb scattering (deviation from their ideal trajectory) and energy losses due to ionization and, in the case of electrons, also due to Bremsstrahlung. Although the reconstruction software can correct for these effects up to a certain level, the interactions always degrade its performance. Therefore, the amount of material should be kept as minimum as possible.

The hit resolutions of the three detector systems are summarised in Table 3.4 together with their required alignment precisions. The accuracy of the position of the detector elements after their installation in the ATLAS cavern was in agreement with the expectations: O(1 mm) relative precision within the volume of the ID for an entire barrel or end-cap, O(100 μm) for a single layer or disk and O(10 μm) for individual modules within a layer or disk. Track-based algorithms are used to resolve these residual misalignments. More information on the alignment procedure and the achieved hit resolutions are given in Ref. [92].

	Region (mm)		Intrinsic	Alignment tolerances (μm)		
	Radius (R)	Length (z)	accuracy (μm)	Radial (R)	Axial (z)	Azimuthal ($R-\phi$)
Pixels						
Barrel: 3 layers	50.5–122.5	0–400.5	10 ($R-\phi$) – 115 (z)	10-20	20	7
End-caps: 2×3 disks	88.8–149.6	495-650	10 ($R-\phi$) – 115 (R)	20	100	7
SCT						
Barrel: 4 layers	299–514	0–749	17 ($R-\phi$) – 580 (z)	100	50	12
End-caps: 2×9 disks	75–560	839–2735	17 ($R-\phi$) – 580 (R)	50	200	12
TRT						
Barrel:73 straw planes	563–1066	0–712	130	–	–	30
End-caps: 160 straw planes	644–1004	839–2710	130	–	–	30

Table 3.4: *Region, intrinsic resolutions and alignment tolerances of the three ID subdetectors.*

3.3.3 Calorimetry

The ID is surrounded by the calorimeters [93]- [94] which cover the range $|\eta| < 4.9$ and have a total diameter of 8.46 m and a length of 13.4 m. Their task is to identify and measure the energy of particles (both charged and neutrals) and jets. It also detects missing transverse energy (which is produced by particles that escape the detector undetected such as neutrinos) by summing all the measured energy deposits: $E_T^{miss} = \sqrt{(\sum E_T \cos\phi)^2 + (\sum E_T \sin\phi)^2}$. This subsystem uses different techniques suited to the widely varying requirements of the physics processes of interest. The fine granularity of the electromagnetic calorimeter (ECAL) is ideally suited for precision measurements of electrons and photons. The coarser granularity of the rest of the calorimeter, the hadronic calorimeter (HCAL), is sufficient to satisfy the physics requirements for jet reconstruction and E_T^{miss} measurements. Like many high energy experiments, ATLAS has separate ECAL and HCAL up to $|\eta| < 3.2$. A special combined electromagnetic and hadronic calorimeter covers the range $3.1 < |\eta| < 4.9$. A representation of the ATLAS calorimeters can be seen in Figure 3.14.

The calorimeters contain dense materials (absorbers), which cause an incoming particle to initiate a shower. Particles created in this shower are detected in the active material, which is interleaved with the absorbers. The total signal in the active material is a measure of the energy of the incoming particle. ATLAS uses two types of active material: liquid-argon and scintillating plastic. Particles that traverse the liquid-argon create charge by ionization, which is collected on readout electrodes. The scintillating plastic is doped with fluorescent molecules, which emit light when the atoms in the plastic are excited by a passing particle. The light is detected and amplified by photomultiplier tubes. For the absorbers several types of material are used: lead, steel, cooper and tungsten.

The ECAL uses liquid-argon as an ionization medium (known as LAr calorimeter), with lead absorbers arranged in an accordion geometry. This kind of geometry provides complete azimuthal symmetry without cracks and the lead thickness in the absorber plates is optimized as a function of η in terms of performance in energy resolution. The $\Delta\eta \times \Delta\phi$ granularity is 0.025×0.025 in the barrel which covers a region of $|\eta| < 1.5$ while the end-caps provide a coverage of $1.375 < |\eta| < 3.2$. In total, the amount of material in the ECAL corresponds to 25-35

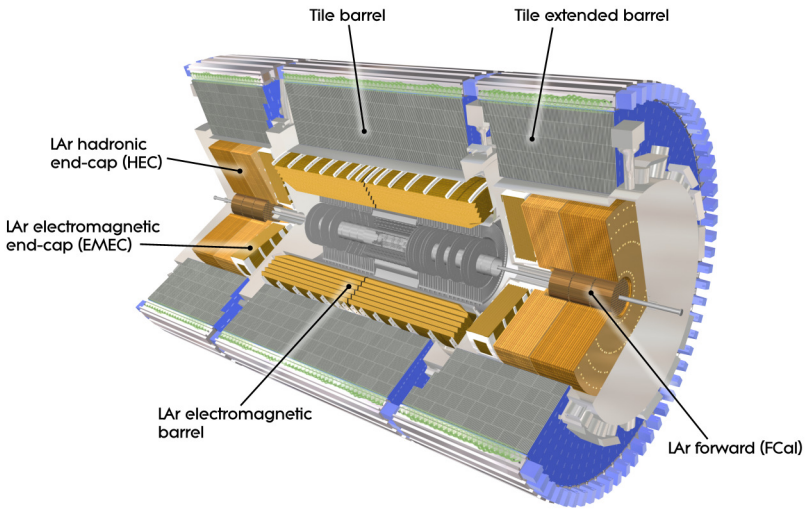

Figure 3.14: *Cut-away view of the ATLAS calorimeter system with its subdetectors labelled.*

radiation lengths[5] (X_0) and to 2-4 nuclear interaction lengths[6] (λ) over the whole pseudo-rapidity range. The ultimate energy resolution is expected to be $\sigma_E/E = 10\%/\sqrt{E} \oplus 0.7\%$. It is surrounded by a cryostat as it needs very low temperatures to operate.

Surrounding the latter is the HCAL, which is divided in the Tile Calorimeter (TileCal), the Hadronic End-cap Calorimeters (HEC) and the Forward Calorimeter (FCal). The TileCal covers the central region ($|\eta| < 1.7$) and uses plastic scintillator plates (called tiles) as active material and steel as absorber. The HEC extends up to $|\eta| = 3.2$ and relies on liquid-argon as active material and copper as absorber material. The ultimate energy resolution of these hadronic calorimeters is expected to be $\sigma_E/E = 50\%/\sqrt{E} \oplus 3\%$. In the very forward region up to $|\eta| = 4.9$, the FCal is installed to improve the measurement of the missing transverse energy. Again liquid-argon was chosen as active material while the absorbing material is composed of copper and tungsten. The ultimate energy resolution is expected to be $\sigma_E/E = 100\%/\sqrt{E} \oplus 10\%$. The cumulative amount of material at the end of the active calorimetry region varies between 10 and 18 nuclear interaction lengths.

3.3.4 Muon Spectrometer

The outermost detector is the muon spectrometer (MS) [95] and its layout is shown in Figure 3.15. It was designed to provide a transverse momentum resolution of approximately 2-4%

[5]The radiation length (X_0) is a characteristic of a material, related to the energy loss of high energy, electromagnetic-interacting particles with it. It is both the mean distance over which a high-energy electron loses all but 1/e of its energy by bremsstrahlung, and 7/9 of the mean free path for pair production by a high-energy photon.

[6]Nuclear interaction length (λ) is the mean path length required to reduce the numbers of relativistic charged particles by the factor 1/e, or 0.368, as they pass through matter.

for muons with a p_T below 200 GeV, possible thanks to the bending power of the magnetic field provided by an air-core toroid system [87]. This magnetic system can be seen in Figure 3.16 and has a barrel (25 m long, with an inner bore of 9.4 m and an outer diameter of 20.1 m) and two inserted end-cap magnets (with a length of 5.0 m, an inner bore of 1.65 m and an outer diameter of 10.7 m). The barrel toroid consists of eight flat coils assembled radially and symmetrically around the beam axis and provides a bending power between 1.5 and 5.5 T · m over $|\eta| < 1.4$. The end-cap toroid coils are rotated in azimuth by an angle of 22.5° with respect to the barrel toroid coils to provide radial overlap, and to optimize the bending power in the transition region ($1.0 \leq |\eta| \leq 1.4$). In the forward region, the magnets produce a bending power of approximately 1-7.5 T · m.

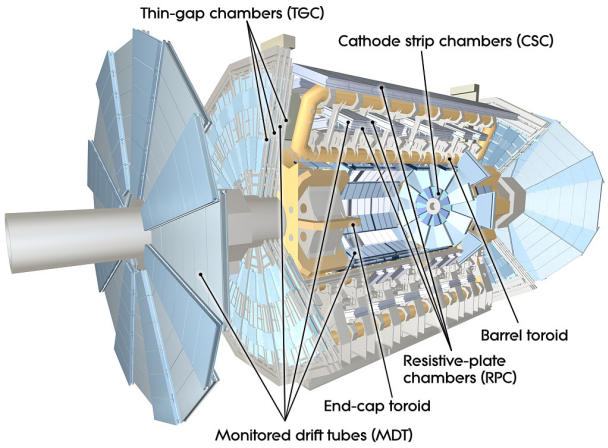

Figure 3.15: *Cut-away view of the ATLAS muon system.*

Four different detector types are used to reconstruct muon trajectories. Monitored Drift Tubes (MDTs) chambers provide a precision measurement of the coordinate in the bending direction of the particles in the central part of the detector. In the forward region, Cathode Strip Chambers (CSCs) are used which have higher granularity in order to deal with the higher background rate. In addition, Resistive Plate Chambers (RPCs) and Thin Gap Chambers (TGCs) are used for triggering and measuring the coordinate orthogonal to the bending direction.

3.3.5 Trigger System

At the LHC design luminosity, the proton-proton collisions at the LHC take place every 25 ns (40 MHz) with around 23 interactions per crossing. To reduce the amount of data and reach the desired event rate of about 100 Hz, the online event selection (called trigger system) has to decide whether a collision looks interesting or not and for that employs several strategies. The trigger system selects events by identifying signatures of muons, electrons, photons, tau leptons, jets and B meson candidates, as well as using global event signatures, such as missing transverse energy. The ATLAS trigger is based on three levels of event selection: Level 1, Level 2 and the

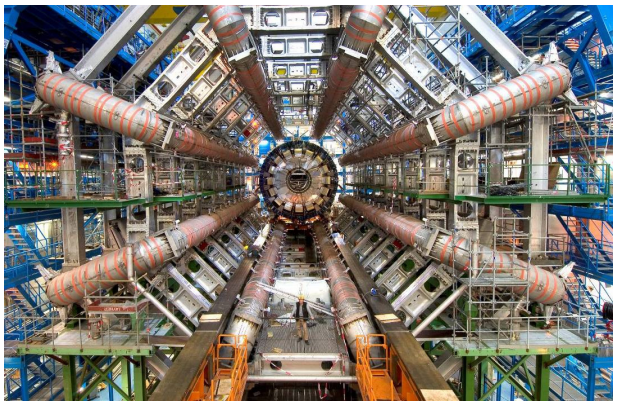

Figure 3.16: *Barrel toroid as installed in the underground cavern.*

Event Filter, as shown in Figure 3.17. Each trigger level refines the event selection done by the previous level.

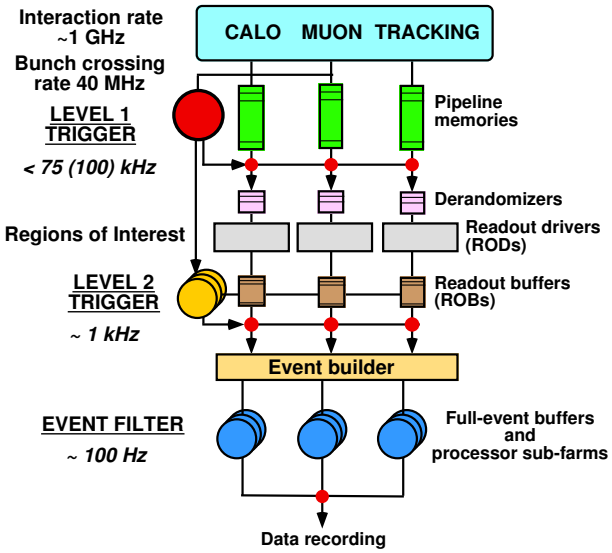

Figure 3.17: *Schematic of the ATLAS trigger system.*

The Level 1 [96] is hardware-based (the logic is implemented with custom electronics) and the trigger decision is made in about 2.5 μs. It is designed to reduce the design 40 MHz bunch crossing rate to about 75-100 kHz. The detector acceptance is split into several *regions of interest* (ROIs) of limited size in pseudo-rapidity and azimuthal angle, and the information from the

calorimeters and the muon system belonging to different ROIs is processed in parallel. Events are accepted and passed to the next level only if some interesting signature is detected in at least one ROI. The subsequent two levels are software-based and are collectively known as the High Level Trigger [97]. The Level 2 makes use of the full granularity from all detectors and is designed to reduce the rate of stored events to around 1 kHz in approximately 40 ms. Finally, the Event Filter uses offline algorithms to further reduce the rate to 100 Hz in around 4 s.

During 2011 and 2012 data-taking periods the LHC bunch-crossing rate was 20 MHz and ATLAS trigger system allowed to reduce the recording rate to around 400 Hz. The output rate of Level 1 was ~60 kHz and ~75 kHz respectively, limited due to detector readout limits. The Level 2 trigger reduced the event rate to 4-5 kHz and 6.5 kHz respectively, with an average event processing time of approximately 90 ms. After the Event Filter the rate was reduced to 300-400 Hz, with an average event processing time of ~1 s. Each selected event has a total size of around 1.6 MB. Figure 3.18 shows trigger rates of primary triggers for some signatures in the 2012 menu as a function of luminosity, most of which exhibit a linear dependence on luminosity.

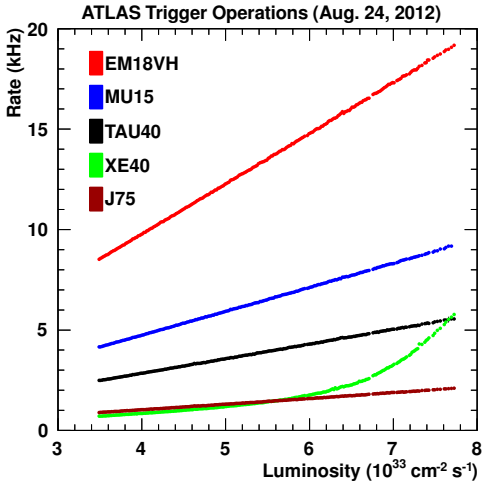

Figure 3.18: *Measured trigger output rates in the 2012 data taking as a function of luminosity. Level 1 rates for the lowest-threshold unprescaled single object triggers are shown: EM18VH for an electron or photon with a threshold at 18 GeV, MU15 for a muon with a threshold near 15 GeV and requiring a three station coincidence in the barrel or end-cap of the detector, TAU40 for a hadronicaly decaying tau above 40 GeV; XE40 for missing transverese energy above 40 GeV and J75 for a jet above 75 GeV.*

3.3.6 Data samples

Prior to proton-proton collisions at the design LHC energy and luminosity, the machine has been running from 2010 to 2012 at a centre-of-mass energy of 7 and 8 TeV and lower instantaneous luminosity. Figure 3.19 shows the luminosity delivered by the LHC and the integrated luminosity recorded in the ATLAS detector versus time for the three years of data taking. In

March 2010, the first proton-proton collisions at the LHC took place at 7 TeV and during that year an instantaneous luminosity of 0.2×10^{33} cm^{-2}s^{-1} was achieved and the delivered integrated luminosity was of 48.1 pb^{-1}. In 2011, a second phase at 7 TeV followed reaching a peak luminosity of 3.7×10^{33} cm^{-2}s^{-1} and an integrated luminosity of 5.6 fb^{-1}. During 2012, collisions delivered at a centre-of-mass energy of 8 TeV took place with a peak luminosity of 7.7×10^{33} cm^{-2}s^{-1} and an integrated luminosity of 23.3 fb^{-1}. The delivered luminosity accounts for the luminosity delivered from the start of stable beams until the LHC requests ATLAS (or other experiment) to stop the acquisition and put the detector in a safe standby mode to allow for a beam dump or beam studies to be performed. The recorded luminosity reflects the data acquisition inefficiency, as well as the inefficiency of the socalled "warm start": when the stable beam flag is raised, the tracking detectors undergo a ramp of the high-voltage. The average ATLAS data-taking efficiency was about 93%. Additional requirements were applied for physics analysis: all reconstructed physics objects should satisfy some good data quality criteria. Overall, about 90% of delivered collisions are available for physics analysis.

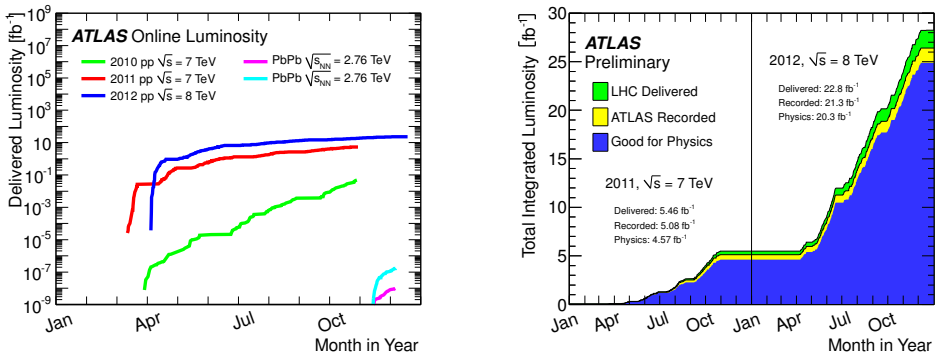

Figure 3.19: *Left: Delivered luminosity versus time for the three years of data taking 2010, 2011 and 2012 (including both proton-proton and Pb-Pb data). Right: Total integrated luminosity versus time delivered by the LHC (green), recorded by ATLAS during stable beams (yellow) and good for physics (blue) in 2011 and 2012 proton-proton collisions at a centre-of-mass energy of 7 and 8 TeV respectively.*

3.4 Objects reconstruction

The events that satisfy the trigger selection are later passed to the offline reconstruction software, which interprets the detector signals as charged tracks, electrons, muons, taus, photons or jets, with their four momentum vectors. The reconstruction of all these final state objects requires combine information of all the subdetectors. Top quarks precise measurements require an excellent reconstruction of its decay products, also called final state objects. Since this thesis only considers top quark events with leptonic W boson decay with an electron or muon in the final state, the relevant reconstruction tools involve electrons, muons, jets and their corresponding b-flavour identification, and $E_{\mathrm{T}}^{\mathrm{miss}}$ (from neutrinos). In this chapter, a brief description of the methods used to reconstruct these particles as well as the systematic uncertainties associated to each object is given. The performance of the reconstruction algorithms used in this work is also discussed.

3.4.1 Tracking and vertexing in the inner detector

The reconstruction of the trajectories of charged particles is essential for experiments at the LHC. For that, the detectors contain precise tracking systems structured in layers around the collision point which measure the positions where particles intersect those layers. The physics analyses mainly need the momentum and direction of the particle and these parameters need to be determined from the initial measurements. The track reconstruction includes a pattern recognition deciding which measurements belong to a track and how many particle tracks can be found and also the estimation of the track parameters. This is a very challenging task given the high event rate at the LHC.

Charged particle tracks with momentum $p_T > 0.5$ GeV and $|\eta| < 2.5$ are reconstructed in the ATLAS ID thanks to the bending power provided by the solenoid magnet. The reconstruction of tracks is divided into three main steps.

1. The first step is the so-called ‘seed finder’ or pre-processing, the raw data from the pixel, SCT and TRT detectors are converted into ‘seeds’.

2. A track-finding stage follows in which the high granularity of the silicon detectors is exploited to find prompt tracks (inside-out algorithm). First, track seeds are formed from the space-points in the three pixel layers and the first SCT layer. Track candidates are formed by extending these seeds throughout the SCT and then they are fitted excluding outlier clusters. This is achieved by applying quality cuts. For example, a cut is made on the number of associated clusters, with explicit limits set on the number of clusters shared between several tracks and the number of holes per track (a hole is defined as a silicon sensor crossed by a track without generating any associated cluster). The selected tracks are then extended into the TRT and refitted with the full information of all three subdetectors. The quality of the refitted tracks is compared to the silicon-only track candidates and hits on track extensions resulting in bad fits are labelled as outliers (they are kept as part of the track but are not included in the fit). A complementary track-finding strategy, called back-tracking, searches for unused track segments in the TRT. Such segments are extended into the SCT and pixel detectors to improve the tracking efficiency for secondary tracks from conversions or decays of long-lived particles.

3. At an advanced (post-processing) stage of event reconstruction dedicated vertex algorithms using exclusively ID information are used to reconstruct primary and secondary vertices. The primary vertex reconstruction algorithm forms vertex candidates by associating tracks and then fits for the vertex position. The tracks associated with the vertex are also refit using the reconstructed interaction point as constraint. Tracks with transverse momentum of at least 150 MeV and with hits in the silicon detector are selected. Vertex seeds are obtained from the z position at the beamline of reconstructed tracks. An iterative χ^2 fit is made using the seed and nearby tracks. Tracks displaced by more than 7σ from the vertex are used to seed a new vertex and the procedure is repeated until no additional vertices can be found. During reconstruction, vertices are required to contain at least two tracks. The primary vertex is selected requiring the largest transverse momentum sum calculated from the transverse momenta of all the tracks associated to it. Figure 3.20 shows the two-dimensional distributions of the primary vertex positions in the x-y and z-x planes in ATLAS obtained with 2011 dataset.

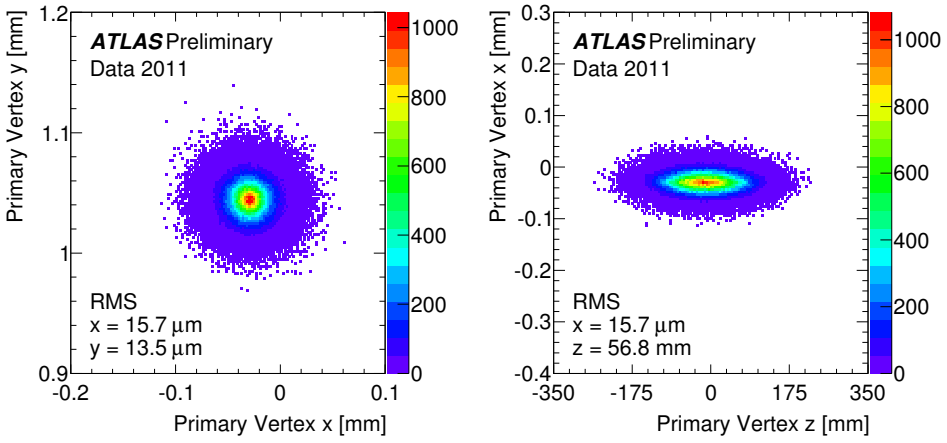

Figure 3.20: *Two-dimensional distribution of reconstructed primary vertices in 7 TeV data, in the x-y plane (left) and in the z-x plane (right).*

3.4.2 Electrons

3.4.2.1 Electron reconstruction and identification

An excellent electron identification is crucial to reject the large backgrounds typically originated from jets (multijets) leading to fake electrons. The standard electron reconstruction algorithm starts from clusters in the calorimeters and then builds the identification variables based on the information from both the ID and the ECAL. A calorimeter cluster seed with transverse energy above 3 GeV is matched to a track in the ID among all the reconstructed tracks which do not belong to a photon-conversion pair. The track, after extrapolation to the ECAL, is required to match the cluster within a $\Delta\eta \times \Delta\phi$ window of 0.05×0.10. The ratio E/p of the energy of the cluster to the momentum of the track is required to be lower than 10. Approximately 93%

of true electrons with $E_T > 20$ GeV and $|\eta| < 2.5$ are selected as electron candidates. The inefficiency is mainly due to the large amount of material in the ID and is therefore η dependent. Three identification criteria are defined based on a combination of cuts: `Loose`, `Medium` and `Tight`, providing different electron efficiency versus jet rejection working points.

- `Loose`**:** The loose identification criteria uses only information from the calorimeters. Cuts are applied on the hadronic leakage (the ratio of the E_T in the first compartment of the HCAL and in the ECAL) -electromagnetic showers deposit a small amount of energy in the HCAL-, and on shower shape variables (lateral shower shape and width) based on the second layer of the ECAL -electromagnetic showers deposit most of their energy in this layer-. This set of cuts provides excellent identification efficiency but low background rejection.

- `Medium`**:** This selection improves the quality by adding cuts on both the ECAL and the tracking variables. The fine longitudinal segmentation of the first layer of the ECAL is exploited, in particular to reject photons from neutral pion decays, which result into very close deposits of energy. In addition, some quality cuts in the matched track are applied, in particular in the number of hits in the Pixel and SCT subdetectors and on the transverse impact parameter. The medium selection increases the jet rejection by a factor 3-4 with respect to the loose identification and reduces the selection efficiency by ~10%.

- `Tight`**:** This set of cuts makes use of all the particle-identification tools currently available for electrons. In addition to the medium selection criteria, further cuts are applied on the tracking variables. An additional energy (and momentum) isolation cut is applied to the cluster using all cell energies within a cone of ΔR <0.2 (and 0.3) around the electron candidate. This selection provides the highest isolated electron identification and rejection against jets.

A re-optimised menu, referred to as the plus-plus menu and providing three additional operating points (`Loose++`, `Medium++`, `Tight++`), has been defined with improved performance in an environment with higher pile-up. In this menu, more variables are used and the cut values of each operating point are varied. The tight criteria `Tight++` is used in top quark analyses in order to provide a good separation between electrons and jets.

Since electrons from the W boson decay are typically isolated from hadronic jet activity, additional isolation requirements are applied in top quark analyses in order to suppress the QCD multijet background. Electrons with the minimum calorimeter activity (calorimeter isolation) and only few tracks (track isolation) in an η-ϕ cone around the electron track are selected. The following cuts are applied: the sum of the calorimeter transverse energy within a cone of radius $\Delta\mathrm{R} = \sqrt{\eta^2 + \phi^2} = 0.2$ (excluding the cells associated to the electron) is required to be below a certain threshold that depends on the electron E_T, the electron η and the number of reconstructed primary vertices and is chosen such that the efficiency for real electrons to pass this isolation requirement is 90%. In addition, the p_T of all tracks within a cone of radius $\Delta\mathrm{R} = 0.3$ around the electron direction, again excluding the track belonging to the electron, is also restricted to fall below an E_T-dependent threshold. The efficiency for this track-based isolation requirement is also 90% for real electrons.

3.4.2.2 Efficiencies

The electron reconstruction and trigger efficiencies are measured with the tag-and-probe method [98] using $Z \to ee$, $W \to e\nu$ and $J/\Psi \to ee$ data and simulated samples. The electron identification efficiencies [99] are derived from combined measurements using $Z \to ee$ and $W \to e\nu$ events. Figure 3.21 shows the identification efficiency for the loose, medium and tight selection criteria described above as a function of E_T for data and simulated $Z \to ee$ events. Scale factors are obtained from the data and Monte Carlo comparisons and allow to correct the Monte Carlo to match the data. These factors are defined as $\varepsilon_{data}/\varepsilon_{MC}$ and are given for different η (and E_{T}) bins and separately for reconstruction, trigger and identification efficiencies. The derived scale factors are close to one with variations of ±5% [100]. The uncertainties due to pile-up effects, to the modelling of the underlying event and to the difference in top quark and W/Z events are evaluated and are found to be within ±1.5%.

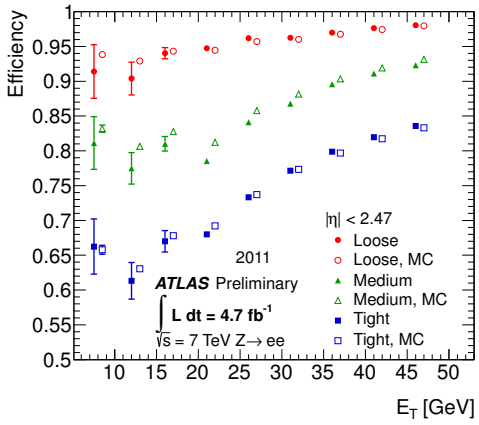

Figure 3.21: *Electron identification efficiency for data and simulated $Z \to ee$ events for the three identification criteria as a function of E_T for $|\eta| < 2.47$.*

3.4.2.3 Energy scale and resolution

The electron energy scale and resolution are obtained from $Z \to ee$, $J/\Psi \to ee$ and $W \to e\nu$. The energy scale is corrected in data as a function of the electron η_{cl}, ϕ_{cl} and E_{T} and systematic uncertainties are within ±1–1.5%. In addition, an energy smearing is applied to the Monte Carlo to match the energy resolution in data [101].

3.4.3 Muons

The outermost subdetector of ATLAS, the MS, is designed for muon identification with an efficiency greater than 95% and a momentum resolution better than 4% for p_T below 200 GeV. A muon signature consists in a track in the ID, minimum energy deposition in the calorimeters and a track in the muon chambers. Before reaching the MS, the muon traverses around 100 radiation

lengths X_0 of material, most part instrumented by the calorimeters. The proper account for multiple scattering and energy loss effects is essential to properly determine the muon momentum. Naively the muon reconstruction is expected to perform better than the electron reconstruction since the first are minimum ionizing particles[7]. This means that generally material effects such as multiple scattering and energy loses will be less important than for electrons.

3.4.3.1 Muon reconstruction algorithms

ATLAS employs a variety of strategies for identifying and reconstructing muons. The direct approach is to reconstruct *standalone* muons by finding tracks in the MS and then extrapolating these to the beam line. *Combined* muons are found by matching and combining the standalone MS tracks with those in the ID. For low-p_T muons, *tagged* muons are found by extrapolating ID tracks to the MS and trying to match them with reconstructed segments. Calorimeter tagging algorithms have also been developed.

In ATLAS, the algorithms are grouped into two families such that each one includes one algorithm of each strategy: `Staco` (which includes `Muonboy`, `Staco` and `MuTag`) and `Muid` (`Moore`, `Muid` and `MuGirl`) [102]. In the analysis presented in this thesis, muons reconstructed by the `Muid` family were used.

- **Standalone muons:** The simplest approach is to reconstruct muon tracks using only information of the MS. The reconstruction of standalone muons starts building track segments in each of the three muon stations. Then these segments are linked to form a track which is then extrapolated back to the beam line. The extrapolation takes into account multiple scattering and energy loses in the calorimeters. `Muonboy`, from the `Staco` family, assigns energy loss based on the material crossed in the calorimeters; while `Moore`, from `Muid`, additionally makes use of the calorimeter energy measurements if they are significantly larger than the most likely value and the muon appears to be isolated.

- **Inner detector muon tracks:** The ID track reconstruction algorithm is described in Section 3.4.1.

- **Combined muons:** Both of the muon combined algorithms, `Staco` and `Muid`, match tracks in the MS with those found in the ID using a χ^2 and combining the measurements from both systems. The χ^2 is defined as the difference between outer (MS) and inner (ID) vector of track parameters $\mathbf{T}$ weighted by their covariance matrix $\mathbf{C}$:

$$\chi^2 = (\mathbf{T_{MS}} - \mathbf{T_{ID}})^{\mathrm{T}} \, (\mathbf{C_{ID}} + \mathbf{C_{MS}})^{-1} \, (\mathbf{T_{MS}} - \mathbf{T_{ID}}) \,, \tag{3.8}$$

  Here MS refers to the standalone track after extrapolation. This χ^2 provides an important measure of the quality of this match and is used to decide which pairs are retained to form the combined muon.

[7] When a particle passes through matter, it ionizes or excites the atoms it encounters, losing energy in small steps. The rate at which the particle loses energy depends on the material, the own nature of the particles and its momentum. Thus, the minimum ionizing particles (so-called mips) are those in which the mean energy loss rate is close to the minimum, as it is the case of muons.

Staco performs a statistical combination of the inner and outer track vectors to obtain the combined track vector:

$$\mathbf{T} = (\mathbf{C}_{\mathbf{ID}}^{-1} + \mathbf{C}_{\mathbf{MS}}^{-1})^{-1} (\mathbf{C}_{\mathbf{ID}}^{-1}\mathbf{T}_{\mathbf{ID}} + \mathbf{C}_{\mathbf{MS}}^{-1}\mathbf{T}_{\mathbf{MS}}) \tag{3.9}$$

Muid does a track refit using the original hits in both ID and MS. The fit accounts for material effects and the magnetic field.

- **Tagged muons:** The spectrometer tagging algorithms, MuTag from Staco and MuGirl from Muid, propagate all ID tracks with sufficient momentum out to the first station of the MS and search for nearby segments. If a segment is sufficiently close to the predicted track position, then the ID track is tagged as corresponding to a muon. MuTag starts from ID tracks, extrapolates them to the MS and tries to match them with reconstructed segments using a χ^2. MuGirl considers all ID tracks and re-does segment finding in the region around the track. It uses an artificial neural network to define a discriminant.

In top quark analyses muons are required to be combined (Muid family) and to pass some track quality cuts. Two isolation requirements are used to suppress the backgrounds originating from heavy flavour decays: $E_T^{0.2} < 4$ GeV and $p_T^{0.3} < 2.5$ GeV.

3.4.3.2 Efficiencies

The efficiency of both the muon reconstruction and trigger are measured using the tag-and-probe method in $Z \to \mu\mu$ data and Monte Carlo events [103]. The trigger efficiency varies during the run due to hardware issues in individual trigger chambers and as such the trigger efficiency is parametrised as a function of muon η and ϕ. In general the Monte Carlo simulation describes the data very well and the obtained data/Monte Carlo scale factors only differ from unity by ±1-2% [100].

3.4.3.3 Momentum scale and resolution

Momentum corrections have been derived from $Z \to \mu\mu$ events by comparing the dimuon mass resolution measured in experimental and simulated data [103]. Scale and smearing corrections have been derived from the peak position of the Z resonance and they are applied separately to the ID and MS extrapolated measurements of the muon p_T in Monte Carlo [101]. Figure 3.22 shows the dimuon invariant mass for combined muons before and after applying the scale and smearing corrections.

3.4.4 Jets

As discussed before, quarks combine to form composite colour-less particles called hadrons. A jet is intuitively a narrow cone of hadrons and other particles produced by the *hadronisation* of a quark (except the top quark that decays before hadronising) or gluon in high energy physics experiments. The hadrons interact with the detector and produce energy clusters. Jets are reconstructed from detector signals using jet clustering algorithms and then are calibrated to the hadronic scale using different methods.

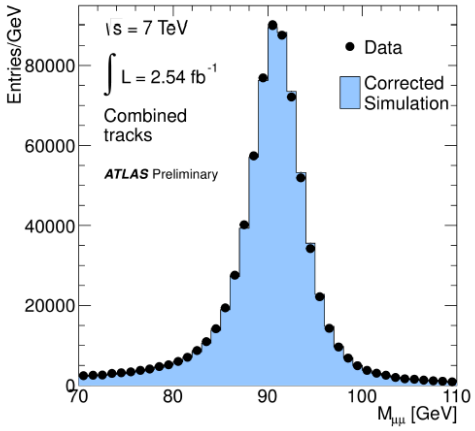

Figure 3.22: *Dimuon invariant mass for combined muons (Muid family), isolated and with p_T >15 GeV, after the application of muon momentum corrections.*

A good jet reconstruction algorithm should be sufficiently insensitive to the details of the hadronisation such that it gives the same result if applied at detector level, at hadron level and directly at parton level. Thus, the properties of the jets (energy and direction) are directly related to the properties of the original partons. The calorimeter is ideally suited for the reconstruction of jets, since it provides an effective way to reconstruct the four momentum of both charged and neutral particles. The reconstruction of the jets and their calibration is essential in order to study the physics of the event.

3.4.4.1 Jet reconstruction algorithms

In ATLAS two types of jet reconstruction algorithms are implemented: fixed cone and sequential recombination algorithms, being the latter the one used in most of the physics analysis. One of the sequential recombination algorithms is the k_t algorithm. All pairs of input objects are analysed with respect to their distance measure defined as:

$$\begin{aligned} d_{ij} &= min(p_{T,i}^2, p_{T,j}^2)\frac{\Delta R_{ij}^2}{R^2} \text{ being } \Delta R_{ij}^2 = \sqrt{\Delta\phi_{ij}^2 + \Delta\eta_{ij}^2}\,, \\ d_{iB} &= p_{T,i}^2 \end{aligned} \tag{3.10}$$

where R is the radius of a cone which determines the size of the jets, d_{ij} is the distance between objects i and j and d_{iB} is the distance of the object i with respect to the beam. The minimum d_{min} of all d_{ij} and d_{iB} is determined. If d_{min} is among one of the d_{ij}, then the corresponding objects i and j are merged into a single new object; while if d_{min} is one of the d_{iB}, the object i is considered to be a jet by itself and removed from the list. This procedure is repeated iteratively, updating all distances at each iteration step. Like this, all input objects end up to be either part of a jet or to be jets by themselves, and no objects are shared between jets. The advantage of

the k_t algorithm is that it is, by construction, collinear and infrared safe (soft emissions do not change the jets); however, it is very sensitive to picking up soft contributions from pile-up and the underlying event.

The k_t algorithm can be generalized [104] by introducing the following particle-particle and particle-beam distance measures:

$$\begin{aligned} d_{ij} &= min(p_{T,i}^{2p}, p_{T,j}^{2p}) \frac{\Delta R_{ij}^2}{R^2} , \\ d_{iB} &= p_{T,i}^{2p} \end{aligned} \tag{3.11}$$

Different algorithms are defined depending on the integer parameter p: the k_t algorithm itself for $p = +1$, the *Cambridge/Aachen* for $p = 0$ and the anti-k_t for $p = -1$. Contrary to k_t, the anti-k_t algorithm clusters first hard objects together, which results in more regular jets. In most top quark physics analyses performed in ATLAS, jets are reconstructed using the anti-k_t algorithm with a cone size $R = 0.4$ starting from topological energy clusters. These are formed from calorimeter cells and its four-momentum is the sum of the energy of the included cells, zero mass and its direction pointing from the center of ATLAS.

3.4.4.2 Jet calibration and jet energy scale

The jet clustering algorithms provide jets at the electromagnetic scale (EM scale), appropriate for the energy deposited by electrons or photons. However, for hadrons, several effects can change substantially the obtained jet energy from the original energy and therefore they need to be calibrated to the hadronic scale. In the calibration process, the jet reconstructed in the calorimeters is corrected to particle level by removing all the effects due to the detector itself: non-compensating[8] calorimeters, energy losses in cracks, due to particles escaping the calorimeters, due to out of cone contributions, etc.

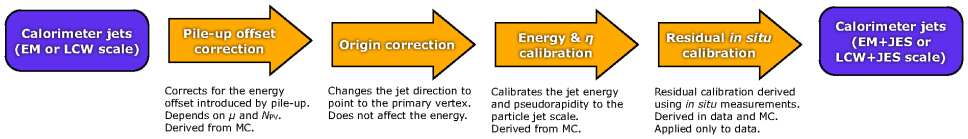

Figure 3.23: *Overview of the ATLAS jet calibration scheme used for the 2011 dataset. The pile-up, absolute JES and the residual in-situ corrections calibrate the scale of the jet, while the origin and the η corrections affect the direction of the jet.*

The calorimeter jets used in this thesis are reconstructed from topoclusters with a positive energy. The topoclusters are built from topologically connected calorimeter cells that contain a

[8] Electromagnetic calorimeters are designed to measure the energy of particles that interact primarily via the electromagnetic interaction, while hadronic calorimeters are designed to measure particles that interact via the strong nuclear force. The response of a calorimeter can be described in terms of the e/h ratio which is a measure of how well a calorimeter responds to leptons or photons versus hadrons. In the ideal case this ratio is ~1 and this condition is called compensation.

significant signal above noise. The cell noise is the electronic noise added in quadrature with the contribution from pile-up fluctuations. The topoclusters are reconstructed at the EM scale and are later calibrated using the local cluster weighting (LCW) method to improve the resolution by reducing fluctuations due to the non-compensating nature of the ATLAS calorimeter. The LCW first classifies the topoclusters as either electromagnetic or hadronic, based on the measured energy density and the longitudinal shower depth. Energy corrections are derived according to this classification from single charged and neutral pion Monte Carlo simulations. Dedicated corrections are derived to account for non-compensation effects, signal losses due to noise threshold and energy lost in non-instrumented regions. Figure 3.23 presents an overview of the ATLAS calorimeter calibration scheme used for the 2011 dataset [105], which restores the jet energy scale (JES) to that of jets reconstructed at particle level. This procedure consist of four steps:

1. First of all, jets formed from topoclusters at the EM or LCW scale are calibrated by applying a correction to account for the energy offset caused by pile-up interactions (both in-time and out-of-time pile-up). This correction [106] is obtained from Monte Carlo simulations as a function of the number of primary vertices in the event and the number of average interactions per crossing (μ), in bins of jet p_T and $|\eta|$.

2. A correction to the jet direction is applied such that the jet points back to the primary vertex instead of the centre of the ATLAS detector.

3. Jets are then calibrated with Monte Carlo based p_T and $|\eta|$ dependent correction factors to restore the full hadronic energy scale, i.e. to bring the measured jet p_T to the truth jet energy (particle level in the simulations) [107]. These corrections can be applied to jets formed from topoclusters at EM or LCW scale with the resulting jets being referred to as calibrated with the EM+JES or LCW+JES scheme. Figure 3.24 shows the average energy response $R(p_T, \eta) = \frac{p_T^{EM/LCW\,jet}}{p_T^{truth}}$, which is equal to the inverse of the jet calibration correction, for various jet energies as a function of the jet $|\eta|$.

4. A residual correction is applied as a last step to jets reconstructed in data to account for differences between data and Monte Carlo. The jet p_T in data is compared to the one in Monte Carlo simulation using in-situ techniques that exploit the p_T balance between the jet p_T and the p_T of a reference object (p_T^{ref}) such as a photon or a Z boson:

$$< \frac{p_T^{\mathrm{jet}}}{p_T^{\mathrm{ref}}} >_{\mathrm{data}} \; / \; < \frac{p_T^{\mathrm{jet}}}{p_T^{\mathrm{ref}}} >_{\mathrm{MC}} \; .$$

   This quantity is the residual in-situ JES correction and it is derived from a combination of γ+jet, Z+jet and multijet techniques. The correction varies from 5% to 2% for 2011 dataset [105] and it is applied to the scale of jets in data.

In the top quark analysis presented here, jets calibrated with LCW+JES scheme are used.

3.4.4.3 Jet energy scale uncertainty

The JES uncertainty is derived using information from test-beam data, LHC collision data and simulation and it has different contributions: in-situ calibration uncertainty and additional

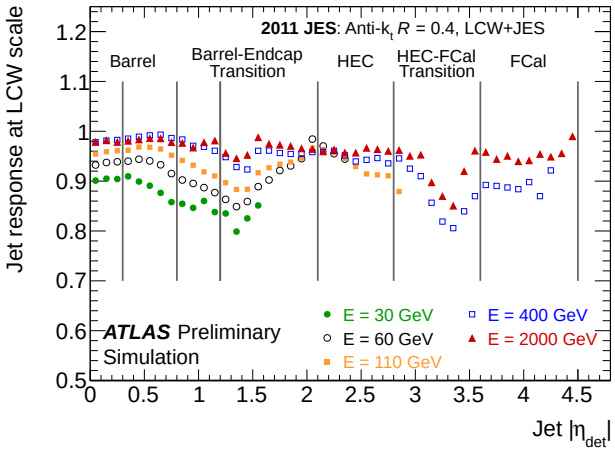

Figure 3.24: *Average energy of jets formed from topoclusters calibrated at the LCW scale with respect to the truth jet energy as a function of the jet $|\eta|$ for various jet energies. The inverse of the response shown in each bin is equal to the average JES correction.*

uncertainties that depend on the event sample used [105].

First of all, the JES uncertainties related to the in-situ JES corrections (labelled *baseline in-situ JES*) are derived from a combination of the γ+jet, Z+jet and multijet techniques. This uncertainty is shown as a function of the jet p_T in the left plot of Figure 3.25 for jets in the central region and it is found to be ~3% for jets with $p_T \sim 17$ GeV, falling to 2% for $p_T \sim 25$ GeV and below 1% for jets with $55 < p_T < 500$ GeV. For very forward low p_T jets, the uncertainty can be close to 6%.

Additional uncertainty contributions due to specific event topologies, such as close-by jets or from selections of event samples with different compositions and response of jets originating from light quarks versus those originating from gluons, and from pile-up uncertainties are also considered and are shown in the right plot of Figure 3.25. An additional p_T dependent uncertainty of less than 2.5% is considered in the case of b-jets [108]. The total uncertainty is calculated by adding all uncertainty sources in quadrature.

3.4.4.4 Jet selection: jet quality and pile-up rejection

Jet quality criteria are applied to identify so-called "bad" [9] jets. These jets are not produced by in-time real energy deposits in the calorimeters, but they are instead caused by various sources

[9] Calorimeter reconstructed jets are classified in ATLAS as "good", "ugly" and "bad". The "ugly" jets correspond to real energy depositions in regions where the energy measurement is not optimal, but these jets can be considered for the analyses. The "bad" jets refer to jets not associated to in-time real energy deposits in the calorimeters caused by various sources ranging from hardware problems in the calorimeter, the LHC beam conditions and the atmospheric cosmic-ray muons induced showers.

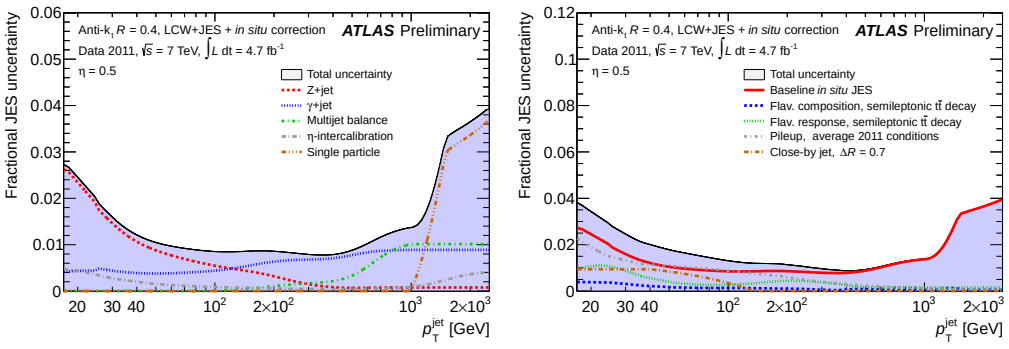

Figure 3.25: *Different contributions to the JES systematic uncertainty as a function of p_T for jets in the central region and calibrated using the LCW+JES. Left: Fractional in-situ calibration. The contributions from each in-situ method are shown separately. Right: Sample-dependent fractional JES uncertainty that applies to top quark pair lepton+jets decays with average 2011 pile-up conditions, and does not include the uncertainty on the JES of b-jets.*

ranging from hardware problems in the calorimeter, LHC beam-gas interactions, and cosmic-ray induced showers. A cut on the "jet vertex fraction" (JVF), which measures the probability that a jet originated from a particular vertex, is applied to further reduce the effect of in-time pile-up [109]. This variable exploits the fraction of tracks coming from the primary vertex that is associated to the jet to estimate the contribution of multiple interactions, providing a discriminant for jets in form of a probability of the jet to not have been generated by pile-up interactions if it has a sufficient fraction of tracks from the primary vertex. The optimal working point for top quark analyses at $\sqrt{s} = 7$ TeV is obtained rejecting jets with $|\mathrm{JVF}| < 0.75$ [2].

3.4.4.5 Jet reconstruction efficiency

The calorimeter jet reconstruction efficiency [110]- [111] is derived relative to jets built from charged tracks reconstructed in the ID, using a tag-and-probe technique. The reconstruction efficiency is defined as the fraction of probe track-jets matched to a calorimeter jet and it has been found to be slightly lower in data than in Monte Carlo. In order to account for the observed difference, a fraction of jets in Monte Carlo was discarded randomly within the inefficiency range.

3.4.4.6 Jet energy resolution

The jet energy resolution (JER) measured with the di-jet balance and the bi-sector techniques [112]- [113] in data and Monte Carlo agrees within uncertainty. For this reason, no systematic smearing is applied to jets in Monte Carlo simulation for central value measurements. The uncertainty on the energy resolution is evaluated by smearing jets according to the systematic uncertainties of the resolution measurements.

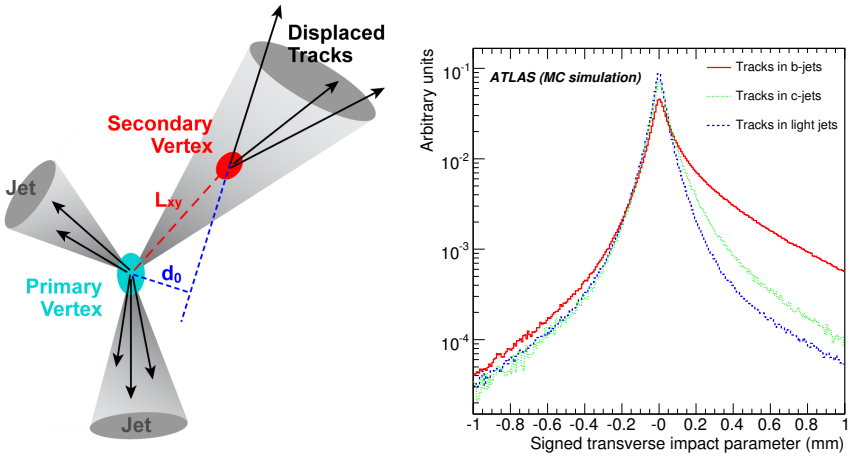

Figure 3.26: *Left: Sketch illustrating the primary vertex (PV), the secondary vertex (SV) and the signed impact parameter (IP) in a b-jet. Right: Distribution of the signed transverse impact parameter d_0 with respect to primary vertex for tracks coming from b-, c- and light-quark jets.*

3.4.5 *b*-tagged jets

The identification of jets originating from *b*-quarks is crucial for most physics processes at the LHC, in particular for the analysis of events containing top quarks[10] in which one of the most important selection criteria is the identification of jets containing *b*-quarks. There are several physical features of the *b*-quark, which allow to distinguish jets originated from *b* quarks (*b*-jets) from *c*- and light-jets.

When a *b*-quark is produced, it hadronises into a *b*-hadron which has a relatively long lifetime of ~1.5 ps. Due to their long lifetime and large boost, many *b*-hadrons travel several millimeters before decaying into several particles. This leads to a measurable flight path length of few millimeters (~5 mm) before their subsequent decay. The precise position measurements (few μm) of the innermost silicon detectors allow to reconstruct the trajectory of the charged particles. Whereas most of the charged particles have trajectories that come close together at one point, called the primary vertex, some of the charged particles from the *b*-hadron decay are significantly displaced from this vertex and have trajectories that come close together at a second point, called the secondary vertex. The decay of the *b*-hadrons at this displaced vertex can be identified by measuring the transverse d_0 and longitudinal z_0 impact parameters, i.e. the distance from the point of closest approach of the track to the interaction vertex. Apart from that, a secondary vertex can also be reconstructed explicitly. As about 10% of *b*-hadron decays produce a muon, the presence of a muon inside a jet is another feature of a *b*-hadron decay. Jets with *c*-hadrons also produce the above signature, although they have a shorter lifetime and lower mass. All these specific properties of the *b*-jets (see sketch Figure 3.26) are exploited by the *b*-tagging algorithms.

[10] As discussed before the top quark decays almost exclusively into a *b*-quark plus a *W* boson.

3.4.5.1 *b*-tagging algorithms

Different *b*-tagging algorithms are used in ATLAS [114,115]. All of them rely on a likelihood ratio to build a measured discriminating variable S_i that can be compared to reference distributions $u(S_i)$ and $b(S_i)$ obtained from Monte Carlo for light- and *b*-jets respectively. The ratio of the probabilities $b(S_i)/u(S_i)$ defines the track or vertex weight, which can be combined into a jet weight w_{jet} as the sum of the logarithms of the N_T tracks within a jet,

$$w_{jet} = \sum_{i=1}^{N_T} log \frac{b(S_i)}{u(S_i)}$$

and allows to separate light- and *b*-jets. The jets that have a weight above a certain cut value are tagged as *b*-jets. This cut value w_{cut} determines the *b*-tagging efficiency ϵ_b, defined as the fraction of true *b*-quarks that are tagged as *b*-jets. It also determines the probability of falsely tagging a jet originating from a *c*-quark or a light parton (*u*-, *d*-, *s*-quark or gluon *g*) as a *b*-jet, referred to as the *c*-tag efficiency ϵ_c and mistag efficiency ϵ_{light} respectively. The inverse of these two are the so-called *c*- and light jet rejection rates, R_c and R_{light}, respectively. Each tagger is characterized by its *b*-tagging efficiency and rejection rates, allowing to define operating points. In general, ϵ_b, R_{light} and R_c are functions of the jet parameters (p_T and η). In the following, the *b*-tagging algorithms used in ATLAS are described.

- `I3PD`: The *IP3D* is an impact parameter tagging algorithm. It relies on the signed impact parameter to discriminate the tracks from a *b*-hadron decay, against tracks stemming from the primary vertex. The sign is positive if the point of closest approach lies upstream with respect to the jet direction and negative in the other case, i.e. it assumes that the decay point of the *b*-hadron lies along its flight path. The distribution of the signed transverse impact parameter d_0 is shown on the right side of Figure 3.26 for tracks coming from *b*-, *c*- and light-quark jets. Tracks from *b*- and *c*-hadron decays tend to have a positive sign, while the sign of prompt tracks from the primary vertex is random. This tagger uses 2-dimensional histograms of the longitudinal versus transverse impact parameter significance (z_0/σ_{z_0} and d_0/σ_{d_0}) to form a likelihood ratio for each track.

- `SV1`: The *SV*1 is a secondary vertex tagger that takes advantage of three vertex properties: the number of track vertices, the ratio of the sum of the energies of the vertex tracks to the sum of the energies of all tracks in the jet, and the invariant mass of all tracks associated to the vertex. The so-called *SV* tagging algorithms rely differently on these properties; in particular the *SV*1 uses a 2-dimensional distribution of the invariant mass of all tracks associated to the vertex and the ratio of the sum of the energies of the tracks in the vertex to the sum of the energies of all tracks in the jet and a 1-dimensional distribution of the number of vertices with two-tracks. These variables are then combined using a likelihood ratio to obtain a tagging discrimination weight.

- `JetFitter`: The *JetFitter* tagger exploits the topology of weak *b*- and *c*-hadron decays inside the jet. A Kalman filter [116] is used to find a common line on which the primary vertex and the *b*- and *c*-hadron decay vertices lie, as well as their position on this line. With this approach, the *b*- and *c*-hadron vertices can be distinguished. The discrimination between *b*-, *c*- and light jets is based on a likelihood using similar variables as in the *SV*1

tagging algorithm: masses, momentum, flight length significances and track multiplicities of the reconstructed vertices.

These taggers can be combined giving rise to more sophisticated algorithms:

- `I3PD+SV1`: Thanks to the likelihood ratio method used for $IP3D$ and $SV1$, these algorithms can be easily combined: the weights of the individual tagging algorithms are simply summed up.

- `JetFitterCombNN`: The *JetFitterCombNN* tagger is the combination of $I3PD$ and *JetFitter* with a neural network. The *JetFitterCombNNc* is identical to *JetFitterCombNN* with the exception that the neural network is trained to reject c-jets rather than light-jets.

- `MV1`: This neural network based algorithm combines the output weights of $IP3D$, $SV1$ and *JetFitterCombNN* to extract a final tagging discrimination weight for each jet.

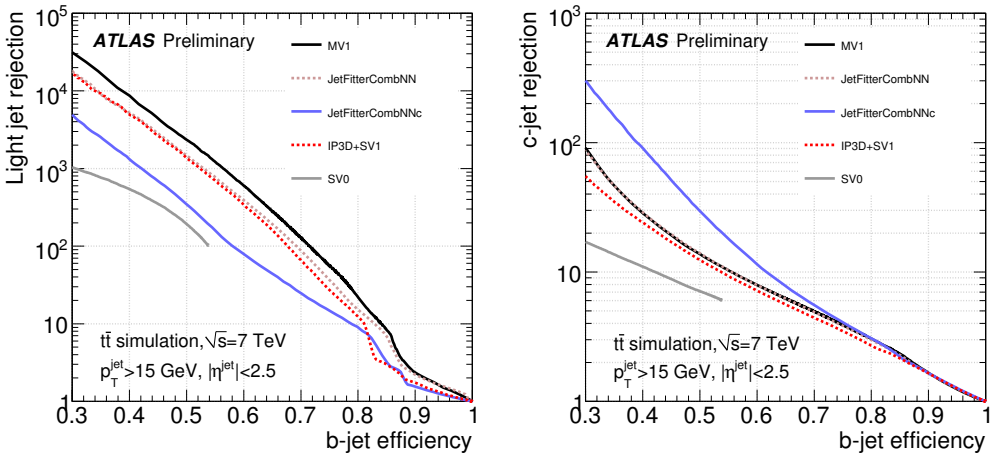

Figure 3.27: *Light-jet rejection (left) and c-jet rejection (right) as a function of the b-tag efficiency for different b-tagging algorithms.*

Figure 3.27 shows a comparison of the light- and c-jet rejection as a function of the b-tag efficiency for different b-tagging algorithms. $MV1$ leads to better performance than *JetFitterCombNN* for light-jet rejection; while for c-jet rejection *JetFitterCombNNc* is the best choice. The dominant backgrounds in t-channel single top quark analyses are W+jets and top quark pair ($t\bar{t}$) production. In particular the largest contribution comes from W+c events, thus it is desirable to reduce this particular background. As already pointed out, the *JetFitterCombNNc* tagger provides an improved rejection capability for background processes with c-jets and therefore is the one used in the analysis presented in this thesis.

3.4.5.2 Calibration of *b*-tagging algorithms

All *b*-tagging algorithms have to be calibrated with data. Several methods have been developed to measure the *b*-tag efficiency in data ϵ_b^{data}, such as the p_T^{rel} and *system*8 [115, 117]. For each *b*-tagging algorithm a set of operating points are defined and these are calibrated. The calibration results are presented as *b*-tagging (and mistag) efficiency scale factors $\kappa_{\epsilon_b}^{\text{data/MC}}$ obtained from data and Monte Carlo comparisons:

$$\kappa_{\epsilon_b}^{\text{data/MC}} = \frac{\epsilon_b^{\text{data}}}{\epsilon_b^{\text{MC}}} \tag{3.12}$$

where ϵ_b^{MC} is the fraction of *b*-flavoured jets which are tagged in simulated events. These scale factors are p_T-dependent and need to be applied to all Monte Carlo samples, as an event weight, to achieve an optimal data/expectation agreement. Figure 3.28 shows the *b*-tag efficiency in data and simulation and the derived scale factor for the *JetFitterCombNNc* tagging algorithm at 55% efficiency, as used in this thesis.

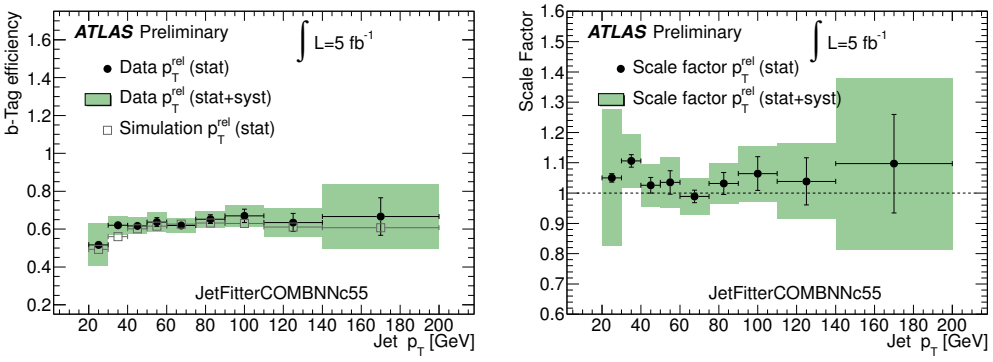

Figure 3.28: *b-tag efficiency in data and simulation (left) and data-to-simulation scale factor (right) for the JetFitterCombNNc tagging algorithm at 55% efficiency.*

3.4.6 Missing transverse momentum

Neutral weakly interacting particles, such as neutrinos, escape from typical collider detectors without producing any direct signal in the detector. The presence of such particles is deduced from the conservation laws of energy and momentum, i.e. it is inferred from the imbalance of total momentum. The vector momentum imbalance in the plane perpendicular to the beam direction is particularly useful in hadron colliders. Its magnitude is called missing transverse momentum and is denoted $E_{\text{T}}^{\text{miss}}$.

In general, $E_{\text{T}}^{\text{miss}}$ is the negative of the vector sum of the transverse momentum of all final state objects: energy deposited in the calorimeters and muon tracks. Therefore, for a precise

$E_{\mathrm{T}}^{\mathrm{miss}}$ determination, it is essential a very good understanding of the detector response and of the reconstructed objects. Apart from the hard scattering process of interest, many other sources, such as the underlying event, multiple interactions and pile-up, lead to energy deposits and/or muon tracks. Classifying the energy deposits into various types and calibrating them accordingly is essential for an optimal $E_{\mathrm{T}}^{\mathrm{miss}}$ measurement. Other important requirement is to minimize the impact of limited detector coverage, finite detector resolution, presence of dead regions and different sources of noise that produce fake $E_{\mathrm{T}}^{\mathrm{miss}}$, $E_T^{miss,fake}$.

The $E_{\mathrm{T}}^{\mathrm{miss}}$ reconstruction [118] includes contributions from transverse energy deposits in the calorimeters, corrections for energy loss in the cryostat and measured muons:

$$E_T^{miss,\mathrm{final}} = E_T^{miss,\mathrm{calo}} + E_T^{miss,\mathrm{cryo}} + E_T^{miss,\mathrm{muon}} \tag{3.13}$$

The first term is the so-called calorimeter term. The second term is the correction to the jet energy due to the loss of energy in the cryostat (dead material). The thickness of the cryostat between the ECAL and HCAL is about half an interaction length where hadronic showers lose energy. This correction turns out to be non-negligible for high-p_T jets. The muon term is calculated from the momentum of the muons, measured in the MS.

The calorimeter term involves two steps: first to select cells from signal (methods for noise suppression are applied and only cells in topoclusters are selected) and then calibrate them taking into account to which high-p_T objects they are associated (i.e. considering differences in the electromagnetic and hadronic showers). These objects include electrons, photons, jets, soft jets and muons. The ordering of these objects given here is the order followed in the association of cells to objects. The remaining energy from cells not associated to any of them are included as a cell-out term, which is calibrated to the EM scale. With all this, the calorimeter term can be written as:

$$E_T^{miss,\mathrm{calo}} = E_T^{miss,\mathrm{e}} + E_T^{miss,\gamma} + E_T^{miss,\mathrm{jets}} + E_T^{miss,\mathrm{soft\ jets}} + E_T^{miss,\mu} + E_T^{miss,\mathrm{cell\text{-}out}} \tag{3.14}$$

where each term is calculated from the negative of the sum of the calibrated cells inside the corresponding objects, as:

$$E_x^{miss,\mathrm{object}} = -\sum_{i=1}^{N_{cell}^{\mathrm{object}}} E_i \, sin\,\theta_i \, cos\,\phi_i \qquad E_x^{miss,\mathrm{object}} = -\sum_{i=1}^{N_{cell}^{\mathrm{object}}} E_i \, sin\,\theta_i \, sin\,\phi_i \tag{3.15}$$

The reconstruction of $E_{\mathrm{T}}^{\mathrm{miss}}$ is very sensitive to particle misidentification, momentum mismeasurements, poorly instrumented regions of the detector, cosmic-ray particles, and beam-halo particles, which may result in artificial $E_{\mathrm{T}}^{\mathrm{miss}}$. Cuts are applied in order to remove the contribution of noise burst events (bursts of large scale coherent noise), sporadic noise and cosmic-ray muons. The main sources of uncertainty related to the $E_{\mathrm{T}}^{\mathrm{miss}}$ come from the scale and resolution of the objects with which the $E_{\mathrm{T}}^{\mathrm{miss}}$ is reconstructed, the cell-out term and the description of additional calorimeter energy from pile-up events. The resolution of $E_{\mathrm{T}}^{\mathrm{miss}}$ is expected to be dependent on the scalar sum of the transverse energy of the cells in the calorimeter $\sum E_T$. This dependence follows a function $\sigma(E_{\mathrm{T}}^{\mathrm{miss}}) = a \cdot \sqrt{\sum E_T}$ where a has fit values variyng between 0.66 and 0.74 $\mathrm{GeV}^{1/2}$ for 2011 data [118], as can be seen in the left plot of Figure 3.29 for $Z \rightarrow ee$ and

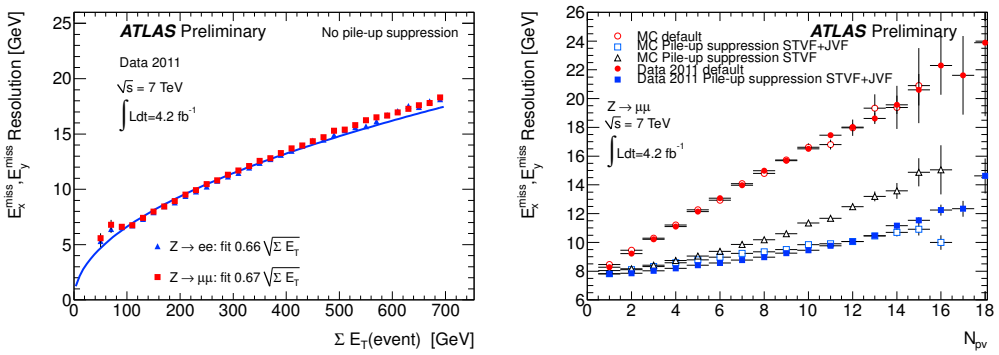

Figure 3.29: *Left:* $E_{\mathrm{T}}^{\mathrm{miss}}$ *resolution as a function of the total transverse energy in the event for 2011 data* $Z \rightarrow ee$ *and* $Z \rightarrow \mu\mu$ *events. Right: Resolution of the reconstructed* $E_{\mathrm{T}}^{\mathrm{miss}}$ *for data and Monte Carlo* $Z \rightarrow \mu\mu$ *events as a funtion of the number of primary vertices in the event before and after pile-up corrections.*

$Z \rightarrow \mu\mu$ events. Compared to the resolution obtained with 2010 dataset [119], where a varied between 0.42 and 0.51 $\mathrm{GeV}^{1/2}$, a significant degradation of the resolution is observed due to the increased pile-up conditions. A large contribution from pile-up is observed in the $E_T^{miss,\text{soft term}}$ term: $E_T^{miss,\text{soft term}} = E_T^{miss,\text{soft jets}} + E_T^{miss,\text{cell-out}}$. Different methods for pile-up suppression have been developed. In the right plot of Figure 3.29, the $E_{\mathrm{T}}^{\mathrm{miss}}$ resolution as a funtion of the number of primary vertices in the event is shown. The default $E_{\mathrm{T}}^{\mathrm{miss}}$ is compared with the $E_{\mathrm{T}}^{\mathrm{miss}}$ after the pile-up corrections for both data and simulated $Z \rightarrow \mu\mu$ events. One can see that after the soft term and JVF corrections, the dependence is reduced. However, in the results presented here, these pile-up corrections were not applied since they were not available when the analysis was carried out.

4

Performance studies with first ATLAS data

This chapter summarizes two studies performed with first ATLAS data: cosmic-rays and first proton-proton collisions. During the commissioning period in 2008 and 2009, millions of cosmic-ray events were recorded and reconstructed in the ATLAS detector allowing commissioning the full operation chain, including data acquisition, reconstruction, analysis software and understanding the detector response to muons. In addition, first alignment and calibration constants to be used with first LHC collisions were derived. In March 2010, the first proton-proton collisions at 7 TeV took place. During that year, around 45 pb^{-1} were recorded by the ATLAS detector allowing for more detailed detector performance studies to be done and to obtain the first cross sections measurements [120].

In the first part of this chapter, a study of the performance of the ATLAS combined muon reconstruction with cosmic-ray data is presented. First, the stand-alone tracking in both ATLAS tracking subsystems, ID (inner) and MS (outer), is compared to check that they are synchronized and to study to which level they are aligned to each other. Latter, the performance of the combined tracking is studied in terms of the number of hits associated to the tracks and the residual distributions. In addition, a measurement of the resolution of the track parameters for combined cosmic-ray tracks crossing the whole ATLAS detector is presented. The method used relies on splitting the full combined tracks into an upper and lower part.

The second part of this chapter presents a performance study related to the reconstruction of jets with the first ATLAS proton-proton collision data (collected in 2010 at $\sqrt{s}$ = 7 TeV). In particular, the *jet shapes* have been measured in data and compared with different Monte Carlo predictions. In addition, the fraction of jet momentum outside the cone of the reconstructed jet, the so-called *out-of-cone energy*, has been estimated in both data and simulations. It is important to compare this quantity with Monte Carlo predictions since it is sensitive to the details of the parton shower, fragmentation and underlying event.

4.1 Commissioning with cosmic-ray data

Cosmic-rays are high-energy particles that originate from the outer space and reach the atmosphere of the Earth from all directions. In collisions with atmospheric atoms, showers of particles are created and from those mostly muons (usually called cosmic-ray muons) and neutrinos reach the surface. Cosmic-ray events provide an excellent test bed to study the initial performance of the detector for various reasons. First of all, there is usually only one muon per event. The low multiplicity of cosmic-ray events allows for less stringent requirements on the pattern recognition and the track reconstruction algorithms compared to the busy environment of proton-proton collisions. Additionally, in contrast to collision events, cosmic-ray muons do not originate from a common vertex. Therefore the non-pointing tracks may help to understand certain (if any) systematic distortions of the detector that cannot be resolved if the alignment algorithms rely on collision data only. Because cosmic-ray muons interact with the detector mainly as minimum ionizing particles, most of them traverse all the subdetectors along their flight path. So, in addition to subdetector-specific cosmic-ray studies, these cosmic-ray data samples provide the first opportunity to study the combined performance of different components of the detector.

After the complete installation of the ATLAS detector in its cavern in July 2008 and in absence of collision data from the LHC, first performance measurements were carried out with muons originating from cosmic-ray events. In Autumn 2008 and in Summer and Autumn of 2009 the ATLAS detector collected a large sample of cosmic-ray events. These extended periods of operation allowed to test the trigger and data acquisition systems as well as other infrastructures such as the data-handling system, to validate the reconstruction software and to optimize tools for hardware and data-quality monitoring. In addition, the shift crews were trained.

In this Section, some studies of the performance of the muon combined reconstruction using cosmic-ray data recorded in 2009 are presented. Prior to a study of combined tracking, it is necessary to establish that the relative alignment of the two tracking systems (ID and MS) is adequate. Therefore, checks were performed by comparing the track parameters for standalone tracks reconstructed in both subsystems, separately in the top and bottom hemispheres of ATLAS. Then the performance of the combined tracking has been investigated by comparing the two reconstructed tracks left by a single cosmic-ray muon passing through the upper and then the lower half of the detector. This involves to separately fit the hits in the two regions to form *split tracks* from the track created by the passage of a single muon. Most of these results were included in the ATLAS combined cosmic-ray paper [1], published in 2010.

4.1.1 Cosmic-ray events in ATLAS

Cosmic-ray events in the ATLAS cavern come mostly from above and arrive mainly via two large access shafts used for the detector installation, as illustrated in Figure 4.1. Certain properties of cosmic-ray events need to be taken into account in the reconstruction of muon tracks. As pointed before, cosmic-ray muons have a typical downward trajectory while tracks from proton-proton collisions arise from (or near) the interaction point. However, in a large sample of cosmic-ray events, some of them pass close to the center of the detector. By applying a set of requirements on the track impact parameters with respect to the nominal interaction point, it is

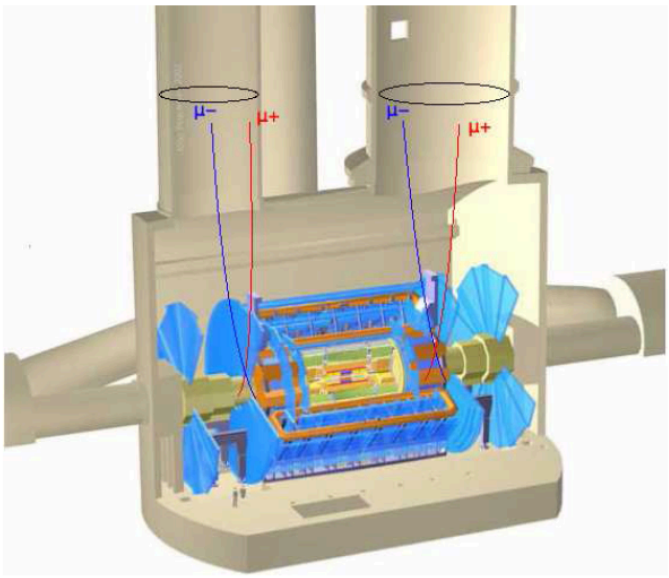

Figure 4.1: *The ATLAS detector in the experimental cavern. Above the cavern are the two access shafts used for the detector installation.*

possible to select a sample of approximately projective muons from those passing through the barrel region of the detector. The rate of such muons is of the order of several Hz. In order to select them, the muons are required to pass through the innermost part of the ID which is the pixel detector. An example of a typical cosmic-ray event is shown in Figure 4.2. The traversing muon leaves hits in all the ATLAS subdetectors and is reconstructed as one track across the whole detector.

The reconstruction of cosmic-ray events is also complicated due to the fact that they occur at random times with respect to the 40 MHz readout clock, which is synchronized to the LHC clock during nominal operation. Therefore, the reconstruction of these events requires first to measure the event time with respect to the readout clock for each subsystem. Another feature is that, in the upper half of the detector, cosmic-ray muons travel from the outside in, rather than from the inside out, as is the case for collisions. These differences have been addressed in the event reconstruction and data analysis. The modifications required for reconstruction of these events in the different detector components are discussed in the subsystem-specific cosmic-ray commissioning papers [121, 122].

The study presented in this section focuses on a data taking period in Autumn 2009 with stable operating conditions of the trigger, with both the MS and ID operational and the associated toroidal and solenoidal fields operating at nominal strength. In order to select a cosmic-ray sample that resembles as much as possible to collision events, a series of quality cuts are applied.

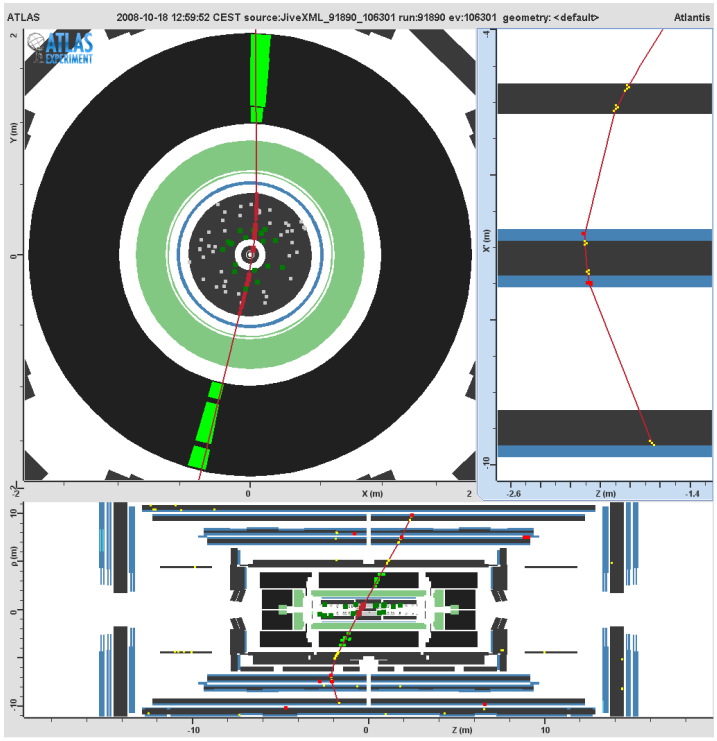

Figure 4.2: *Event display of a cosmic-ray muon crossing the entire ATLAS detector, from the top to the bottom hemisphere, and leaving hits in all tracking subdetectors and significant energy deposits in the calorimeter. The upper left view shows the projection into the $r\phi$ plane. The lower plot shows the projection in the rz plane. The upper right projection is a longitudinal slice through the central part of the MS at the ϕ value of the MDT planes in which the muon hits were recorded.*

Events passing Level 1 trigger with the presence of a track in the ID, i.e. streamed[1] by the High Level Trigger, are selected. Events are required to have been triggered by the RPC chambers, since these also provide measurements along the azimuthal angle (ϕ coordinate), which is not measured by the precision chambers MDTs. Only events with one track reconstructed in the ID, one or two tracks reconstructed in the MS and one combined track that crosses both subdetectors have been considered. Following the procedure used in the ID performance studies [121], a cut on a time measurement, the event phase, has been applied to select cosmic events triggered in a good ID time window. The event phase[2] is a measurement of the time difference between

[1] High Level Trigger output is organized into different *streams* using filter algorithms to select interesting events for particular studies: express stream, physics streams (EGamma, JetTauEtmiss, Muon and MinBias) or special-use streams (cosmic rays, calibration, debug). This is done just after data are taken and a fast reconstruction is performed in the *Tier-0* at CERN. Experts have 48 hours to update the detector conditions such as alignment and calibration constants for full reconstruction.

[2] The limit on this time window is set by the TRT and SCT detectors which read three bunch crossings (while the pixel detector reads eight), that is 75 ns. In order to have a clear pulse shape in the TRT (related to its operation with drift chambers), the window is further reduced. Therefore, only events with an event phase between -15 and 25 ns (excluding

the arrival time of the muon and the readout time. After all these cuts, the number of events is reduced from initially 2.3M to 176k (8%), as can be seen in Table 4.1.

Selection criterion	Cosmic 2009 data Events that pass this cut
Initial events	2292.8k (100%)
1 ID track	1240.3k (54%)
1 or 2 MS tracks	1752.7k (76%)
1 Combined track	360.1k (16%)
-15< Event Phase <25ns (≠0)	665.9k (29%)
RPC trigger	763.6k(33%)
After all cuts	175.6k (8%)

Table 4.1: *Selection cuts applied to cosmic events. Only events with a combined track, triggered by RPC and in a 40 ns time window are selected. The number of events is reduced from initially 2.3M to 176k. The accumulated efficiency is shown for each cut.*

Since cosmic-rays come predominantly from the above, the alignment in the end-cap region is not as good as in the barrel region. Therefore, the analysis is focused only in the barrel region. Track quality cuts are applied to the different collections of split tracks as listed in Table 4.2. For studies of the angular and impact parameter resolution, the track quality cuts are tightened somewhat, with the requirements of at least two pixel hits, $|d_0| < 100$ mm and $|z_0| < 400$ mm. In both cases, only projective muons are considered.

As explained in Chapter 3, the helical track parameter model in ATLAS has five free parameters Λ that are defined at the interaction point called *perigee*. The perigee is the point of closest approach to the beam axis. It is well defined also for cosmic-ray muons as it corresponds to the point of closest approach to the origin (0,0,0) of the global ATLAS coordinate system. The perigee parameters of a track are defined as:

$$\Lambda = (\phi_0, \theta_0, d_0, z_0, q/p) \tag{4.1}$$

which represent the azimuthal and polar angles, the transverse and longitudinal impact parameters and the charge-signed inverse momentum (see Figure 3.12).

4.1.2 Inner Detector and Muon Spectrometer track comparisons

Before attempting to reconstruct a combined track passing through the muon chambers in the top hemisphere, the calorimeters and the inner tracker, and the mirror in the bottom half of the detector, it is essential to check that the different ATLAS subdetectors are synchronized and aligned. Figure 4.3 shows the correlation between the azimuthal ϕ_0 and the polar angle θ_0 measured in the ID and in the MS. The observed good correlation shows that both subdetectors are well synchronized and reconstruct the same cosmic-ray event. It is important to point out

0 ns) are selected.

Selection criterion	ID tracks	MS tracks	Combined tracks
Initial # of tracks	292.2k (100%)	280.6k (100%)	309.9k (100%)
Pixel hits ≥1	47.3k (16%)	-	47.0k (15%)
SCT hits ≥6	223.9k (77%)	-	231.5k (75%)
TRT hits ≥20	228.4k (78%)	-	242.0k (78%)
Hits in 3 MS chambers	-	199.0k (71%)	194.1k (63%)
MDT hits ≥17, in the same ϕ sector	-	250.4k (89%)	242.8k (78%)
RPC hits ≥4	-	242.8k (87%)	235.7(76%)
RPC ϕ hits ≥2, in different layers	-	231.0k (82%)	225.0(73%)
$\|d_0\|$ <400 mm	278.8k (95%)	-	290.4k (94%)
$\|d_0\|$ <1000 mm	-	275.9k (98%)	-
$\|z_0\|$ <500 mm	191.7k (66%)	-	201.2k (65%)
$\|z_0\|$ <2000 mm	-	279.7k (100%)	-
p >5 GeV	219.0k (75%)	232.7k (83%)	239.8k (77%)
χ^2/ν <3	290.8k (100%)	275.0k (98%)	303.3k (98%)
η <1	286.3k (98%)	265.5k (95%)	304.2k (98%)
After all cuts	50.1k (17%)	138.3k (49%)	19.5k (6%)

Table 4.2: *Quality cuts applied to the different collections of split tracks. The efficiency of each individual cut is shown and the accumulated efficiency is given in the last row. The number of tracks in the ID is reduced from initially 292k to 50k (17%) -25k track pairs-. In the case of tracks in the MS, 138k (49%) tracks -69k track pairs- pass the cuts from the initial 281k. Finally, the number of combined tracks is reduced from the initial 310k to 20k (6%) -10k track pairs-.*

that no relative alignment between the two subdetectors has been applied at this stage.

In addition, one can look at the difference between those two measurements in each of the subsystems, as shown in Figures 4.4 and 4.5 for the angular and impact parameters for tracks in the top and the bottom hemisphere separately. The distributions are fitted to a Gaussian function and their mean and width, shown in Table 4.3, give an estimation of the relative mechanical alignment between the innermost and outermost detectors. The somewhat narrower distributions obtained for tracks in the upper half of the detector are attributed to the higher average momentum of the cosmic-ray muons in this part of the detector. Small biases are observed for the ϕ_0 and d_0 parameters. These are consistent with a slight translational misalignment between the MS and ID that is of order 1 mm. However, the combined tracking study presented below was performed without any relative ID-MS alignment corrections.

4.1.3 Combined tracking performance

Cosmic-ray muons cross the detector from top to bottom, therefore a combined track passing through both hemispheres can be reconstructed. The combined tracking is performed with the *Globalχ^2Fitter* algorithm [123], which is based on the scattering angle formulation of the track fit. In what follows, the performance of the combined tracking for muons using information of all ATLAS subdetectors is studied. First, the distributions of the track parameters for the reconstructed combined tracks are presented. Later the number of hits associated to the tracks as well

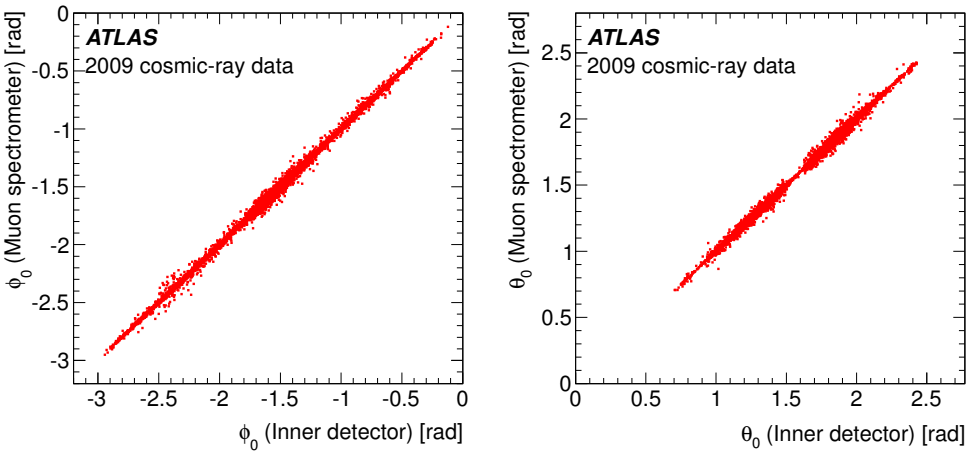

Figure 4.3: *Correlation between ϕ_0 and θ_0 parameters measured in the inner detector and the muon spectrometer.*

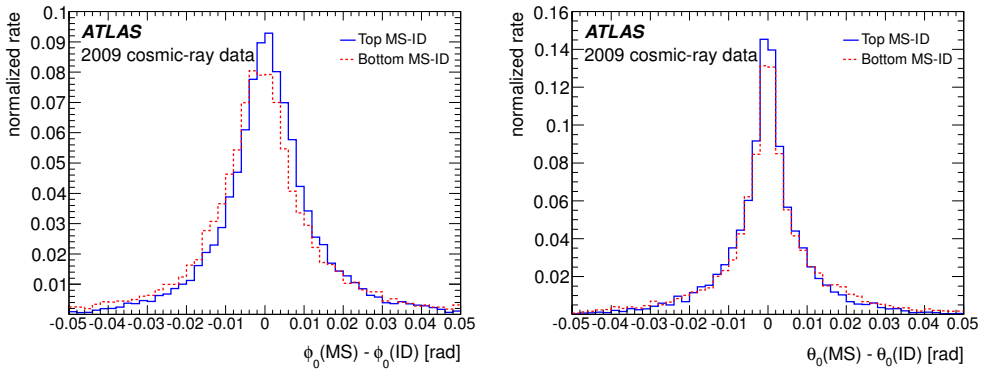

Figure 4.4: *Difference between angular parameters (at perigee) measured in the inner detector and the muon spectrometer for tracks in top (solid line) and bottom (dashed line) hemisphere.*

as the track residuals for each individual subdetector are described. Finally, the track parameter resolutions are measured with the so-called *split method*.

Track parameter distributions

Figure 4.6 shows, separately for positive and negative charged muons, the reconstructed parameters of combined tracks crossing the whole detector. The shapes of the distributions reflect the fact that particles reach the ATLAS detector more easily when traversing the access shafts than the rock. The distribution of the azimuthal angle ϕ_0 is always negative as both upper and

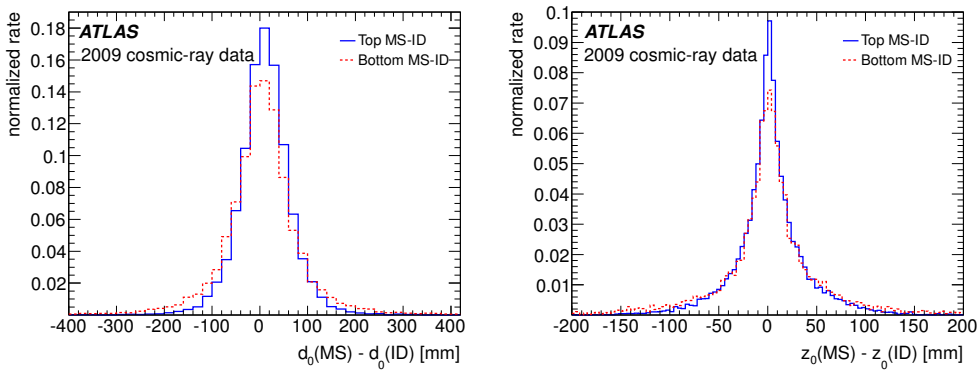

Figure 4.5: *Difference between impact parameters (at perigee) measured in the inner detector and the muon spectrometer for tracks in top (solid line) and bottom (dashed line) hemisphere.*

Track parameter	Top hemisphere	Bottom hemisphere
$\Delta\phi_0$	μ= 0.5 ± 0.1 mrad σ= 7.3 ± 0.1 mrad	μ= -1.0 ± 0.1 mrad σ= 8.2 ± 0.2 mrad
$\Delta\theta_0$	μ= -0.09 ± 0.06 mrad σ= 4.36 ± 0.07 mrad	μ= -0.09 ± 0.08 mrad σ= 4.51 ± 0.10 mrad
Δd_0	μ= 9.3 ± 0.4 mm σ= 39.5 ± 1.0 mm	μ= 3.6 ± 0.7 mm σ= 44.5 ± 1.1 mm
Δz_0	μ= 0.9 ± 0.2 mm σ= 11.3 ± 0.3 mm	μ= 1.3 ± 0.3 mm σ= 13.0 ± 0.5 mm

Table 4.3: *Difference between the track parameters measured in the inner detector and the muon spectrometer for top and bottom hemispheres. Mean and width are obtained by fitting a Gaussian function to the distributions.*

lower tracks were reconstructed from top to bottom. The highest peak at ϕ_0 = - 1.7 originates from the two supply shafts whereas the two satellite peaks represent a third shaft which is an elevator (see Figure 4.1). The distribution of the polar angle θ_0 shows that the tracks are restricted to the barrel region ($0.7 < \theta_0 < 2.4$). The two peaks correspond to the two supply shafts directly above the detector. The peak in the right side (θ_0 = 1.8) is higher due to the different size of the supply shafts. As expected, the transverse d_0 and longitudinal z_0 impact parameters have flat distributions between the boundaries imposed by the track requirements while they peak at zero for collision events when computed with respect to the primary vertex. The momentum spectrum has its maximum around 10 GeV and decreases rapidly towards higher momenta. Only few muons are reconstructed with a momentum above 100 GeV.

The observed charge asymmetry of positive and negative muons is caused by the muon charge ratio μ^+/μ^- of approximately 1.3 [17] for cosmic-ray muons and under the influence of the magnet system. Cosmic-ray muons are originated when cosmic-rays interact in the atmosphere

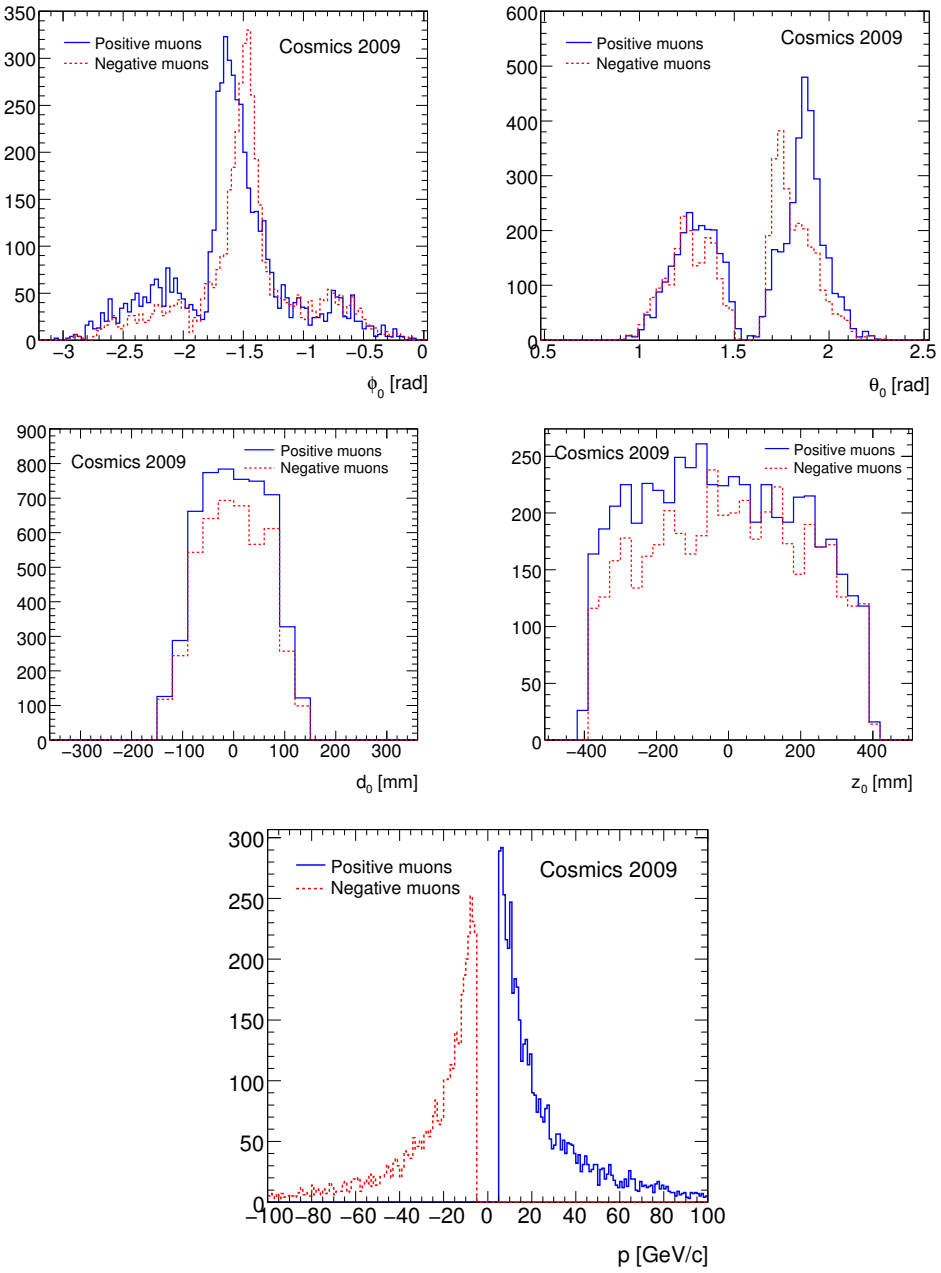

Figure 4.6: *Reconstructed track parameters at perigee: azimuthal ϕ_0 and polar θ_0 angles (top), transverse d_0 and longitudinal z_0 impact parameters (middle) and momentum (bottom) of combined tracks for positive (solid line) and negative (dashed line) muons.*

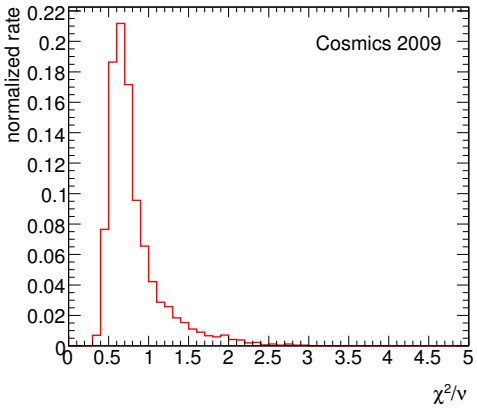

Figure 4.7: *Distribution of the reduced χ^2 for the reconstructed combined tracks.*

producing mesons (pions and kaons) which decay into muons. The collisions of cosmic-rays (mainly protons and nuclei) with air favour the production of positive mesons, hence more positive muons are expected as can been seen in the distributions. Due to the magnetic field, unlike-sign charged particles bend in opposite directions, as shown in Figure 4.1. Since the toroidal field is right-handed with respect to the positive z axis, positive muons entering the large shaft (z>0) bend towards the center of the detector while the negative ones are bend out, and the opposite for muons entering the small shaft (z<0). Therefore, the muon charge asymmetry is enhanced in the region of the large shaft while it is reduced in the small one, as can be seen in the distribution of polar angle distribution of Figure 4.6. The solenoid field is right-handed with respect to the x axis. Therefore, positive muons are bent in region x>0 while negative muons are bent out, the inverse for muons in negative x axis. These effect can be seen in the azimuthal angle distribution of Figure 4.6. Since most muons come from the large shaft, the net effect is an enhancement of the muon charge asymmetry.

Figure 4.7 shows the reduced[3] χ^2 of the fitted combined tracks for real data. The distribution shows the good quality of the combined tracks.

Number of hits associated to tracks

A unique feature of the cosmic-ray muons is that they traverse the entire detector from top to bottom. Thus it is possible to split such a track into parts traversing only the upper or lower hemisphere of the detector and performing the track fit again separately for the two arms. In this way, two distinct tracks (called *split tracks*) that resemble tracks from collision events are obtained. Given the quality cuts applied to the split tracks used in this analysis, the selected tracks cross all the layers in the tracking subdetectors in the barrel region: 3 pixel layers, 8 SCT wafers, 36 straw layers and the three muon chambers (20 and 6 layers in the MDT and RPC detectors respectively). Figure 4.8 shows the number of hits associated to the combined split

[3]The reduced χ^2 is simply the χ^2 divided by the number of degrees of freedom in the fit.

tracks for each detector technology, which is in accordance with the number of tracking layers crossed.

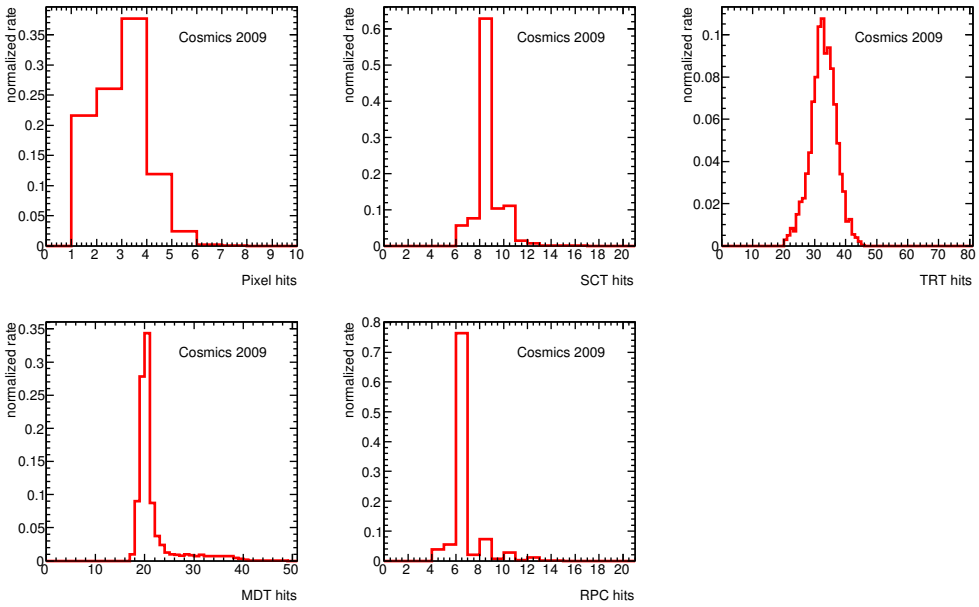

Figure 4.8: *Number of hits associated to combined split tracks.*

Residual distributions

The track parameter resolutions strongly depend on the accuracy with which the position and orientation of the tracking sensors are known. As discussed in Chapter 3, the initial accuracy for individual modules is of $O(10\,\mu\text{m})$. The remaining misalignments are recovered with track-based alignment algorithms which basically consists in a χ^2 minimisation of the hit residuals, i.e. the distance from the predicted track position on a given detector module to the hit position recorded in the module. The χ^2 minimisation is performed with respect to the alignment parameters using a global χ^2 algorithm [124]. Figure 4.9 shows the residuals distributions of the combined tracks obtained for each tracking technology. In order to compare with stand-alone studies [121,122], the distributions of the residuals in the ID have been fitted to a Gaussian function and the ones for the MS are fitted to a double Gaussian with common mean (normalized such that the 75% of the distribution is in the narrow one). The results obtained are shown in Table 4.4.

Angular and impact parameter bias and resolutions

The resolutions of the track parameters are obtained from the comparison of the parameters of each split track: λ_{up} and λ_{low}. Since they are derived from the same cosmic-ray muon track,

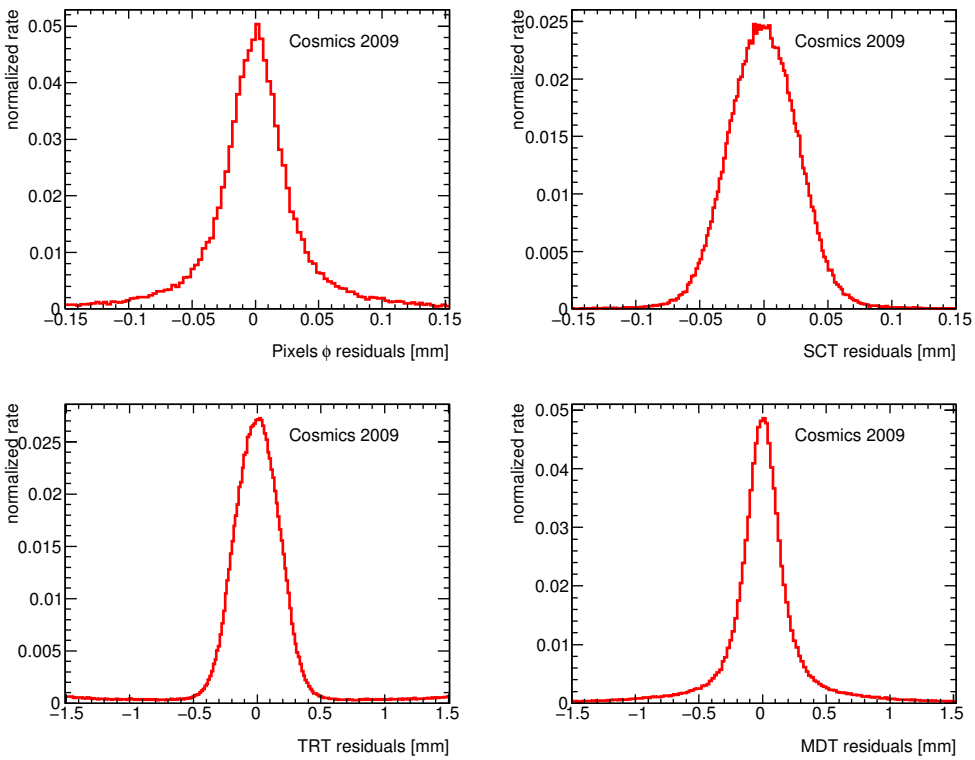

Figure 4.9: *Residual distributions in the different subdetectors for combined tracks. In order to extract the mean and sigma of the distributions, a Gaussian fit is performed to the ID distributions and a double Gaussian with common mean value to the MS.*

Coordinates	**Residuals**
Pixels ϕ	μ= 0.1±0.2 μm σ= 22.5±0.2 μm
SCT	μ= -0.5±0.1 μm σ= 27.9±0.1 μm
TRT	μ= 0.1±0.4 μm σ= 174.2±0.4 μm
MDT	μ= 0.5±0.4 μm σ_{narrow}= 114.2±0.5 μm

Table 4.4: *Mean and sigma of the residual distributions for combined split tracks obtained for each tracking technology.*

their difference $\Delta\lambda = \lambda_{up} - \lambda_{low}$ for each parameter λ has an expectation value of 0 and a variance equals to two times the square of the parameter resolution, $var(\Delta\lambda) = 2\sigma^2(\lambda)$. Therefore, the resolutions are given as the root mean square of the $\Delta\lambda$ distributions divided by $\sqrt{2}$ (since both measurements are independent). The boundaries for each distribution are estimated such that 99.7% (i.e. an equivalent of 3σ of a Gaussian distribution) of all entries are included in the root mean square calculation. The obtained biases and resolutions for the angular and impact parameters for tracks with momentum greater than 30 GeV are shown in Table 4.5. The bias and resolutions for each parameter λ have been studied in bins of p_T and η, such that each bin has at least 50 tracks to guarantee statistically meaningful results. The means are roughly independent of p_T and η, with the exception of the z_0 distribution in which a small bias (within 60 μm) that varies with η is observed and might be due to misalignment between the ID and the MS (note that no alignment corrections between both subdetectors are applied). Figures 4.10 and 4.11 show the resolution for each parameter λ as a function of p_T and η. In general the resolution improves with the momentum and is independent of η, except for θ_0 parameter in which the resolution is slightly worse in the central pseudo-rapidity region.

Parameter	Bias	Resolution
ϕ_0 (mrad)	-0.053±0.005	0.164±0.004
θ_0 (mrad)	0.27±0.03	0.80±0.02
d_0 (μm)	-0.9±0.7	26.8±0.8
z_0 (μm)	2.0±3.7	116.6±2.9

Table 4.5: *Overview of the track parameter bias and resolution for combined tracks using the track-split method for tracks with p_T >30 GeV.*

Relative momentum resolution

The relative momentum resolution has also been estimated by comparing the two independent momentum measurements in the top and the bottom hemispheres. For these studies, slightly looser cuts (see Table 4.2) are employed in order to increase the statistics, particularly in the high-p_T region. For tracks having momenta above 50 GeV the requirement of a pixel hit is removed and the cuts on $|d_0|$ and $|z_0|$ are loosened to 1000 mm. For each reconstructed track pair, the value of transverse momentum is evaluated at the perigee. The difference between the values obtained from the upper and lower parts of the detector, divided by their average

$$\frac{\Delta p_T}{p_T} = \frac{p_{T,up} - p_{T,down}}{\frac{p_{T,up}+p_{T,down}}{2}}$$

is measured and plotted in eleven p_T bins[4] (being the center of the bin the mean of the p_T distribution in that bin). The distribution of $\Delta p_T/p_T$ is fitted in each bin by a double Gaussian function with a common mean value and such that 70% of the events are in the narrow Gaussian. The width of the narrow Gaussian divided by $\sqrt{2}$ is taken as an estimate of the relative transverse momentum resolution for each p_T bin. Figure 4.12 shows the measured momentum

[4]The p_T bins defined here are different to those used to study the resolution of the other track parameters.

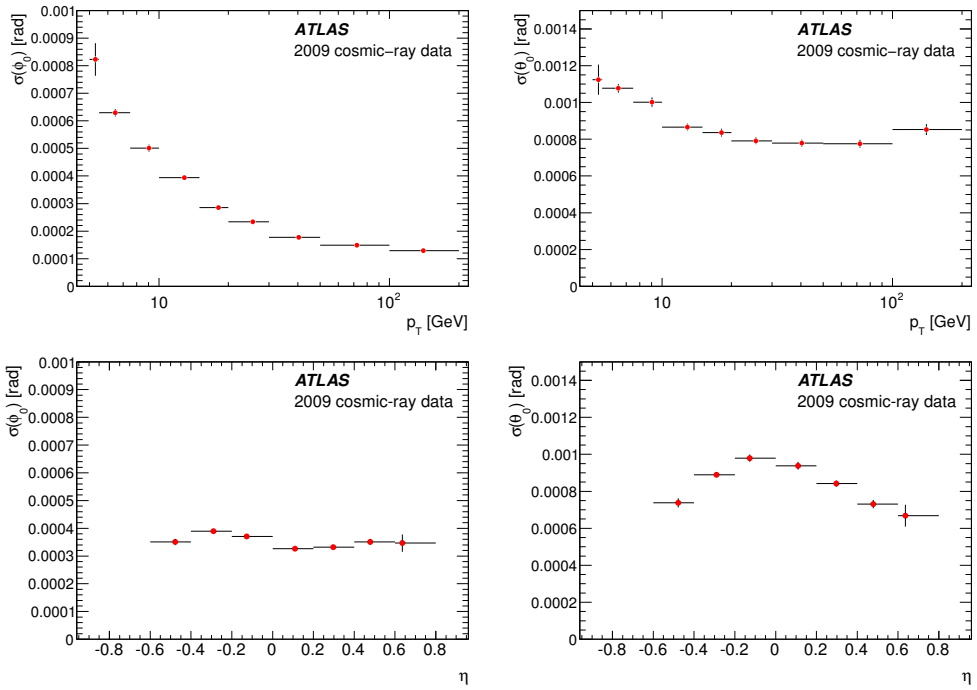

Figure 4.10: *Resolution of ϕ_0 (left) and θ_0 (right) parameters as a function of muon transverse momentum (top) and η (bottom).*

resolution for ID, MS and combined tracks. One can notice that combining the information from the two tracking systems improves the relative momentum resolution. One can also see that the resolution is degraded at higher momentum. This is expected since particles with higher p_T bend less in the magnetic field and make a determination of the curvature and hence of the transverse momentum more difficult. In the low transverse momentum region, the combined resolution reflects directly the dominant performance of the ID, which is itself limited by multiple scattering.

At low transverse momentum, the MS stand-alone resolution is dominated by fluctuations in the energy loss in the calorimeters, whereas at higher momentum, it is dominated by the intrinsic accuracy. The momentum resolution in the MS as a function of p_T can be fitted with the sum in quadrature of three terms, the energy loss term p_0, the multiple scattering contribution p_1 and the intrinsic resolution p_2:

$$\frac{\sigma_{p_T}(\mathrm{MS})}{p_T} = \frac{p_0}{p_T} \oplus p_1 \oplus p_2 p_T \tag{4.2}$$

In the case of the ID, the energy loss in its material is negligible and the resolution is domi-

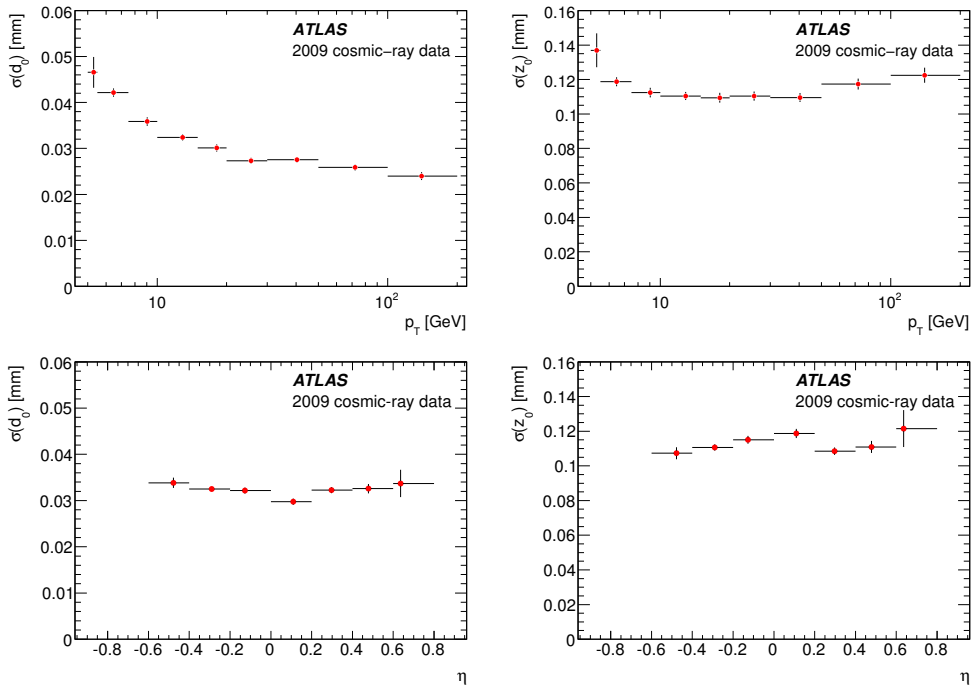

Figure 4.11: *Resolution of d_0 (left) and z_0 (right) parameters as a function of muon transverse momentum (top) and η (bottom).*

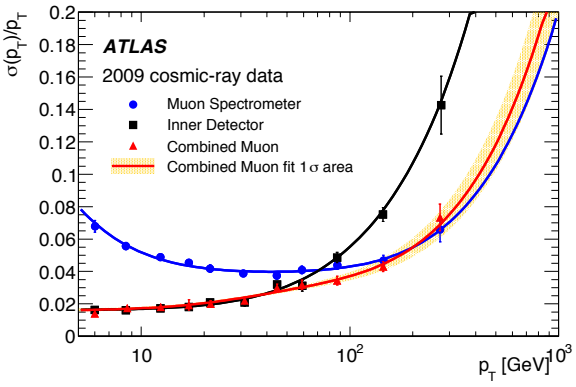

Figure 4.12: *Relative momentum resolution as a function of the muon transverse momentum for muon spectrometer (dots), inner detector (squares) and combined tracks (triangles).*

nated at low momentum by the multiple scattering. Therefore, the appropriate fit function is:

$$\frac{\sigma_{p_T}(\mathrm{ID})}{p_T} = p_1 \oplus p_2 p_T \tag{4.3}$$

The momentum resolution of the combined tracks can be fitted to a function that takes into account the resolution in the ID and in the MS:

$$\frac{1}{\frac{\sigma_{p_T}(\text{Muon Combined})}{p_T}} = \frac{1}{\frac{\sigma_{p_T}(\mathrm{MS})}{p_T}} \oplus \frac{1}{\frac{\sigma_{p_T}(\mathrm{ID})}{p_T}} \tag{4.4}$$

Assuming that the energy loss contribution is negligible, since at low momentum the resolution of combined tracks is dominated by the ID, the fit function for combined momentum resolution can be written as:

$$\frac{\sigma_{p_T}(\text{Muon Combined})}{p_T} = p_1 \oplus p_2 p_T \oplus \frac{p_0 p_T}{\sqrt{1 + (p_3 p_T)^2}} \tag{4.5}$$

where p_0 is related to uncertainties on the energy loss corrections, p_1 to the multiple scattering term, p_2 to the intrinsic resolution at very high momentum and p_3 describes the intermediate region where ID and MS resolutions are comparable.

Table 4.6 compares the fitted sizes of the multiple scattering and intrinsic resolution terms for the ID, MS and combined tracks. For combined tracks the multiple scattering term is determined mainly by the ID contribution while the intrinsic high-energy resolution comes mainly from the MS measurement. Extrapolation of the fit result yields an ID momentum resolution of about 1.6% at low momenta and of about 50% at 1 TeV. For MS standalone tracks, a resolution of 20% is obtained for muons of 1 TeV. As expected the ID and MS systems dominate the resolution at low and high p_T, respectively. However, at intermediate momentum (50-150 GeV) both systems are required to achieve the best resolution.

Momentum resolution	Multiple scattering (p_1)	Intrinsic (p_2)
Inner Detector	(1.6±0.1)%	(53±2)×10^{-5} GeV^{-1}
Muon Spectrometer	(3.8±0.1)%	(20±3)×10^{-5} GeV^{-1}
Combined Muon	(1.6±0.1)%	(23±3)×10^{-5} GeV^{-1}

Table 4.6: *Fit results of the different terms that contribute to the momentum resolution.*

4.2 Jet performance studies with first ATLAS collision data

In December 2009, the first proton-proton collisions at the LHC took place at a center of mass energy of 900 GeV. During that year, the ATLAS detector recorded almost 1 million collision candidates at $\sqrt{s}$ = 900 GeV (~500k during stable beams) and about 34k candidates at $\sqrt{s}$ = 2.36 TeV. These corresponds to an integrated luminosity of 20 μb^{-1} (12 μb^{-1} with stable beams) and 1 μb^{-1}, respectively, with an estimated systematic uncertainty of 30% in these numbers. In March 2010, proton-proton collisions at a center of mass energy of 7 TeV took place at the LHC and the ATLAS detector recorded around 45 pb^{-1} during that year. These data allowed to carry out several performance studies and to obtain the first cross section measurements.

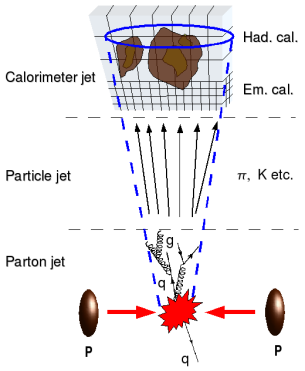

Figure 4.13: *A jet is a narrow cone of hadrons and other particles produced by the hadronisation of a quark or gluon. It is reconstructed in the calorimeter system. The goal of the jet reconstruction is to obtain the initial parton energy out of the measured jet energy. In this procedure one has to take into account both the detector effects (non-compensating calorimeter, dead regions, passive material, calorimeter noise, etc.) and the physics effects (final state radiation, multiple interactions, jet algorithm features, etc.).*

Among the different studies carried out with 2010 collision data, this section presents a performance study related to the jet energy flow, which is sensitive to both QCD perturbative and non-perturbative effects. A proper jet reconstruction and a precise determination of their energy at hadron colliders is essential in many physics analysis since quarks and gluons produced in the hard scattering are seen in the detector as jets (see Figure 4.13). Monte Carlo simulations are used to understand the transition from hard-scatter partons to jets. Thus, it is crucial to understand at which level the Monte Carlo predictions reproduce the data and to assign the appropriate systematic uncertainty. The study of the internal structure of a jet (the so-called "jet shapes") provides information about the details of the parton-to-jet process in proton-proton collisions. Partons evolve into hadronic jets in a two-step process (see Figure 4.14): the parton showering which can be described by perturbative QCD and the hadronisation process in which non-perturbative effects become important. The latter is not well known because of its non-perturbative nature and thus it is modeled using an empirical approach. There are two successful parametrisation models, one of them implemented in PYTHIA Monte Carlo generator and the other one in HERWIG.

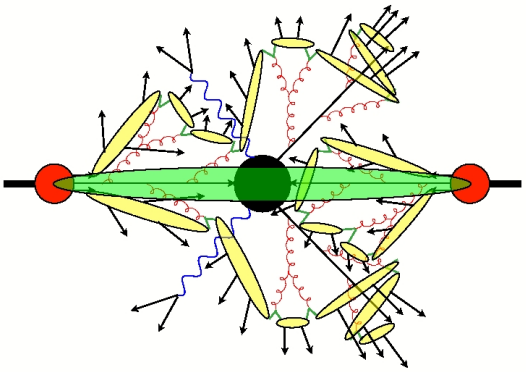

Figure 4.14: *Schematic depicting the stages in the simulation of a hadron-hadron collision with a parton shower Monte Carlo event generator. The partons (quarks and gluons) involved, and new particles with colour, radiate virtual gluons, which can themselves emit further gluons or produce quark-antiquark pairs, leading to the formation of parton showers (brown). During parton showering the interaction scale falls and the strong interaction coupling rises, eventually triggering the process of hadronisation (yellow), in which the partons are bound into colour-less hadrons. The other constituent partons of the incoming hadrons undergo multiple interactions which produce the underlying event (green).*

Reconstructed jets are only providing energy inside the jet cone radius; however, this energy differs of the parton energy due to several effects. One potentially important contribution arises from a fraction of the parton energy that falls outside the cone of reconstructed jet ($R_C = 0.4$) -usually called the "out-of-cone" (OOC) energy- and is lost due to FSR at large angles with respect to the parent parton or due to particles exiting the cone either in the fragmentation process or due to low p_T particles bending in the magnetic field. This was one of the largest uncertainties in the CDF experiment[5] [125] for jets with $p_T < 50$ GeV, i.e. relevant for top quark physics. On the other hand the particle jet can also have contributions not related to the actual mother parton of the hard interaction of interest, such as particles from ISR, or particles from spectator partons with colour connection to the other partons of the proton ("beam-beam-remnant"). These two contributions are the so-called "underlying event" (UE) -see Section 3.2.5-. FSR and hadronisation effects are correlated with the energy and direction of the primary parton, and are expected to decrease with increasing distance from the jet core. On the contrary, the underlying event is uncorrelated with the direction of the outgoing parton and thus independent of the distance from the jet axis and the energy. In this section, the jet shapes are measured using dijet events, and from them the out-of-cone energy and the underlying event are extracted. The results are compared to various Monte Carlo predictions. These measurements are sensitive to the details of the parton shower, fragmentation and underlying event models in the Monte Carlo generators. Therefore, a difference in the data and Monte Carlo jet shapes, in particular the amount of out-of-cone energy, would lead to biases in some physics measurements. For instance, whether

[5] In CDF experiment the jet energy was corrected up to parton level.

more or less energy is detected inside the radius could affect the acceptance of the top quark pairs production cross section or the top quark mass measurements. As already mentioned, the jet algorithm used is the anti-k_t with a distance parameter $R_C = 0.4$. No attempts to correct for acceptance and detector effects were made in this analysis with first collision data.

4.2.1 Data and Monte Carlo samples

Dijet events from 2010 proton-proton collision data collected by ATLAS at a center of mass energy $\sqrt{s} = 7$ TeV are used in this study. Events are selected online using Level 1 triggers, either by the system of minimum-bias trigger scintillators (MBTS)[6] or by the calorimeter trigger. The results are compared with simulated samples of inclusive jet events [126]. Two different Monte Carlo generators are used: Pythia 6.4.21 [127] with the ATLAS-MC09 tune [128] and Herwig 6.5 [129]. Both Monte Carlo samples are produced using LO QCD matrix elements for $2 \rightarrow 2$ processes but with different models for the parton shower, hadronisation and underlying event. The underlying event in the Herwig samples is simulated using Jimmy 3.41 [130].

4.2.2 Event selection and jet sample definition

Events are selected online using different Level 1 trigger configurations in such a way that, in each kinematic range, the trigger selection is fully efficient and does not introduce any significant bias in the measurements. The unprescaled trigger thresholds were increased with time to keep pace with the LHC instantaneous luminosity evolution. Table 4.7 shows the trigger configurations employed in each p_T region. For jets with p_T below 60 GeV, only events in which the MBTS recorded one or more counters above threshold on at least one side are retained. For larger p_T, the events are selected using either MBTS or Level 1 calorimeter based triggers with a minimum transverse energy threshold at the EM scale that varies between 5 GeV (L1_J5) and 55 GeV (L1_J55), depending on when the data were collected and the p_T range considered.

Events are required to have only one reconstructed primary vertex with five tracks or more in order to suppress pile-up contributions from multiple proton-proton interactions. Additional cuts based on the quality of the reconstructed jets are also applied. Events are required to have at least two jets with $p_T > 20$ GeV (at the EM+JES scale), $|\eta| < 2.5$ and the difference in azimuthal angle between the two most energetic jets must satisfy $\Delta\phi(j_1, j_2) > 2.8$ rad. Events are rejected if there is a third jet with a $p_T(j_3) > 0.1 p_T(j_1)$ or if they have at least one "bad" jet with $p_T > 20$ GeV. The event and jet selection used are described in Table 4.8.

4.2.3 Differential and integrated jet shapes

The energy flow within and outside the leading jet is studied in terms of the differential and integrated jet shapes (see Figure 4.15), reconstructed using the energy of topoclusters - see Section 3.4.4- at the EM scale. The differential jet shape $\rho(r)$ as a function of the distance r

[6]The MBTS detector [8] is one of the forward detector systems in ATLAS. It consists of 32 scintillator counters of thickness 2 cm organized in two disks. The disks are installed on the inner face of the end-cap calorimeter cryostats at z=±356 cm on either side of the interaction point and such that the disk surface is perpendicular to the beam direction. This leads to a coverage of 2.09< $|\eta|$ <3.84.

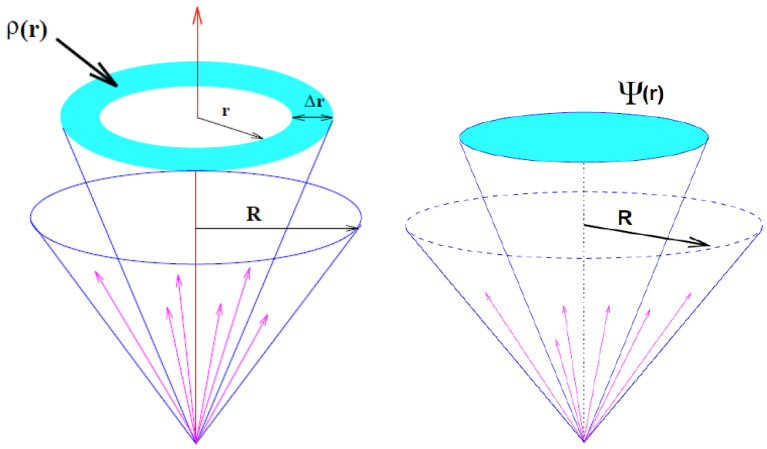

Figure 4.15: *Definition of the differential (left) and integrated (right) jet shape.*

($r = \sqrt{\Delta y^2 + \Delta\phi^2}$) to the jet axis is defined as the summed p_T of the clusters inside an annulus of inner radius $r - \Delta r/2$ and outer radius $r + \Delta r/2$ around the jet axis with respect to the jet p_T:

$$\rho(r) = \frac{1}{\Delta r}\frac{1}{N^{jet}}\sum_{jets}\frac{p_T(r-\Delta r/2, r+\Delta r/2)}{p_T(0,R)}, \Delta r/2 \leq r \leq R - \Delta r/2 \tag{4.6}$$

where N^{jet} is the number of jets and $p_T(r_1, r_2)$ denotes the summed p_T of the clusters in the annulus between radius r_1 and r_2. Alternatively, the integrated jet shape $\Psi(r)$ is defined as the summed p_T of the clusters that are inside a cone of radius r concentric with the jet cone, with respect to the jet p_T:

Data period	Stream	p_T threshold (GeV)	Trigger
A and B	MinBias	20	L1_MBTS_1
B	L1Calo	60	L1_J5
C	L1Calo	60	L1_J5
D	L1Calo	80	L1_J10
D	L1Calo	110	L1_J15
E	JetEtMiss	110	L1_J15
E	JetEtMiss	160	L1_J30
F	JetEtMiss	160	L1_J30
F	JetEtMiss	210	L1_J55

Table 4.7: *Table of data periods, streams and trigger paths used for the listed jet p_T thresholds. MBTS denotes the use of the minimum-bias trigger scintillators, while L1_J5, L1_J10, L1_J15, L1_J30 and L1_J55 correspond to Level 1 calorimeter triggers with 5, 10, 15, 30 and 55 GeV thresholds, respectively.*

Event selection
1 primary vertex with at least 5 tracks
remove events with bad jets
≥ 2 jets ($p_T > 20$ GeV)
$\Delta\phi(j_1, j_2) > 2.8$ rad
$p_T(j_3) < 0.1 p_T(j_1)$
Trigger requirement
Jet selection
anti-k_t R=0.4 jets
$p_T > 20$ GeV
$\|\eta\| < 2.5$

Table 4.8: *Event and jet selection.*

$$\Psi(r) = \frac{1}{N^{jet}} \sum_{jets} \frac{p_T(0,r)}{p_T(0,R)}, 0 \leq r \leq R \tag{4.7}$$

where, by definition, $\Psi(r = R_C) = 1$. Figures 4.16-4.19 show the jet shapes measured in different regions of jet p_T using the minimum bias, L1Calo and JetEtMiss stream data collected by the ATLAS experiment in 2010 for R_C=0.4 and $\Delta r = 0.1$. These are compared to Monte Carlo simulations and the values are listed in Appendix A. In the region $r < R_C = 0.4$ (inside the cone size), the jet shapes predicted by Herwig and Pythia provide a reasonable description of the data. Only statistical uncertainties are quoted.

4.2.4 Out-of-cone energy and underlying event correction

The left plot of Figure 4.20 shows a schematic representation of the scalar p_T distribution around the jet axis. R_C is the distance parameter of the jet algorithm used -in this case R_C=0.4- and R_0 is a reasonably large radius which includes the whole hadronic shower and where the differential jet shapes keep constant. One can see that the out-of-cone region, $R_C < \Delta R < R_0$, has contributions from both the hadronic shower originating from the initial parton and from the underlying event. From Figures 4.16-4.17, it seems reasonable to define the out-of-cone region from R_C=0.4 to R_0=0.8. The so called out-of-cone transverse momentum fraction is defined as the summed p_T of the topoclusters in that region with respect to the jet p_T and is shown in Figure 4.21 for data and Monte Carlo samples. The largest relative difference between data and predictions in this quantity is found to be ~2.9% for jets of 20-25 GeV, ~1.6% for jets of 25-40 GeV and less than 1% for jets with p_T higher than 40 GeV, as shown in Figure 4.22. Herwig interfaced with Jimmy gives a better description of the out-of-cone transverse energy fraction than Pythia.

In order to disentangle effects due to differences in the modelling of the underlying event, the contribution due to such effect is measured for both and the two Monte Carlo samples separately, and subtracted to the corresponding out-of-cone transverse momentum. The underlying event is determined from the summed p_T of the topoclusters in the transverse region defined as $60^o <$

$|\Delta\phi| < 120^o$ with respect to the leading jet axis (see right plot of Figure 4.20) normalized to $\eta - \phi$ unit and it is shown in Figure 4.23. In this case, PYTHIA and HERWIG are also comparable in terms of reproducing data. More underlying event is seen in data than Monte Carlo, which is consistent with previous studies in ATLAS [131]. After subtracting this contribution to the out-of-cone transverse momentum, the largest relative difference in data and Monte Carlo of the out-of-cone transverse momentum with respect to the jet p_T is found to be $\sim$2% for jets of 20-30 GeV and $\sim$1% for jets of higher p_T, as shown in Figure 4.24. The level of agreement is good compared to the uncertainties associated to the showering, hadronisation and radiation effects in top quark analyses at the time this study was done. The larger datasets recorded afterwards have allowed to perform more precise measurements with jets from different topologies and even to distinguish between light and b-jets originated in top quark decays. These later studies also correct for acceptance and detector effects.

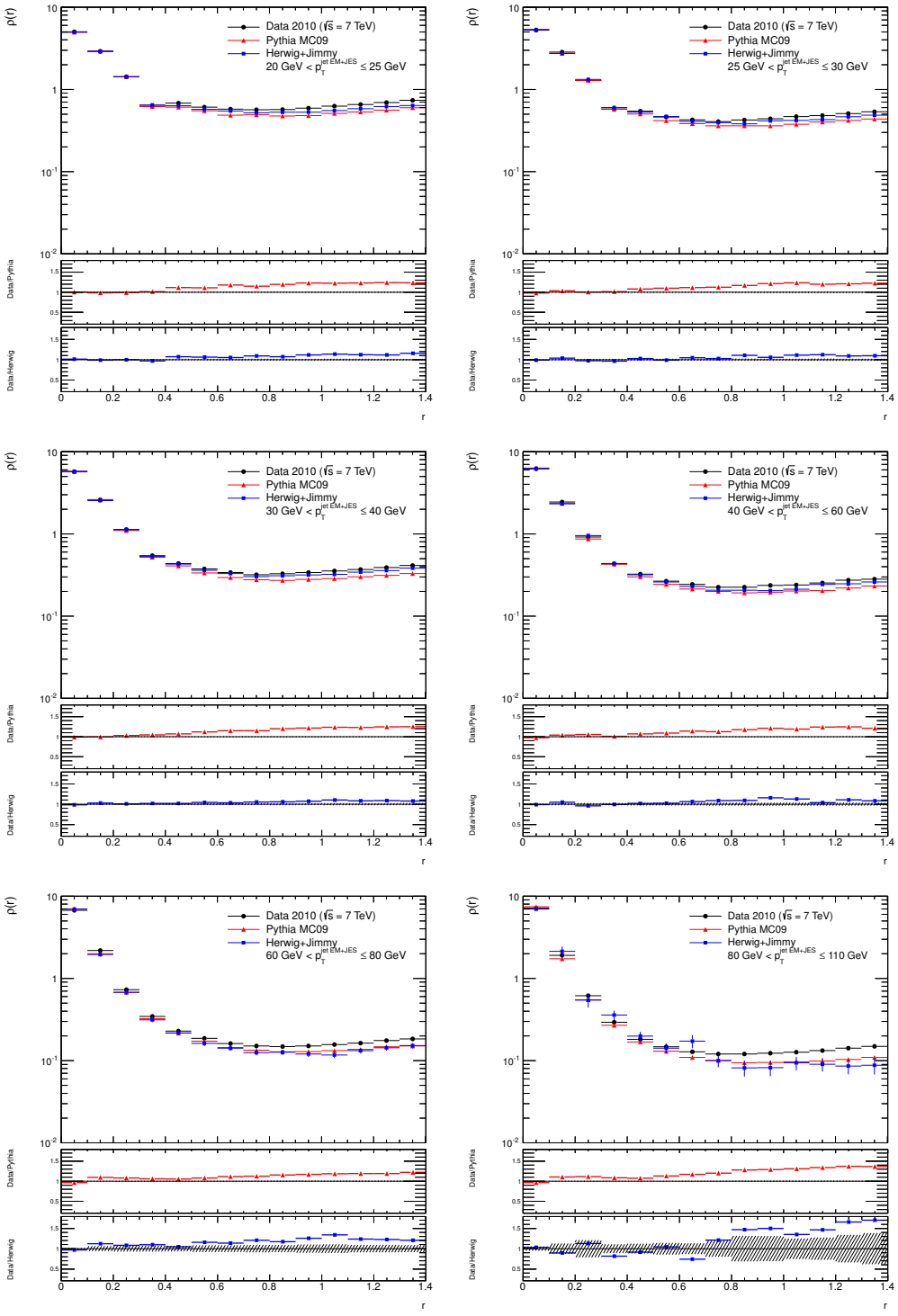

Figure 4.16: *Measured differential jet shapes at reconstructed level, $\rho(r)$, in dijet events with $|\eta| < 2.5$ and 20 GeV $< p_T \leq$ 110 GeV for different p_T regions. The predictions of* Pythia *and* Herwig *are also shown.*

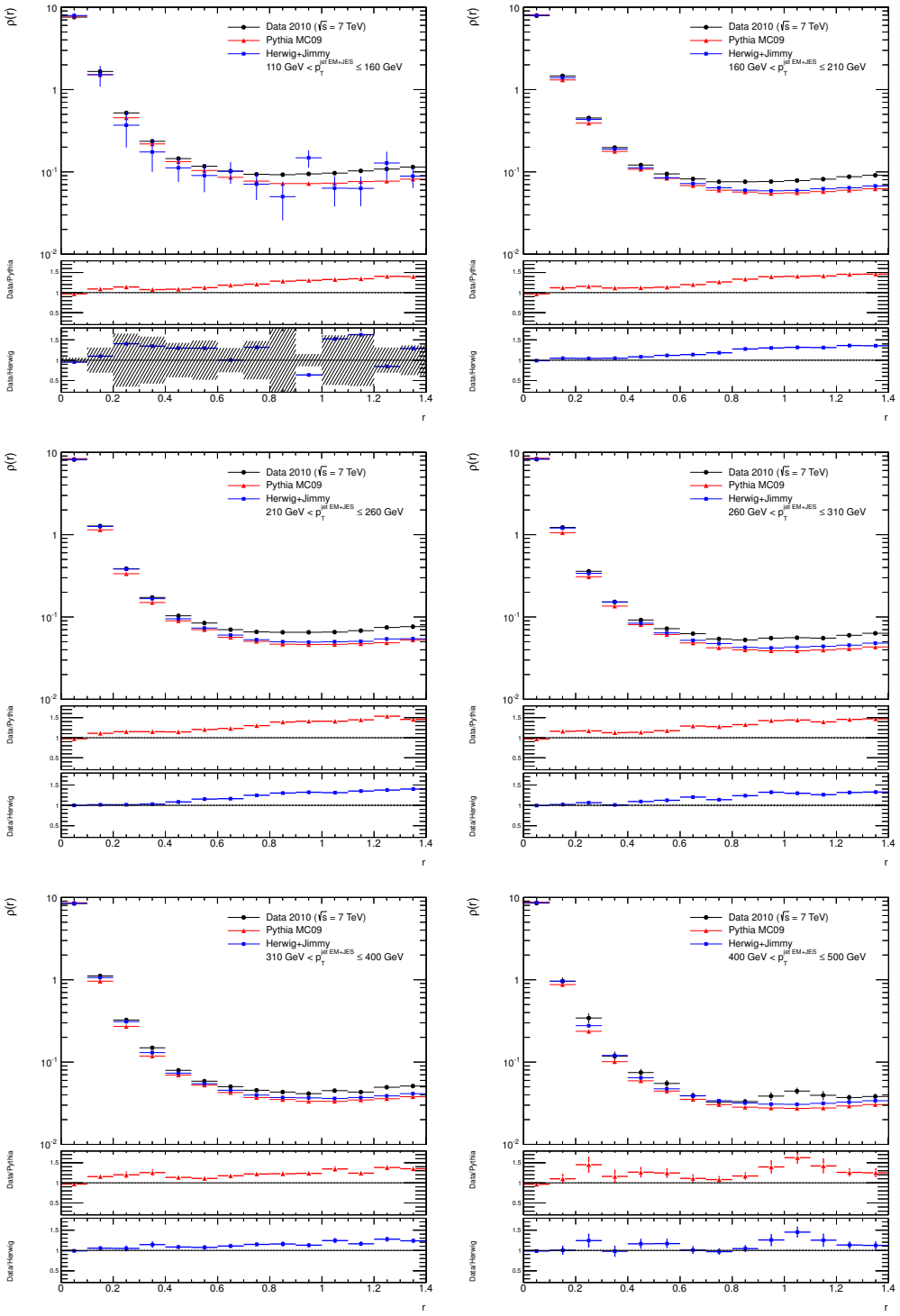

Figure 4.17: *Measured differential jet shapes at reconstructed level, $\rho(r)$, in dijet events with $|\eta| < 2.5$ and 110 GeV $< p_T \leq$ 500 GeV for different p_T regions. The predictions of* Pythia *and* Herwig *are also shown.*

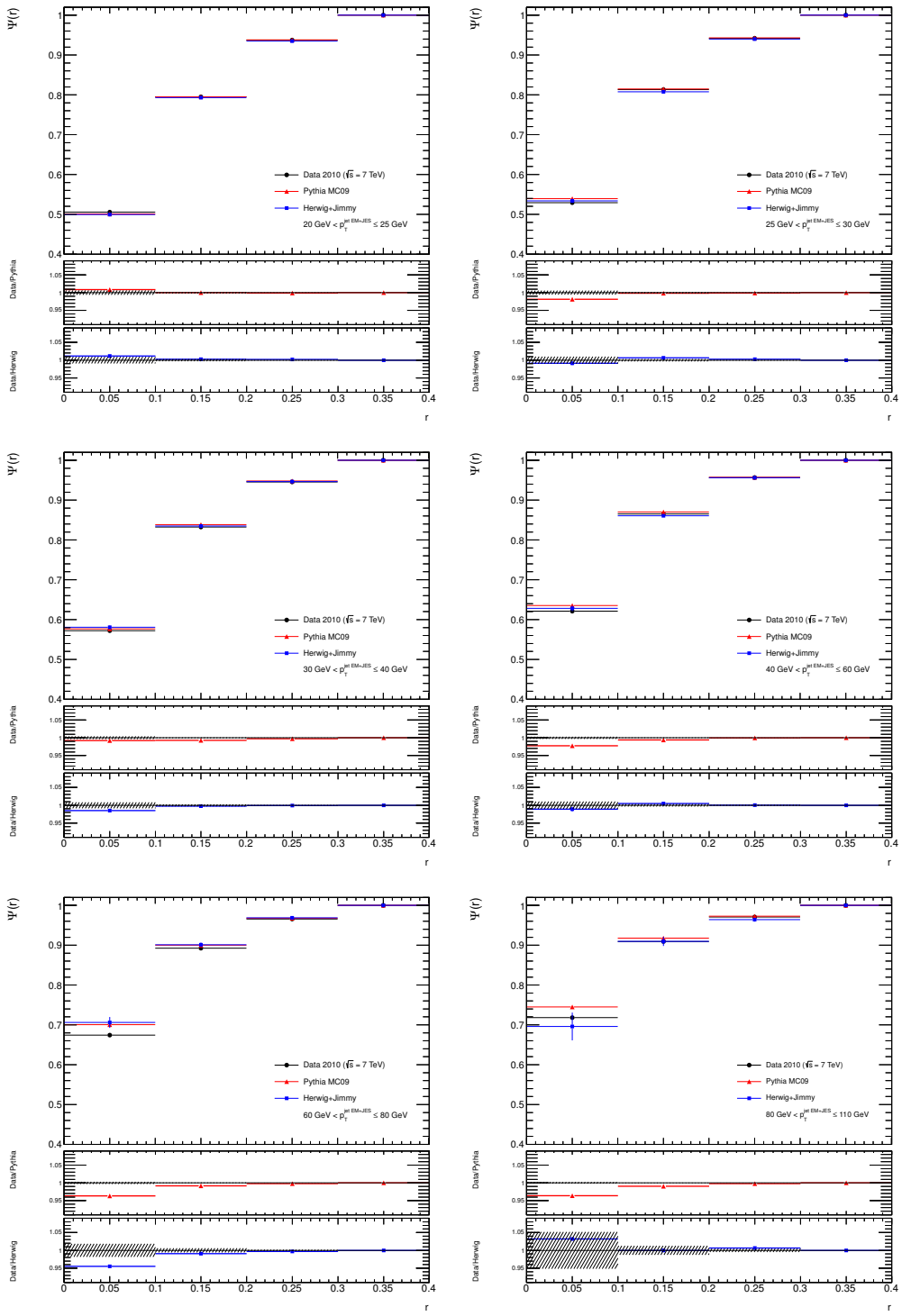

Figure 4.18: *Measured integrated jet shapes at reconstructed level, $\Psi(r)$, in dijet events with $|\eta| < 2.5$ and 20 GeV $< p_T \leq$ 110 GeV for different p_T regions.*

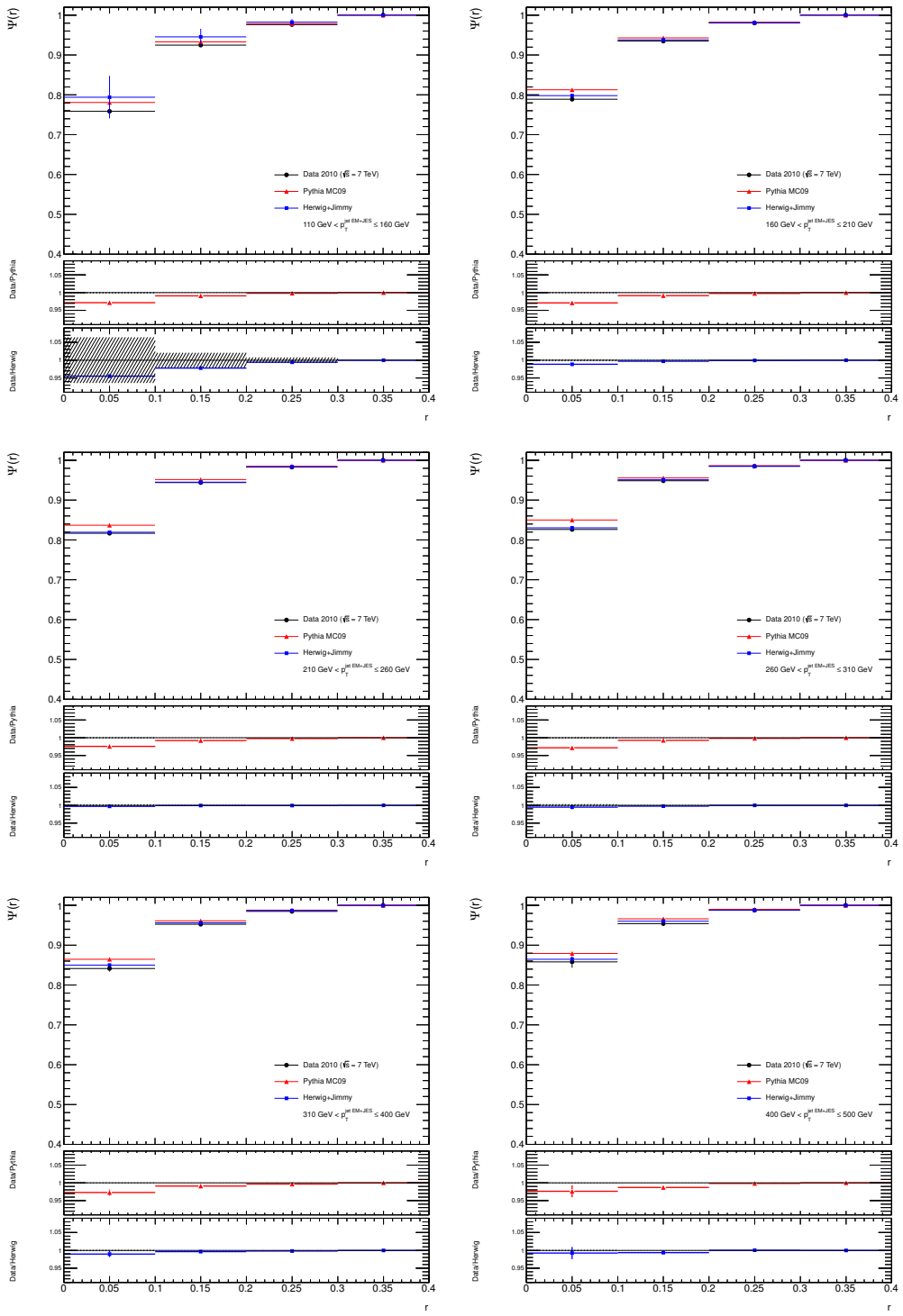

Figure 4.19: *Measured integrated jet shapes at reconstructed level, $\Psi(r)$, in dijet events with $|\eta| < 2.5$ and 110 GeV $< p_T \leq$ 500 GeV for different p_T regions.*

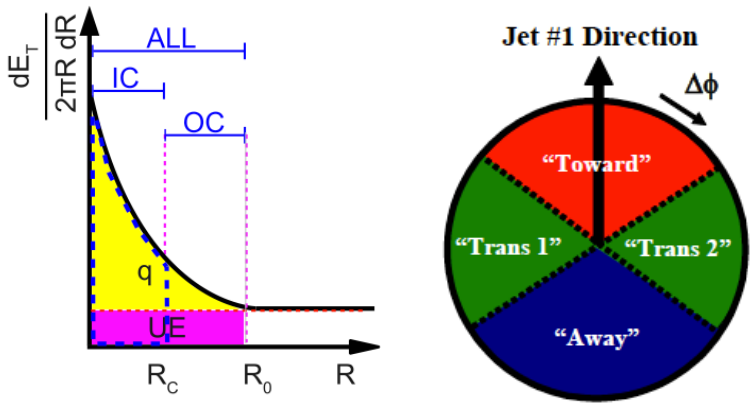

Figure 4.20: *Left: Schematic representation of the scalar p_T distribution around the jet axis. 'R_C' stands for the jet cone radius and 'R_0' for a reasonably large radius to include the whole hadronic shower. 'IC' stands for 'in-cone' region which corresponds to $\Delta R < R_C$, 'OC' for 'out-cone' region which corresponds to $R_C < \Delta R < R_0$ and 'ALL' includes both. The yellow (light shaded) area is the total p_T in the hadronic shower originating from the initial parton that is eventually reconstructed as a jet. The purple (dark shaded) block is the p_T coming from underlying event and the dashed blue area contributes to p_T^{truth}, assuming an idealized conical jet, which is fair for isolated anti-k_t jets. Right: Illustration of correlations in azimuthal angle $\Delta\phi$ relative to the direction of the leading jet (highest p_T jet) in the event. The toward region is defined by $\Delta\phi \leq 60°$, the away region by $\Delta\phi > 120°$ and the two transverse regions by $60° < \Delta\phi \leq 120°$.*

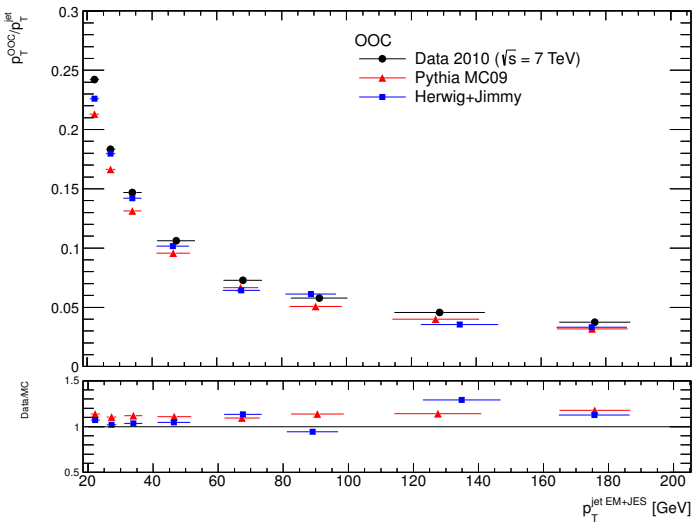

Figure 4.21: *Sum of transverse momentum of topoclusters in the out-of-cone region, from R_C=0.4 to R_0=0.8, relative to the jet p_T in data and Monte Carlo, as a function of the jet p_T.*

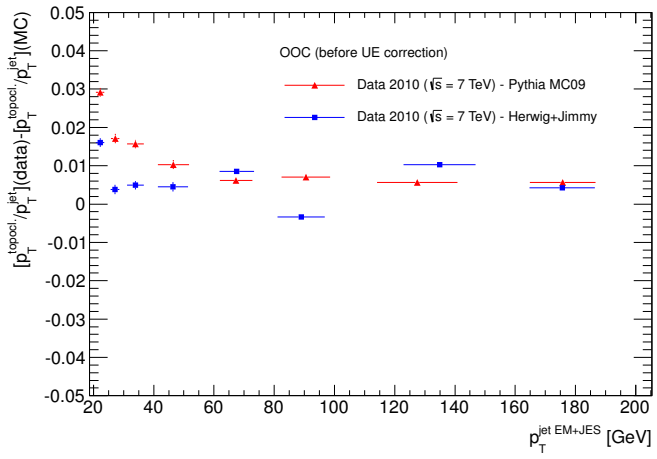

Figure 4.22: *Difference between data and Monte Carlo for the sum of transverse momentum of topoclusters in the out-of-cone region, from R_C=0.4 to R_0=0.8, relative to the jet p_T in data and Monte Carlo, as a function of the jet p_T.*

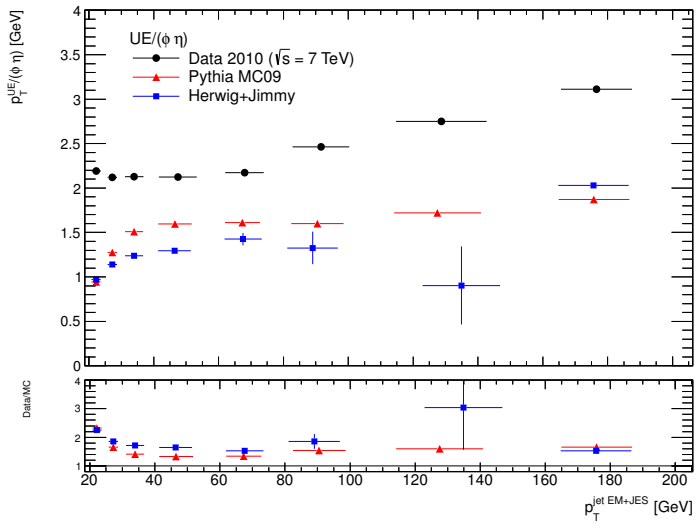

Figure 4.23: *Sum of transverse momentum of topoclusters in the transverse region per unit of $\eta - \phi$, as a function of the leading jet p_T.*

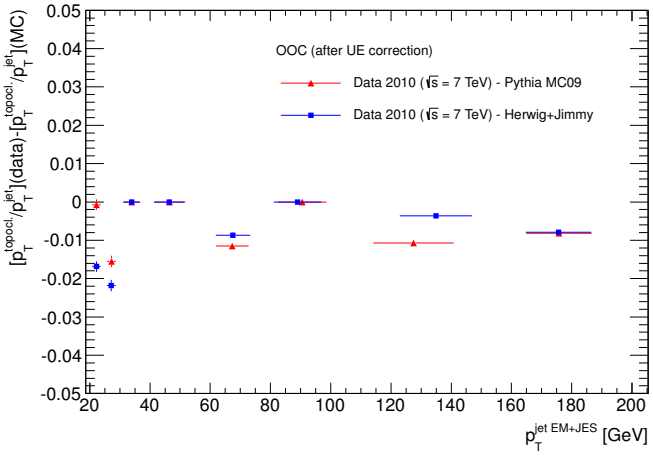

Figure 4.24: *Difference between data and Monte Carlo for the sum of transverse momentum of topoclusters in the out-of-cone region, from R_C=0.4 to R_0=0.8, subtracting the contribution from the measured underlying event relative to the jet p_T in data and Monte Carlo, as a function of the jet p_T.*

5

Measurement of the forward-backward asymmetry in the normal direction

This chapter presents the measurement of a forward-backward asymmetry, denoted as $A_{\mathrm{FB}}^{\mathrm{N}}$, using t-channel single top quark events with a lepton+jets final state and in which top quarks are highly polarised. As discussed in Chapter 2, a non-zero value of this asymmetry signals the existence of complex anomalous couplings in the Wtb vertex not expected in the SM. The data analysed are from 2011 proton-proton collisions at a center of mass energy of 7 TeV and corresponds to an integrated luminosity of $4.66\,\mathrm{fb}^{-1}$. The signal final state signature has a charged lepton (electron or muon), large missing transverse energy from the neutrino, and two jets, at least one of them originated from a b quark.

5.1 t-channel single top quark production

The analysis is carried out with 2011 data from proton-proton collisions at 7 TeV and the signal are t-channel single top quark events produced via the exchange of a virtual W boson. The Feynman diagrams representing this process at LO are shown in Figure 5.1. For antitop quark production, the charge conjugate processes are implied. In the QCD calculation, the treatment of the b quark involved in the initial state leads to two LO schemes in the t-channel. The $2\to3$ process, $g + q \to q' + t + \bar{b}$, is the so-called 4-flavour scheme where the proton is considered to be composed of only four light quarks (u, d, c and s) and the b quarks arise from the splitting of a virtual gluon into nearly collinear $b\bar{b}$[1]. In this scheme, the $\bar{b}$ quark in the final state (usually called spectator b quark or second b-jet) is characterized by its soft transverse momentum spectrum, being most of the time outside the kinematic acceptance. The $2\to2$ process with a b quark in the initial state, $b + q \to q' + t$, is the so-called 5-flavour scheme. In order to construct a

[1]This is why the t-channel is sometimes called the 'Wgluon fusion' in the literature.

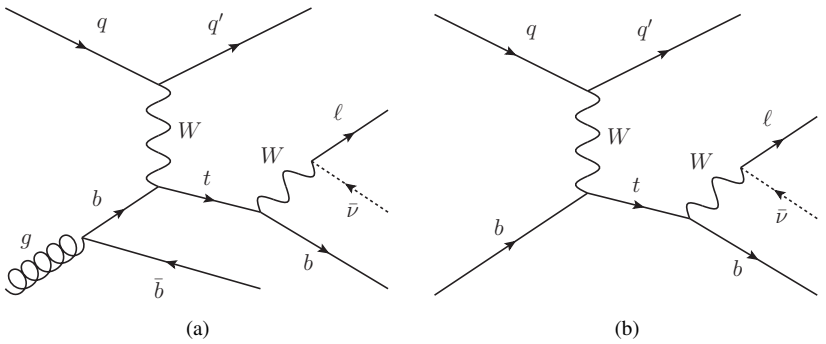

Figure 5.1: *Leading order Feynman diagrams for t-channel single top quark production. The b quark stems from a gluon splitting into a $b\bar{b}$ pair in the 2→3 (a) or from a b sea quark in the 2→2 process (b).*

Monte Carlo sample which closely follows NLO predictions, both processes must be combined. Single top quark production provides a clean source of polarized top quarks in the direction of the q' (d-type) quark in the event. In the t-channel, this is usually referred as 'spectator quark', and tends to be produced in the forward direction. In this basis, called 'spectator basis' since the spin axis tends to be aligned with the momentum of the spectator jet, the top quark is produced in the spin up state more than 90% of the time according to the SM.

Since top quarks promptly decay to a W boson and a b quark, the final state of a single top quark production event has a W boson and two or three quarks, at least one of which is a b quark. The W boson can decay into either two quarks or a charged lepton and a neutrino. The branching ratio to quarks is twice as large as that to leptons, however, the corresponding signature is not practical due to the huge contribution of QCD multijet background. By contrast, the leptonic decay of the W into an electron or a muon, and its corresponding antineutrino provides a much cleaner signature. The non-detectable neutrino is required to manifest itself as large missing transverse energy in the detector. Because of the difficulty identifying taus, the W boson leptonic decay into a tau and its neutrino only enters the event selection when the tau further decays into detectable electrons or muons. Thus, the final state is composed of exactly one isolated high-p_T charged lepton (electron or muon), large missing transverse energy and two jets, one of them originated from a b quark. Figure 5.2 shows an event display with a candidate event.

There are several processes whose final state is very similar to the one just described and therefore fake our signal. The most important backgrounds are the top quark pair production $t\bar{t}$, W+jets, Z+jets, diboson, QCD multijets and other single top quark processes. Based on the t-channel lepton+jets signature, a tight event selection is applied in this analysis to maximize the amount of signal and minimize the amount of background in the final data sample.

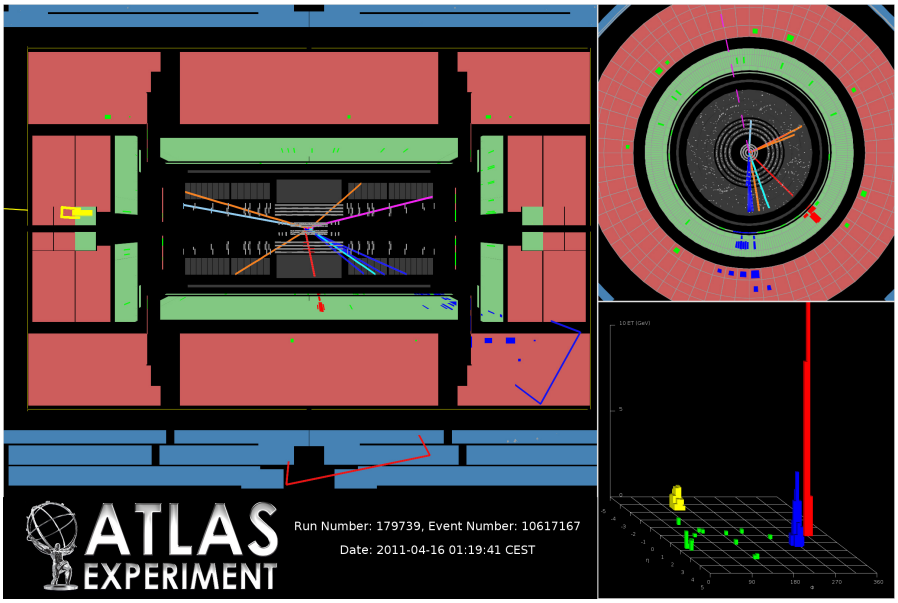

Figure 5.2: *Event display of a t-channel single top quark candidate event. The lepton (electron in this case) is shown in red, the b-tagged jet in blue and the light quark jet in yellow. The* $E_{\mathrm{T}}^{\mathrm{miss}}$ *is indicated by the dashed line in the* $x-y$ *projection (upper right). The light quark jet is in the forward calorimeter and does not appear in the* $x-y$ *projection.*

5.2 Analysed data samples

The data analysed here are from proton-proton collisions delivered by the LHC in 2011 at $\sqrt{s}$ = 7 TeV and collected by the ATLAS detector using a single lepton trigger (electron or muon). This corresponds to a total integrated luminosity of 4.66±0.08 fb^{-1} [132]. With the increasing instantaneous luminosity of the LHC, the average number of simultaneous proton-proton interactions per beam crossing increased from about 6 to 17 during the 2011 data-taking period (see Figure 3.19). Due to these changes, different triggers were used to select events for different data periods. These changing pile-up conditions are included in the Monte Carlo simulation. Table 5.1 gives an overview of the different data-taking periods of 2011 with their respective integrated luminosities and the triggers applied.

5.3 Object and event selection

5.3.1 Final state objects

The reconstruction, calibration and selection procedures used for the objects (electrons, muons, jets, *b*-jets and missing transverse momentum) required to select events with a *t*-channel signature are fully explained in Chapter 3 (Section 3.4). Here a brief overview of the selected objects is presented.

Run period	Run numbers	Integrated luminosity (pb^{-1})	Electron trigger	Muon trigger
B–D	177986 – 180481	176 ± 3	e_20_medium	mu_18
E–H	180614 – 184169	938 ± 17	e_20_medium	mu_18
I	185353 – 186493	333 ± 6	e_20_medium	mu_18
J	186516 – 186755	224 ± 4	e_20_medium	mu_18_medium
K	186873 – 187815	583 ± 11	e_22_medium	mu_18_medium
L–M	188902 – 191933	2402 ± 43	e_22vh_medium1	mu_18_medium

Table 5.1: *Summary of the analysed 2011 ATLAS dataset with data-taking period, run range, integrated luminosity (relative systematic uncertainty of 1.8%) and trigger requirements. The trigger items denote the lepton, the transverse momentum threshold (in GeV) and the lepton identification criterion (see Section 3.3.5).*

Electrons

Electron candidates are reconstructed using a cluster-based algorithm and are required to have a transverse energy $E_T > 25$ GeV and a pseudo-rapidity for the calorimeter cluster $|\eta| < 2.47$. Events with electrons falling in the calorimeter transition region between the barrel and the end-caps ($1.37 < |\eta| < 1.52$) are rejected. High-quality electron candidates are selected by applying stringent `Tight++` requirements. Additional isolation criteria based on the calorimeter transverse energy of all cells and on the transverse momentum of all tracks within cones of radius $\Delta R = 0.2$ and 0.3 respectively around the electron direction (excluding the cells or the tracks associated with the electron candidate) are applied to suppress the QCD multijet background.

Muons

Muon candidates are reconstructed by combining track segments found in the ID and in the MS and are required to have a transverse momentum $p_T > 25$ GeV and $|\eta| < 2.5$. Selected muons must additionally satisfy a series of cuts on the number of track hits present in the various tracking subdetectors. Muon candidates are required to be isolated using a criteria similar to the one applied to electron candidates.

Jets

Jets are reconstructed from calorimeter clusters using the anti-k_t algorithm with a radius parameter of $R_C = 0.4$. The response of the calorimeter is corrected by p_T and η-dependent factors which are applied to each jet to provide an average energy scale correction. Jets are required to have $p_T > 30$ GeV, $|\eta| < 4.5$ and a jet vertex fraction (see Section 3.4.4) greater than 0.75. In the region where $2.75 < |\eta| < 3.5$, the p_{T} cut for jets is increased to 35 GeV. Jets overlapping with selected electron candidates within $\Delta R < 0.2$ are removed.

Jets originating from b quarks are identified in the region $|\eta| < 2.5$ by reconstructing secondary and tertiary vertices from the tracks associated with each jet and by combining lifetime-related information with a neural network. The b-tagging algorithm used for this analysis is

the JetFitterCombNNc [115, 117] which is optimised for c-quark rejection. The working point (threshold applied to the algorithm output) corresponds to a b-tagging efficiency of 55% estimated in $t\bar{t}$ events. The associated rejection factors for light quark and c-quark jets are of ~200 and ~20, respectively. A comparison of the performance of this algorithm with the one used in ATLAS $t\bar{t}$ analyses, the MV1, can be found in Appendix B.

E_T^{miss}

The $E_{\mathrm{T}}^{\mathrm{miss}}$ is defined as the momentum imbalance in the transverse plane to the beam axis, where momentum conservation is expected. An imbalance indicates the presence of undetectable particle, such as neutrinos, but it also includes energy loses due to detector inefficiencies and its resolution. The $E_{\mathrm{T}}^{\mathrm{miss}}$ is calculated as the vector sum over all topoclusters in the event, and is further refined by applying object level corrections for the contributions which arise from identified electrons, muons and jets. The cells not associated to any reconstructed physics objects are taken into account by the calorimeter cell out term.

5.3.2 W boson and top quark reconstruction

In order to obtain the angular distributions proposed in Chapter 2 to probe the Wtb vertex, the four-vectors of all the involved particles are needed, i.e. a full reconstruction of the event is required. The top quark and W boson are not observed directly and need to be reconstructed from their observable decay products. In the case of $t\bar{t}$ events, the assignment of the observed charged lepton, $E_{\mathrm{T}}^{\mathrm{miss}}$ and jets to the decay products of W bosons and top quarks is not unambiguous. In single top quark events, there is only one possibility to combine the final physics objects to obtain the top quark. Nevertheless, the reconstruction of the leptonic W boson poses a difficult challenge which comes from the kinematics of the neutrino that escapes undetected. The most common criterion (and the one exploited here) to solve this is to assume that the $E_{\mathrm{T}}^{\mathrm{miss}}$ of the event corresponds to the transverse momentum of the undetected neutrino (i.e. $E_{\mathrm{T}}^{\mathrm{miss}} \equiv p_T^{\nu}$). Although it is true that the neutrino is the main contributor to the $E_{\mathrm{T}}^{\mathrm{miss}}$ at LO, there are additional contributions: extra neutrinos from other processes, ISR/FSR effects, miscalibration of the $E_{\mathrm{T}}^{\mathrm{miss}}$, fake missing $E_{\mathrm{T}}^{\mathrm{miss}}$ due to the detector energy resolution and acceptance, etc. Ignoring these, the only missing piece is the longitudinal momentum of the neutrino, p_z^{ν}, which is derived from the measured $E_{\mathrm{T}}^{\mathrm{miss}}$ and using the constraint of the W boson mass when calculating the invariant mass of the lepton and the neutrino.

The four-momentum conservation law for the leptonic W boson decay gives:

$$(p^W)^2 = (p^l + p^{\nu})^2 \quad \rightarrow \quad m_W^2 = m_l^2 + 2(E^l, \vec{p}^{\,l})(E^{\nu}, \vec{p}^{\,\nu}) = m_l^2 + 2(E^l E^{\nu} - \vec{p}^{\,l} \cdot \vec{p}^{\,\nu}) \,, \tag{5.1}$$

where the neutrino mass has been neglected. Assuming that the transverse energy in the center of mass of the collision is zero and that $E_{\mathrm{T}}^{\mathrm{miss}}$ measured in the detector is only due to the neutrino, its energy and its transverse momentum can be expressed as:

$$E^{\nu} = \sqrt{(p_{\mathrm{T}}^{\nu})^2 + (p_z^{\nu})^2} = \sqrt{(E_{\mathrm{T}}^{\mathrm{miss}})^2 + (p_z^{\nu})^2}$$

$$p_x^{\nu} = E_{\mathrm{T}}^{\mathrm{miss}} \cos\phi^{E_{\mathrm{T}}^{\mathrm{miss}}} \quad \text{and} \quad p_y^{\nu} = E_{\mathrm{T}}^{\mathrm{miss}} \sin\phi^{E_{\mathrm{T}}^{\mathrm{miss}}} \,.$$

From these, the m_W^2 expression can be re-written as:

$$m_W^2 = m_l^2 + 2E^l E^\nu - 2\left(p_x^l p_x^\nu + p_y^l p_y^\nu + p_z^l p_z^\nu\right) =$$

$$= m_l^2 + 2E^l\sqrt{(E_{\mathrm{T}}^{\mathrm{miss}})^2 + (p_z^\nu)^2} - 2\left[E_{\mathrm{T}}^{\mathrm{miss}}(p_x^l \cos\phi^{E_{\mathrm{T}}^{\mathrm{miss}}} + p_y^l \sin\phi^{E_{\mathrm{T}}^{\mathrm{miss}}}) + p_z^l p_z^\nu\right] . \tag{5.2}$$

The only unknown quantity in this equation is the neutrino longitudinal momentum p_z^ν which can be obtained solving the following equation:

$$a(p_z^\nu)^2 + bp_z^\nu + c = 0 \;\rightarrow\; \begin{cases} a = (E^l)^2 - (p_z^l)^2 \\ b = p_z^l\left[-m_W^2 + m_l^2 - 2(p_x^l p_x^\nu + p_y^l p_y^\nu)\right] \\ c = (E^l)^2(E_{\mathrm{T}}^{\mathrm{miss}})^2 - \frac{1}{4}\left[m_W^2 - m_l^2 + 2(p_x^l p_x^\nu + p_y^l p_y^\nu)\right]^2 \end{cases}$$

with two possible solutions,

$$p_z^\nu = \frac{-p_z^l\left(-m_W^2 + m_l^2 - 2(p_x^l p_x^\nu + p_y^l p_y^\nu)\right)}{2\left((E^l)^2 - (p_z^l)^2\right)} \pm \sqrt{\Delta}\,, \tag{5.3}$$

where the discriminant Δ is defined as:

$$\Delta \equiv (E^l)^2\left[\left(m_W^2 - m_l^2 + 2(p_x^l p_x^\nu + p_y^l p_y^\nu)\right)^2 + 4(E_{\mathrm{T}}^{\mathrm{miss}})^2(-(E^l)^2 + \left(p_z^l\right)^2)\right] .$$

If the two solutions are real ($\Delta > 0$), the one giving the lower p_z^ν value is taken. If just one solution is real ($\Delta = 0$), this is the chosen one. In case that $\Delta < 0$, which happens when the assumption that the neutrino is the only contributor to the $E_{\mathrm{T}}^{\mathrm{miss}}$ is not valid and therefore p_z^ν is overestimated, there are several options:

- Claim that the obtained complex solution is unphysical, assume $\Delta = 0$, and then choose the single p_z^ν value.
- Another solution is to decrease the $E_{\mathrm{T}}^{\mathrm{miss}}$, i.e. p_{T}^ν, step by step until a real pair of solutions is found ($\Delta \geq 0$). This decreasing can be done within the $E_{\mathrm{T}}^{\mathrm{miss}}$ resolution using the Monte Carlo information or using the restriction that $m_{\mathrm{T}}(W)$ has to remain below 90 GeV.
- The other option (used here) consists in finding the $E_{\mathrm{T}}^{\mathrm{miss}}$ values for which the Δ term becomes positive. By doing so, one just scales $E_{\mathrm{T}}^{\mathrm{miss}}$ (scaled value denoted as $E_{\mathrm{T}}^{\mathrm{miss}\,\prime}$) but preserves its direction ($\cos\phi^{E_{\mathrm{T}}^{\mathrm{miss}}}, \sin\phi^{E_{\mathrm{T}}^{\mathrm{miss}}}$). To do this, one can solve the discriminant equation, i.e. $\Delta = 0$, in terms of $E_{\mathrm{T}}^{\mathrm{miss}\,\prime}$ and two possible solutions will be obtained from this equation:

$$E_{\mathrm{T}}^{\mathrm{miss}\,\prime} = \frac{-(-m_W^2 + m_l^2)(p_x^l \cos\phi^{E_{\mathrm{T}}^{\mathrm{miss}}} + p_y^l \sin\phi^{E_{\mathrm{T}}^{\mathrm{miss}}}) \pm (-m_W^2 + m_l^2)\sqrt{(E^l)^2 - (p_z^l)^2}}{2\left[(E^l)^2 - (p_z^l)^2 - (p_x^l \cos\phi^{E_{\mathrm{T}}^{\mathrm{miss}}} + p_y^l \sin\phi^{E_{\mathrm{T}}^{\mathrm{miss}}})^2\right]} .$$

  If just one solution is positive, this is the chosen one. If the two solutions are positive, the one closer to the initial $E_{\mathrm{T}}^{\mathrm{miss}}$ is chosen and used in Equation 5.3 to finally compute p_z^ν.

Once the neutrino four-momentum is fully determined, the W boson four-momentum can be computed and finally that of the top quark.

5.3.3 Kinematic properties of the reconstructed objects

In Figures 5.3-5.8 the kinematic properties of the final state objects in t-channel single top quark simulated events are shown. The order of the objects is the following: the spectator quark which is the light jet, the b quark from the top quark decay, the lepton -electron or muon-, the $E_{\mathrm{T}}^{\mathrm{miss}}$ and the reconstructed top quark. First the p_T and η distributions for all generated events are presented. Then the comparison of the generated and reconstructed properties are shown for events passing the preselection cuts.

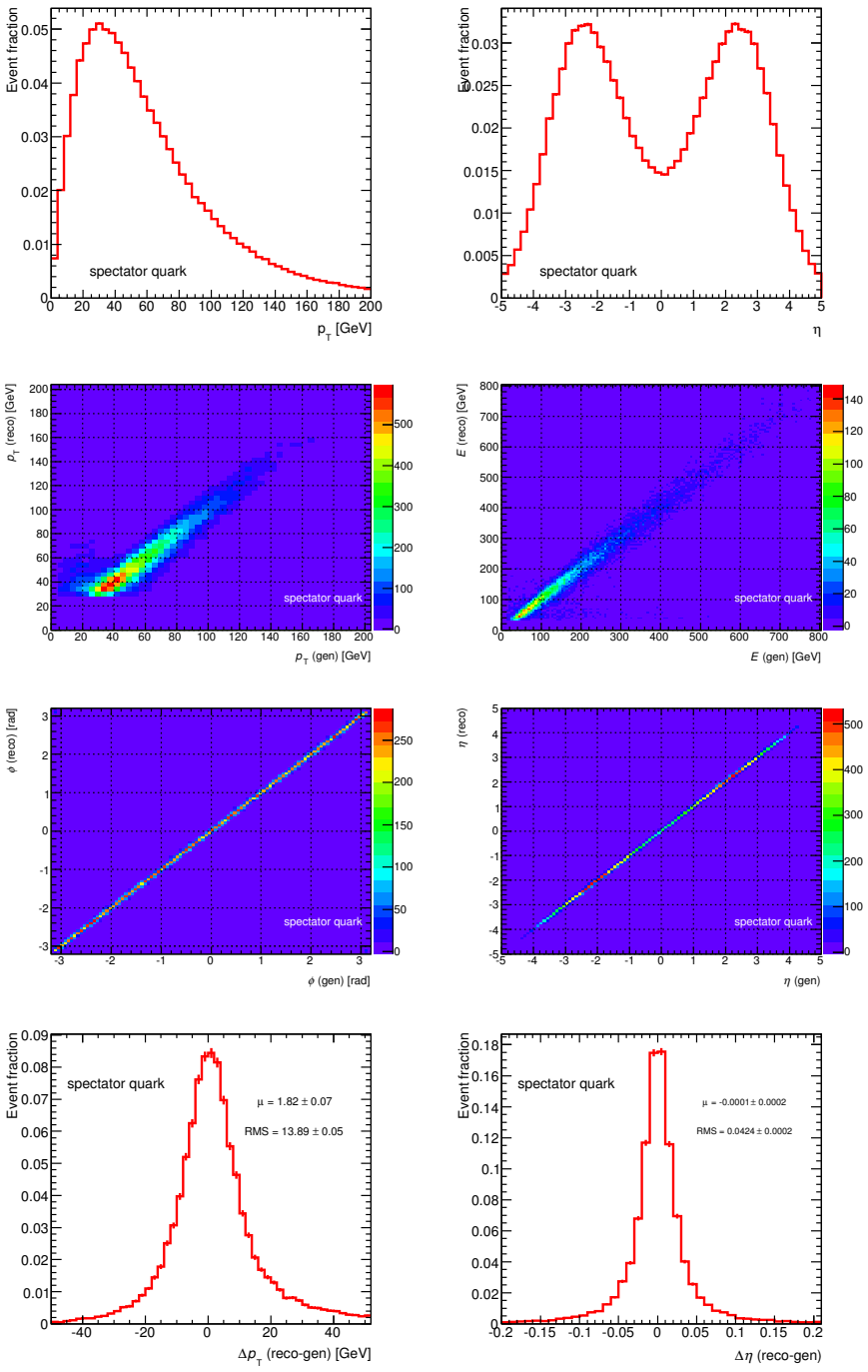

Figure 5.3: *Kinematic properties of the reconstructed light jet (spectator quark).*

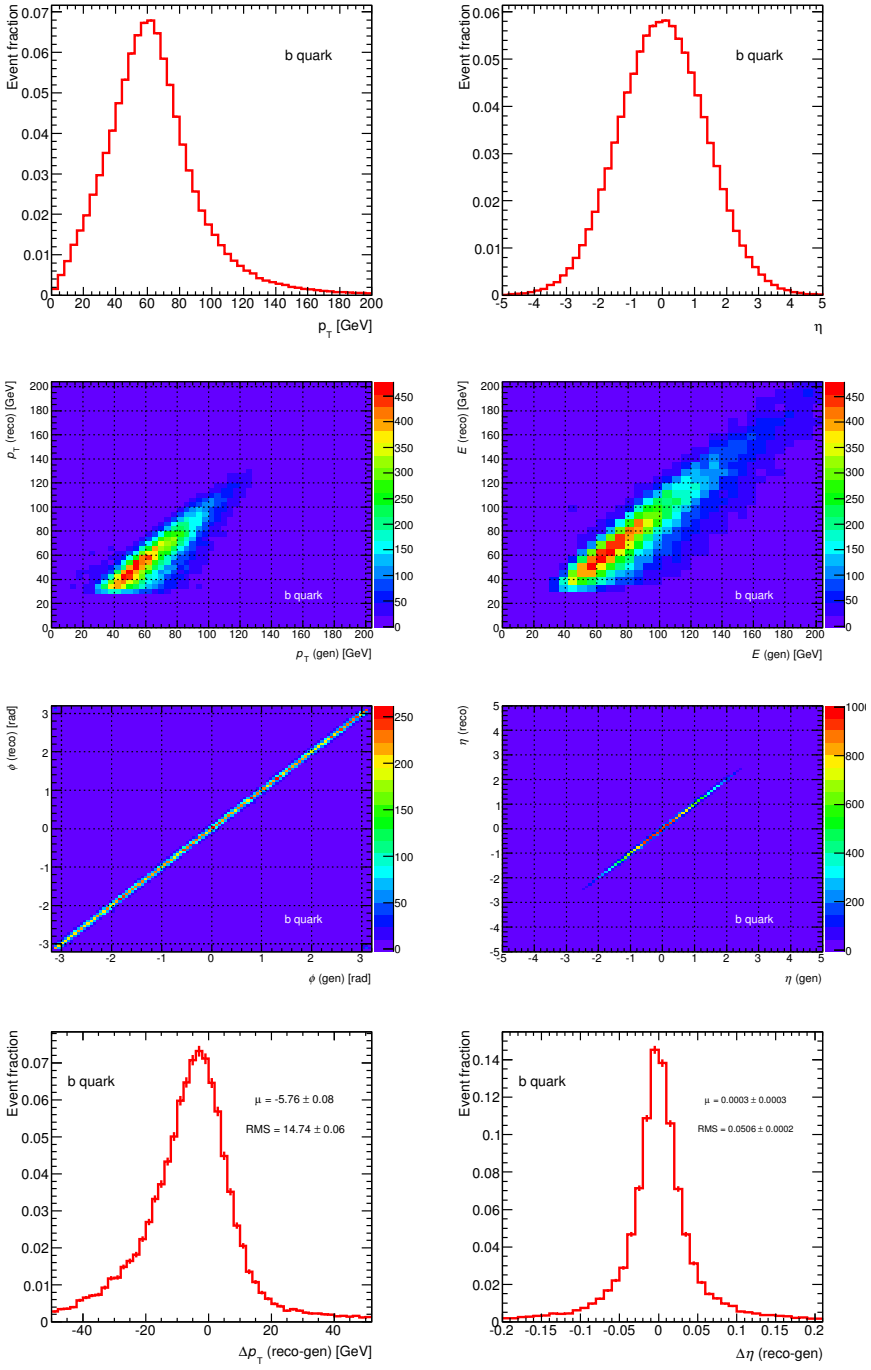

Figure 5.4: *Kinematic properties of the reconstructed b-jet (b quark).*

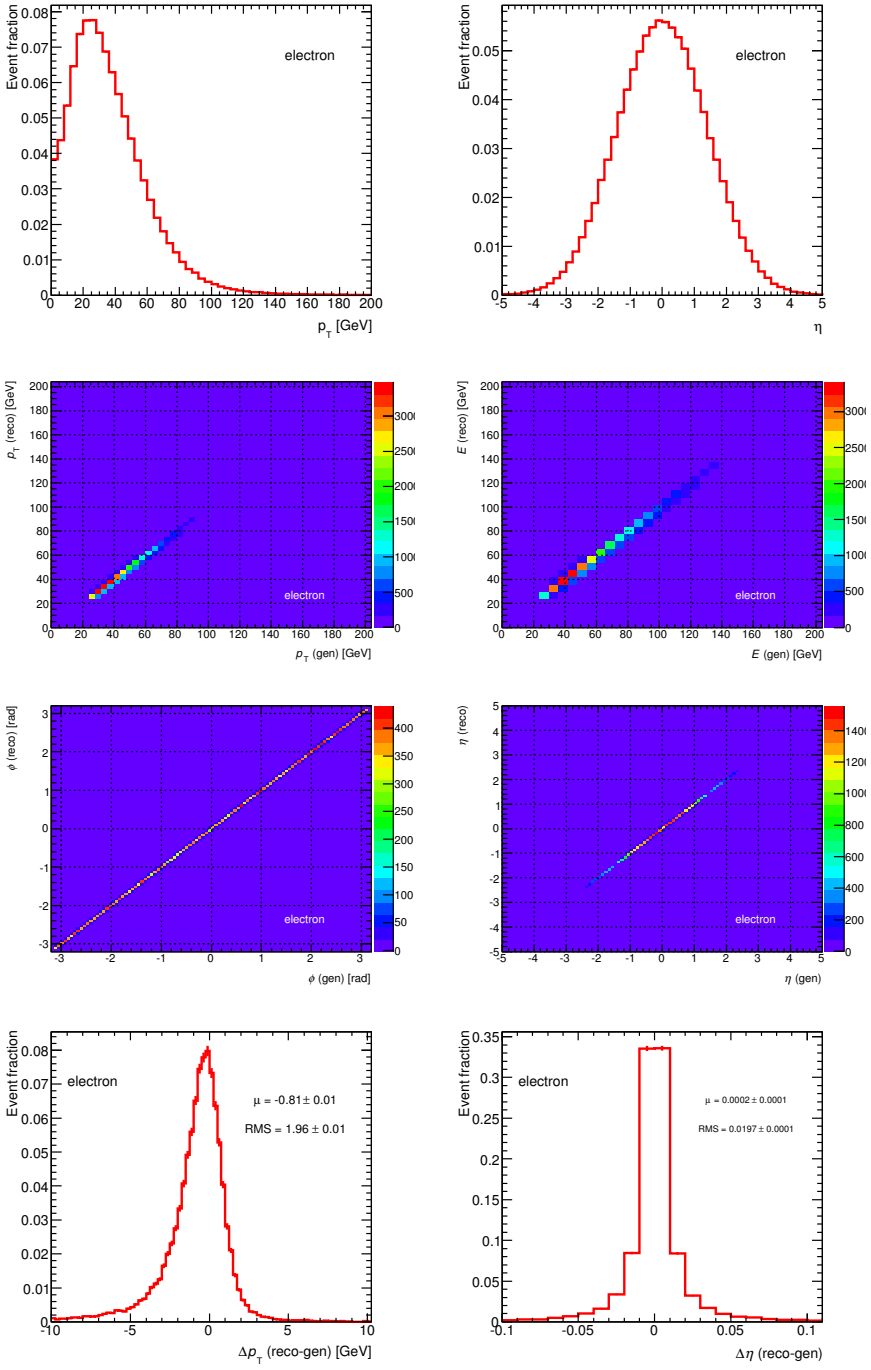

Figure 5.5: *Kinematic properties of the reconstructed electron.*

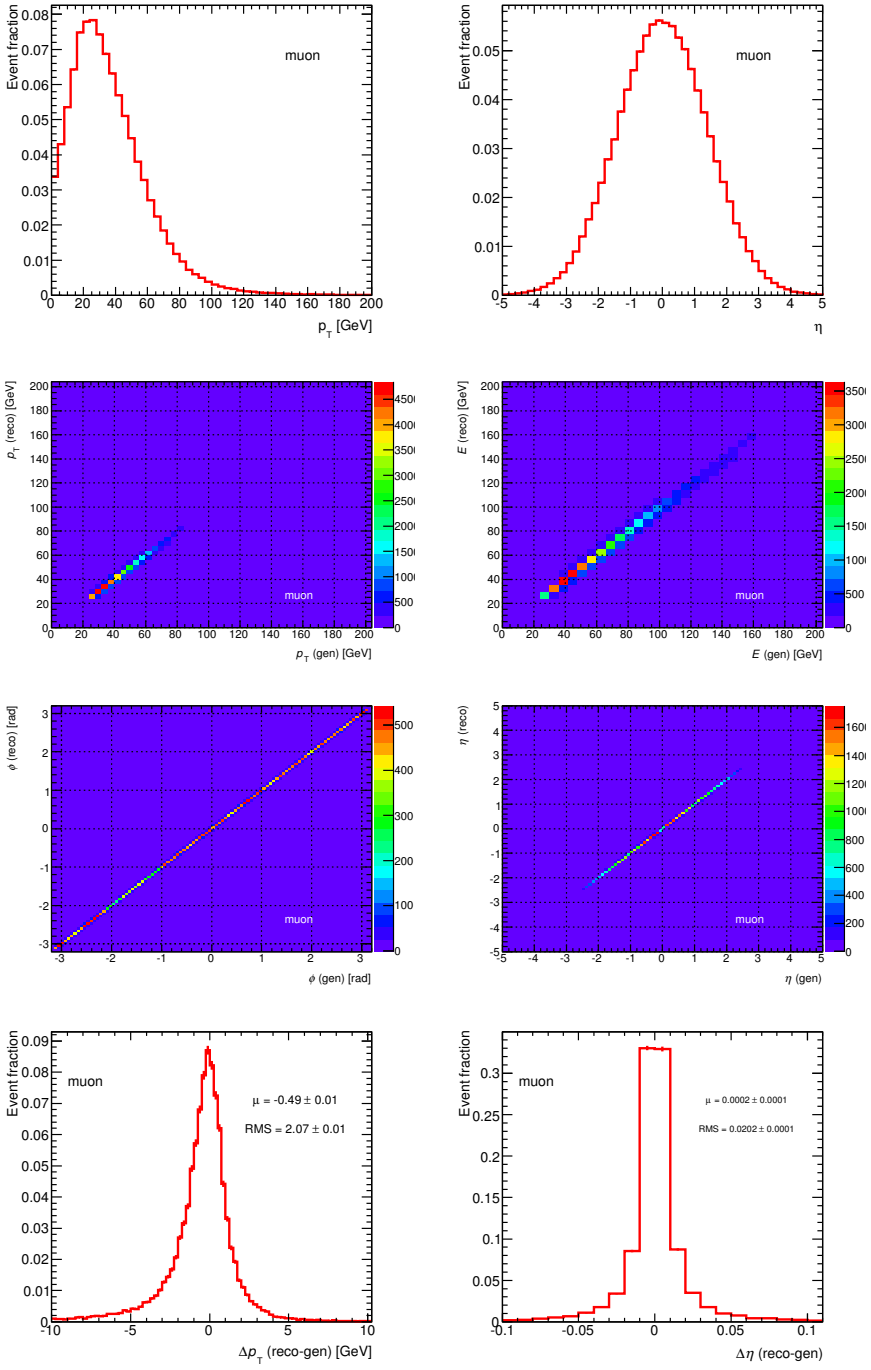

Figure 5.6: *Kinematic properties of the reconstructed muon.*

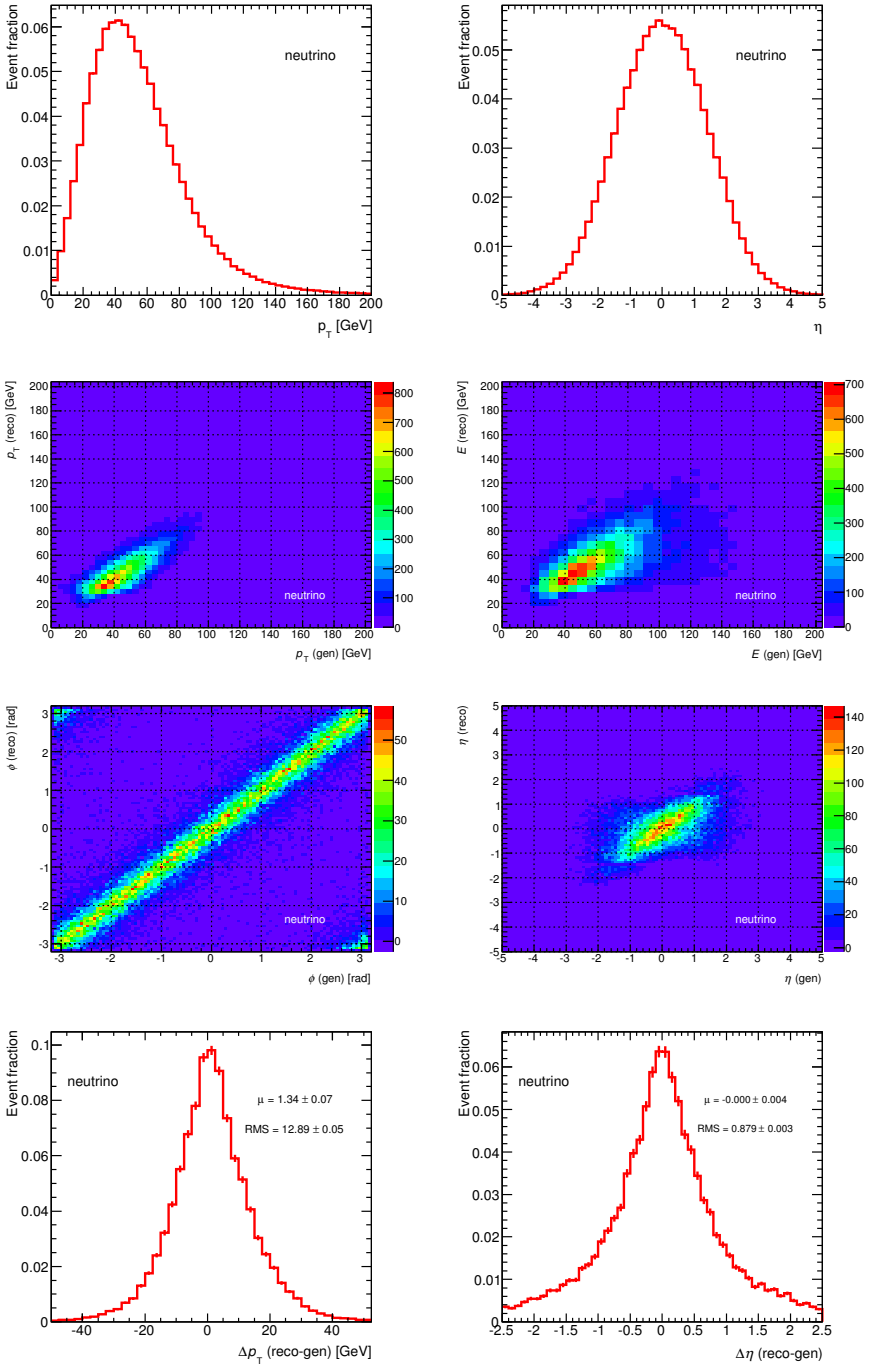

Figure 5.7: *Kinematic properties of the reconstructed neutrino ($E_{\mathrm{T}}^{\mathrm{miss}}$).*

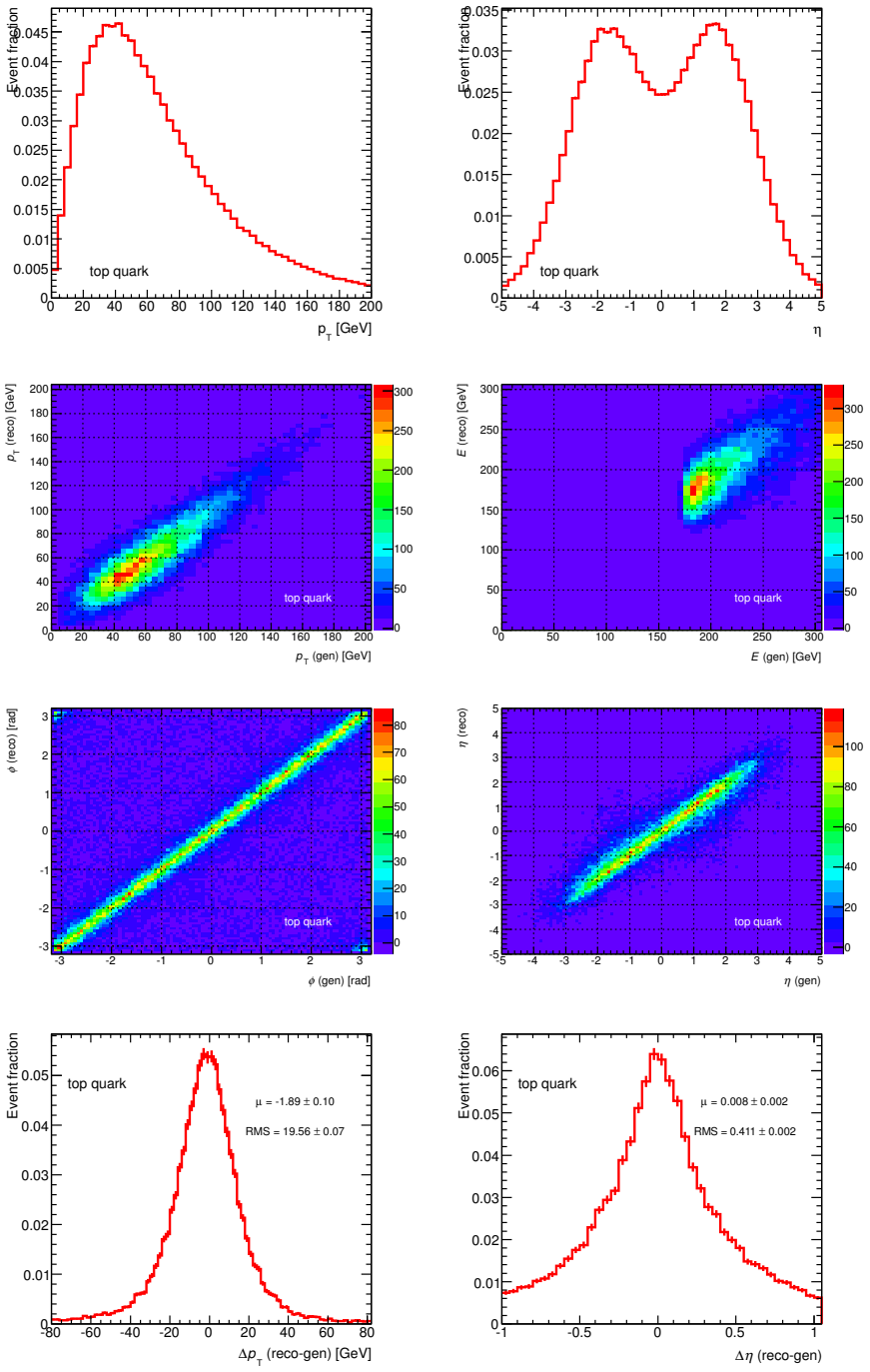

Figure 5.8: *Kinematic properties of the reconstructed top quark.*

5.3.4 Event selection

Events are required to contain exactly one lepton (electron or muon) and two jets being one of them b-tagged, as defined above. In order to reject background events, both the $E_{\mathrm{T}}^{\mathrm{miss}}$ and the transverse W mass[2] (denoted as $m_{\mathrm{T}}(W)$) are required to be greater than 30 GeV. Finally, an additional requirement is applied in the lepton p_{T} in order to exclude badly modelled events. This set of cuts corresponds to the 'preselection' cuts and they are listed in Table 5.2.

Preselection cuts
GRL defined by the top group (just for data)
Single lepton trigger (trigger and offline match)
Primary vertex ≥ 5 tracks
No loose bad jet with $p_T > 20$ GeV (just for data)
No noise burst in the liquid argon calorimeter
Exactly 1 lepton with $\|\eta\| < 2.5$ and $p_T > 25$ GeV (veto the opposite channel)
2 jets with $p_T > 30$ GeV, $\|\eta\| < 4.5$ and $\|JVF\| > 0.75$ ($p_T > 35$ GeV in $2.75 < \|\eta\| < 3.5$)
$E_{\mathrm{T}}^{\mathrm{miss}} > 30$ GeV
$m_T(W) > 30$ GeV
Exactly one b-jet (JetFitterCOMBNNc 55%) with $\|\eta\| < 2.5$
$p_T^l > (40 \mp \frac{40}{\pi-1}(\Delta\phi(j_1, l) \pm \pi))$ GeV
Selection cuts
$\|\eta_{\text{light-jet}}\| > 2$
$H_T > 210$ GeV
150 GeV $< m_{top} <$ 190 GeV
$\Delta\eta_{\text{(light-jet, b-jet)}} > 1$

Table 5.2: *List of 'preselection' and 'selection' cuts.*

Given the small fraction of signal events in the dataset at preselection level, further requirements are applied to further separate the signal from background events. These four additional cuts (called 'selection' cuts) are listed in Table 5.2 and exploit the topology of t-channel single top quark events: light jet (i.e. spectator quark) in the forward region, the sum of the transverse energy of all final objects involved[3], denoted as H_{T}, must be large, the mass of the reconstructed top quark (m_{lvb}) must be around the expected value, and the distance in η between the light jet and the b-jet, $\Delta\eta$(light-jet, b-jet), must be large. In Figure 5.9 a shape comparison for these variables between the t-channel signal and the main backgrounds at preselection level is presented. From these distributions one can understand the cut values chosen. Figures 5.10-5.11 show the comparison between data and expectation for the discriminant variables used to define the signal after applying all selection cuts except the one on the shown variable.

[2]The transverse mass of the W boson is defined as: $m_{\mathrm{T}}(W) = \sqrt{2p_T^l E_{\mathrm{T}}^{\mathrm{miss}}\left[1 - \cos\left(\phi^l - \phi^{E_{\mathrm{T}}^{\mathrm{miss}}}\right)\right]}$. This variable has the advantage that its spectrum is relatively insensitive to the production dynamics of the W boson.

[3]The quantity H_{T} is defined as: $H_{\mathrm{T}} = p_T^l + p_T^{light-jet} + p_T^{b-jet} + E_{\mathrm{T}}^{\mathrm{miss}}$.

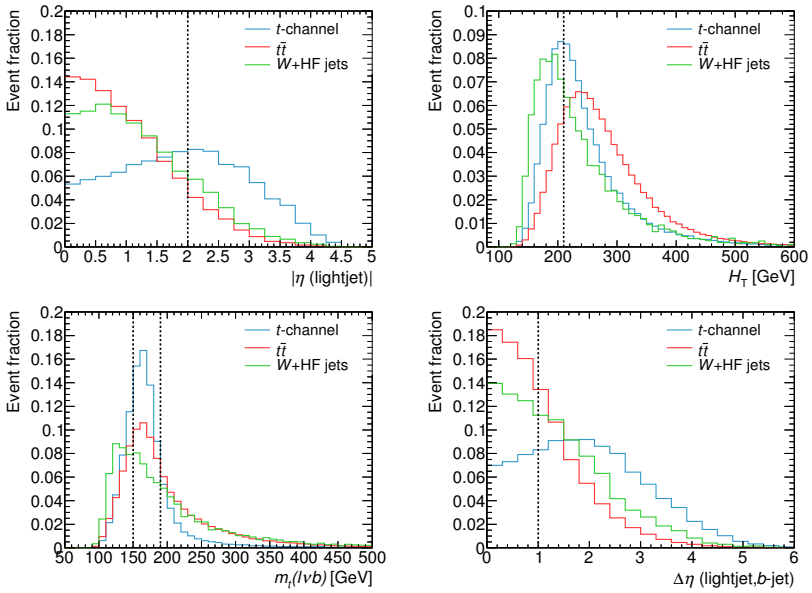

Figure 5.9: *Comparison of the shape of the discriminant variables used in the final selection between the signal and the main backgrounds. From top left to bottom right: η of the light jet, H_{T}, mass of the reconstructed top quark and $\Delta\eta$(light-jet, b-jet) at preselection level for the muon channel.*

5.4 Modelling of signal and background processes

In order to perform a precise measurement, accurate models predicting the characteristics of the expected data are needed for both the signal and the SM background processes. Special care must be taken in this analysis since the final observable, an angular distribution, is highly sensitive to kinematic mismodelling. Most of the processes involved in this analysis are described using Monte Carlo simulations including a detailed detector simulation.

Signal modelling

The matrix element generator AcerMC [133] is used to simulate t-channel single top quark events. The MRST LO** [134] parametrisation of the PDFs is used. The AcerMC output is passed to Pythia [127] for showering and hadronisation using the AUET2 tune [135]. The simulation includes both the $q{+}b{\to}q'{+}t$ and $q{+}g{\to}q'{+}t{+}\bar{b}$ diagrams, and a procedure to remove the overlap in phase space between them [136]. The factorisation and renormalisation scales have been set to $\mu_{\mathrm{F}} = \mu_{\mathrm{R}} = \sqrt{\hat{s}}$, the centre-of-mass energy of the partonic system, and a top quark mass of 172.5 GeV has been used.

In order to test the method to derive the forward-backward asymmetry $A_{\mathrm{FB}}^{\mathrm{N}}$ and its sensitivity to values deviating from the SM prediction, samples with non-SM values for $A_{\mathrm{FB}}^{\mathrm{N}}$ -which correspond to non-vanishing $Im(g_{\mathrm{R}})$ couplings- have been generated with Protos LO generator [137].

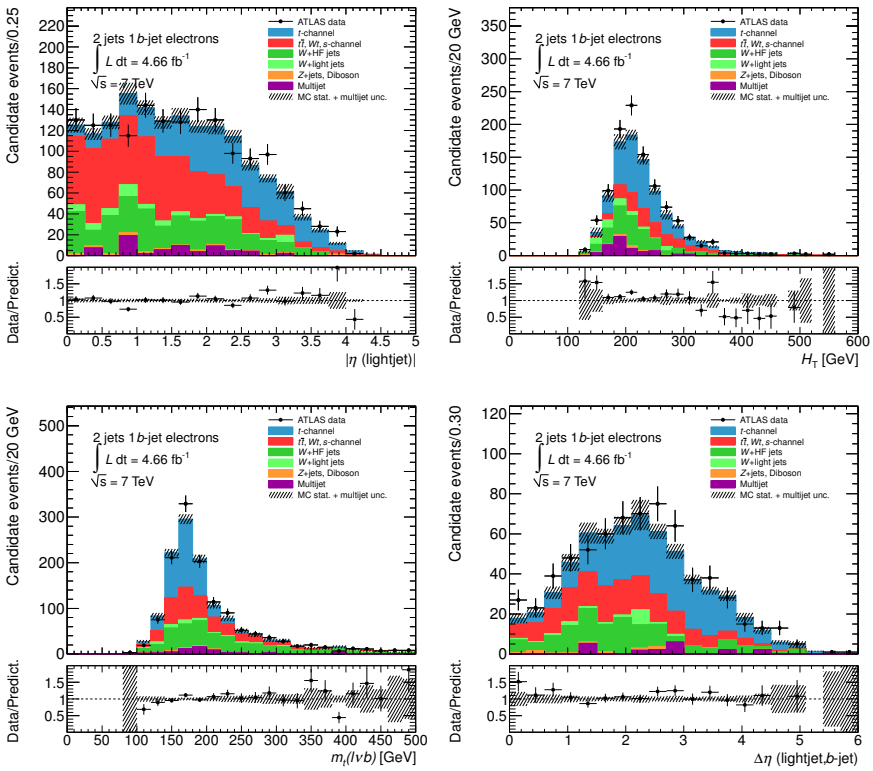

Figure 5.10: *Comparison between data and expectation for the electron channel of the discriminant variables after applying all selection cuts except the one shown.*

Background modelling

The measured dataset is contaminated with background processes that mimic the experimental signature of t-channel single top quark events. These processes can be divided into four groups:

- **top quark pair**, ***s*-channel** and ***Wt*-channel**: background processes that include the production of top quarks via strong interaction and other channels of electroweak production.
- ***W*+ jets**: production of a real W boson in association with heavy flavour (W+HF jets, which include $W+b\bar{b}$, $W+c\bar{c}$ and $W+c$) or light (W+LF jets) quark jets.
- ***Z*+jets** and **diboson**: electroweak production of a single Z boson and diboson (WW, ZZ and WZ).
- **Multijet**: events originating from QCD multijet production in which one of the jets is misidentified as a lepton ('fake leptons') and a mismeasurement creates a large missing transverse energy.

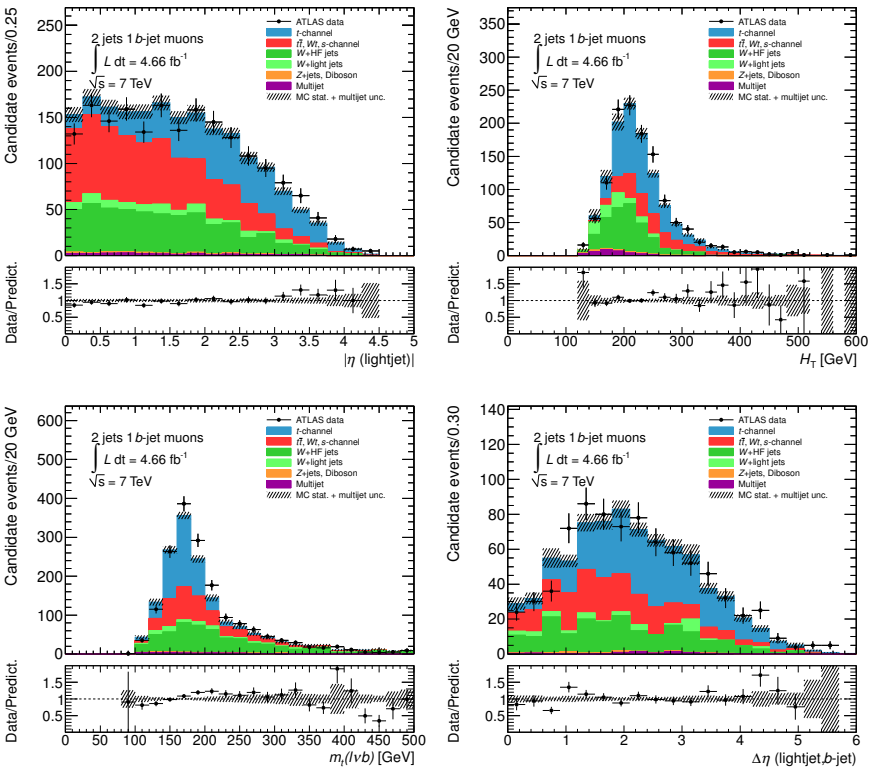

Figure 5.11: *Comparison between data and expectation of the discriminant variables after applying all selection cuts except the one shown for the muon channel.*

Monte Carlo samples are used to model the shapes of the distributions for all the these background processes except for multijets in the muon channel. The list of simulated processes, their predicted cross sections and the Monte Carlo generators and parton shower models used are summarized in Table 5.3.

For the generation of the two single top quark background processes (Wt and s-channel), the POWHEG NLO generator [142] coupled with CT10 [143] set of PDFs and with AUET2 Pythia tune for the parton shower have been used. Samples for the $t\bar{t}$ processes were generated using the same generator and PDF set but a different Pythia tune, Perugia2011 [144]. For these processes involving top quarks additional samples with varied parameters for ISR and FSR were generated using ACERMC to study their impact on the analysis. For the evaluation of the systematic uncertainties due to the $t\bar{t}$ generator modelling, parton shower and hadronisation model, samples were produced with the ALPGEN LO generator [145] and interfaced to HERWIG [129] in connection with the JIMMY underlying event model [130]. All these processes were generated assuming a top quark mass of 172.5 GeV and the corresponding Feynman diagrams are shown in Chapter 2.

Process	Cross section σ [pb]	Generator	K-factor
single top t-channel (signal)	$64.6^{+2.7}_{-2.0}$ ($\text{NNLO}_{\text{approx}}$)	AcerMC+Pythia (LO)	0.87
single top Wt	15.7 ± 1.1 ($\text{NNLO}_{\text{approx}}$)	Powheg+Pythia (NLO)	1.083
single top s-channel	4.6 ± 0.2 ($\text{NNLO}_{\text{approx}}$)	Powheg+Pythia (NLO)	1.079
$t\bar{t}$	167^{+17}_{-18} ($\text{NNLO}_{\text{approx}}$)	Powheg+Pythia (NLO)	1.131
W+jets	10^5 (NLO)	Alpgen+Jimmy (LO)	1.20-1.52
Z+jets	$3 \cdot 10^3$ (NNLO)	Alpgen+Jimmy (LO)	1.25
Diboson	68 (NLO)	Herwig (LO)	1.30-1.60

Table 5.3: *Predicted cross sections for the simulated processes. For single top and top quark pairs samples m_{top}=172.5 GeV is assumed and the theoretical cross sections are calculated at approximate NNLO [51–53, 138]. The W+jets cross section is obtained from MCFM [139] at NLO. For Z+jets backgrounds the inclusive cross sections are calculated to NNLO with FEWZ [140]. The diboson cross sections are normalised to NLO theoretical calculations [141]. The K-factors are used to normalise the simulated samples to higher order cross section calculations.*

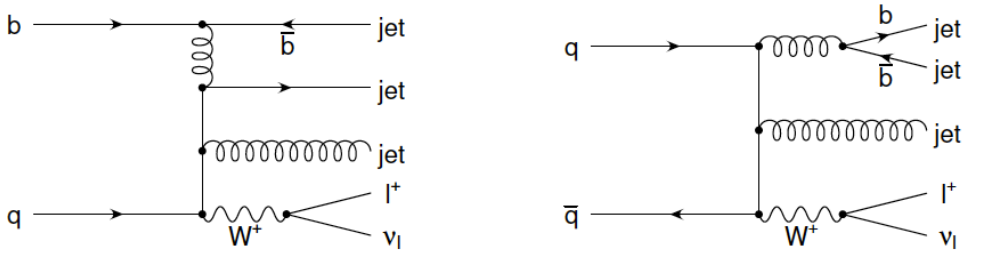

Figure 5.12: *Example Feynman diagrams of W+jets: the Wb production with 2 additional jets (left) and the $Wb\bar{b}$ production with 1 additional jet (right).*

Vector boson (W/Z) production in association with jets have been simulated using the Alpgen generator, separately for light and heavy flavour jets ($b\bar{b}, c\bar{c}, c$) processes. The advantage of using this generator is that it models accurately events with multiple jets which are well-separated and hard. The drawback is the lack of a good description of the parton shower development. Thus, it is interfaced with Herwig for the parton showering and hadronisation. This combination leads to a difficulty in unambiguously separating the components of the event that belong to the hard process from those developing during its evolution. The Feynman diagrams for some of these processes are shown in Figure 5.12 and Figure 5.13-top left. Alpgen generates events at the matrix element level with ISR and FSR, and Herwig approximates the effects of radiation by its showering. Consider an event with $W + n + 1$ jets. The $n + 1$ jets in the final state can be obtained in two ways: n partons in the final state and radiation from one of them during its evolution and the other possibility is that there are $n + 1$ partons in the final state. A matching (or factorisation) scheme is necessary to avoid double counting events. The so-called "MLM" jet-parton matching scheme [145] is employed in Alpgen to remove overlaps between the n and

$n+1$ parton samples. In this method, after parton showering, the final state particles are grouped into jets. Each jet is then matched to a parton if the latter lies within the cone of the jet. Only one parton can be matched to each jet. An event is rejected if it cannot match every parton to a jet, and the number of jets is required to be the same as the number of partons. Exclusive samples are generated with different numbers of partons, then added together after the matching is performed. This removes double counting in the showering. However, there is another problem of double counting when using HERWIG with ALPGEN, and it involves heavy flavour quarks. It is important to separate events with these quarks because their kinematic behaviour is different from the lighter quarks. They can arise in two different ways: they can be created at the matrix element level in a $W + b\bar{b}$ event, or they can arise from gluon splitting in the parton shower from a W+light flavour event. Because there is no difference between these two cases (they have the same Feynman diagram), combining ALPGEN and HERWIG will overestimate the heavy flavour rate. The scheme for removing the overlap, the so-called "heavy flavour overlap removal", divides heavy flavour events into two disjoint sets based on the matching to fully reconstructed jets. Heavy flavour events generated by the matrix element are kept only if the heavy quarks lie in two different jets, while events generated by the parton shower are kept only if the heavy quarks lie in the same jet. This division is motivated by the expectation that quarks from showering will usually be close to their parents, while quarks from the matrix element are more likely to be well separated.

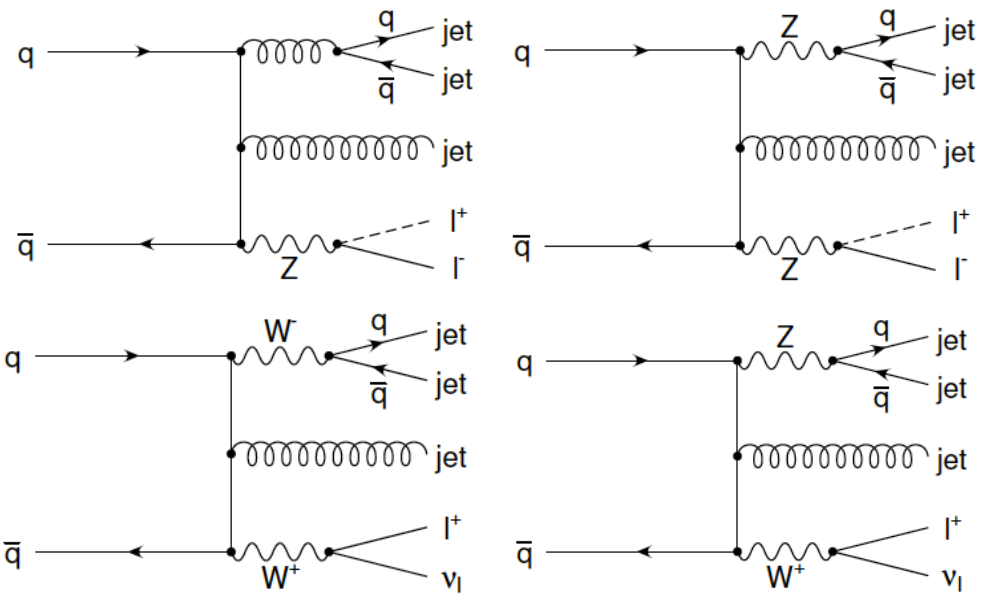

Figure 5.13: *Example Feynman diagrams of Z+jets (top left) and diboson production (top right and bottom) processes. The dashed line indicates the lepton not being identified due to imperfections of the detector acceptance or the event reconstruction.*

The diboson processes WW, WZ and ZZ have been generated using HERWIG. The Feynman

diagrams are presented in Figure 5.13.

In order to model the background coming from multijet, an inclusive PYTHIA sample with a filter for dijet events is used for the electron channel while a generic data sample is used for the muon channel (see Figure 5.14 for Feynman diagrams).

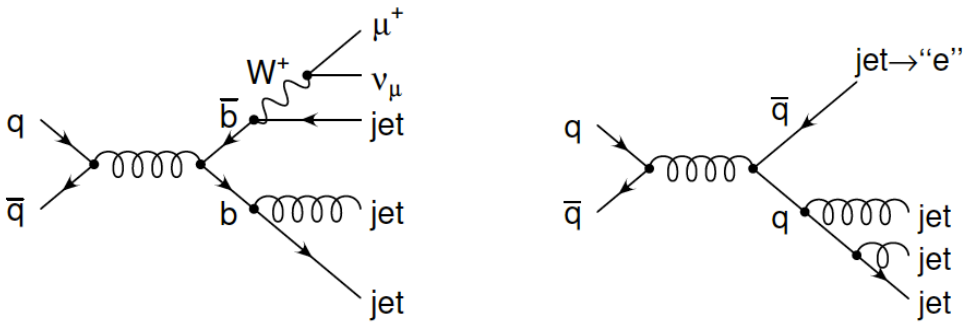

Figure 5.14: *Example Feynman diagrams of the QCD multijet events with an extra lepton coming from the decay from a heavy flavor quark (left) or a misidentified jet (right).*

After the event generation step, all samples were passed through the full simulation of the ATLAS detector [146] based on GEANT4 [147] and were then reconstructed using the same procedure as for collision data. The simulated samples were generated within the ATLAS MC11c production [148], which includes knowledge gained from the data collected in 2011 about alignment, material distribution, underlying event and minimum bias tunings. A list of all used simulated samples can be found in Appendix C. The included tables show all the relevant information for each sample: event generator and parton shower model used, their corresponding theoretical cross section and K-factors[4], and the number of events in each simulated sample. Total cross sections (cross section times K-factor) are used to normalise each simulated sample to the integrated luminosity of 4.66 fb^{-1}, except for W+jets and multijet backgrounds for which the normalisation is determined in-situ as explained in the next sections.

5.4.1 Estimation of the multijet background

Multijet events may pass the event selection if one of the jets is misidentified as an electron or muon. Even though the probability that this happens is very low, due to the extremely large production cross section of multijet events, which is several orders of magnitude higher than the t-channel signal cross section, it is still a significant background. Because this probability depends on the detector configuration and geometry, methods based on data are the most appropriate estimate for the multijet background.

[4]The so-called K-factors are used to normalise the simulated samples to higher order cross section calculations. They are conventionally defined as the ratio between the cross sections at the highest order available and at the order used in the simulated samples.

5.4.1.1 The jet-electron model for the electron channel

The multijet background fraction is determined in the electron channel using a binned likelihood fit to the $E_{\mathrm{T}}^{\mathrm{miss}}$ distribution. The multijet template is obtained from a dijet sample simulated with PYTHIA and the basic concept is to accept a reconstructed jet as a lepton if it has a electron-like signature (see right diagram of Figure 5.14). This method is called jet-electron model [149]. The selection cuts for the 'fake leptons', i.e. the jets, are $E_T > 25$ GeV, $|\eta| < 2.47$, an electromagnetic fraction between 0.8 and 0.95 and at least three reconstructed tracks. The kinematic shapes of all other processes (top quark, W/Z+jets and diboson) are taken from Monte Carlo simulation samples. The QCD multijet normalization is determined in the low $E_{\mathrm{T}}^{\mathrm{miss}}$ region where QCD multijet events are expected to be dominant. The fit is performed after applying the single top quark t-channel event preselection cuts, including the $m_{\mathrm{T}}(W) > 30$ GeV cut, but removing the $E_{\mathrm{T}}^{\mathrm{miss}}$ cut. Two separate electron η regions are fitted: central ($|\eta| < 1.37$) and forward ($1.52 < |\eta| < 2.47$). From these fits, the multijet fraction in the region of $E_{\mathrm{T}}^{\mathrm{miss}} > 30$ GeV is determined (see sketch in left side of Figure 5.15). The fitted $E_{\mathrm{T}}^{\mathrm{miss}}$ distribution is shown in the right plot of Figure 5.15 and one can see a good description of the data after performing the likelihood fit. The estimates of multijet background at preselection level are shown in Table 5.4. The expected number of events after all final selection cuts (see Section 5.3.4) are derived from these numbers taking into account the selection efficiency.

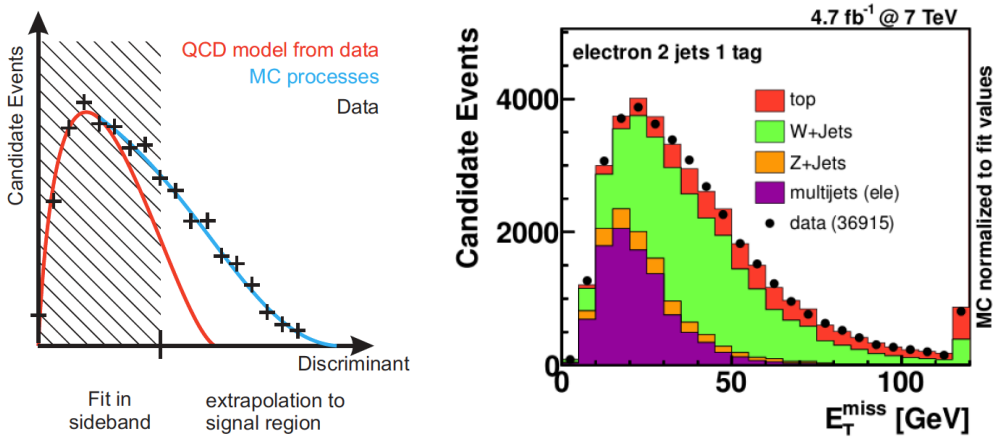

Figure 5.15: *Left: Sketch that shows the idea of the fitting method to estimate the rate of multijet background. A binned likelihood fit is performed, using the shapes of the jet-electron model and the shapes of the processes containing real leptons taken from Monte Carlo simulations. Both shapes are fitted in a sideband (QCD-enriched sample) to the data distribution of a discriminant variable, in this case* $E_{\mathrm{T}}^{\mathrm{miss}}$. *Right: Fit result for the electron channel [100].*

5.4.1.2 The matrix method for the muon channel

In the muon channel, the multijet background is estimated using the 'matrix method' whereby the sample of data events that pass the full selection criteria, except for the isolation requirement,

Lepton	Technique	η region	Multijet events	Multijet fraction
Electron	Jet-Electron model	central	664 ± 332	6.0%
		forward	426 ± 213	11.5%
Muon	Matrix Method	whole	550 ± 275	3.0%

Table 5.4: *Expected number of multijet background events at preselection level for both the electron and muon channel estimated by the jet-electron model and matrix method respectively. A systematic uncertainty of 50% is assumed on the multijet rate.*

is compared before and after its application. This distinguishes a 'loose' from a 'tight' sample in which the number of events can be written as:

$$\begin{aligned} N^{loose} &= N^{loose}_{real} + N^{loose}_{fake} \\ N^{tight} &= N^{tight}_{real} + N^{tight}_{fake} = \epsilon_{real} N^{loose}_{real} + \epsilon_{fake} N^{loose}_{fake} , \end{aligned} \tag{5.4}$$

The samples obtained before and after isolation can be defined in terms of a QCD multijet (fake) and non-QCD multijet (real) component. The two unknown ingredients in the above equation are N^{tight}_{real} and N^{tight}_{fake} which are the number of real and fake lepton events passing the tight selection requirements, respectively. By solving the two equations, one get the number of QCD multijet events:

$$N^{tight}_{fake} = \frac{\epsilon_{fake}}{\epsilon_{real} - \epsilon_{fake}} (N^{loose} \epsilon_{real} - N^{tight}) \tag{5.5}$$

The efficiency $\epsilon = N^{tight}/N^{loose}$ is different for real and fake leptons:

$$\epsilon_{real} = N^{tight}_{real}/N^{loose}_{real} \qquad \epsilon_{fake} = N^{tight}_{fake}/N^{loose}_{fake} \tag{5.6}$$

These efficiencies are obtained from dedicated control samples enriched in either real lepton events (containing mainly W and Z bosons decaying leptonically) or fake lepton events (mainly QCD multijet events) for different ranges of the muon $|\eta|$ phase space (see Figure 5.16). ϵ_{real} is estimated in a signal-muon dominated data sample such as $Z \rightarrow \mu\mu$ events with the tag-and-probe method [103]. ϵ_{fake} is measured from data in a multijet-enriched region where $m_{\mathrm{T}}(W) < 20$ GeV and $E^{\mathrm{miss}}_{\mathrm{T}} + m_{\mathrm{T}}(W) < 60$ GeV and using only muons with a high significance of the transverse impact parameter d_0 relative to the primary vertex. This measurement assumes that the multijet background to top quark production in the muon channel is dominated by heavy flavour jets which produce muons with a large impact parameter (see left diagram of Figure 5.14). By counting the tight and loose muons with d_0 significance larger than a given threshold x, a loose-to-tight efficiency function can be defined as:

$$\epsilon(x) = \frac{\sum_{d_0^{sign} > x} N^{tight}}{\sum_{d_0^{sign} > x} N^{loose}} \tag{5.7}$$

and it can be parametrised as:

$$f(x) = a e^{-bx^2} + cx + d \tag{5.8}$$

assuming that the contributions to $\epsilon(x)$ from prompt and non-prompt muons can be approximated by a Gaussian and a linear function, respectively. The asymptote constant d is considered as the fake efficiency [150].

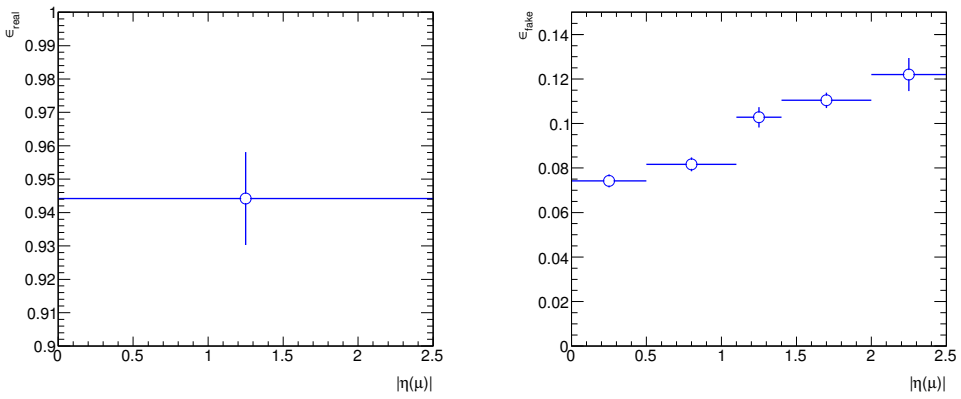

Figure 5.16: *Efficiencies for real (left) and fake (right) muons. ϵ_{real} is independent of the muon $|\eta|$ while ϵ_{fake} has a notable dependency.*

To calculate the contribution of the multijet background in the various control and signal datasets, each event of the corresponding 'loose' data sample is reweighted according to the quality (loose or tight) of the selected lepton by using the following formula:

$$\begin{aligned} w_{tight} &= -(1-\epsilon_{real})\epsilon_{fake}/(\epsilon_{real}-\epsilon_{fake}) \\ w_{loose} &= \epsilon_{real}\epsilon_{fake}/(\epsilon_{real}-\epsilon_{fake}) \end{aligned} \tag{5.9}$$

Table 5.4 shows the estimate of multijet background at preselection level using this method for the muon channel. For the final event selection, the QCD multijet rates are also directly determined from reweighted data and the obtained event yields are listed in Section 5.6.

5.4.1.3 Systematic uncertainties of the multijet background

In the electron channel, the systematic uncertainty for the normalisation is evaluated by dividing the jet-electron data sample into a high pile-up sample and a low pile-up sample based on the number of primary vertices. The method is applied to both subsamples separately to gauge the effect of pile-up on the procedure and from the comparison a systematic uncertainty of 50% is assigned on the multijet rate. In the muon channel, the systematic uncertainty was evaluated by varying the real/fake efficiencies within their uncertainties, and a 50% normalisation uncertainty was obtained.

5.4.2 Estimation of the W+jets background

The production of W+jets has a large production cross section at LHC ($\sigma_{W+jets} \sim 10^5$ pb). As discussed before, the shape of the distributions for this background is obtained from simulated samples using ALPGEN+HERWIG after removing double-counting. The predictions are multiplied by K-factors to correct the cross sections to the NLO predictions provided by theory. The K-factor for the $W+b\bar{b}$, $W+c\bar{c}$ and W+light jet samples is 1.20, and for the Wc+jets process is scaled by a factor of 1.52 obtained from MCFM [139]. The cross sections and K-factors for all simulated samples are given in Appendix C (see Table C.2).

In-situ data driven techniques are used to estimate the different flavour composition and the overall normalisation. This is done in a control region dominated by W+jets events, by selecting events that pass the preselection cuts except the requirement in the number of jets and to pass the top quark mass veto, i.e. the mass of the reconstructed top quark is required to be outside the expected value (that is m_t <150 GeV or m_t >190 GeV). The sample is classified in four regions with one or two jets before and after requiring b-tagging: '1-jet pretag', '1-jet tag', '2-jets pretag' and '2-jets tag'. Both the overall normalisation and flavour fraction scale factors (denoted by K_i being i the flavour) are determined simultaneously and for different jet multiplicities in the following way:

- The overall normalisation factor is obtained by computing the ratio of the number of data events with all the background to the W+jets signal subtracted over the number of Monte Carlo W+jets events. It is determined for each jet bin using:

$$\frac{N_{W+jets,Data}}{N_{W+jets,MC}} = \frac{N_{data} - N_{EWK} - N_{top} - N_{QCD}}{N_{W+jets,MC}} \,. \tag{5.10}$$

- The flavour fractions ($W+b\bar{b}$, $W+c\bar{c}$, $W+c$ and W+light jets) are derived using total event yields in the '1-jet' and '2-jets' bins of the 'pretag' and 'tag' data sample. A numerical fit, using MINUIT, is performed to obtain them.

A detailed explanation on the method can be found in Appendix D. The total W+jets scale factor for each flavour component is the product of the overall normalization and the corresponding flavour fraction scale factors. Values obtained for events with 2 jets are shown in Tables 5.5 and 5.6 with their respective statistical and systematic uncertainties.

Electron	Muon
0.992 ± 0.004 (stat.) ± 0.183 (syst.)	1.031 ± 0.003 (stat.) ± 0.156 (syst.)

Table 5.5: *Overall W+jets normalisation factors in the 2-jets bin for the electron and muon channel individually with the statistical and systematic uncertainties.*

The difference between the flavour fractions for electrons and muons is understood as coming from the different selection requirements and the different multijet background contribution for each channel. The latter is quite different in both channels, and it is one of the largest systematic

	Electron	Muon
$K_{bb} = K_{cc}$	1.135 ± 0.112 (stat.) ± 0.575 (syst.)	1.413 ± 0.086 (stat.) ± 0.668 (syst.)
K_c	1.423 ± 0.087 (stat.) ± 0.343 (syst.)	1.236 ± 0.071 (stat.) ± 0.271 (syst.)
K_{light}	0.887 ± 0.002 (stat.) ± 0.048 (syst.)	0.890 ± 0.002 (stat.) ± 0.043 (syst.)

Table 5.6: *W+jets flavour fraction scale factors in the 2-jets bin for the electron and muon channel individually with the statistical and systematic uncertainties.*

to this method (see Tables D.1 and D.2 of Appendix D). The fractions are very sensitive to these differences since the method assumes that the sum of the four fractions for each channel is equal to unit. Despite these discrepancies in the flavour fractions, the scale factors are still compatible.

To evaluate the uncertainty of the method, samples which include each of the systematic variations (described in Section 5.8) are used to recompute the overall normalisation and flavour fractions (e.g. for the uncertainty on jet energy scale, samples with jet energy scale up and down within 1σ are used). In this way a different set of values for the scale factors are obtained for each systematic source as shown in Appendix D.

5.5 Distributions in control regions

At preselection level, the sample is dominated by $t\bar{t}$ and W+jets backgrounds. Apart from this control region, other two background enriched regions are studied to ensure a good modelling and understanding of the backgrounds before the signal region is examined. The following three control regions are used:

- **Preselection control region:** Events passing the preselection cuts, including the requirement of having only two jets (fraction of signal events: 12%, W+jets: 45% and $t\bar{t}$ 28%).
- **Top quark pair enriched control region:** Events with exactly four jets and passing the preselection cuts together with the final selection top quark mass and H_{T} cuts are used to define the top quark pair enriched control region. In this region, the fraction of $t\bar{t}$ events is around 84% and the signal contamination is less than 4%.
- **W+jets enriched control region:** To define the W+jets control region, events with exactly two jets passing the preselection cuts and the top quark mass veto ($m_t < 150$ GeV or $m_t > 190$ GeV) are selected. The fraction of W+jets events is above 50% and the signal contamination is below 8%.

Figures 5.17-5.18 show the data/expectation comparison for some basic kinematic distributions such as the missing transverse energy and the transverse mass of the reconstructed W boson for the three control regions for electron and muon channels. The multijet and W+jets background contribution have been estimated using data driven methods in both channels, as explained before. The hatched band indicates the statistical uncertainty from the simulated samples as well as the multijet background normalisation uncertainty; these uncertainties are added in quadrature. Overall, these kinematic distributions show a good data/expectation agreement.

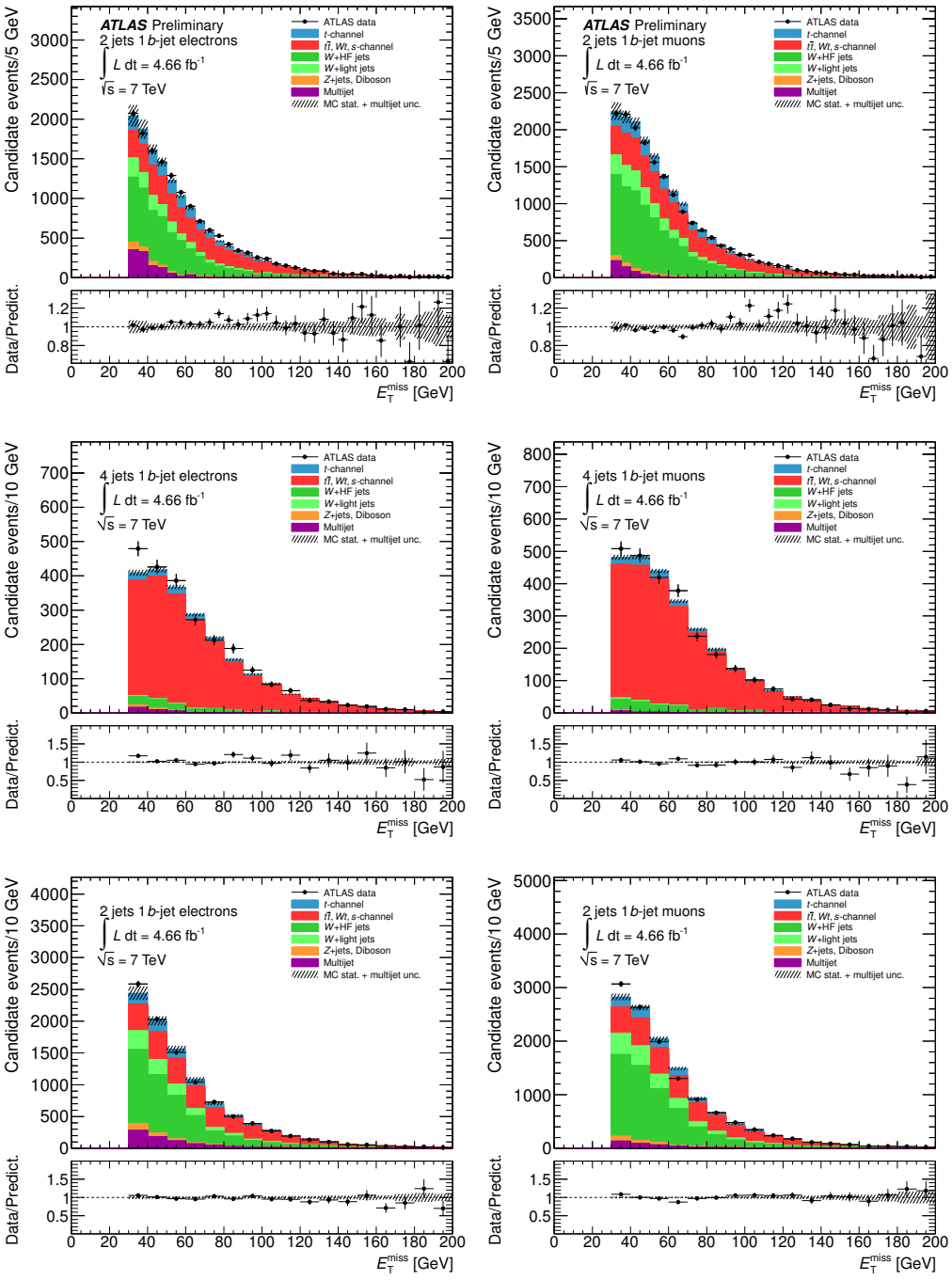

Figure 5.17: *$E_{\mathrm{T}}^{\mathrm{miss}}$ distributions for the different control regions for the electron (left) and muon channel (right): preselection (top), top quark pair (middle) and W+jets (bottom) enriched regions.*

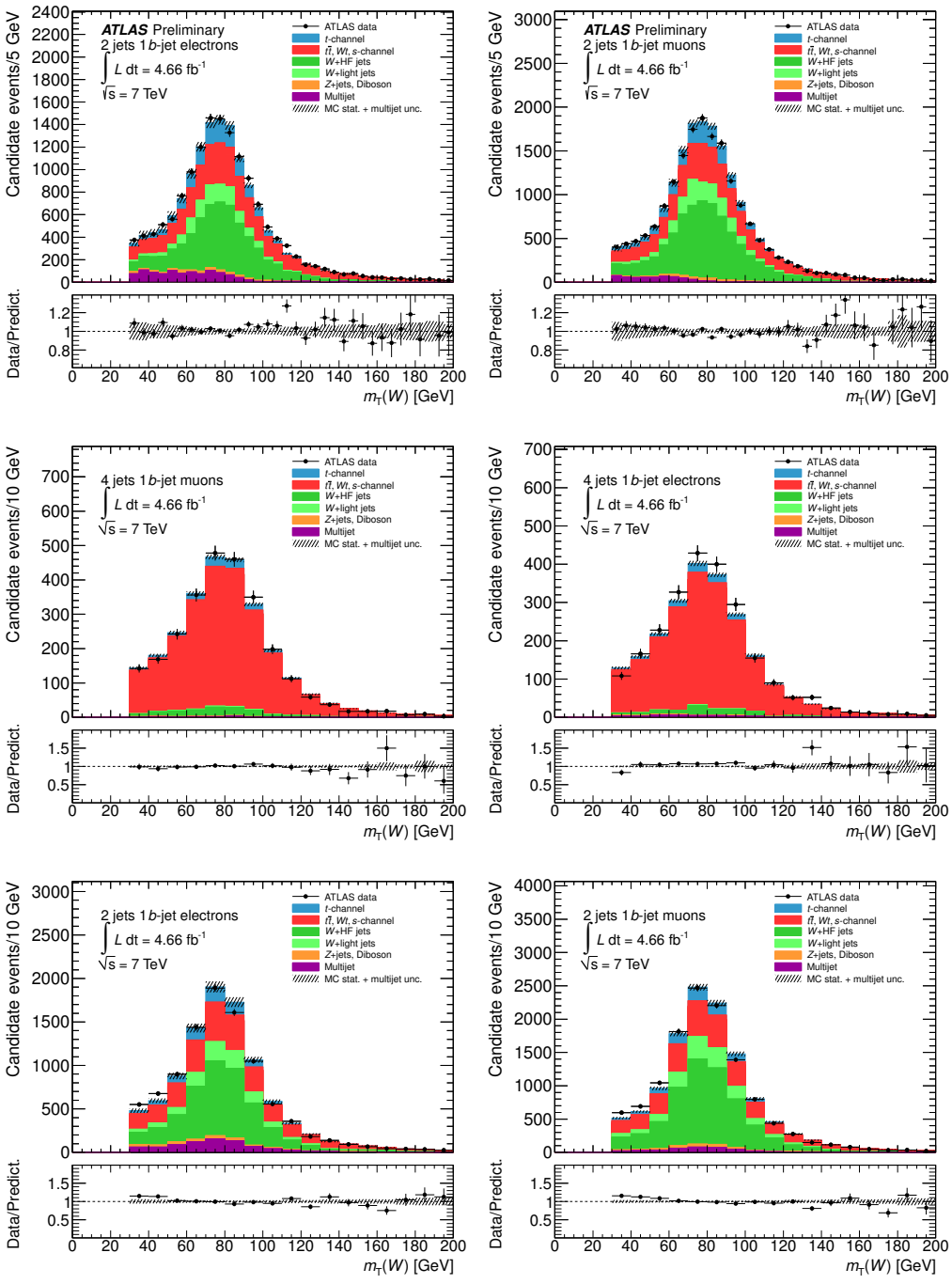

Figure 5.18: *$m_T(W)$ distributions for the different control regions for the electron (left) and muon channel (right): preselection (top), top quark pair (middle) and W+jets (bottom) enriched regions.*

Angular distributions to probe the *Wtb* vertex

As explained in Chapter 2, several angular distributions can be defined in single top quark *t*-channel events to probe the *Wtb* vertex. Although the aim of this analysis is to measure the $A_{\mathrm{FB}}^{\mathrm{N}}$ asymmetry from the $\cos\theta^{\mathrm{N}}$ distribution, the data/expectation agreement for the different distributions is checked in the different control regions. The following angles are defined between the final state objects:

- $\theta^{\mathbf{N}}$: angle between the normal direction N and the lepton in the W boson rest frame
- $\theta^{\mathbf{T}}$: angle between the transverse direction T and the lepton in the W boson rest frame
- θ^{*}: angle between the W boson momentum in the top quark rest frame and the lepton in the W boson rest frame
- $\theta^{\mathbf{X}}$: angle between the top spin direction $\vec{s}_t$ (in the t-channel given by the light jet momentum) and the lepton, both in the top quark rest frame
- $\theta^{\mathbf{W}}$: angle between the $\vec{s}_t$ direction (light jet momentum) and the W boson, both in the top quark rest frame

Figures 5.19-5.24 show the data and expectation comparisons for the these angular distributions for the different control regions. In general, good agreement is observed between data and prediction. More comparisons between data and expectation in these control regions can be seen in Appendix E.

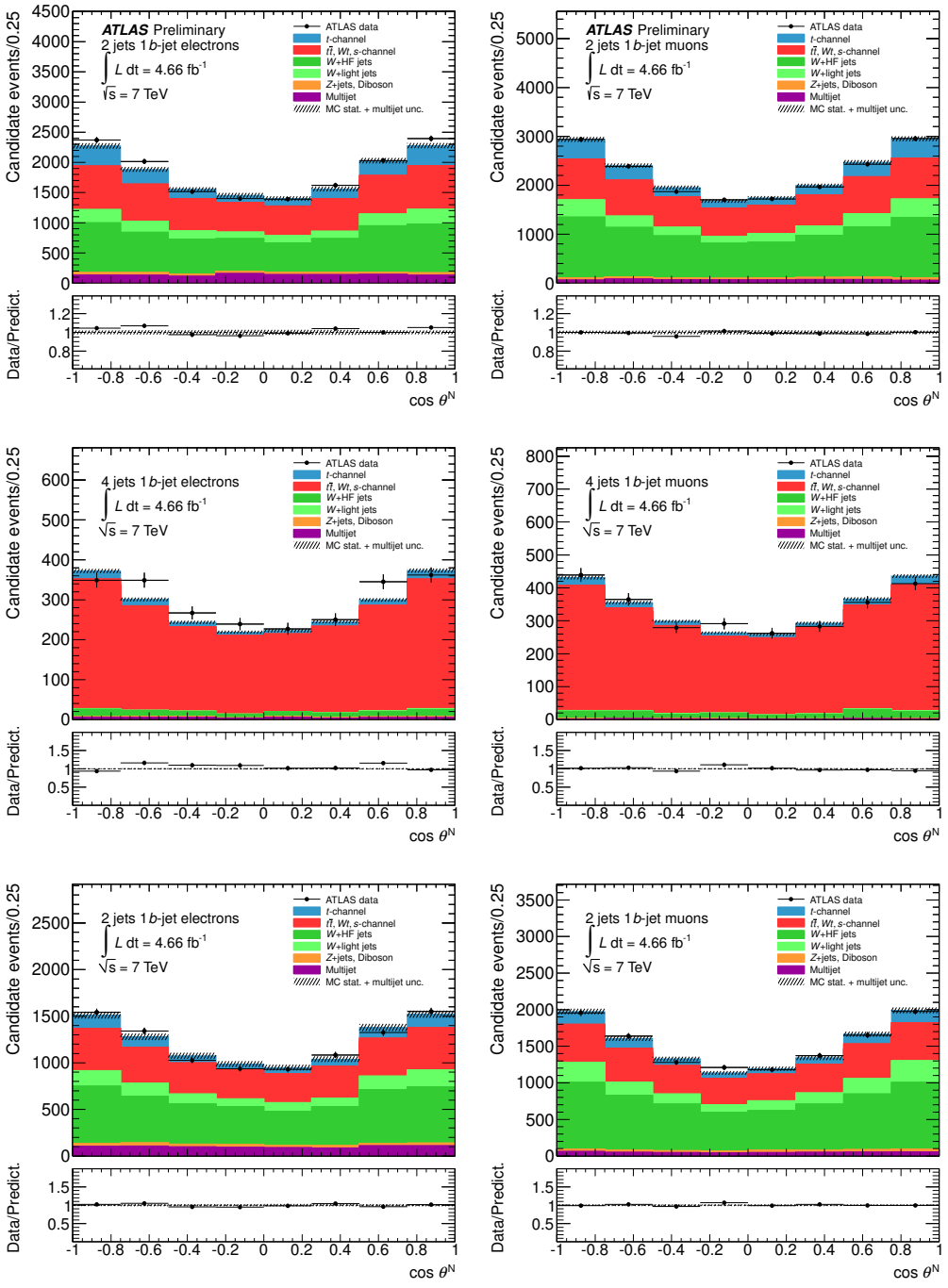

Figure 5.19: *Angular distribution cos θ^N for the different control regions for the electron (left) and muon channel (right): preselection (top), top quark pair (middle) and W+jets (bottom) enriched regions.*

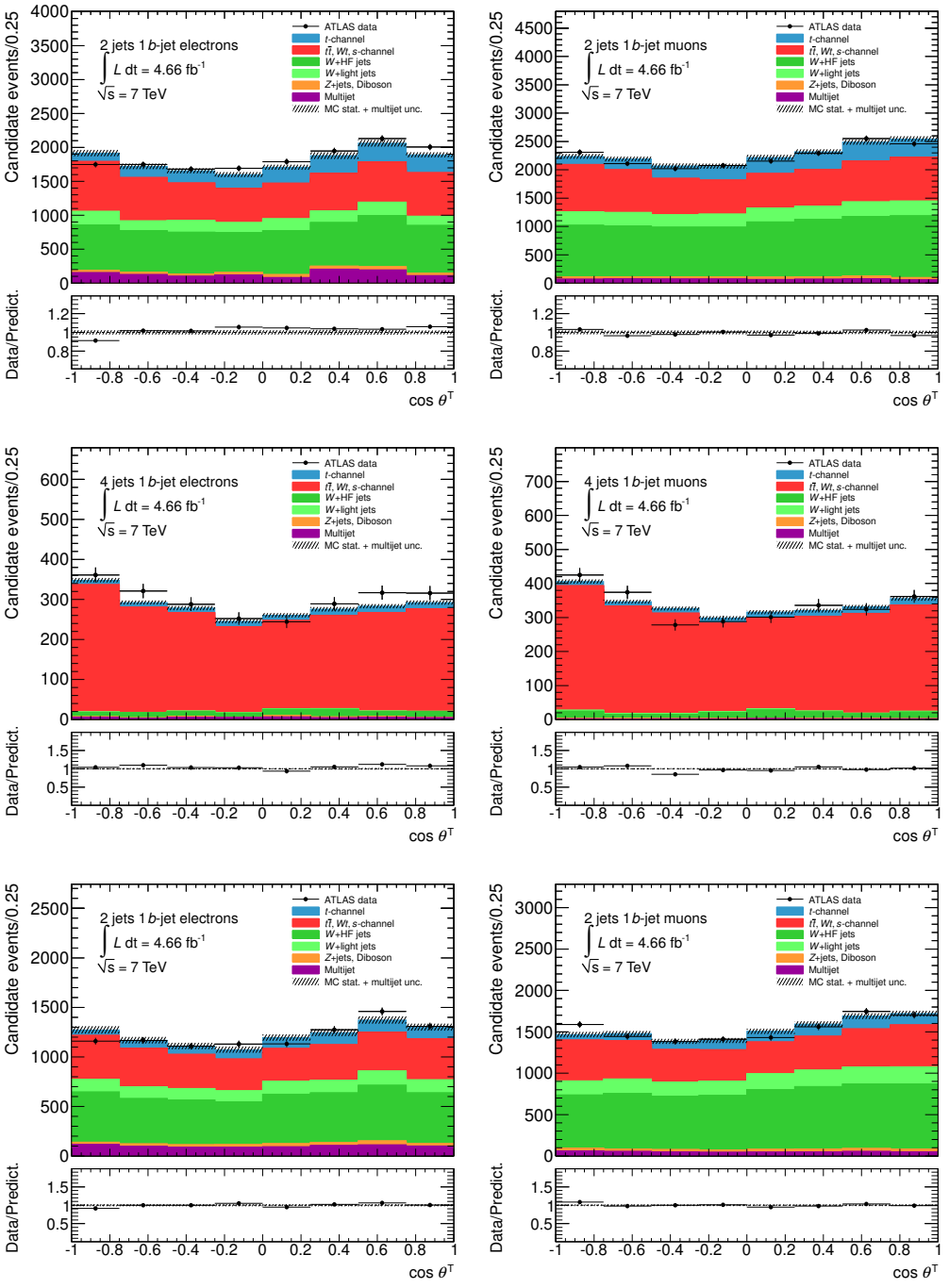

Figure 5.20: *Angular distribution cos θ^T for the different control regions for the electron (left) and muon channel (right): preselection (top), top quark pair (middle) and W+jets (bottom) enriched regions.*

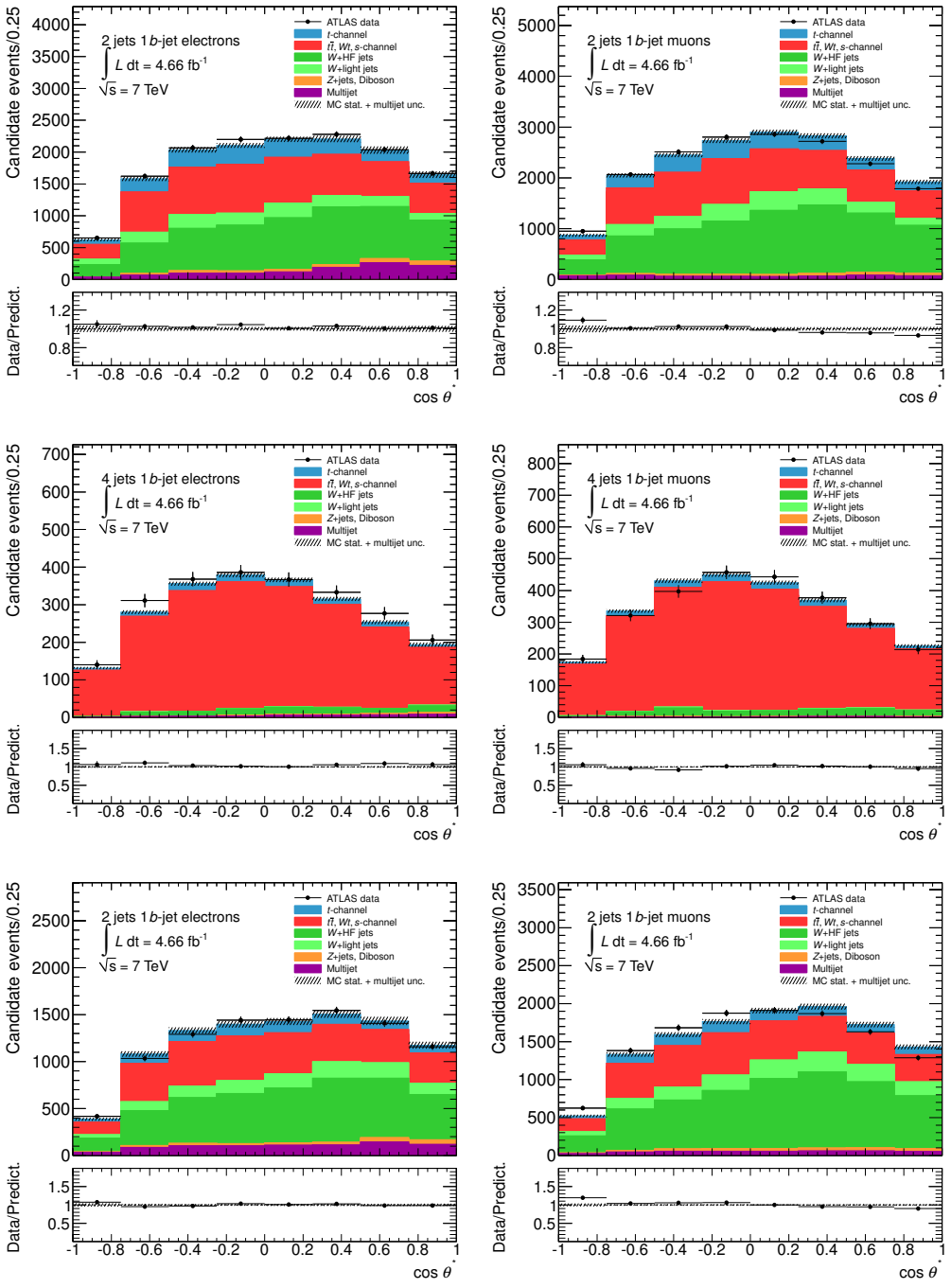

Figure 5.21: *Angular distribution cos θ^* for the different control regions for the electron (left) and muon channel (right): preselection (top), top quark pair (middle) and W+jets (bottom) enriched regions.*

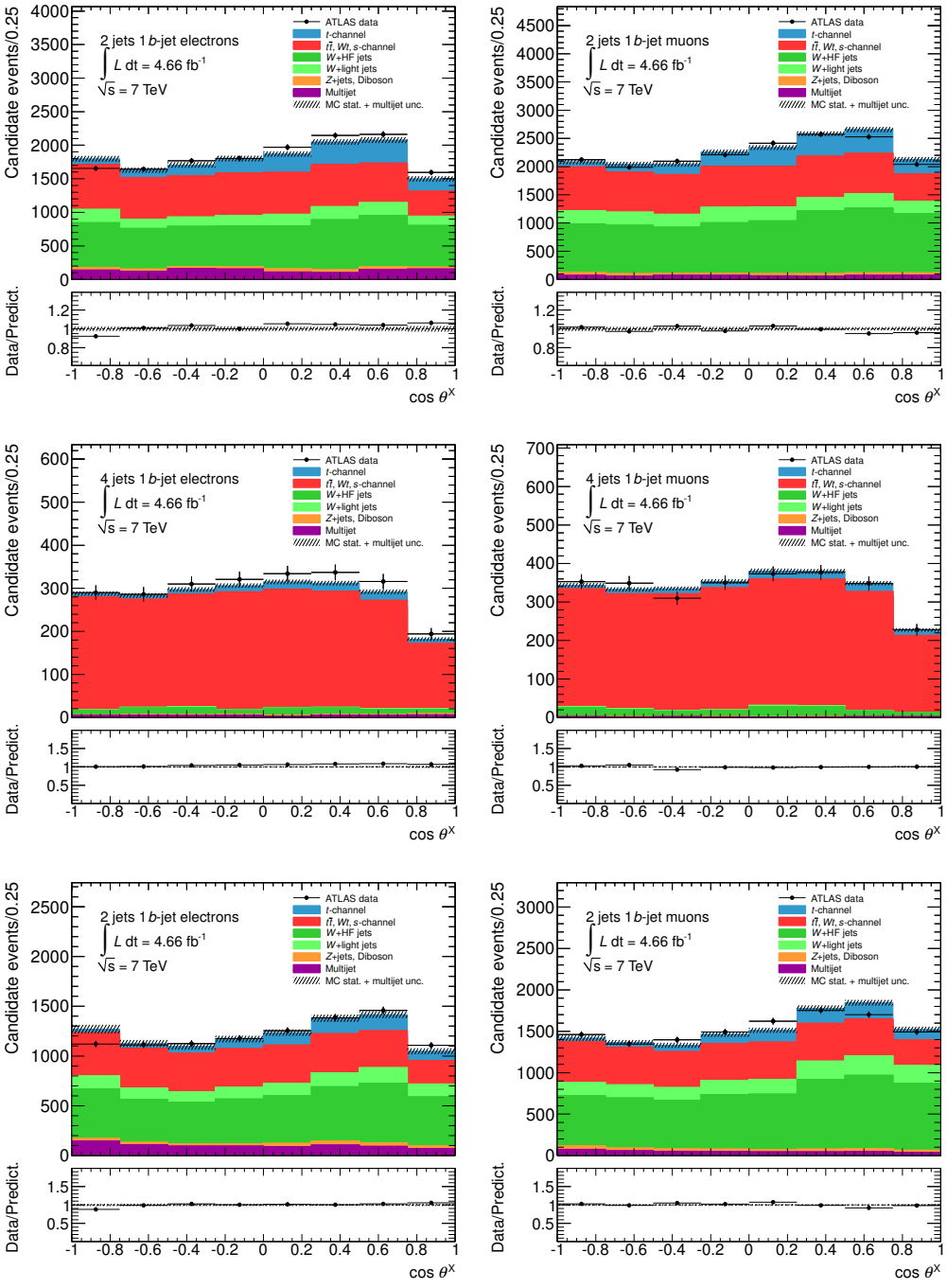

Figure 5.22: *Angular distribution cos θ^X for the different control regions for the electron (left) and muon channel (right): preselection (top), top quark pair (middle) and W+jets (bottom) enriched regions.*

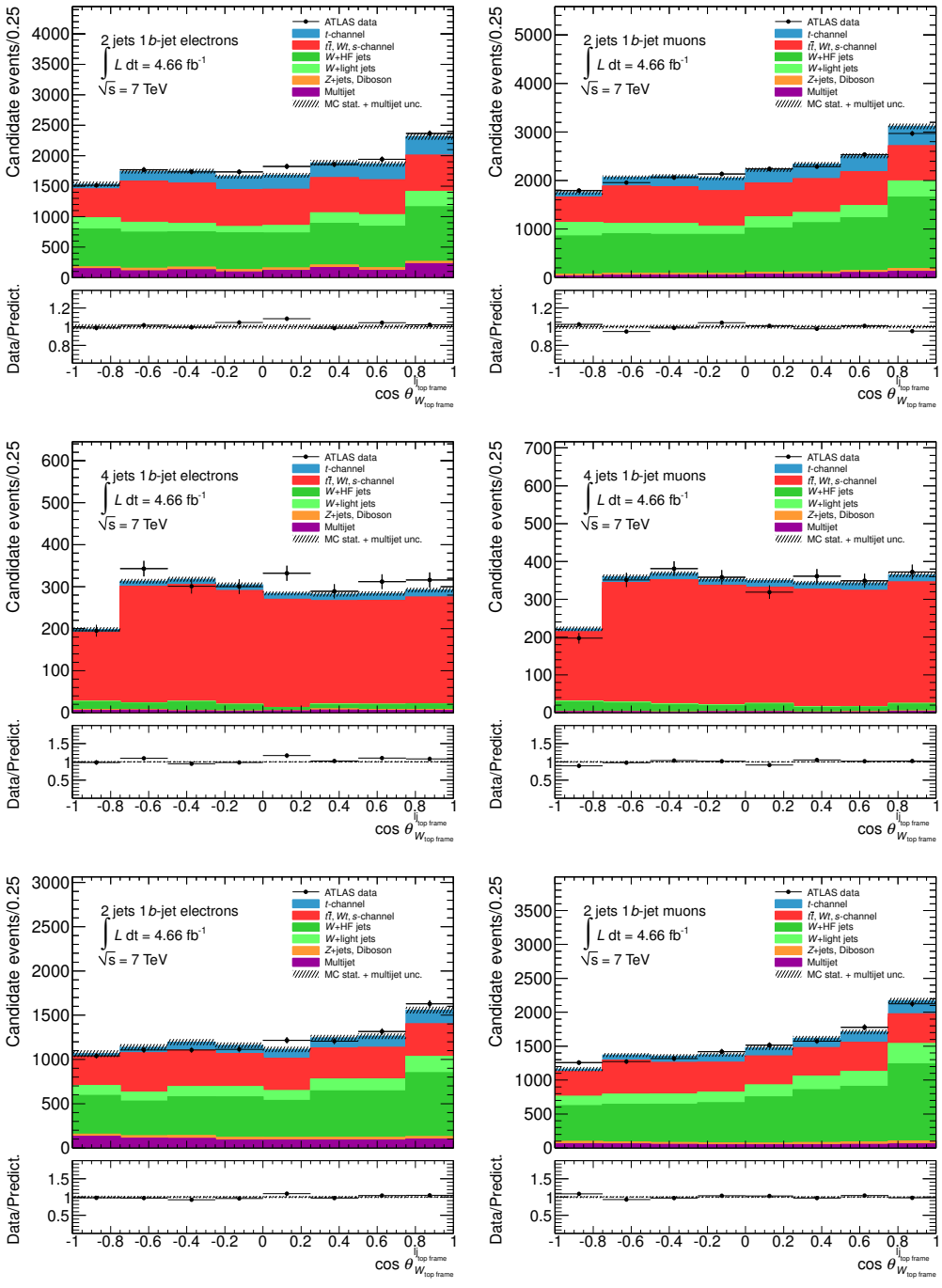

Figure 5.23: *Angular distribution cos θ^W for the different control regions for the electron (left) and muon channel (right): preselection (top), top quark pair (middle) and W+jets (bottom) enriched regions.*

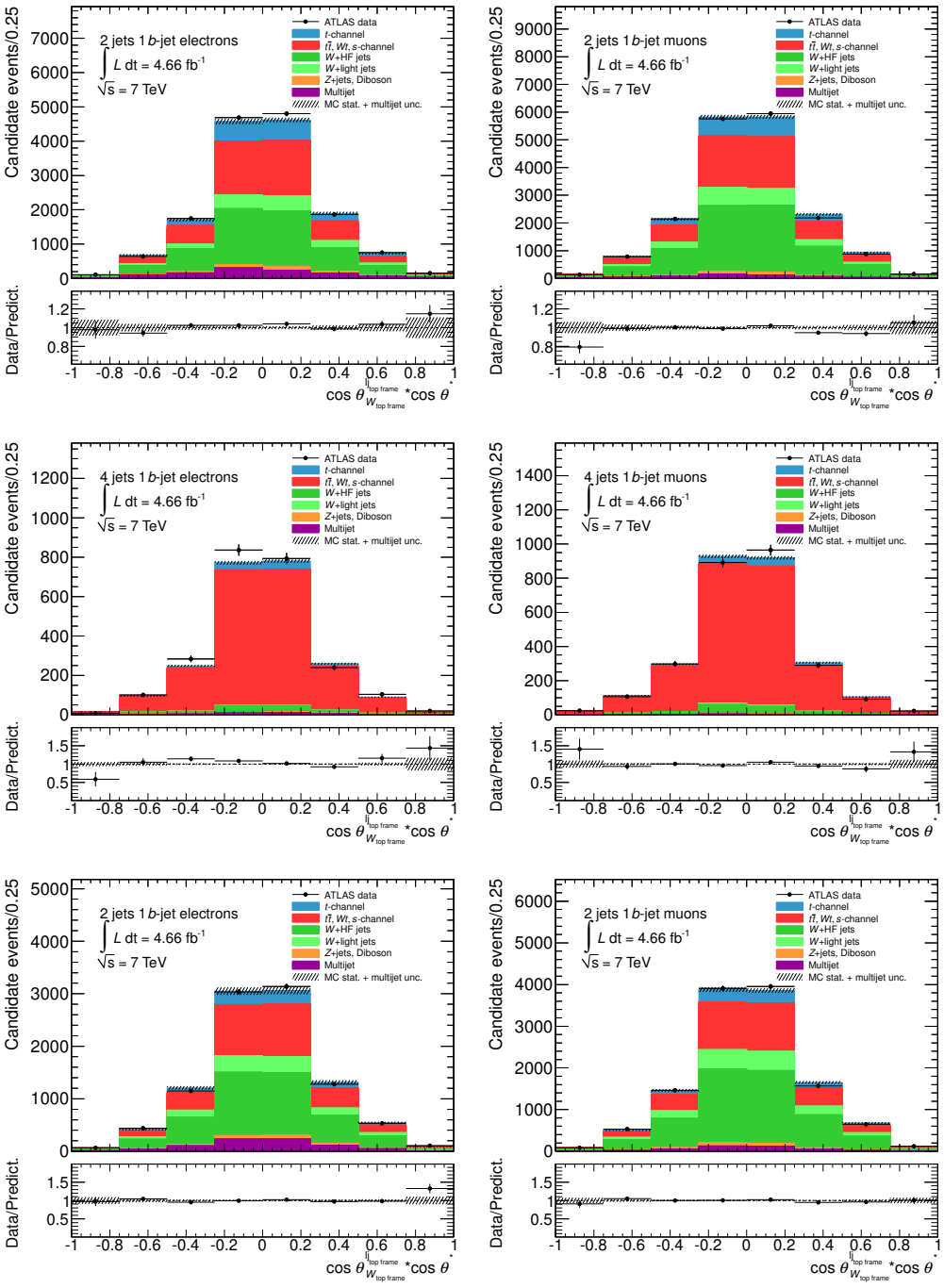

Figure 5.24: *Double angular distribution cos $\theta^W \times$ cos θ^* for the different control regions for the electron (left) and muon channel (right): preselection (top), top quark pair (middle) and W+jets (bottom) enriched regions.*

5.6 Final event selection yields

The number of observed and expected signal and background events for a luminosity of 4.66 fb^{-1} are listed in Table 5.7. The event yields and the signal-to-background ratio in the electron and the muon channels at preselection and selection levels are shown. The predictions are derived from simulated samples and their theoretical cross sections (see Table 5.3 and Appendix C), except for W+jets and multijet background. For single top quark samples, approximate NNLO theoretical cross sections are used [51–53]. The $t\bar{t}$ cross section is normalised to the approximate NNLO[5] predicted value using HATHOR [138]. The diboson cross sections are normalised to NLO theoretical calculations [141]. For Z+jets backgrounds the inclusive cross sections are calculated to NNLO with FEWZ [140]. For W+jets background, the overall normalisation factor and heavy flavour composition factors derived in-situ are applied. For multijet background the normalisation is also determined in-situ as explained before. The statistical uncertainty shown is due to the limited statistics in the simulated samples, except for the uncertainty of multijet production which is derived from the data-driven methods.

	Electron		Muon	
	Preselection	Selection	Preselection	Selection
t-channel	1703 ± 9	262 ± 3	2053 ± 10	318 ± 4
s-channel	114 ± 2	3 ± 0	147 ± 2	5 ± 0
Wt-channel	574 ± 15	14 ± 3	700 ± 17	15 ± 2
Top quark pair	4065 ± 13	114 ± 2	4740 ± 15	140 ± 2
Diboson	121 ± 2	1 ± 0	142 ± 2	2 ± 0
Z+jets	196 ± 9	4 ± 1	190 ± 7	3 ± 1
W+HF jets	5226 ± 57	106 ± 8	7686 ± 65	137 ± 8
W+light jets	1339 ± 58	15 ± 8	1919 ± 70	23 ± 6
Multijet	1090 ± 545	20 ± 10	550 ± 275	6 ± 3
TOTAL expected	14427 ± 644	539 ± 19	18128 ± 292	649 ± 12
ATLAS data	14738	576	17966	691
S/B	0.13	0.95	0.13	0.96

Table 5.7: *Event yields for both the electron (left) and muon (right) channels at preselection and selection level. The predictions are derived from simulated samples together with their theoretical cross section. W+jets contributions are scaled by a factor determined from data and multijet is estimated using data-driven techniques, the jet-electron model for the electron channel and the matrix method for the muon channel. The uncertainties correspond to the statistical uncertainty but for multijet that corresponds to the estimated 50% systematic uncertainty.*

One can notice that the dominant backgrounds are top quark pair and W+jets events. In the preselection control region, dominated by these backgrounds, there is a good agreement between data and prediction. At selection level (signal region), data is above expectation but the normalization difference is within the statistical uncertainties. It is important to point out that at this level the signal-to-background ratio is of ~0.95.

[5] At the time of writing a more accurate calculation at NNLO+NNLL [50] became available and will be used in future analysis.

After applying all selection cuts, the statistics to model the shape of multijet and W+light jets backgrounds is very low and therefore templates are used to properly model them in the angular distribution of interest. For the multijet background, a template obtained from Monte Carlo samples for similar backgrounds such as diboson, Z+jets and multijet itself is built and then normalised to the yields obtained for multijet in the data driven techniques (diboson and Z+jets are not changed). For W+jets, the shape obtained at preselection level is used. Figure 5.25 shows the $E_{\mathrm{T}}^{\mathrm{miss}}$and $m_{\mathrm{T}}(W)$ distributions in the signal region.

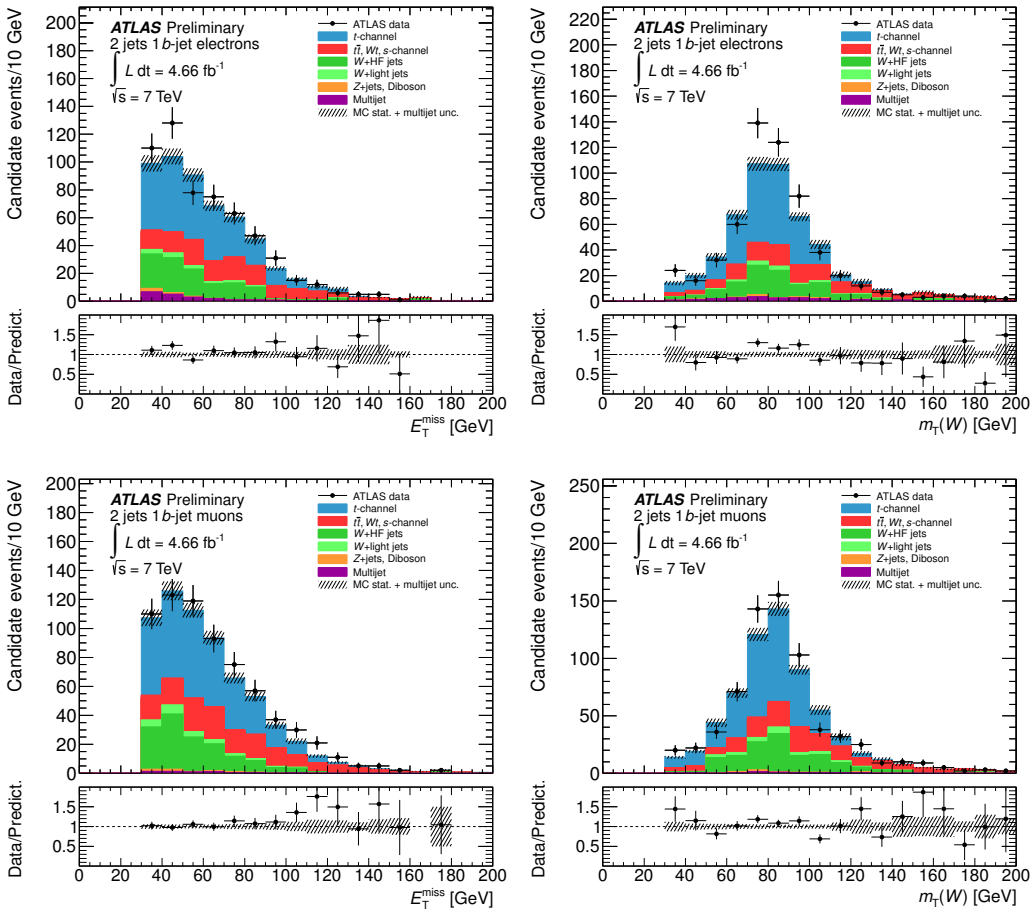

Figure 5.25: *$E_{\mathrm{T}}^{\mathrm{miss}}$(left) and $m_T(W)$ (right) distributions in the signal region (selection level) for the electron (top) and muon (bottom) channel.*

5.7 Measurement of the forward-backward asymmetry $A_{\mathrm{FB}}^{\mathrm{N}}$

The scope of this section is to probe the anomalous coupling g_{R} of the Wtb vertex. As described in Chapter 2, the forward-backward asymmetry $A_{\mathrm{FB}}^{\mathrm{N}}$ is especially sensitive to the imaginary part of the coupling g_{R}. This asymmetry $A_{\mathrm{FB}}^{\mathrm{N}}$ is computed from the angular distribution $\cos\theta^{\mathrm{N}}$ in the signal region shown in Figure 5.26 and the obtained values are shown in Table 5.8 before (raw) and after background subtraction.

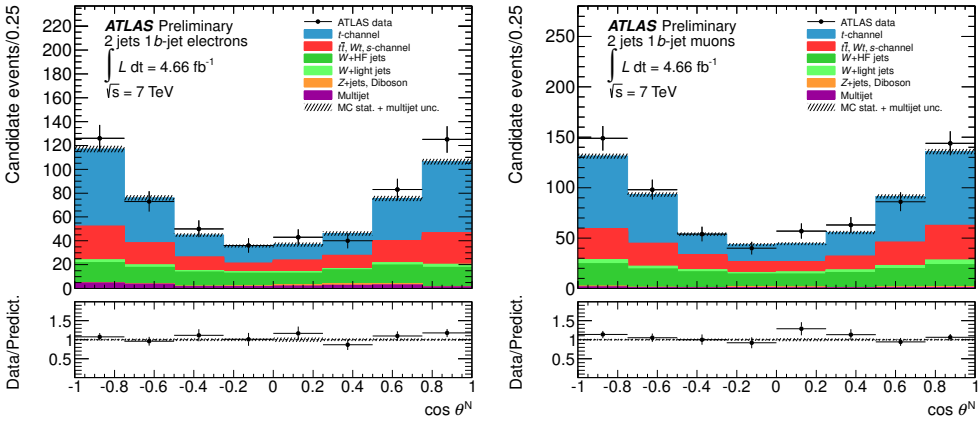

Figure 5.26: *Reconstructed* $\cos\theta^{N}$ *angular distribution obtained at selection level for electron (left) and muon (right) channel. ATLAS data, simulated signal and different background contributions are shown. The uncertainty band includes the statistical uncertainty in the simulated samples except for multijet which shows the systematic uncertainty on normalisation.*

	$A_{\mathrm{FB}}^{\mathrm{N}}$
Electrons (raw data)	0.010 ± 0.042 (data stat.)
Bkg. subtracted	0.018 ± 0.081 (total stat.)
Muons (raw data)	0.013 ± 0.038 (data stat.)
Bkg. subtracted	0.017 ± 0.074 (total stat.)
Combined (raw data)	0.012 ± 0.028 (data stat.)
Bkg. subtracted	0.018 ± 0.055 (total stat.)

Table 5.8: *Raw and after background subtraction* A_{FB}^{N} *values for the electron, muon and combined channel. Only the statistical uncertainties are shown.*

The influence of pile-up conditions on the measured (raw) $A_{\mathrm{FB}}^{\mathrm{N}}$ values has been studied in two regimes: low pile-up and high pile-up. The low pile-up region includes events with less than ten interactions per bunch crossing, while the high pile-up region includes events with ten or more. As shown in Figure 5.27 (left) the low pile-up event selection collects mainly all events from run periods B-K and low pile-up events from periods L-M while the high pile-up event selection

collects mostly events from periods L-M. Figure 5.27 (right) shows the $A_{\mathrm{FB}}^{\mathrm{N}}$ measurements for these two pile-up regimes together with the measurement considering all events. No dependence is observed on different pile-up conditions within the statistical uncertainties.

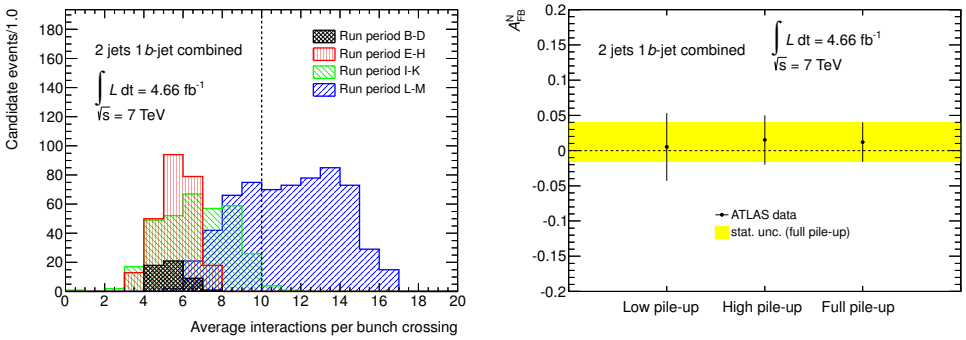

Figure 5.27: *Left: Average interactions per bunch crossing in data at selection level for the combined electron and muon channel. The vertical dash line divides the low pile-up and high pile-up selected regions. Right: A_{FB}^{N} measurements using low pile-up and high pile-up data events together with the measurement using the full pile-up range shown for comparison. The uncertainties are statistical only.*

5.7.1 Distortions of the angular distribution $\cos\theta^{\mathrm{N}}$

The measured distributions are distorted from experimental limitations (i.e. detector resolution, geometric acceptance of the detector, selection of events, etc.). In order to allow a direct comparison of measurements from different experiments, the distributions must be deconvoluted by such effects. This procedure is called 'unfolding' and there are different approaches for that, all based on Monte Carlo simulations to model these effects. Without unfolding, the measurement cannot be compared with the results of other experiments, for which the detector response will in general be different. If the goal is only to compare the result with a theoretical prediction, one can simply modify the prediction to include the distortions of the detector, and this can be directly compared with the measurement. This approach is called 'folding' and is considerably simpler than 'unfolding' the measurement and comparing it with the original (unmodified) theory. However there are cases in which the shape of the predicted distribution is not well known or when comparisons with other experiments are desired, and therefore the use of 'unfolding' techniques are required. With all this, different procedures have been developed (see Ref. [151] for a survey):

- Folding the theoretical distribution
- Bin-by-bin correction factors
- Unfolding by inversion of the response matrix
- Regularized unfolding
- An iterative unfolding method by D'Agostini

In the analysis presented here, the unfolding technique with matrix inversion has been used. The different effects distorting the measured distributions are described below and their impact in the angular distribution $\cos\theta^{N}$ is shown in Figure 5.28.

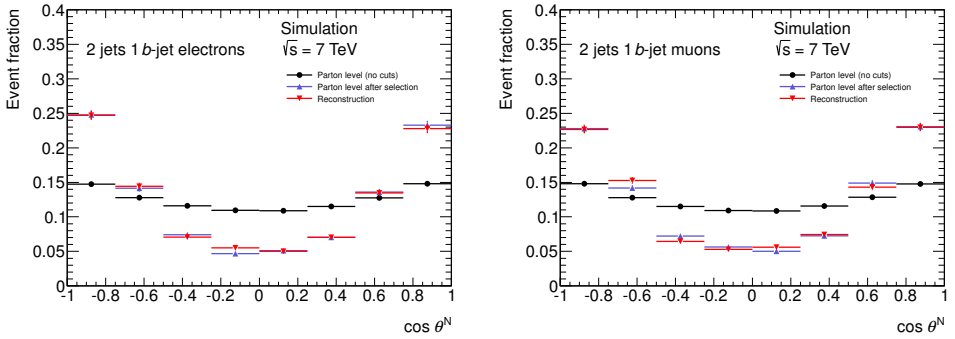

Figure 5.28: *Comparison of the angular distribution* $\cos\theta^{N}$ *for the electron (left) and muon (right) channel obtained for simulated signal events at different stages: using generated objects before and after the event selection and using reconstructed objects for selected events.*

- **Impact of the event selection:** Comparing the $\cos\theta^{N}$ distribution obtained from the generated objects (i.e. partons from the hard process[6]) before and after applying the event selection, one can observe a strong suppression of events in the central region. This is due to the requirement of an isolated lepton. In fact, $\cos\theta^{N} \simeq 0$ means that the angle θ^{N} between the lepton and the normal direction is $\sim\pi/2$; that is, the lepton is in the plane formed by the W momentum and the top quark spin direction. Taking into account that the W boson and the b quark in the top quark rest frame are back-to-back and that the top quark spin direction in the t-channel is given by the momentum of the light jet, one can see that the lepton and the two jets in the event are all in the same plane. Thus, the efficiency is lower in that region when one requires lepton isolation. Indeed this is the reason why the event selection efficiency (ϵ_j) is not flat as a function of $\cos\theta^{N}$, as it can be seen in Figure 5.29 for the combined electron and muon channel.

- **Impact of the event reconstruction:** The shape of the simulated $\cos\theta^{N}$ distribution is also affected by the reconstruction of the final state objects in the detector. Several effects contribute to this deviation: imperfect measurement of physics objects quantities due to limited detector acceptance or inefficiencies, as well as resolution effects due to the reconstruction of the neutrino and the top quark. All these smearing effects lead to the migration of events between different bins in the $\cos\theta^{N}$ distribution. These bin migrations can be described by a matrix M_{ji} (the so-called migration matrix) that translates reconstructed $\cos\theta^{N}$ values in bin i into the corresponding parton level values in bin j and that is equivalent to a detector resolution function. First, a transfer matrix T_{ji} is calculated using simulated t-channel events filling one entry for each event passing the acceptance cuts. The migration matrix M_{ji} is obtained from this transfer matrix, by normalising each row (bin j) to the sum of the entries of all bins j of the truth physical quantity, i.e. to unity.

[6]For Pythia generator, partons from the hard process have status = 3.

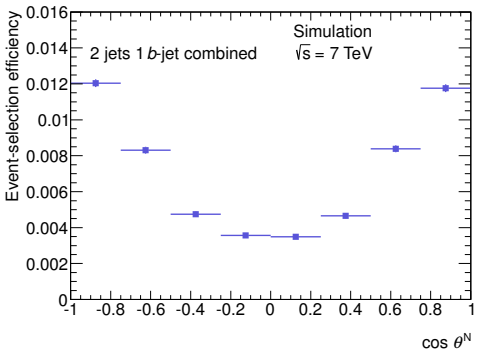

Figure 5.29: *Event selection efficiency as a function of* $\cos\theta^N$.

In this way, the migration matrix M_{ji} gives the probability for a value of the truth (bin j) physical quantity to be reconstructed at another value (bin i).

$$T_{ji} \Rightarrow M_{ji} \text{ ; by construction } \sum_i M_{ji} = 1 \ .$$

The strategy followed to choose the optimal binning is to take the smallest bin size without substantially deteriorating the total uncertainty. A reasonable approach is to require that the bin width corresponds to the average resolution of the corresponding reconstructed distribution. In case of using an 'unfolding' technique, where the migration matrix needs to be inverted, the following items should be taken into account:

- Keep around 68% of the events on the diagonal of the migration matrix.
- Evaluate the condition number[7] since it is an indicative measurement of how much the matrix inversion inflates the error propagation.

5.7.2 Unfolding to parton level

Since the aim is to measure a forward-backward asymmetry, the choice of two bins ($\cos\theta^{\mathrm{N}} < 0$ and $\cos\theta^{\mathrm{N}} > 0$) is reasonable. The obtained 2x2 transfer T_{ji} and migration M_{ji} matrices are shown in Figure 5.30. The $\cos\theta^{\mathrm{N}}$ distribution at parton level is recovered using the following formula:

$$N_i^{\text{data}} = M_{ji}\epsilon_j N_j^{\text{signal, parton level}} + N_i^{\text{bkg}} \ , \tag{5.11}$$

$$N_j^{\text{signal, parton level}} = \frac{M_{ji}^{-1}(N_i^{\text{data}} - N_i^{\text{bkg}})}{\epsilon_j} \ , \tag{5.12}$$

where N_i^{data} is the number of events in data for bin i, N_i^{bkg} is the sum of all expected backgrounds, $N_j^{\text{signal, parton level}}$ is the number of signal events corrected at parton level, ϵ_j is the event selection

[7] The condition number of a matrix, k, is defined as $k = \|M\|\|M^{-1}\|$.

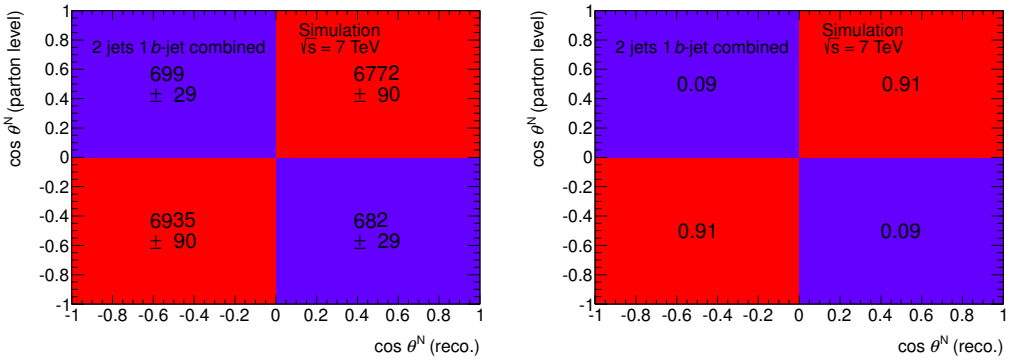

Figure 5.30: *Transfer matrix T_{ji} (left) and migration matrix M_{ji} (right) for the combined channel. The latter is obtained from the former by normalising the sum of the entries in each row.*

efficiency (i.e. acceptance correction) and M_{ji} (M_{ji}^{-1}) the (inverse) migration matrix (i.e. detector resolution correction). A schematic representation of the unfolding procedure can be seen in Figure 5.31.

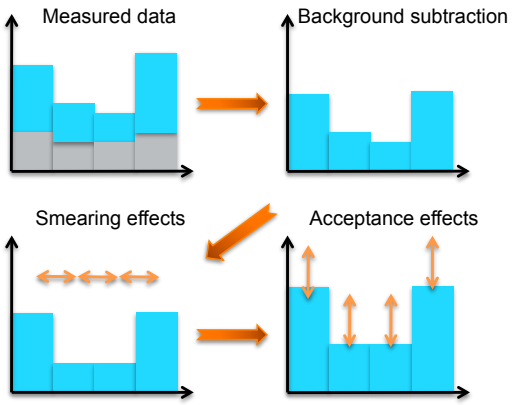

Figure 5.31: *Schematic representation of the unfolding procedure. The acceptance selection affects the number of entries in each bin of the angular distribution while the detector effects lead to the migration of events between different bins.*

The measurement of the asymmetry $A_{\mathrm{FB}}^{\mathrm{N}}$ and the limits for g_{R} coupling are obtained for the combined electron and muon channel although, for completeness, intermediate steps are presented separately for both channels in Appendix F. Figure 5.32 shows the angular distribution measured at reconstructed level for the combined channel and using two bins, from which the asymmetry $A_{\mathrm{FB}}^{\mathrm{N}}$ is computed.

Before attempting to unfold a measured distribution, the procedure needs to be validated. Two

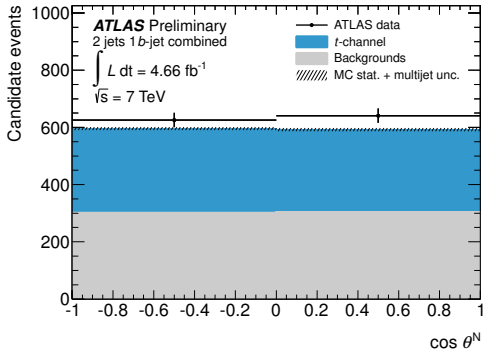

Figure 5.32: *Angular distribution for the combined electron and muon channel. ATLAS data, Monte Carlo signal and the merged backgrounds (red) are shown. Uncertainties are statistical and for multijet include also the 50% systematic uncertainty on normalisation.*

checks have been performed using signal simulated samples: a closure test and a linearity test.

5.7.2.1 Closure test

A closure test has been performed to check that the procedure is able to reproduce the distribution at generator level. It consists basically in a folding of the simulated signal distribution followed by an unfolding. Then the deviation of the unfolded $A_{\mathrm{FB}}^{\mathrm{N}}$ value to the input asymmetry value is compared. The test is done splitting the signal Monte Carlo sample in two statistically independent sets of events: half of the events are used to derive the acceptance efficiency and migration matrix, and the other half to obtain the angular distribution that needs to be unfolded. The different between the $A_{\mathrm{FB}}^{\mathrm{N}}$ derived from the unfolded distribution and the generated value is found to be 0.003 ± 0.010, i.e. they are compatible within statistical uncertainties.

5.7.2.2 Linearity test

In addition, a linearity test has been performed in order to probe that asymmetry values deviating from the SM prediction (i.e. from zero) could be measured correctly. These checks are performed with samples of single top quark t-channel events with different (non-zero) values of $A_{\mathrm{FB}}^{\mathrm{N}}$ generated with Protos [137]. The generated $A_{\mathrm{FB}}^{\mathrm{N}}$ values and the corresponding values of the coupling $Im(g_{\mathrm{R}})$ (see Equation 2.28) are shown in Table 5.9. One can see that the top quark polarisation P does not differ too much from the SM prediction ($P \sim 0.9$) for the simulated samples while they have different values of $A_{\mathrm{FB}}^{\mathrm{N}}$. For each sample, 500k events have been generated.

A reweighting technique has been used to check that the method is sensitive to non-zero values of $A_{\mathrm{FB}}^{\mathrm{N}}$. By comparing SM and non-SM samples at generator level, one can obtain weights to go from SM to non-SM $A_{\mathrm{FB}}^{\mathrm{N}}$ values, as can be seen in Figure 5.33. Then the SM angular distribution at reconstructed level is reweighted with these weights and the reweighted distributions are assumed to be the reconstructed non-SM. The standard unfolding procedure (SM migration matrix and event-selection efficiency) is applied and the input and unfolded asymmetry are com-

Coupling configuration		P	$A_{\mathrm{FB}}^{\mathrm{N}}$
$Im(g_{\mathrm{R}})$	$Re(V_{\mathrm{L}})$		
0.000	1.0000	0.889 ± 0.002	0.000 ± 0.002
+0.094	0.9931	0.882 ± 0.002	+0.050 ± 0.002
-0.094	0.9931	0.882 ± 0.002	-0.050 ± 0.002
+0.230	0.9581	0.728 ± 0.002	+0.100 ± 0.002
-0.230	0.9581	0.728 ± 0.002	-0.100 ± 0.002

Table 5.9: *Top quark polarisation P and forward-backward asymmetry A_{FB}^{N} at generator level for different $Im(g_R)$ anomalous couplings in both production and decay Wtb vertices. No uncertainty is shown for the couplings since they are input numbers to the* Protos *generator, while the observables P and A_{FB}^{N} are quoted with their statistical uncertainties (given the limited -500k- number of generated events).*

pared to check how linear is the response. Figure 5.34 shows good agreement between the input asymmetry value and the unfolded value and proofs that the method is bias free.

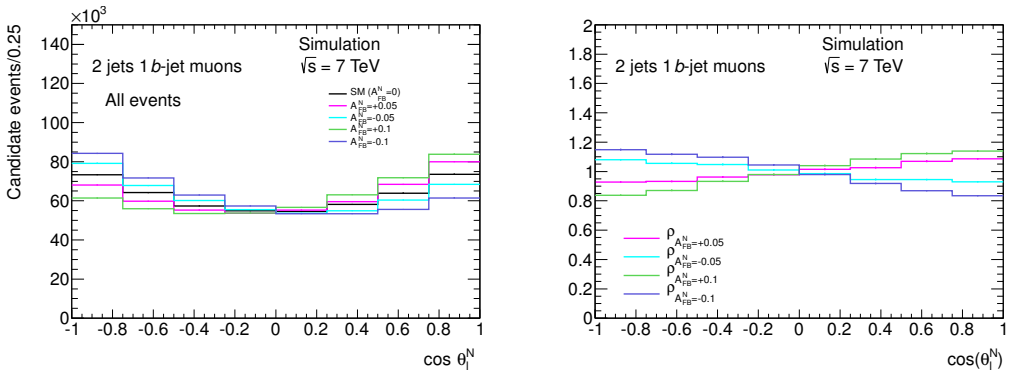

Figure 5.33: *The $\cos\theta^{N}$ angular distribution for different A_{FB}^{N} inputs at generator level (left) and the estimated weights to go from SM (A_{FB}^{N}=0) to non-SM values (right) for the muon channel.*

In order to check that the statistical uncertainty of the points (output $A_{\mathrm{FB}}^{\mathrm{N}}$) in Figure 5.34 are properly estimated, ensembles of pseudo-experiments are performed. For each input value of $A_{\mathrm{FB}}^{\mathrm{N}}$ 15k pseudo-experiments are carried out. In each pseudo-experiment, the measurement is repeated on a simulated data sample in which the number of signal events is thrown according to a Poisson distribution and for each of them the $A_{\mathrm{FB}}^{\mathrm{N}}$ is computed. The distribution of the obtained asymmetry results is then fitted with a Gaussian and the mean fit result is calculated. The difference between the fit value and the true value divided by the statistical uncertainty of the asymmetry is the so-called pull distribution, which is expected to be centered at zero and its width is a measure of the correctness of the estimated statistical uncertainty. In Figure 5.35 the means and the widths of the pull distributions as a function of $A_{\mathrm{FB}}^{\mathrm{N}}$ are presented. The pull means are consistent with zero and their widths are consistent with the expected value of one.

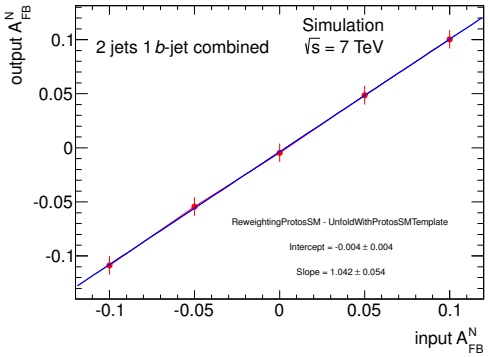

Figure 5.34: *Linear test with reweighting technique: The obtained A_{FB}^N values after unfolding are shown as a function of the injected asymmetry at generator level (*x *axis) for the combination of electrons and muons. The uncertainties are statistical only.*

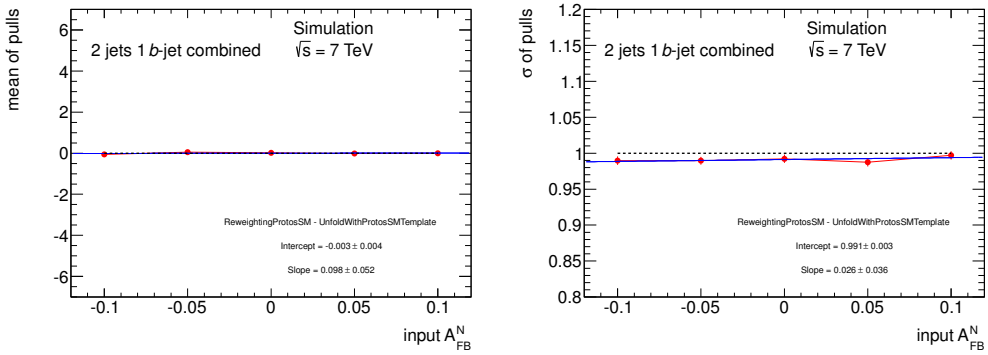

Figure 5.35: *Linear test with reweighting technique: Means (left) and widths (right) of the pull distributions as a function of the A_{FB}^N input values for the combination of electron and muon channel.*

The above successful closure and linearity tests show that the unfolding procedure can be used to correct for acceptance and reconstruction effects to parton level.

5.7.2.3 Unfolded data distribution

Once the unfolding procedure has been validated, it can be used to unfold the measured data distribution after background subtraction. The obtained values of $A_{\mathrm{FB}}^{\mathrm{N}}$ are presented in Table 5.10.

5.7.2.4 Statistical uncertainty: pulls

The observed statistical uncertainty shown in Table 5.10 is calculated from the measured data distribution propagating the statistical uncertainties through the unfolding procedure. The sta-

	$A_{\mathrm{FB}}^{\mathrm{N}}$ (unfolded)
Electrons	0.065 ± 0.098 (data stat.) ± 0.019 (bkg. MC stat.) ± 0.009 (signal MC stat.) = 0.065 ± 0.102 (total stat.)
Muons	0.004 ± 0.089 (data stat.) ± 0.015 (bkg. MC stat.) ± 0.008 (signal MC stat.) = 0.004 ± 0.091 (total stat.)
Combined	0.031 ± 0.064 (data stat.) ± 0.012 (bkg. MC stat.) ± 0.006 (signal MC stat.) = 0.031 ± 0.065 (total stat.)

Table 5.10: *A_{FB}^{N} values after the unfolding for the electron, muon and combined channel. Only the statistical uncertainties are shown.*

tistical uncertainties are propagated using 5k pseudo-experiments, fluctuating each component in Equation 5.12 within their uncertainties. In each pseudo-experiment, the input data (before background subtraction) and the transfer matrix (the one containing the numbers of events) are fluctuated using Poisson distributions. The background distribution and the acceptance efficiency are fluctuated taken into account the statistical uncertainty in each bin. Each of the fluctuated transfer matrices is normalised (per row) to obtain the fluctuated migration matrix and then the latter is inverted. The unfolding is performed using the fluctuated inputs. The fluctuations of the unfolded spectrum are then measured, and the information on their size and correlations are saved in a covariance matrix. From the unfolded distribution and the covariance matrix, the forward-backward asymmetry and its associated statistical uncertainty are calculated.

In order to validate that this uncertainty is properly estimated, the observed statistical uncertainty is compared to the expected one. The expected uncertainty is calculated using 15k ensembles, being each of them a pseudo-data distribution of $\cos\theta^{\mathrm{N}}$ corresponding to the luminosity of the analysed dataset. The pseudo-data ensembles are built from Monte Carlo signal and background. The number of events per ensemble is allowed to fluctuate by varying the contents of each $\cos\theta^{\mathrm{N}}$ bin according to a Poisson distribution. For each pseudo-data the expected $A_{\mathrm{FB}}^{\mathrm{N}}$ mean value and its expected statistical uncertainty have been calculated and they are shown in Figure 5.36. The measured $A_{\mathrm{FB}}^{\mathrm{N}}$ mean value and its uncertainty (vertical lines) are compared with the expected values. The pull distribution are also shown. One can see that they are centered around 0 and the width is close to 1, as expected, and therefore one can conclude that the statistical uncertainty is properly estimated.

5.7.2.5 Consistency check: *t*-channel cross section measurement

An additional consistency check can be performed using unfolded data events: derive the single top quark *t*-channel cross section and compare with ATLAS measurements and its theoretical prediction. The cross section can be obtained using the following formula:

$$\sigma_j = \frac{M_{ji}^{-1}(N_i^{\mathrm{data}} - N_i^{\mathrm{bkg}})}{\epsilon_j \mathcal{L}} \,, \tag{5.13}$$

where σ_j is the cross section and $\mathcal{L}$ is the integrated luminosity in the analysed dataset. Since only W leptonic decay modes with electron or muon in the final state are considered, one has to

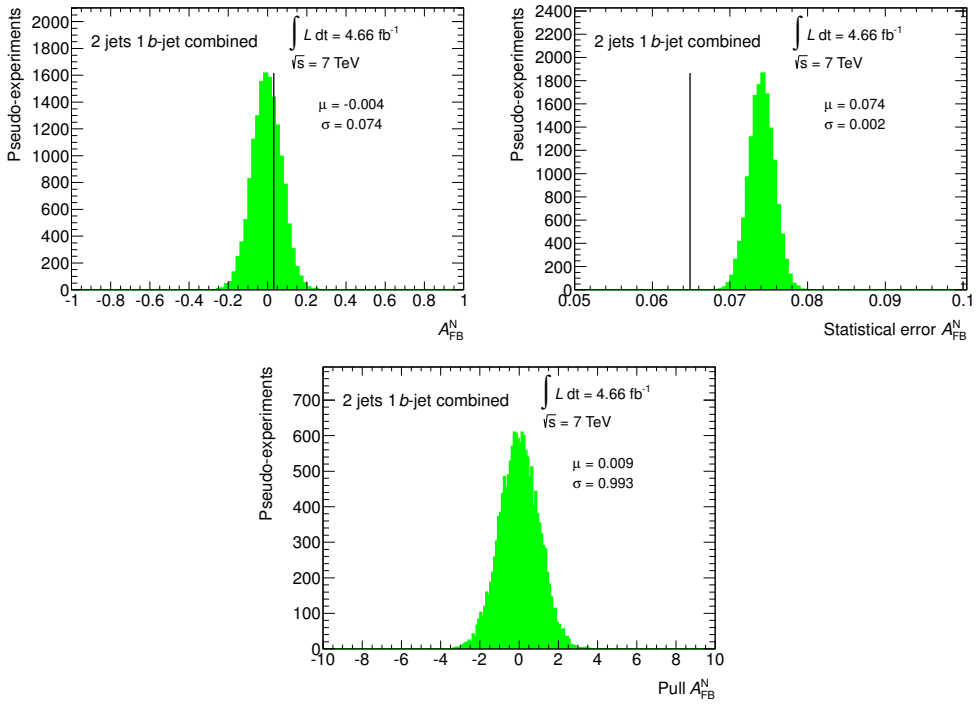

Figure 5.36: *Expected statistical uncertainty obtained with pseudo-experiments. For each ensemble, the A_{FB}^{N} value (top left), its expected statistical uncertainty (top right) and the pull distributions (bottom) are shown for the combined electron and muon channel. In the upper plots the vertical lines indicate the measured A_{FB}^{N} mean value and its uncertainty shown in Table 5.10.*

add the appropriate branching ratio of the corresponding channels to the denominator in Equation 5.13: $\mathcal{BR}(W^+ \rightarrow e^+\nu_e) = 10.75\%$, $\mathcal{BR}(W^+ \rightarrow \mu^+\nu_\mu) = 10.57\%$ and $\mathcal{BR}(W^+ \rightarrow \tau^+\tau_\mu) = 11.25\%$ (same for their charge conjugates) [17]. In addition, one has to consider $\mathcal{BR}(\tau^+ \rightarrow e^+\nu_e\overline{\nu}_\tau) = 17.85\%$ for the electron channel and $\mathcal{BR}(\tau^+ \rightarrow \mu^+\nu_\mu\overline{\nu}_\tau) = 17.36\%$ for the muon channel (and their charge conjugates in both cases).

The measured value for the single top quark t-channel cross section in proton-proton collisions at $\sqrt{s} = 7$ TeV is $\sigma_{t-ch} = 74 \pm 9$ (stat.) pb using the combined electron and muon channel (including events with leptonic τ decays). The associated systematic uncertainties have not been evaluated since this was only a cross check. This measurement is compatible with the current ATLAS and CMS measurements which are $\sigma_{t-ch}^{ATLAS} = 83 \pm 4$ (stat.)$^{+20}_{-19}$ (syst.) pb [152] and $\sigma_{t-ch}^{CMS} = 67.2 \pm 3.7$ (stat.) ± 4.9 (syst.) pb [153], with 1.0 fb^{-1}and 1.5 fb^{-1}respectively. In addition, it is also in good agreement with the SM expectation which is $64.6^{+2.7}_{-2.0}$ pb at approximate NNLO [51] assuming $m_t = 172.5$ GeV.

5.8 Systematic uncertainties

The uncertainties in modelling the physics processes and detector effects are the systematic uncertainties affecting this measurement. These uncertainties cannot be removed by repeating measurements and do not automatically decrease by collecting more data. The systematic uncertainties can affect both the rate of predicted signal and background events as well as the shape of the angular distribution studied in this analysis. The impact of these various sources of uncertainties is determined using a frequentist method based on the generation of pseudo-experiments.

For each source of systematic uncertainty d_k, the angular distribution $\cos\theta^{\mathrm{N}}$ is obtained by adding the varied signal and background contributions. The obtained sample is the so-called 'pseudo-data'. In the framework of the frequentist interpretation, pseudo-experiments are used to propagate the systematic uncertainties to the measurement. In each pseudo-experiment, the numbers of events for the background and signal processes are determined from Poisson distributions with means N^{bkg} and $N^{\mathrm{signal,\,reco}}$, respectively. The total number of events in the new 'pseudo-data' sample, $N^{\mathrm{pseudo\text{-}data}}$, is forced to have the same statistics as in the original dataset. Then the angular distribution is obtained from the corresponding template distributions for each contributing process, and the asymmetry $A_{\mathrm{FB}}^{\mathrm{N}}$ is extracted from this pseudo-data distribution using the unfolding method explained before. By performing the asymmetry measurement from these pseudo-experiments, one obtains an estimator of the probability density of all possible outcomes of the measurement; the standard deviation of this distribution is an estimator of the measurement statistical uncertainty and the mean value is the estimated asymmetry for every systematic variation. The difference between the estimated asymmetry with (d_k) and without (nominal d_0) variation is quoted as systematic uncertainty. The total uncertainty is then derived by adding quadratically all the individual uncertainties.

The procedure is the following:

- Vary the source of systematic uncertainty (e.g., jet energy scale) up and down and create new pseudo-data sets: $N_i^{\mathrm{pseudo\text{-}data}}(d_k) = N_i^{\mathrm{signal,\,reco}}(d_k) + N_i^{\mathrm{bkg}}(d_k)$.
- Perform the ensemble tests (15k times) with the scaled inputs and estimate the expectation of the asymmetry value leaving the background, migration matrix and event selection efficiency unchanged:

$$N_j^{\mathrm{signal,\,parton\,level}}(d_k) = \frac{M_{ji}^{-1}(d_0)(N_i^{\mathrm{pseudo\text{-}data}}(d_k) - N_i^{\mathrm{bkg}}(d_0))}{\epsilon_j(d_0)}\,,$$

$$A_{FB}^{N}(d_k) = \frac{N^{\mathrm{signal,\,parton\,level}}(\cos\theta^{\mathrm{N}} > 0; d_k) - N^{\mathrm{signal,\,parton\,level}}(\cos\theta^{\mathrm{N}} < 0; d_k)}{N^{\mathrm{signal,\,parton\,level}}(\cos\theta^{\mathrm{N}} > 0; d_k) + N^{\mathrm{signal,\,parton\,level}}(\cos\theta^{\mathrm{N}} < 0; d_k)}\,.$$

- Quote the difference of the expectation values of the estimator for the scaled and unscaled ensemble tests as systematic uncertainty: $\Delta\, A_{FB}^{N} = A_{FB}^{N}(d_k) - A_{FB}^{N}(d_0)$.

Different sources of systematic uncertainties are taken into account and they are implemented following the standard ATLAS procedures [154]. As commented before, the W+jets overall normalisation and flavour fractions are recomputed for each systematic uncertainty variation.

5.8.1 Detector uncertainties

There are three sources of detector modelling uncertainties: the efficiency corrections (scale factors) associated to the trigger, reconstruction and identification of the physics objects (detailed in Section 3.4), the energy or momentum scale and resolution. These uncertainties are due to the residual differences between data and Monte Carlo simulations for these quantities. The systematic effects are evaluated by shifting the efficiencies, energy or momentum within their uncertainties (1σ), and the missing transverse energy is recalculated accordingly. The object and event selections are reapplied to estimate the effect on the expected number of events and on the reconstructed distributions.

Lepton trigger, reconstruction and identification efficiencies

The mismodelling of electron or muon trigger, reconstruction and identification efficiencies in simulations are corrected by applying scale factors. The uncertainties are evaluated by varying these scale factors by their uncertainties and the shifts of the event yields are then calculated for the signal and all backgrounds. The scale factor uncertainties are around 3%.

Lepton energy or momentum scale

$Z \to \ell\ell$ processes are used to measure the lepton energy or momentum scale and resolution. As explained in Section 3.4, correction factors and their associated uncertainties are derived to match the simulated distribution to the observed in collision data. To estimate this systematic uncertainty, the correction scale factors shifted up and down by 1σ uncertainty are applied to recalculate the energy (momentum), leading to different event rates and angular distributions after selections.

Lepton energy or momentum resolution

Due to the discrepancies in the electron energy and muon momentum resolutions measured in data and predicted by the Monte Carlo, an smearing is applied to Monte Carlo to match the resolutions in data. The smearing factor is a random number drawn from a Gaussian distribution with mean and width dependent on the electron E_T and η and muon p_T. For the electrons, a systematic uncertainty is associated by smearing the electron energy two times: one to assign the upward fluctuation and the other for the downward fluctuation. For the muons, this systematic effect is evaluated by smearing the muon momentum four times: first, the muon momentum measured in the inner tracker is smeared by 1σ twice, once for the upward fluctuation and the other for downward fluctuation; then, the muon momentum measured in the muon chambers is smeared by 1σ again to assign the upward and downward fluctuations. The maximum and minimum value of $A_{\mathrm{FB}}^{\mathrm{N}}$ for all the four variations are taken and its difference divided by two is quoted as final muon momentum resolution systematic uncertainty.

Jet reconstruction efficiency

The jet reconstruction efficiency is defined as the fraction of probe track-jets matched to a calorimeter jet and is estimated using minimum bias and multijet events [111]. The observed

difference between data and Monte Carlo efficiencies is taken into account by randomly dropping jets from events in the Monte Carlo samples.

Jet energy scale

An accurate knowledge of the JES is very important for precise measurements. The JES was derived using data from the full 2011 dataset and Monte Carlo simulations [105]. Its total uncertainty depends on the p_{T} and η of the reconstructed jet and varies between 2% and 13%. The energy of each jet is scaled up or down by 1σ. An additional uncertainty is applied to b-flavoured jets.

Jet energy resolution

The JER measured in data agrees well within uncertainty with the simulated resolution. For this reason, the jet energy in the simulated samples is not smeared by default. To estimate the uncertainty, the jet energy in Monte Carlo samples is smeared by a Gaussian function with mean and width dependent on the jet p_T and η to assign the upward and the downward fluctuations.

JVF scale factors

The application of a cut on the JVF to reduce contamination by pile-up jets introduces an uncertainty related to the efficiency with which this cut selects jets from hard scattering processes. Scale factors are introduced to account for this. The corresponding uncertainty is estimated by varying the scale factor within 1σ of its uncertainty.

***b*-tagging efficiency**

Since the b-tagging efficiencies and misidentification rates are not identical in data and Monte Carlo, all jets are assigned a specific p_T (and η)-dependent scale factor to account for this difference. The obtained scale factors for each jet are combined into an event weight. The weights have an associated uncertainty which is evaluated separately for b quarks [115], c quarks [155]) and light flavour quark jets [117] in the Monte Carlo.

E_T^{miss}

The uncertainties from the energy scale and resolution corrections on leptons and jets are propagated into the calculation of the $E_{\mathrm{T}}^{\mathrm{miss}}$. Additional uncertainties are added from contributions of calorimeter cells not associated to any jet and due to soft-jets ($7 < p_T < 20$ GeV). The two uncertainties are treated as fully correlated. The uncertainty in the description of extra energy deposited due to pile-up interactions is treated as a separate $E_{\mathrm{T}}^{\mathrm{miss}}$ scale uncertainty.

5.8.2 Signal and background modelling uncertainties

Systematic effects from signal Monte Carlo modelling are estimated by comparing different generators and varying specific parameters in the simulations.

Monte Carlo generator and parton shower

The effect of the signal Monte Carlo generator modelling is evaluated by comparing AcerMC and Protos event generators, both interfaced with Pythia for the parton shower. The Protos reconstructed sample is unfolded using the AcerMC migration matrix and efficiency. This uncertainty is symmetrized (one-sided systematic). For $t\bar{t}$ process, being one of the dominant backgrounds, Powheg+Pythia and Alpgen+Herwig are compared and the difference is taken as a combined Monte Carlo generator and parton shower systematic uncertainty. These generator uncertainties are the dominant source of systematic uncertainty in this analysis. Due to the limited statistics in the samples used, the estimated systematic uncertainties have a significant statistical uncertainty associated.

Initial and final state radiation

The effect of variations of the ISR/FSR model on the signal acceptance and background contributions involving top quarks is estimated using AcerMC+Pythia samples generated with various ISR/FSR tunes constrained by data [156]. Some Pythia parameters are varied to obtain samples with more or less ISR and FSR. The number of jets in an event can be different if there is a different amount of ISR or FSR. These changes affect the expected event yields and therefore the signal and backgrounds acceptance. The uncertainty on the ISR/FSR modelling is assigned as half of the difference between the more and less ISR and FSR variations, and it is found to have a small impact in the $A_{\mathrm{FB}}^{\mathrm{N}}$ measurement.

Parton distribution functions

The impact of the choice of the PDF set can be estimated by comparing different Monte Carlo samples. However this is very time consuming, and thus not optimal. The PDF uncertainties are estimated for all top quark processes by reweighting the Monte Carlo events according to various PDF uncertainty eigenvector sets. Apart from the CT10 PDF set used in the nominal sample, the MSTW2008nlo and the NNPDF sets have been considered. Each PDF is accompanied by a set of uncertainties, and the variations up and down of these uncertainties are transformed in an event weight. To evaluate the impact on the asymmetry measurement, all top quark Monte Carlo samples, including the signal, are reweighted and the resulting angular distribution is then unfolded using the method explained before. Figure 5.37 shows the $A_{\mathrm{FB}}^{\mathrm{N}}$ values obtained for the different variations for the three PDF sets considered. The final uncertainty is calculated taking into account both the uncertainty within each PDF set (intra-PDF uncertainty) and the differences between different sets (inter-PDF uncertainty). The results of different eigenvectors are combined following the recommendations of the PDF4LHC [157].

Multijet background

For the electron channel, the shape of multijet background is estimated using simulated events and the normalisation is estimated from data using the jet-electron model as discussed in Section 5.4.1. For the muon channel, both the normalisation and shape are obtained from data using the matrix method. A global normalisation and shape uncertainty for this background is obtained by taking the largest variation between considering a change of 50% (see Section 5.4.1.3)

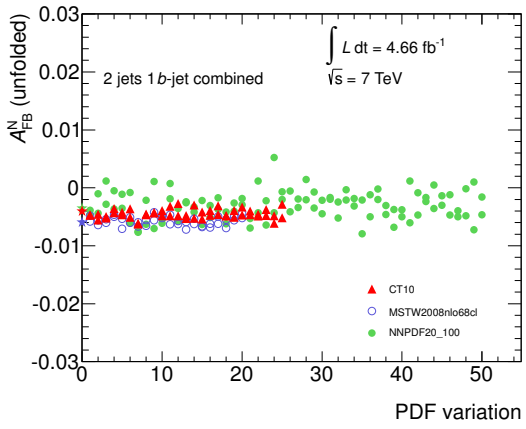

Figure 5.37: *Impact of the PDF variations for three different sets in the A_{FB}^{N} measurement.*

in the normalisation and completely removing the multijet background. It is found that in both channels the latter is more conservative.

W+jets background

W+jets is the dominant background and it is very important to study the impact of changing its shape and normalisation in the $A_{\mathrm{FB}}^{\mathrm{N}}$ measurement. As explained before, the overall normalisation and flavour fractions are recalculated for each systematic source (JER, JES, etc.) using the corresponding Monte Carlo samples that include these systematic variations. Thus, a new set of normalisation values is obtained for each of the systematic uncertainty. These sets are applied when computing the corresponding uncertainty; in this way, the normalisation uncertainty on the W+jets is already included in the evaluation of the different systematic sources, avoiding double counting. A shape uncertainty is assigned based on the variation of the choices of the matching scale and the functional form of the factorisation scale in ALPGEN.

Background normalisation

This uncertainty impacts all simulated processes. The $t\bar{t}$ cross section and its uncertainty are taken to be 167^{+17}_{-18} pb [138] [8]. For the single top quark s and Wt channels, a 10% uncertainty is used. An uncertainty of 5% is assigned to the diboson background and of 60% to the Z+jets background. These account for the scale, PDF and running α_S uncertainties.

[8] This was the best prediction at the time of data analysis. However, at the time of writing, a more accurate prediction at NNLO+NNLL is available for $t\bar{t}$ cross section: $177.3^{+10.1}_{-10.8}$ pb [50].

5.8.3 Other systematic uncertainties

Luminosity

The relative uncertainty on the integrated luminosity measured in 2011 data is 1.8%, based on dedicated *van der Meer* scans [132]. The impact of this uncertainty in the asymmetry measurement is found to be negligible.

Unfolding method

The uncertainty introduced due to the unfolding technique used is derived from the closure test: the comparison of the unfolded Monte Carlo signal $A_{\mathrm{FB}}^{\mathrm{N}}$ value and the generated $A_{\mathrm{FB}}^{\mathrm{N}}$ value. The difference is taken as a systematic uncertainty due to the unfolding method.

Table 5.11 shows the breakdown of the systematic uncertainties and their contribution to the $A_{\mathrm{FB}}^{\mathrm{N}}$ measurement for the combined channel. The largest sources of systematic uncertainties originate from the t-channel generator and the $t\bar{t}$ generator and parton shower modelling uncertainties. Other important contributions are the background modelling, the jet energy resolution and the jet energy scale. All other contributions are small.

Source	$\Delta A_{\mathrm{FB}}^{\mathrm{N}}$
t-channel generator	+0.024 / −0.024
$t\bar{t}$ generator and parton shower	+0.010 / −0.010
Background normalisation	+0.008 / −0.008
Jet energy resolution	+0.007 / −0.007
Jet energy scale	+0.005 / −0.009
Lepton id, reco., trigger and scale	+0.004 / −0.006
PDFs	+0.003 / −0.003
Unfolding	+0.003 / −0.003
$E_{\mathrm{T}}^{\mathrm{miss}}$	+0.002 / −0.004
b-tagging	+0.002 / −0.002
W+jets shape	+0.001 / −0.001
ISR/FSR	+0.001 / −0.001
Jet reconstruction efficiency	+0.001 / −0.001
Luminosity	+0.001 / −0.001
Jet vertex fraction	<0.001 / <0.001
Total systematic	+0.029 / −0.031

Table 5.11: *The effect of each systematic uncertainty on the A_{FB}^{N} measurement.*

5.9 Results

The final result for the forward-backward asymmetry $A_{\mathrm{FB}}^{\mathrm{N}}$ is:

$$A_{\mathrm{FB}}^{\mathrm{N}} = 0.031 \pm 0.065\,(\mathrm{stat.})\,^{+0.029}_{-0.031}\,(\mathrm{syst.})\,.$$

This measurement is dominated by the statistical uncertainty and therefore improvements are expected using the full 2012 dataset. In addition, an increase in the statistics of the simulated samples would allow more precise estimates of the systematic uncertainties. This measurement is consistent with $\mathcal{CP}$ invariance in top quark decays ($A_{\mathrm{FB}}^{\mathrm{N}} = 0$). Using the relation between $A_{\mathrm{FB}}^{\mathrm{N}}$ and $Im(g_{\mathrm{R}})$ in Equation 2.28 (assuming $V_{\mathrm{L}} = 1$, $V_{\mathrm{R}} = g_{\mathrm{L}} = 0$, and g_{R} small and purely imaginary), it is possible to constrain the imaginary part of the anomalous coupling g_{R}. Figure 5.38 shows the allowed regions given by the $A_{\mathrm{FB}}^{\mathrm{N}}$ measurement in the top quark polarisation versus $Im(g_{\mathrm{R}})$ plane. Two bands are shown corresponding to the 68% and 95% confidence level. Assuming a value of $P = 0.9$ for the top quark polarisation[9], the first experimental limits on $Im(g_{\mathrm{R}})$ are determined to be $[-0.20, 0.30]$ at 95% confidence level. This limit is also consistent with SM predictions at LO and including one loop electroweak corrections [47].

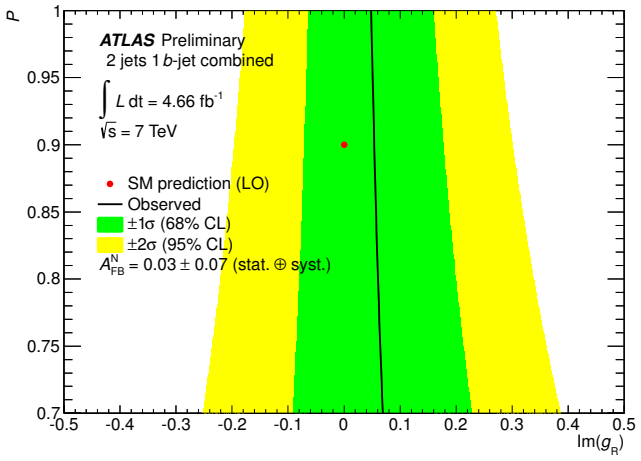

Figure 5.38: *Constraints in the top quark polarisation versus $Im(g_R)$ plane from the A_{FB}^{N} measurement. The allowed regions at 68% and 95% confidence level are shown. The SM prediction at LO ($Im(g_R) = 0$ and $P = 0.9$) is also shown.*

Additionally one can consider the relation between the asymmetry $A_{\mathrm{FB}}^{\mathrm{N}}$ and the right and left-handed W boson polarisation fractions in the normal direction which is:

$$A_{\mathrm{FB}}^{\mathrm{N}} = \frac{3}{4} P (F_{\mathrm{R}}^{N} - F_{\mathrm{L}}^{N})\,. \tag{5.14}$$

[9] This value of the top quark polarisation is close to the one predicted for the single top t-channel production [4, 5]. Any uncertainty is explicitly neglected when computing the experimental limits on $Im(g_{\mathrm{R}})$.

Figure 5.39 shows the constraints in the top quark polarisation versus the difference $F_{\mathrm{R}}^{N} - F_{\mathrm{L}}^{N}$ plane derived from the $A_{\mathrm{FB}}^{\mathrm{N}}$ measurement. The allowed regions at 68% and 95% confidence level are shown.

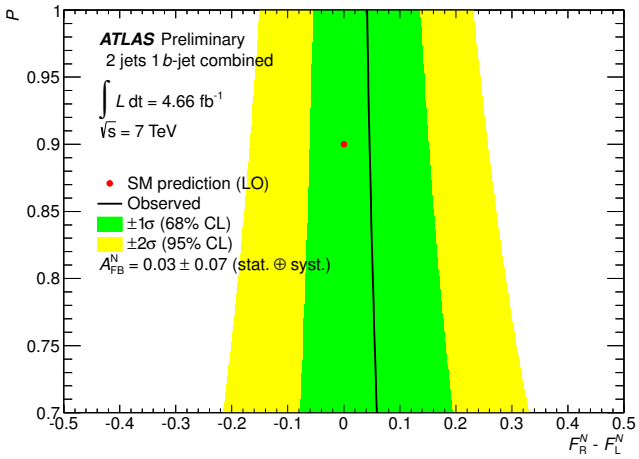

Figure 5.39: *Constraints in the top quark polarisation versus the difference $F_R^N - F_L^N$ plane using the A_{FB}^N measurement. The allowed regions at 68% and 95% confidence level are shown. The SM prediction at LO ($Im(g_R) = 0$ and $P = 0.9$) is also presented for comparison.*

6

Prospects to further constrain the *Wtb* vertex

The structure of the *Wtb* vertex can be tested and determined from a global fit using several observables both from single top quark and $t\bar{t}$ events. The W helicity fractions measured in $t\bar{t}$ events have allowed to set limits to the real part of the *Wtb* anomalous couplings. The $A_{\mathrm{FB}}^{\mathrm{N}}$ measurement presented in this thesis sets the first constraints in the imaginary part of one of them. The obtained limits can be improved if these and additional observables are combined. The measurement of the t-channel single top quark production cross section, the degree of polarisation of the top quarks produced via electroweak interaction and additional asymmetries as the $A_{\mathrm{FB}}^{\mathrm{T}}$ proposed in Chapter 2 can be used to further constrain the *Wtb* vertex. The full 2012 dataset at 8 TeV is now being analyzed and will allow to measure all these observables with an unprecedented precision and set stringent limits.

6.1 Constraints on the *Wtb* vertex couplings

The structure of the *Wtb* vertex can be determined by a global fit using several observables.

6.1.1 Extraction of limits from observables

The extraction of limits on the anomalous couplings from the measurement of the experimental observables can be done using TopFit [158]. The current version does not take into account correlations among the different observables, thus new techniques to combine several measurement are being developed at the time of writing.

The method implemented in TopFit is briefly described here for a generic observable O, e.g. an angular asymmetry (in our case $A_{\mathrm{FB}}^{\mathrm{N}}$), that depends on a parameter x (in our case the anomalous coupling $Im(g_{\mathrm{R}})$) which value is unknown in advance, and for which confidence intervals

can be obtained. O is experimentally measured and is assumed to obey a Gaussian distribution (with mean and standard deviation given by its measurement). However, if the dependence $O(x)$ is non-linear in the region of interest, the probability density function derived for the parameter x will no longer be a Gaussian and a Monte Carlo method must be used to determine a confidence interval on x. The probability density function of x is determined numerically using the acceptance-rejection method. For that the next steps are repeated iteratively:

1. generate a random value (with uniform probability) x_i within a suitable interval;
2. evaluate the probability of $O(x_i)$, given by the probability density function of O;
3. generate an independent random number r_i (with uniform probability);
4. accept the value x_i if the probability of $O(x_i)$ is larger than r_i. The resulting set of values x_i is distributed according to the probability density function of x given by the measurement of O.

The determination of a central interval with a given confidence level γ is done numerically, requiring:

- that it contains a fraction γ of the total number of values x_i;
- that is central, i.e. fractions (1-γ)/2 of the values generated are on each side of the interval.

6.1.2 Constraining g_R coupling combining observables

TopFit has been used to obtain the limits on both the real and imaginary part of g_R from the W helicity fractions and A_{FB}^N measurements keeping only this anomalous coupling non-vanishing. No correlations between the observables are taken into account so far. The dependence on g_R of these observables is approximately linear. For the W helicity fractions, the latest combination from ATLAS and CMS measurements [63] using top quark pair events are used:

$$\begin{aligned} F_R &= 0.626 \pm 0.034\,(\text{stat.}) \pm 0.048\,(\text{syst.}), \\ F_0 &= 0.359 \pm 0.021\,(\text{stat.}) \pm 0.028\,(\text{syst.}), \end{aligned}$$

with a total correlation of $\rho = -0.86$; and for A_{FB}^N, the ATLAS result [6] (main part of this thesis) derived using t-channel single top quark events is considered:

$$A_{FB}^N = 0.031 \pm 0.065\,(\text{stat.})\,^{+0.029}_{-0.031}\,(\text{syst.})\,.$$

The allowed region at 95% confidence level for the real and imaginary part of the anomalous coupling g_R is shown in Figure 6.1. The two bands shown correspond to different assumptions for the top quark polarisation.

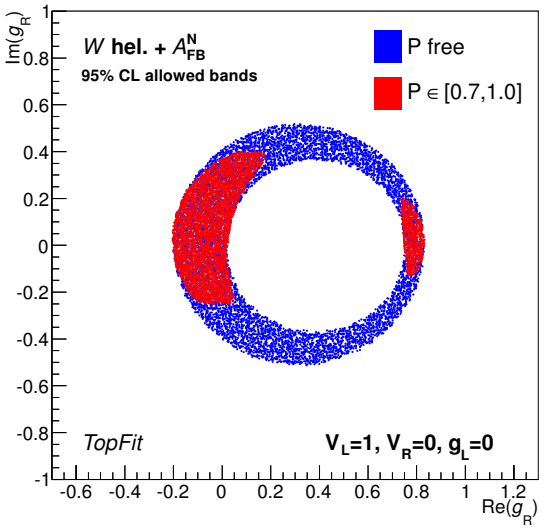

Figure 6.1: *Observed 95% confidence level region on the anomalous coupling g_R derived from the W helicity fractions and A_{FB}^{N} measurements.*

6.2 Other angular distributions to probe the *Wtb* vertex

As discussed in Chapter 2, several angular distributions can be defined in t-channel single top quark events exploiting the spin direction of the top quark. The following angles and their corresponding forward-backward asymmetries were proposed (see Figure 2.8):

- Angle θ^{N} between the direction N (normal to the plane formed by the top spin direction and the W boson momentum) and the lepton in the W boson rest frame $\Longrightarrow$ $A_{\mathrm{FB}}^{\mathrm{N}}$
- Angle θ^{T} between the direction T (transverse to the plane formed by the top spin direction and the W boson momentum) and the lepton in the W boson rest frame $\Longrightarrow$ $A_{\mathrm{FB}}^{\mathrm{T}}$
- Angle θ^{*} between the W boson momentum in the top quark rest frame and the lepton in the W boson rest frame $\Longrightarrow$ A_{FB}
- Angle θ^{X} between the $\vec{s}_t$ direction (spectator quark momentum) and the lepton, both in the top quark rest frame $\Longrightarrow$ $A_{\mathrm{FB}}^{\mathrm{X}}$

Apart from the $A_{\mathrm{FB}}^{\mathrm{N}}$ measurement (sensitive to the imaginary part of one of the anomalous couplings in the Wtb vertex), the $A_{\mathrm{FB}}^{\mathrm{T}}$ and A_{FB} asymmetries which are sensitive to the real part of the anomalous couplings can be derived following the same strategy. Although the study of these additional angular distributions is beyond the scope of the present thesis, very preliminary values for the corresponding forward-backward asymmetries are obtained in this section. The associated systematic uncertainties have not been estimated.

The angular distributions and expected asymmetry values obtained at generator level in simulated events and before applying any event selection were presented in Figure 2.10. The measured distributions for the electron and muon channels are shown in the top plots of Figures 6.3-6.2. As before, the distributions reconstructed from the data are distorted by effects coming from the detector response, the selection cuts and the contamination of background events not completely removed by the final event selection. The event selection efficiency and the migration matrix are shown in the bottom plots of Figures 6.3-6.2. The measured distributions are deconvoluted back to parton level using the 'unfolding' procedure discussed in Section 5.7. The forward-backward asymmetries obtained from data (observed measurements) and from signal simulated events (expected measurements) are presented in Tables 6.2-6.1. Overall, the observed values agree with the expected ones and with the theoretical predicition within the statistical uncertainty.

In addition, the degree of polarization of the top quarks produced in the t-channel via electroweak interaction can be measured through the angular distribution $\cos\theta^{X}$ of their decay products (called spin analyzer, e.g. the lepton from the W decay) with respect to a chosen spin quantization axis. Here, the spectator quark momentum is chosen as spin axis (spectator spin basis). The angular distribution obtained at parton level for the lepton spin analyzer in this basis were shown in Figure 2.12. Figure 6.4 shows the reconstructed distributions for the electron and muon channel, the selection efficiency and migration matrix. From the forward-backward asymmetry, the product $\alpha\ P$ can be directly measurable and is presented in Table 6.3. By assuming the SM value for the spin analyzing power α, the degree of top quark polarization can be derived. This measurement is also compatible with the SM prediction.

The results presented here are limited by the statistical uncertainties. At the time of writing more precise measurements are being derived with the full available ATLAS dataset. In the future, these observables including the $A_{\mathrm{FB}}^{\mathrm{N}}$ asymmetry, the top quark polarization, the W boson helicity fractions as well as the single top quark cross section, can be combined in a global fit in order to strongly constrain the anomalous *Wtb* couplings.

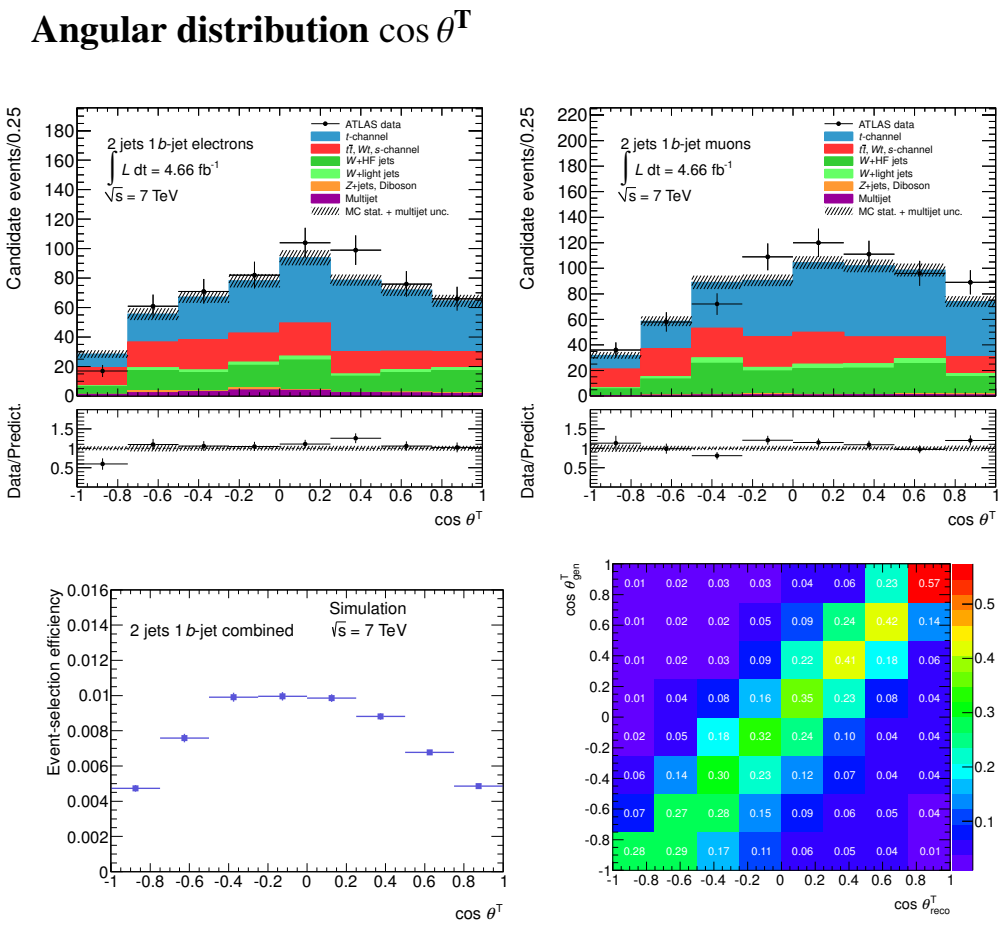

Figure 6.2: *Top: Reconstructed* $\cos\theta^T$ *angular distribution for the electron and muon channel. Bottom: Event selection efficiency and migration matrix* M_{ji} *derived using simulated events.*

	$A_{\mathrm{FB}}^{\mathrm{T}}$
Raw data	0.201 ± 0.028 (stat.)
Bkg. subtracted	0.388 ± 0.055 (stat.)
Data unfolded (obs.)	0.510 ± 0.095 (stat.)
MC unfolded (exp.)	0.341 ± 0.014 (stat.)
SM prediction	0.34

Table 6.1: *Observed and expected* A_{FB}^{T} *values for the combined channel for raw data, after background subtraction and after applying the unfolding procedure. Only the statistical uncertainties are shown.*

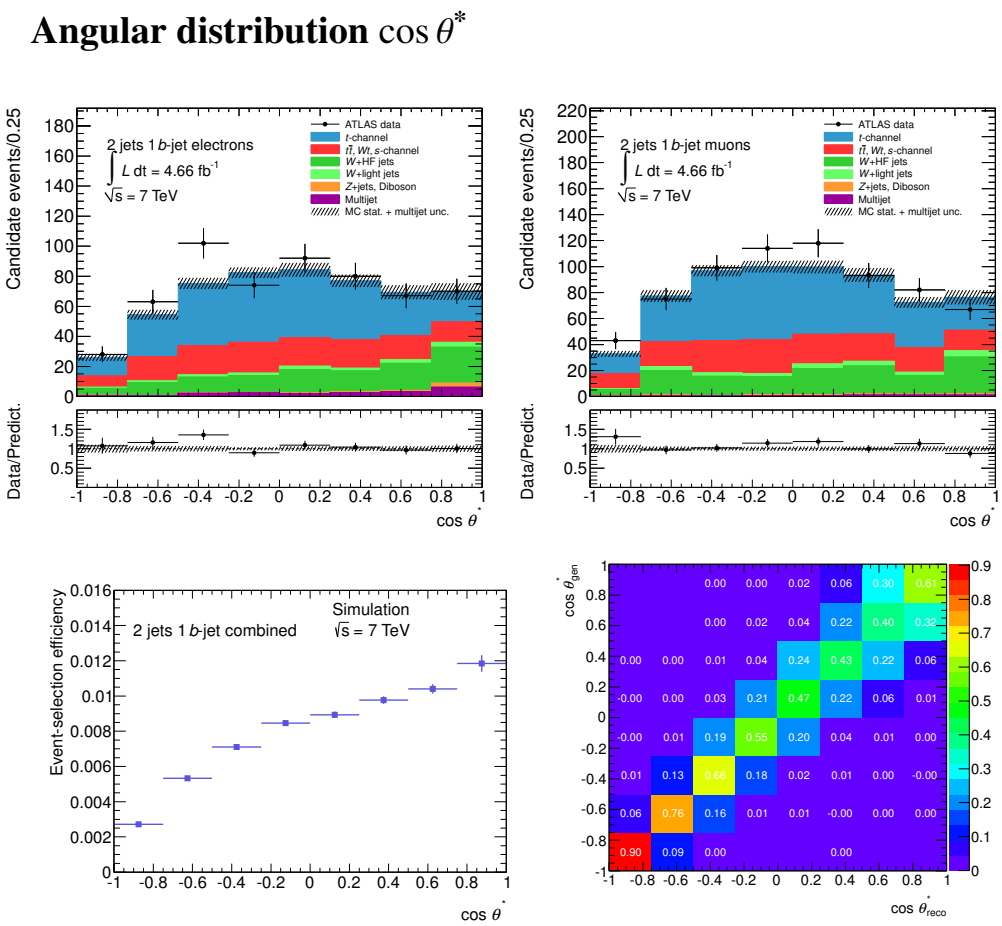

Figure 6.3: *Top: Reconstructed* $\cos\theta^*$ *angular distribution for the electron and muon channel. Bottom: Event selection efficiency and migration matrix* M_{ji} *derived using simulated events.*

	A_{FB}
Raw data	0.056 ± 0.028 (stat.)
Bkg. subtracted	-0.001 ± 0.055 (stat.)
Data unfolded (obs.)	-0.237 ± 0.065 (stat.)
MC unfolded (exp.)	-0.232 ± 0.010 (stat.)
SM prediction	-0.22

Table 6.2: *Observed and expected* A_{FB} *values for the combined channel for raw data, after background subtraction and after applying the unfolding procedure. Only the statistical uncertainties are shown.*

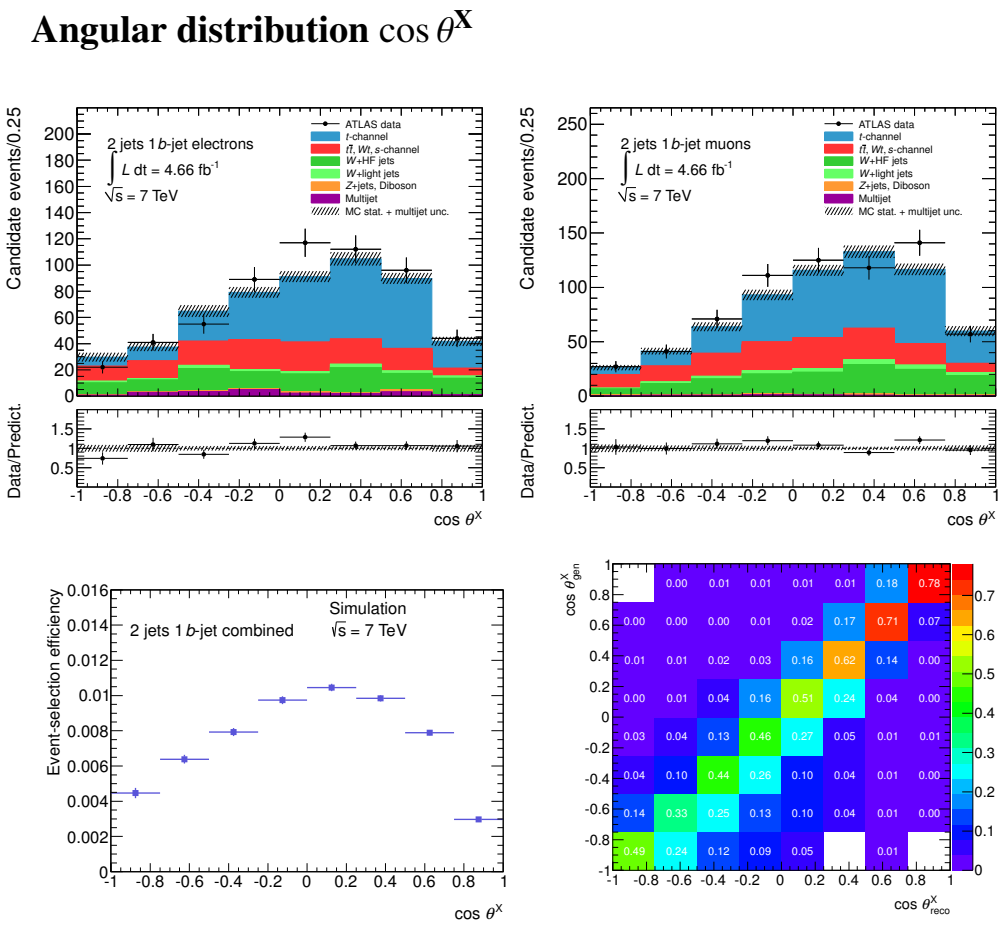

Figure 6.4: *Top: Reconstructed* $\cos\theta^X$ *angular distribution for the electron and muon channel. Bottom: Event selection efficiency and migration matrix* M_{ji} *derived using simulated events.*

	$A_{\mathrm{FB}}^{\mathrm{X}}$	$\alpha P{=}2A_{\mathrm{FB}}^{\mathrm{X}}$
Raw data	0.150 ± 0.021 (stat.)	
Bkg. subtracted	0.399 ± 0.063 (stat.)	
Data unfolded (obs.)	0.508 ± 0.090 (stat.)	1.016 ± 0.180 (stat.)
MC unfolded (exp.)	0.447 ± 0.010 (stat.)	0.894± 0.020 (stat.)
SM prediction	0.45	0.89

Table 6.3: *Observed and expected* A_{FB}^{X} *and top polarization values for the combined channel for raw data, after background subtraction and after applying the unfolding procedure. Only the statistical uncertainties are shown.*

Conclusions

The elementary particles, their properties and their interactions are described by the SM, which is the theoretical framework constructed for the study of the strong interactions of quarks and gluons and the unified electroweak force and that is based on local gauge invariance. The SM is very successful in giving account of most of the observed phenomena at the microscopic frontier of physics, having been verified and tested in many experiments in the last decades. The SM has also induced the search of novel phenomena, such as the recent discovery of the Higgs boson by the ATLAS and CMS experiments at the LHC. Despite these spectacular successes, there are evidences that the theory cannot be complete since, besides some possible theoretical diseases (the hierarchy problem), it is unable to explain some observed phenomena in nature. First of all, it does not include gravity and its constituents can only account for around 5% of the energy-matter content of our universe and no SM particle can be a candidate to describe dark matter. Furthermore, the observation of neutrino oscillations implies neutrino mass and mixing, incompatible with the minimal version of the SM. And, in addition, the standard flavour physics framework for $\mathcal{CP}$ violation, the mismatch between weak interaction and mass eigenstates of quarks by means of the CKM mixing matrix, is unable to explain the baryon asymmetry of the universe by many orders of magnitude. Although precision experiments in the K and B meson facilities agree with the predictions of the SM, **new physics sources of $\mathcal{CP}$ violation are unavoidable**. With all this, it is clear that extensions of the SM are needed. New physics models that modify the SM in ways subtle enough to be consistent with existing data are being proposed.

In this thesis, an extension of the SM with additional sources of $\mathcal{CP}$ violation in the top quark sector is proposed. The top quark decays almost exclusively into a b quark and a W boson via the weak interaction, thus it allows to probe the chiral structure of the $W-t-b$ interaction. The Wtb vertex can be parametrised with the effective Lagrangian given by:

$$\mathcal{L}_{Wtb} = -\frac{g}{\sqrt{2}}\bar{u}_b\gamma^\mu\left(V_L P_L + V_R P_R\right)u_t W^+_\mu - \frac{g}{\sqrt{2}}\bar{u}_b\frac{i\sigma^{\mu\nu}}{M_W}q_\nu\left(g_L P_L + g_R P_R\right)u_t W^+_\mu + \text{h.c.} \quad (6.1)$$

where V_L, V_R, g_L and g_R are left and right-handed vector and tensor couplings respectively, and are in general complex. $P_{L/R} \equiv (1 \mp \gamma^5)/2$ are the left and right-handed projection operators. At tree level in the SM, the coupling V_L is given by the CKM matrix element V_{tb} and is therefore almost equal to one, while the other three couplings (so-called anomalous couplings) V_R, g_R and g_L vanish, leading to the pure vector minus axial structure ($\gamma^\mu - \gamma^\mu\gamma^5$, abbreviated V-A structure) of the weak interaction in the SM. Although non-vanishing values of the right-handed coupling V_R and of the tensor couplings g_R and g_L are not forbidden, several constraints on these anomalous couplings exist from both indirect observations and direct measurements. Deviations from the expected values can be probed by measuring the W polarisation fractions or angular asymmetries in the decay products of top quarks. Indeed, the W helicity fractions measured in

$t\bar{t}$ events have allowed to set limits to the real part of the anomalous couplings V_{R}, g_{L} and g_{R}. However, they are not sensitive to their complex phases which would imply that the top quark decay has a $\mathcal{CP}$-violating component.

For unpolarised top quark production the only meaningful reference direction in the top quark rest frame is the momentum $\vec{q}$ of the W boson (or $-\vec{q}$ of the b quark). However for polarised top quarks, such as those produced via electroweak interactions, one can also exploit the spin direction given by $\vec{s}_t$. From these two directions, further references can be defined normal $\vec{N}$ and transverse $\vec{T}$ to the plane formed by the W boson momentum direction $\vec{q}$ and the top quark spin direction $\vec{s}_t$. In a similar way that the helicity angle θ^* is defined between the lepton in the W boson rest frame and the W boson momentum, the angles θ^{N} and θ^{T} are defined between the lepton and these new directions. In addition, two further sets of W boson polarisation fractions can be defined. The most interesting remark is that the normal set of polarisation fractions (F_+^N, F_0^N and F_-^N) depend on the imaginary part of the anomalous coupling g_R; so observables depending on these will deserve special attention. If $\mathcal{CP}$ is conserved in the Wtb vertex, i.e. if all anomalous couplings are real, then $F_+^N = F_-^N$. A net normal W polarisation ($F_+^N \neq F_-^N$) can only be produced if $\mathcal{CP}$ is violated in the $t \to Wb$ decay. This property is unique of the normal direction and is here explored in the decay of polarised top quarks produced through electroweak interaction in proton-proton collisions at the LHC.

The measurement of this forward-backward asymmetry $A_{\mathrm{FB}}^{\mathrm{N}}$ (using t-channel single top quark events) is the major contribution of this thesis. The full 7 TeV dataset collected by the ATLAS detector in 2011 has been analyzed, which corresponds to an integrated luminosity of $4.66\,\mathrm{fb}^{-1}$. Events with an isolated electron or muon, missing transverse momentum and two jets being one tagged as a b-jet have been selected in this analysis. A full reconstruction of the top quark from its decay products is required to define the angle θ^{N}.

In order to understand the modelling of the t-channel single top quark events provided by Monte Carlo generators, studies of the kinematic properties of the final state particles have been conducted and different event generators have been compared. A special emphasis has been devoted to determine the W+jets background, that constitutes the dominant background contribution. An in-situ technique has been employed using data events in control regions in order to estimate the number of events of this background in the analysed dataset. Other processes such as multijet events are also estimated with dedicated data-driven methods. Finally, top quark background processes and diboson and Z+jets production are determined from Monte Carlo simulations. A cut-based strategy is followed exploiting the properties of the signal events. The final signal-to-background ratio is close to one. The reconstructed distribution of $\cos\theta^{\mathrm{N}}$ is affected by the acceptance cuts and detector effects. In order to allow a direct comparison of the experimental measurement with the theoretical prediction, the measured angular distribution must be unfolded, i.e. deconvoluted back to parton level (partons from the hard process). An unfolding technique by inversion of the response matrix has been applied to correct for acceptance and reconstruction effects which are modelled using t-channel simulated events. In addition, systematic uncertainties in modelling the physics processes and detector effects have been estimated, being the modelling of top quark processes the largest one.

The final asymmetry with its statistical and systematic uncertainties is:

$$A_{\mathrm{FB}}^{\mathrm{N}} = 0.031 \pm 0.065\,(\mathrm{stat.})\,^{+0.029}_{-0.031}\,(\mathrm{syst.})\,.$$

The result is dominated by the statistical uncertainty, so improvements are expected using the full 2012 dataset at 8 TeV with four times more statistics. Using the relation between $A_{\mathrm{FB}}^{\mathrm{N}}$ and $Im(g_{\mathrm{R}})$, it is possible to constrain the allowed regions in the top quark polarisation versus $Im(g_{\mathrm{R}})$ plane. Assuming a value of $P = 0.9$ for the top quark polarisation, which is the SM prediction for the single top t-channel production, the first experimental limits on $Im(g_{\mathrm{R}})$ are found to be $[-0.20, 0.30]$ at 95% confidence level. Both the asymmetry and the limit are consistent with SM predictions. This measurement involves understanding the process at generator level, a precise determination of the background processes, applying an unfolding procedure and estimating the corresponding systematic uncertainties.

At the time of writing this thesis, other analyses to probe the Wtb vertex anomalous couplings in single top quark events with the full 8 TeV dataset are being completed in ATLAS, including studies of other unfolding techniques, in addition to the one explored in this document. The combination of several observables will allow to obtain higher precision and set tighter constraints in the Wtb vertex.

In order to achieve the level of accuracy and precision required in these measurements, and to be sensitive to new physics, an excellent understanding of the detector is required. Thus performance studies are crucial to properly calibrate and align the detectors, improve the reconstruction algorithms and minimize systematic uncertainties. Indeed this thesis work includes two performance studies carried out with the first ATLAS data: global cosmic-ray runs recorded during the commissioning period and first proton-proton collisions runs at $\sqrt{s}$=7 TeV. In the commissioning period, prior to the first collisions in 2010, millions of cosmic-ray events were recorded and reconstructed in the ATLAS detector, and allowed to test the full operation chain, including data acquisition, reconstruction and analysis software. Most of the studies were focused on understanding the performance of individual subdetectors, while in the work presented in the first part of this thesis the performance of the reconstruction of cosmic-ray muons was studied combining information of all the subdetectors (inner detector, calorimeters and muon spectrometer). The performance of the combined tracking was evaluated by comparing the two reconstructed tracks left by a single cosmic-ray muon passing through the upper and then the lower half of the detector. In addition, the track parameter resolutions were derived using information only from data. Once the LHC delivered the first collisions, the reconstruction of other final state objects could also be studied in detailed. The contribution presented here is focused on the reconstruction of jets, in particular the jet structure. The jet shapes were measured in both regions inside and outside the jet cone, and the fraction of the jet momentum left out of the cone was extracted from them. Both measurements were compared to Monte Carlo predictions.

In 2015, the LHC will provide proton-proton collisions at 13-14 TeV and the detectors will resume data-taking, accessing a range of energies never studied before, and giving the opportunity for new exciting discoveries in top quark decays. These data will allow to improve the calibration and reconstruction methods, to carry out more performance studies and to improve the understanding of Monte Carlo generators, to minimize any possible systematic uncertainty and to reach the needed accuracy.

7 Resumen en castellano

7.1 Introducción

El Modelo Estándar de Física de Partículas (ME) es la descripción más fundamental de la materia y sus interacciones. Es una teoría cuántica de campos que combina tres de las cuatro interacciones fundamentales: la fuerza electromagnética, la débil y la fuerte. La teoría de la gravitación no está incluída. El ME explica satisfactoriamente una multitud de observaciones, incluso ha predicho la existencia de partículas que luego han sido descubiertas experimentalmente. Sin embargo, a pesar de sus formidables logros como el reciente descubrimiento del bosón de Higgs en los experimentos ATLAS (A Toroidal LHC ApparatuS) [8] y CMS (Compact Muon Solenoid) [9] del Gran Colisionador de Hadrones -en inglés, Large Hadron Collider (LHC)-, siguen abiertos muchos interrogantes. El modelo es incompleto por varias razones: no tiene en cuenta la gravedad, no explica la materia y energía oscura, ni explica por qué el universo está hecho de materia y no de antimateria. Esta última asimetría, llamada asimetría bariónica, evidencia que la simetría $\mathcal{CP}$ (combinación de las transformaciones $\mathcal{C}$ -conjugación de carga- y $\mathcal{P}$ -paridad-) no es una buena simetría en la naturaleza. Es evidente, por tanto, que el ME debe ser ampliado para tener en cuenta estos fenómenos. En esta tesis se presentan algunos observables sensibles a nueva física en la desintegración del quark top, en particular a la existencia de nuevos acomplamientos en el vértice Wtb (interacción electrodébil) que podrían introducir nuevas fuentes de violación de $\mathcal{CP}$. Dentro del ME este vértice es puramente levógiro, y su valor viene determinado por el elemento V_{tb} de la matrix de Cabibbo-Kobayashi-Maskawa (CKM). Desviaciones de la predicción del ME o correcciones radiativas pueden ser parametrizadas con el formalismo de un operador efectivo con nuevos acoplamientos (acoplamientos anómalos).

El quark top es la partícula fundamental más masiva observada experimentalmente. Su tiempo de vida es extremadamente corto (un orden de magnitud más pequeño que la escala temporal típica de la interacción fuerte que confina los quarks en hadrones) que se desintegre antes de

hadronizar y la información de espín se transfiera a sus productos de desintegración. Los datos registrados en los experimentos del LHC permiten medir con gran precisión las propiedades del quark top, entre ellas sus acoplamientos siendo sin duda el vértice Wtb de relevante importancia ya que el quark top decae casi exclusivamente a un bosón W y un quark b. Además, en el caso de quarks top producidos vía la interacción electrodébil, éstos están casi 100 % polarizados. En presencia de quarks top polarizados, es posible definir observables que permiten acceder a los acoplamientos anómalos tensoriales y son particularmente sensibles a sus partes imaginarias, lo que los hace especialmente adecuados para el estudio de la eventual violación de $\mathcal{CP}$ en el vértice Wtb. La parte principal de este trabajo es precisamente la medida de uno de estos observables (una asimetría) con datos registrados por el detector ATLAS durante 2011.

7.2 Marco teórico

7.2.1 El Modelo Estándar de Física de Partículas

El ME es la teoría que describe las partículas elementales que componen toda la materia y las interacciones entre ellas. Es una teoría cuántica de campos consistente con la mecánica cuántica y la relatividad especial, que combina la fuerza electromagnética, la débil y la fuerte. Según el ME, las partículas elementales se clasifican en *fermiones* (constituyentes de la materia) y *bosones* (mediadores de las fuerzas). Las partículas de la materia llevan cargas que las hacen susceptibles a las fuerzas fundamentales, siendo una de ellas el espín. Todas las partículas estables y con masa que conocemos están constituidas por fermiones, las cuales tienen espín 1/2. Siguen, por tanto, el teorema de la estadística de Fermi-Dirac y el principio de exclusión de Pauli. En el ME existen doce tipos de fermiones, seis de éstos se clasifican como quarks (up, down, charm, strange, top y bottom), y los otros seis como leptones (electrón, muón, tau, y sus neutrinos correspondientes), que se agrupan en tres familias o generaciones. Cada familia difiere de las otras en su sabor, i.e. el tipo de fermión y la masa de las partículas, mientras que tienen los mismos números cuánticos. Además, cada partícula tiene asociada una antipartícula, con la misma masa pero cargas opuestas. Los quarks no se encuentran libres en la naturaleza sino que se combinan formando hadrones. Éstos, junto a los leptones, forman la materia visible del universo.

Los quarks tienen carga eléctrica fraccionaria, los de tipo 'down' (down, strange y bottom) de -1/3, y los de tipo 'up' (up, charm y top) de +2/3, permitiendo a ambos tipos participar en interacciones electromagnéticas. Los leptones tipo 'down' (electrón, muón y tau) llevan una carga eléctrica de -1; mientras que los leptones tipo 'up' (neutrinos) no llevan y por tanto no sienten esta interacción. Los quarks y los leptones llevan varias cargas de sabor, incluyendo el isospín débil, permitiendo a todas ellas interaccionar recíprocamente vía la interacción débil. Los quarks tienen un número cúantico adicional, la carga de color. Existen tres tipos: roja, verde o azul, e indican como interactúan mediante la fuerza fuerte. Los leptones no llevan ninguna carga de color –son neutros en este sentido–, por lo que no participan en estas interacciones.

Las fuerzas que actúan entre los quarks y los leptones se describen mediante las llamadas teorías cuánticas de campos gauge. Los cuantos de estos campos tienen spin 1 y se llaman bosones de gauge. Consecuentemente, hay tantos bosones de gauge como generadores de campo en $SU_C(3)xSU_L(2)xU_Y(1)$: ocho tipo de gluones que transportan la interacción fuerte, los bosones

W^+, W^- y Z^0 de la interacción débil y los fotones que median la interacción electromagnética. La teoría gauge explica satisfactoriamente todas las interacciones siempre que la simetría sea exacta, lo cual requiere que todas las partículas mediadoras tengan masa nula y que las fuerzas sean de largo alcance. Sin embargo, las observaciones experimentales de los años 1983 y 1984 revelan que los bosones W^+, W^- y Z^0 son masivos. Los términos de masa para los campos en el lagrangiano del ME rompen la simetría de gauge, siendo necesario incorporar un mecanismo ad-hoc para generar partículas masivas. En el marco del ME, la teoría aceptada es el conocido Mecanismo de Higgs, que propone la introducción de un campo escalar que induce la rotura espontánea de la simetría, proporcionando de esta manera masa a fermiones y bosones. La partícula asociada a este campo es el bosón de Higgs, una partícula elemental masiva y de espín 0. Uno de los propósitos del LHC es la búsqueda del bosón de Higgs, delucidar este problema y entender cómo se generan las masas. En julio del 2012 tanto ATLAS [27] como CMS [28] anunciaron la observación de una nueva partícula "consistente con el bosón de Higgs", y tiempo después confirmaron que ésta se ve cada vez más como el bosón de Higgs del ME. Sin embargo, el estudio de sus propiedades necesita aún más tiempo para poder confirmar si realmente es así.

7.2.2 Violación de la simetría $\mathcal{CP}$ en el Modelo Estándar

La simetría $\mathcal{CP}$ se basa en la composición de la simetría C (conjugación de carga, i.e. intercambio de partículas y antipartículas) y la simetría $\mathcal{P}$ (paridad, i.e inversiones especulares). La interacción fuerte y la electromagnética son invariantes bajo la simetría C, $\mathcal{P}$ y $\mathcal{CP}$, es decir, el lagrangiano que describe estas interacciones es invariante respecto a transformaciones matemáticas asociadas a estas simetrías. Sin embargo, las interacciones débiles violan las simetrías discretas C y $\mathcal{P}$ de forma separada. A pesar de ello, la combinación de ambas, $\mathcal{CP}$, parece ser una buena simetría en la mayoria de los fenómenos observados. En la desintegración de mesones K y B hay señales de violación de $\mathcal{CP}$. Pero no sólo a esta escala, sino que la enorme asimetría que existe entre el contenido de materia del universo y el de antimateria implica que la violación de simetría $\mathcal{CP}$ tiene un rol crucial a la hora de explicar la generación primordial de bariones.

La violación $\mathcal{CP}$ está relacionada con la presencia de fases complejas entre amplitudes que interfieren. En el ME la única fuente de violación de $\mathcal{CP}$ es la fase compleja de la matriz de mezcla CKM[1]. Esto impone fuertes restricciones en la estructura del sector de sabor, como por ejemplo, el hecho de que deben existir al menos tres generaciones de quarks para que la matriz de mezcla tenga una fase compleja. El mecanismo de violación de $\mathcal{CP}$ del ME explica (hasta ahora) todos los datos experimentales pero no es capaz de explicar la asimetría bariónica observada en el universo ($Y_B = \frac{n_B - n_{\overline{B}}}{n_\gamma} \sim 10^{-9}$) y por tanto deben existir fuentes adicionales de violación de $\mathcal{CP}$. Este trabajo de tesis se centra en el estudio de la desintegración del quark top en el marco de modelos de nueva física (eventual violación de $\mathcal{CP}$) en el vértice Wtb.

7.2.3 Acomplamientos anómalos del quark top en el vértice Wtb

En el ME la estructura e intensidad del vértice Wtb viene dada por la interacción cargada:

[1]La matriz CKM relaciona los autoestados de la interacción con los de masa dentro del sector de los quarks. Es una matriz 3x3 y unitaria, tiene 4 parámetros independientes: tres ángulos de mezcla y una fase asociada a violación $\mathcal{CP}$.

$$\mathcal{L}_{Wtb}^{ME} = -\frac{g}{\sqrt{2}}\overline{u}_b\gamma^\mu V_{tb}\frac{1}{2}\left(1-\gamma^5\right)\overline{u}_t W_\mu + \text{h.c.}\,, \tag{7.1}$$

donde $\overline{u}_b$ y u_t representan los espinores correspondientes al quark b saliente y el quark top entrante, W representa el vector de polarización del bosón W saliente con cuadrimomento $\vec{q}$ y masa M_W, y V_{tb} es el elemento de la matriz de mezcla V_{CKM}. A continuación se presenta una parametrización más general del lagrangiano que describe este vértice que introduce momentos anómalos del quark top. La amplitud de la desintegración del quark top $t(p) \rightarrow b(k)W^+(q)$ más general para partículas en la capa de masa puede escribirse del siguiente modo:

$$\mathcal{L}_{W^+tb} = -\frac{g}{\sqrt{2}}\overline{u}_b\gamma^\mu\left(V_L P_L + V_R P_R\right)u_t W_\mu^+ - \frac{g}{\sqrt{2}}\overline{u}_b\frac{i\sigma^{\mu\nu}}{M_W}q_\nu\left(g_L P_L + g_R P_R\right)u_t W_\mu^+ \tag{7.2}$$

donde $P_{L/R} \equiv (1 \mp \gamma^5)/2$ son los proyectores de quiralidad izquierda/derecha, y $\sigma^{\mu\nu} = [\gamma^\mu, \gamma^\nu]/2$. V_L y V_R parametrizan los acoplamientos vectoriales mientras que g_L y g_R los tensoriales (llamados también momentos magnéticos tensoriales), y a priori pueden ser números complejos. A nivel árbol en el ME, los factores de forma se reducen a V_L=V_{tb} y V_R=g_L=g_R=0, obteniéndose la expresión de la Ecuación 7.1. Los acoplamientos tensoriales son cantidades que aparecen como correcciones cuánticas finitas en diagramas con loops [47].

Para la desintegración del quark antitop $\bar{t}(p) \rightarrow \bar{b}(k)W^-(q)$, la amplitud correspondiente es:

$$\mathcal{L}_{W^-\bar{t}\bar{b}} = -\frac{g}{\sqrt{2}}\overline{v}_t\gamma^\mu\left(V'_L P_L + V'_R P_R\right)v_b W_\mu^- - \frac{g}{\sqrt{2}}\overline{v}_t\frac{i\sigma^{\mu\nu}}{M_W}q_\nu\left(g'_L P_L + g'_R P_R\right)v_b W_\mu^- \tag{7.3}$$

La invariancia $\mathcal{CP}$ implica, no sólo que V_L sea real, sino también las siguientes relaciones entre los factores de forma [48, 49]:

$$CP \;\Rightarrow\; V'_i = V_i \quad g'_i = g_i \quad (i = L, R). \tag{7.4}$$

La violación de $\mathcal{CP}$ implica que los acoplamientos tengan partes imaginarias no nulas que son iguales en magnitud pero con signo opuesto:

$$CPV \;\Rightarrow\; Im(V'_i) = -Im(V_i) \quad Im(g'_i) = -Im(g_i) \quad (i = L, R). \tag{7.5}$$

La presencia de fases absortivas, inducidas en los diagramas con loops por la presencia de estados intermedios en la capa de masa, también da lugar a partes imaginarias en los acoplamientos tensoriales. Si $\mathcal{CP}$ se conserva éstas son iguales en magnitud y signo:

$$\text{Fases absortivas y } CP \;\Rightarrow\; Im(g'_i) = Im(g_i) \quad (i = L, R). \tag{7.6}$$

7.2.4 Observables sensibles a violación de $\mathcal{CP}$ en el vértice Wtb

Una prueba básica de la estructura del vértice Wtb es la medida de las fracciones de desintegración F_L, F_0 y F_R a bosones W de helicidades[2] λ: -1, 0 y +1, respectivamente. Éstas se

[2]La helicidad de una partícula es la proyección de su espín en la dirección de movimiento, así una partícula puede ser izquierda (helicidad negativa) o derecha (helicidad positiva).

pueden obtener a partir de las distribuciones angulares de sus productos de desintegración a leptones $W \to l\nu$, como $\cos\theta^*$ donde θ^* es el ángulo entre la dirección de salida del leptón en el sistema de referencia en reposo del bosón W y la dirección de salida del bosón W en el referencial en reposo del quark top. La estructura V-A (vector - axial) del vértice ($P_L \equiv (1-\gamma^5)/2$) en el ME y la conservación del momento angular permiten la desintegración a estados de helicidad cero (F_0 ~0.7) o negativa (F_L ~0.3) del bosón W, pero no con helicidad positiva (F_R ~0). La supresión de esta última ocurre porque el proyector P_L fuerza el quark b a tener helicidad negativa (si no tuviera masa, lo cual es una buena aproximación si se compara con la del bosón W o la del quark top), y por tanto, por conservación del momento angular, $\lambda = +1$ no es posible. Los valores medidos en los experimentos ATLAS y CMS [63] para las fracciones de helicidad son:

$$\begin{aligned} F_{\mathrm{L}} &= 0{,}359 \pm 0{,}021\ (\text{stat.}) \pm 0{,}028\ (\text{syst.}) \\ F_0 &= 0{,}626 \pm 0{,}034\ (\text{stat.}) \pm 0{,}048\ (\text{syst.}) \\ F_{\mathrm{R}} &= 0{,}015 \pm 0{,}034\ (\text{stat.} \oplus \text{syst.})\ . \end{aligned} \tag{7.7}$$

Estas medidas son compatibles con las predicciones del ME y han permitido poner límites a la parte real de los acomplamientos anómalos V_{R}, g_{L} y g_{R}. Sin embargo, estos observables no dan información sobre posibles fases complejas que implicarían violación de $\mathcal{CP}$ en este vértice. En presencia de quarks top polarizados, es posible definir observables particularmente sensibles a la parte imaginaria de los acoplamientos tensoriales. Esto los hace especialmente adecuados para el estudio de la eventual violación de $\mathcal{CP}$ en el vértice Wtb, siendo su medida experimental el objetivo principal de este trabajo.

En la desintegración de quarks top no polarizados, la única dirección con significado físico en el sistema de referencia en reposo del quark top es la del momento del bosón W ($\vec{q}$) o del quark b ($-\vec{q}$) salientes. Sin embargo, para quarks polarizados en la dirección $\vec{s}_t$, se pueden considerar dos nuevas direcciones normal $\vec{N}$ y transversal $\vec{T}$ al plano definido por $\vec{q}$ y $\vec{s}_t$, como muestra la Figura 7.1. Éstas se definen como:

$$\begin{aligned} \vec{N} &= \vec{s}_t \times \vec{q}\ , \\ \vec{T} &= \vec{q} \times \vec{N}\ , \end{aligned} \tag{7.8}$$

Así, de igual modo que se define θ^* para medir las fracciones de helicidad, se pueden definir distribuciones angulares para θ^{N} y θ^{T} y nuevas fracciones de polarización del bosón W con respecto a estas dos nuevas direcciones: F_-^N, F_0^N y F_+^N (normal), y F_-^T, F_0^T y F_+^T (transversal). En particular, las anchuras de desintegración en la dirección normal son proporcionales a la parte imaginaria de los acoplamientos anómalos y el término dominante es $Im(V_{\mathrm{L}} g_{\mathrm{R}}^*)$. Ésto implica que una polarización neta del bosón W en la dirección normal ($F_+^N \neq F_-^N$) sólo puede tener lugar si existen fases complejas en los acoplamientos anómalos del vértice Wtb. Ésta es una propiedad exclusiva de la dirección normal.

De igual modo que para medir las fracciones de helicidad se definen asimetrías adeltante-detras (FB) $A_{\mathrm{FB}} = \frac{3}{4}(F_{\mathrm{R}} - F_{\mathrm{L}})$ con respecto a $\cos\theta^*$, aquí nuevas asimetrías pueden definirse:

$$\begin{aligned} A_{\mathrm{FB}}^{\mathrm{N}} &= \tfrac{3}{4}\, P\, (F_{\mathrm{R}}^N - F_{\mathrm{L}}^N) \\ A_{\mathrm{FB}}^{\mathrm{T}} &= \tfrac{3}{4}\, P\, (F_{\mathrm{R}}^T - F_{\mathrm{L}}^T) \end{aligned} \tag{7.9}$$

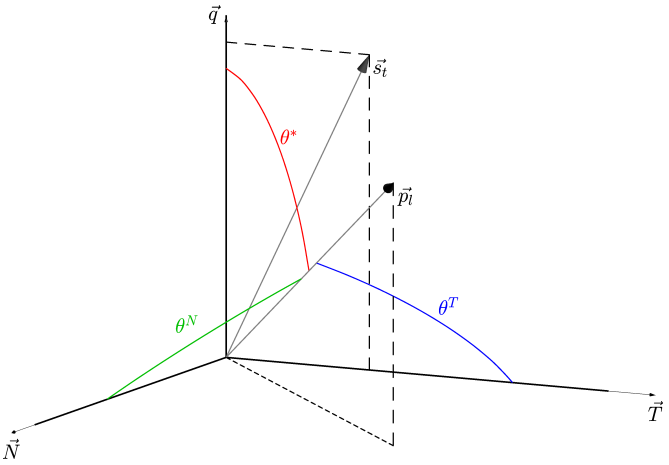

Figura 7.1: *Definición de las direcciones normal $\vec{N}$ y transversal $\vec{T}$ al plano definido por la dirección de polarización del quark top, $\vec{s}_t$, y del momento del bosón W en el sistema de referencia del quark top, $\vec{q}$. Los ángulos θ^*, θ^N y θ^T se definen entre cada uno de los ejes ($\vec{q}$, $\vec{N}$ y $\vec{T}$) y el momento del leptón en el sistema de referencia en reposo del bosón W, $\vec{p}_l$.*

En este caso las asimetrías dependen del grado de polarización del quark top. En especial la asimetría $A_{\rm FB}^{\rm N}$ se anula para acoplamientos reales (y en particular en el ME) y es muy sensible a $Im(g_{\rm R})$. Para valores de $g_{\rm R}$ pequeños y tomando $V_{\rm L}$=1, $V_{\rm R}$=$g_{\rm L}$=0, se obtiene: $A_{\rm FB}^{\rm N}\approx$ 0,64 P $Im(g_{\rm R})$ [3].

Hay que tener en cuenta que partes absortivas de los diagramas involucrados pueden inducir una asimetría y violaciones de $\mathcal{CP}$ no genuinas. Es por tanto conveniente medir $A_{\rm FB}^{\rm N}$ en sucesos con quarks top y antitop por separado, y sumar las asimetrías obtenidas ya que ésta señala, sin ambiguedad, la presencia de violación de $\mathcal{CP}$: $A_{FB}^{CP} = A_{FB}^{N}(t) + A_{FB}^{N}(\bar{t})$.

En esta tesis se presenta una primera medida de esta asimetría con datos registrados por el detector ATLAS del LHC en 2011, a partir de la cual se ha podido extraer la primera cota experimental a la parte imaginaria del acomplamiento anómalo $Im(g_{\rm R})$. La incertidumbre obtenida en el resultado obtenido está limitado por el error estadístico por lo que se ha preferido no dividir en sucesos con quarks top y antitops. Los datos registrados en 2012 y en la próxima fase de toma de datos de este acelerador permitirán alcanzar mayor precisión y además medir por separado estas asimetrías.

7.3 El acelerador LHC y el detector ATLAS

7.3.1 El acelerador LHC

El LHC es un acelerador y colisionador de partículas ubicado en la Organización Europea para la Investigación Nuclear (CERN) cerca de Ginebra, en la frontera franco-suiza. En la actualidad, el LHC es el acelerador de partículas más grande y energético del mundo. Tiene forma

circular y está ubicado en un túnel de 27 km de circunferencia a 100 m de profundidad. Dentro del colisionador, dos haces de protones son acelerados en sentidos opuestos hasta alcanzar casi la velocidad de la luz. Para lograr tal energía, los imanes que curvan la trayectoria de las partículas son enfriados a una temperatura de 1.9 K (-271.15 °C). Estos haces chocan entre sí en cuatro puntos del anillo en los que se han construido detectores de partículas.

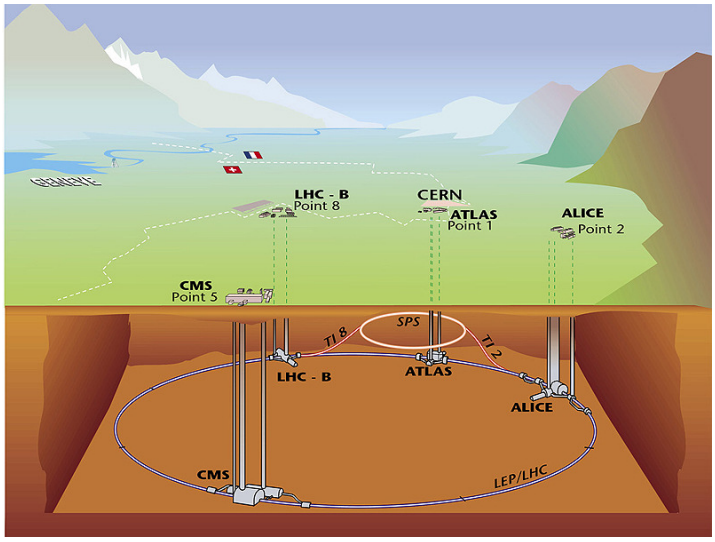

Figura 7.2: *Ilustración del acelerador LHC y cuatro de sus experimentos ATLAS, CMS, ALICE y LHCb.*

En el LHC hay seis experimentos, siendo cuatro de ellos grandes detectores localizados en los cuatro puntos de colisión del acelerador (ver Figura 7.2) y otros dos más pequeños y específicos. ATLAS y CMS son detectores de propósito general, es decir, diseñados para estudiar un amplio rango de procesos físicos, desde medidas de alta precisión dentro del ME como la búsqueda del bosón de Higgs o evidencias de nueva física. Estos tipos de detectores constan de una serie de cilindros concéntricos de tamaños crecientes que rodean el punto donde colisionan los haces de protones. Poseen imanes que curvan las partículas cargadas y están compuestos por diferentes subdetectores: detectores de trazas, calorímetros y cámaras de muones. ATLAS es el detector más grande, con 44 m de largo y 25 m de alto y un peso de 7000 toneladas. Posee dos imanes, uno solenoidal de 2 T envolviendo el subdetector más interno y uno toroidal que genera un campo de hasta 6 $\mathrm{T}\cdot\mathrm{m}$ en las cámaras de muones. CMS es algo más pequeño, con 21 m de largo y 15 m de alto, pero más pesado que el primero, con 12500 toneladas. Posee un único imán que genera un campo magnético no lineal de hasta 4 T. LHCf (Large Hadron Collider forward) [69], en ATLAS, y TOTEM (Total Cross Section, Elastic Scattering and Diffraction Dissociation) [68], en CMS, tienen como objetivo estudiar procesos difractivos y dispersiones inelásticas a ángulos bajos, es decir, producidos en las regiones hacia delante de las colisiones. A continuación, ALICE (A Large Ion Collider Experiment) [66] está especializado en el estudio de colisiones de iones pesados y del plasma de quarks y gluones. Por último, LHCb (Large Hadron Collider beauty) [67] está diseñado para estudiar las interacciones de hadrones B.

La gran cantidad de datos producidos por el LHC y registrados en sus detectores requiere una enorme red de computación. Con tal objetivo, se ha desarrollado el proyecto Grid: una tecnología innovadora que permite utilizar de forma coordinada todo tipo de recursos (infraestructura necesaria para el análisis y almacenamiento de los datos) siendo en este sentido una nueva forma de computación distribuida.

Sistema de coordenadas

El sistema de coordenadas elegido corresponde a un sistema cartesiano, cuyo origen coincide con el punto de interacción nominal. Dada la simetría cilíndrica de los detectores, resulta adecuado definir el eje z en la dirección del haz, siendo el plano $x - y$ transverso a la dirección del haz. El eje x se define apuntando desde el punto de interacción hacia el centro del anillo del LHC, mientras que el eje y apunta hacia arriba. Para describir la posición de los distintos subdetectores y la trayectoria de las partículas se utilizan frecuentemente sistemas de coordenadas cilíndricas o polares. El radio R se define como la distancia perpendicular al eje del haz. El ángulo azimutal ϕ se mide con respecto al eje x positivo y crece en sentido horario entorno al eje z positivo, mientras que el ángulo polar θ se mide con respecto a este último. Una cantidad muy importante utilizada en física de altas energías es la llamada pseudo-rapidez η cuya definición es:

$$\eta = - \log[\tan(\theta/2)] \, . \tag{7.10}$$

La razón detrás de esta transformación de coordenadas es el hecho que la multiplicidad de partículas producidas es aproximadamente constante con respecto a η, y que la diferencia de pseudo-rapidez entre dos partículas es invariante frente a transformaciones de Lorentz a lo largo de la dirección del haz. En colisionadores de hadrones, debido a su estructura interna con quarks y gluones, los partones que colisionan llevan tan sólo una fracción del momento del hadrón (en el caso del LHC del protón) y ésta es desconocida. Otra parte escapa a lo largo del haz. Así, no es posible reconstruir el movimiento longitudinal del centro de masa en la interacción. Sin embargo, dado que los protones inciden a lo largo de la dirección del haz, el impulso total transverso es conservado durante la colisión. Por esta razón, sólo las componentes transversales son utilizadas en la descripción de la cinemática de un suceso, e.g. $E_T = E \sin\theta$ y $p_T = p \sin\theta$.

Luminosidad

La luminosidad es una cantidad proporcional al número de partículas por unidad de superficie y de tiempo en un haz. Al integrar esta cantidad en un intervalo de tiempo se obtiene la luminosidad integrada. Su valor depende de la capacidad del experimento para generar paquetes de partículas que interactuarán luego, mientras que la sección eficaz es una cantidad que sólo está relacionada con la física propia de la interacción. La luminosidad integrada se mide en unidades inversas de área o barns[3]. En física de partículas se utilizan normalmente los pb^{-1} (10^{-12} b^{-1}) o fb^{-1} (10^{-15} b^{-1}).

[3]El barn es una unidad de área: 1 b = 10^{-28} m^2 = 100 fm^2

7.3.2 El detector ATLAS

El trabajo desarrollado en esta tesis se enmarca en el detector ATLAS. Éste se compone de un barril y dos tapas (en inglés 'end-caps') y, como se ha anticipado, está compuesto por tres subdetectores: el detector interno o de trazas, los calorímetros y las cámaras de muones. Cada parte se subdivide a su vez en más capas.

Detector de trazas

El detector de trazas es el sistema más cercano al haz, por lo que también se llama detector interno, y está diseñado para proporcionar una excelente resolución en la reconstrucción del momento de las partículas cargadas así como de sus vértices primarios y secundarios. Se compone de tres tipos de subdetectores, dos basados en silicio y uno en tubos de deriva, resistentes a altas dosis de radiación. Posee dos tecnologías diferentes para los detectores de silicio, píxeles y microbandas. Está inmerso en un campo magnético de 2 T creado por un solenoide y tiene una cobertura espacial de $|\eta| < 2{,}5$.

Calorímetros

Inmediatamente después del solenoide se encuentran los calorímetros. En primer lugar se encuentra el calorímetro electromagnético ECAL que permite la identificación y reconstrucción de electrones y fotones, y a continuación el hadrónico HCAL para medir la energía de los jets así como determinar la energía transversa faltante (energía que se llevan los neutrinos y que no es directamente detectada). El primero utiliza argón líquido como medio de ionización y posee una geometría en forma de acordeón, mientras que el segundo usa una tecnología de tejas centelleadoras.

Cámaras de muones o espectrómetro de muones

Finalmente, en la parte más exterior de ATLAS, se encuentran las cámaras de muones, inmersas en un intenso (1.5-7.5 $\mathrm{T} \cdot \mathrm{m}$) campo magnético generado por un toroide. Existen cuatro tipos de tecnologías, optimizadas para identificar los sucesos más interesantes (conocido como sistema de 'trigger' en inglés y 'disparo' en castellano) y medir con precisión el momento de los muones.

La Tabla 7.1 muestra la resolución que se espera alcanzar en cada uno de los subdetectores.

Por último cabe mencionar el sistema de trigger de ATLAS, cuya finalidad es seleccionar los sucesos más interesantes desde el punto de vista físico, reduciendo de este modo la cantidad de datos a almacenar. Así, se pasa de 40 millones de sucesos por segundo a tan sólo unos 100. Existen tres niveles en la selección: el primero se basa en la información de la electrónica del detector ('hardware'), en concreto de los calorímetros y de las cámaras de muones, mientras que los otros están basados en 'software' y se ejecutan en un gran cluster situado cerca del detector.

Subdetector	Resolución	Cobertura en $\|\eta\|$
Detector de trazas	$\sigma_{p_T}/p_T = 0{,}05\,\% \times p_T \oplus 1\,\%$	±2.5
ECAL	$\sigma_E/E = 10\,\%/\sqrt{E} \oplus 0{,}7\,\%$	±3.2
HCAL		
central	$\sigma_E/E = 50\,\%/\sqrt{E} \oplus 3\,\%$	±3.2
lateral	$\sigma_E/E = 100\,\%/\sqrt{E} \oplus 10\,\%$	3.1 < $\|\eta\|$ <4.9
Cámaras de muones	$\sigma_{p_T}/p_T = 10\,\%$ at $p_T = 1\,TeV$	±2.7

Tabla 7.1: *Resoluciones esperadas y cobertura en $|\eta|$ de los diferentes subdetectores de ATLAS.*

7.3.3 Muestras de datos tomados por el detector ATLAS

Puesta a punto con rayos cósmicos

La instalación del detector ATLAS en la caverna, i.e. en uno de los puntos del túnel del LHC a 100 m de profundidad, finalizó en julio de 2008. Desde entonces y hasta las primeras colisiones del LHC a finales del 2009, tuvo lugar una campaña de puesta a punto con sucesos de rayos cósmicos en la que todos los subdetectores estuvieron registrando datos de forma combinada con diferentes configuraciones, tanto de los subdetectores como de los imanes. Hubo tres períodos de toma de datos, otoño de 2008 y verano y otoño de 2009. En total se registraron más de 200 millones de sucesos, que permitieron poner a prueba todo el sistema de adquisión y procesado de datos, desde el 'software' de control hasta la reconstrucción.

Datos de colisiones de protones

Las primeras colisiones de protones en el LHC tuvieron lugar a finales del 2009, primero a energías en centro de masas de 0.9 TeV y posteriormente 2.36 TeV, convirtiéndose en el acelerador de partículas más potente del mundo. En marzo de 2010 las colisiones de protones alcanzaron una energía en centro de masas de 7 TeV. Durante ese año y hasta finales de 2011 se registraron unos 5.6 fb^{-1} de datos a 7 TeV, y durante el año 2012 unos 23.3 fb^{-1} a 8 TeV. En febrero de 2013 se paró para realizar una serie de mejoras necesarias para la operación a la energía máxima de 13–14 TeV, y se espera que retome su funcionamiento en 2015.

7.4 Estudios con los primeros datos de ATLAS

7.4.1 Reconstrucción combinada de muones de rayos cósmicos

Los rayos cósmicos son partículas subatómicas y muy energéticas procedentes del espacio exterior cuya velocidad es cercana a la de la luz. Cuando un rayo cósmico llega a la atmósfera terrestre interactúa con átomos de ésta, los excita y genera nuevas partículas. Éstas, a su vez, colisionan con otras generando otras nuevas y así se van creando cascadas de reacciones nucleares. Los rayos cósmicos que alcanzan la capa superior de la atmósfera son mayoritariamente protones y partículas α de alta energía, mientras que a nivel del mar están constituidos principalmente por muones (llamados muones cósmicos).

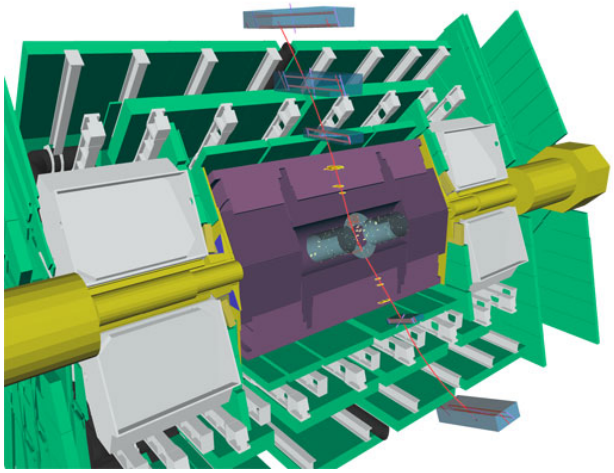

Figura 7.3: *Suceso registrado en ATLAS en el que un muón cósmico cruza el detector de arriba a abajo dejando señal en todos los subdetectores: las cámaras de muones (gris claro), los calorímetros (gris oscuro) y el detector interno en el centro.*

En ausencia de colisiones, los muones cósmicos permitieron testear toda la cadena de funcionamiento del detector con datos reales, desde el sistema de adquisición hasta las algoritmos de calibración, alineamiento y reconstrucción. Los sucesos de rayos cósmicos llegan a la caverna de ATLAS desde la superficie y atraviesan el detector de arriba a abajo, como puede verse en la Figura 7.3. Puesto que los muones interaccionan como partículas de mínima ionización ('mips') dejan señal en todos los subdetectores. Así, los muones cósmicos permiten no solo estudiar cada subdetector por separado sino también combinar la información de todos ellos y reconstruir una traza combinada que cruza ambos hemisferios del detector. La primera parte de esta tesis es precisamente un estudio de la reconstrucción combinada de estos muones usando el algoritmo global χ^2 [123]. El análisis se basa en los datos de rayos cósmicos registrados en ATLAS en otoño del 2009 durante la fase de puesta a punto y se centra en la zona del barril, ya que es la región donde se registraron la mayoría de los rayos cósmicos.

La reconstrucción de muones cósmicos tiene unas diferencias fundamentales respecto a los de colisiones del LHC ya que éstos vienen de cualquier dirección y además en tiempos aleatorios, de modo que estos sucesos no están sincronizados con el reloj de lectura de los detectores. Debido a ello, los algoritmos de reconstrucción de muones fueron adaptados para tener en cuenta estas características.

La detección de muones tiene lugar principalmente en el detector de trazas y las cámaras de muones. Previo a la reconstrucción global de muones, es importante verificar que ambos subdetectores están sincronizados y alineados espacialmente. La Figura 7.4-izquierda muestra el parámetro θ_0 (ángulo con el eje del haz) medido en el detector interno y en las cámaras de muones. La correlación entre ellos verifica que ambos subdetectores están sincronizados entre sí. De

hecho, la diferencia entre las dos medidas es una distribución centrada en cero, indicando que el alineamiento mecánico es relativamente bueno teniendo en cuenta que no se habián utilizado correcciones de alineamiento globales en la reconstrucción (ver Figura 7.4-derecha).

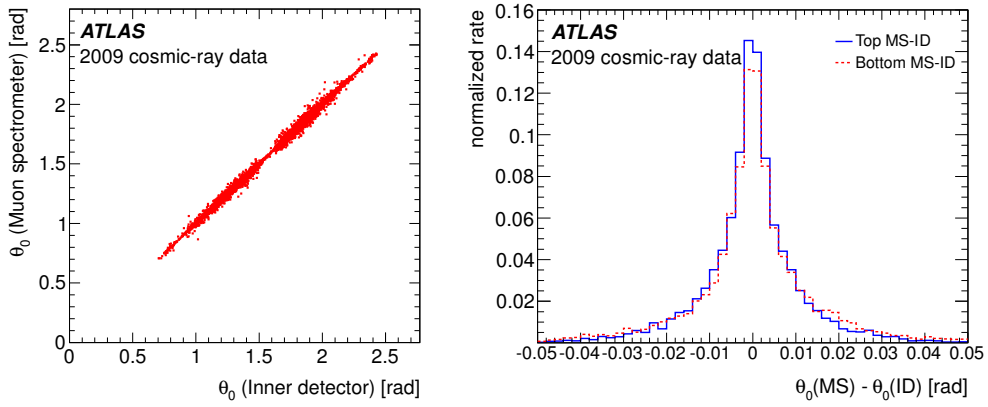

Figura 7.4: *Correlación (izquierda) y diferencia (derecha) del parámetro angular θ_0 medido en el detector interno y en las cámaras de muones.*

Una vez se han reconstruido ambas trazas, se hace un ajuste χ^2 global de las mismas a lo largo de todo el detector obteniendo así trazas combinadas de muones. La información de la energía depositada por el muón en los calorímetros (∼3 GeV) se tiene en cuenta al extrapolar la traza exterior al perigeo[4] La Figura 7.5 muestra la resolución de los parámetros angulares ϕ_0 (ángulo azimutal) y θ_0 en función del momento del muón reconstruido con ambos detectores (muón combinado). Para altos valores del momento transverso se alcanza una resolución de unos 0.16 y 0.80 mrad respectivamente. La resolución en momento transverso se muestra en la Figura 7.6 para las trazas reconstruidas en cada uno de los subdetectores y la combinada. La resolución en el detector interno es de ∼1.6 % a bajo momento y de ∼50 % para muones de 1 TeV. Para trazas reconstruidas en las cámaras de muones, ésta última mejora hasta ∼20 %. Se puede ver que la resolución mejora combinando la información de ambos subdetectores. Cabe destacar también que ésta se degrada a valores altos del momento debido a que el radio de curvatura es menor y por tanto la medida del momento es menos precisa. A bajo momento transverso la resolución está dominada por efectos de dispersión debidos al material, mientras que a alto momento depende de la resolución intrínseca.

7.4.2 Estudios de jets con los primeros datos de colisiones a 7 TeV

En marzo del 2010 tuvieron lugar las primeras colisiones de protones a 7 TeV y durante ese año ATLAS registró unos 45 pb^{-1}. Estos datos permitieron estudiar la reconstrucción de los objetos en el estado final así como obtener las primeras medidas de secciones eficaces de diferentes procesos. La contribución de este trabajo es un estudio relacionado con la estructura de los jets

[4]El perigeo es el punto de la trayectoria más cercano al eje z.

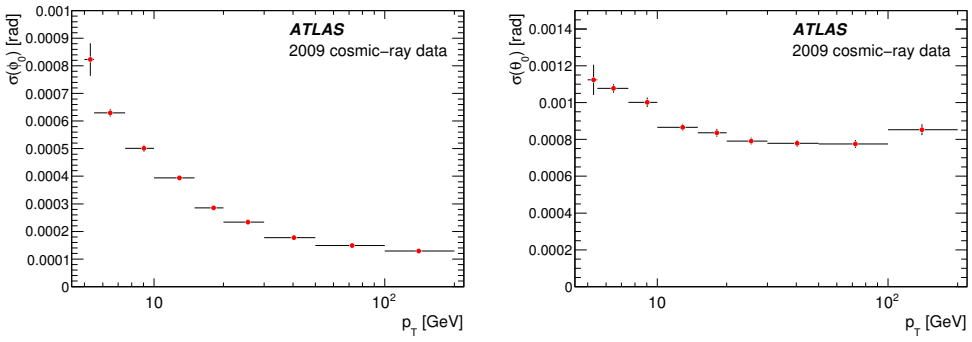

Figura 7.5: *Resolución de los parámetros angulares ϕ_0 (izquierda) y θ_0 (derecha) en función de p_T del muón reconstruido.*

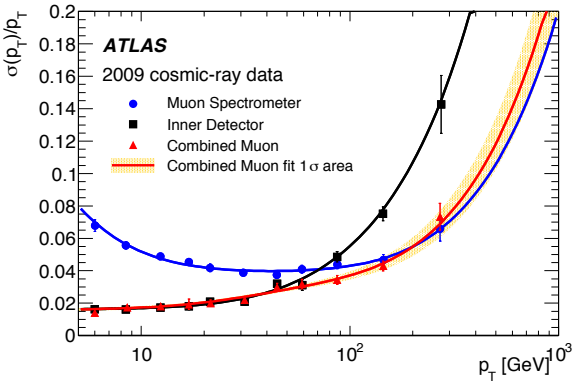

Figura 7.6: *Resolución en la medida del momento transverso de los muones reconstruidos en las cámaras de muones (puntos), en el detector interno (cuadrados) y de forma combinada (triángulos).*

a través de la medida de las conocidas 'jet shapes', que proporciona información de los detalles del proceso de radiación de gluones y de hadronización en colisiones de hadrones.

Los jets resultan de la fragmentación de los partones y aparecen en el detector como una composición de materia hadrónica cargada (principalmente piones), de materia hadrónica neutra (kaones y neutrones) y electromagnética neutra (fotones procedentes del piones neutros). La transición de partones a jets puede describirse en dos pasos: radiación y fragmentación de gluones (llamada 'lluvia partónica', en inglés 'parton shower') que es descrita mediante la teoría QCD en su régimen perturbativo y el proceso de hadronización (proceso no perturbativo). Aunque este último no se conoce con precisión, existen varios modelos fenomenológicos para describir el fenómeno de la hadronización: uno implementado en el generador PYTHIA y otro en HERWIG.

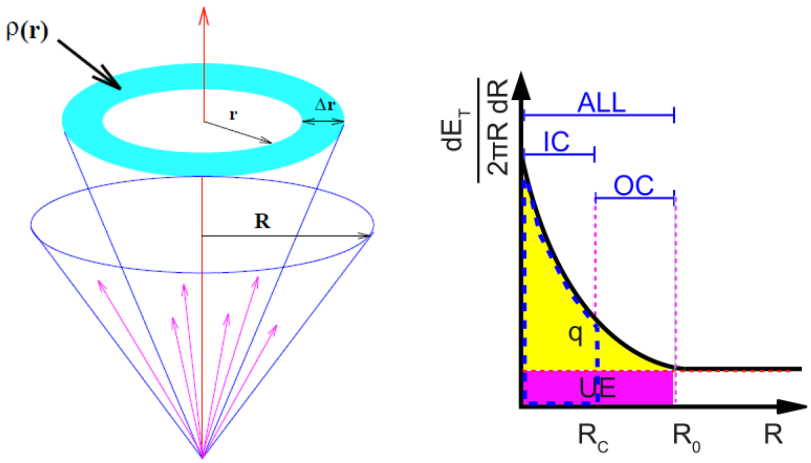

Figura 7.7: *Izquierda: Definición de 'jet shapes' diferenciales. Derecha: Representación esquemática de la distribución escalar de p_T alrededor del eje del jet. 'R_C' es el tamaño del cono usado en la reconstrucción y 'R_0' es un radio relativamente grande que incluye toda la cascada hadrónica. 'IC' se refiere a la región dentro del cono ('in-cone', $R \leq R_C$), 'OC' a la región fuera del cono ('out-cone', $R_C < R \leq R_0$) y 'ALL' incluye ambas. La zona amarilla incluye todo el p_T de la cascada hadrónica originada por el partón inicial que es eventualmente reconstruida en el jet; la región morada es la contribución de p_T procedente del 'underlying event'; y la zona dentro de la línea discontinua azul corresponde al jet a nivel de hadrones.*

La correspondencia entre la energía de los partones producidos en el 'hard scattering' y la reconstruida en el calorímetro está influenciada por diversos factores: efectos físicos tales como la fragmentación, radiación inicial y final e interacciones de otros partones del protón, y efectos del detector, como el campo magnético, no linealidades, material muerto, ruido electrónico, fugas longitudinales de energía, etc. Por tanto, la reconstrucción de los jets no es trivial, y en muchas ocasiones además depende del algoritmo utilizado en la reconstrucción del jet (tamaño del cono o algoritmo de clusterización, separación entre jets, solapamiento, etc.). El trabajo presentado aquí consiste en estudiar la estructura de los jets a través de la distribución escalar de su p_T ('jet shapes'), y en particular comparar la fracción de energía que queda fuera del cono utilizado en la reconstrucción, en inglés 'out-of-cone energy' (OOC), en datos reales con las predicciones de Monte Carlo.

En este análisis se han seleccionado sucesos con dos jets producidos en colisiones de protones a una energía en centro de masas de 7 TeV. Los jets son reconstruidos con el algoritmo anti-k_t R_C=0.4 [104] a partir del cuadrimomento de los topoclusters (celdas) en el calorímetro, y deben cumplir unos criterios de selección, entre ellos momento transverso $p_T > 20$ GeV y pseudo-rapidez $\eta < 2.5$. Las 'jet shapes' obtenidas en datos se han comparado con los modelos Pythia 6.4.21 [127] y Herwig 6.5 [129]. Análisis similares se estaban realizando con estos datos, sin embargo utilizaban un parámetro R_C algo mayor (R_C=0.6) al empleado en los análisis con quarks top y solo se centraban en la región de dentro del cono ($r \leq R_C$).

Como se ha comentado, la distribución de momento del jet en función de la distancia al eje r (flujo de energía, como puede verse en los esquema de la Figura 7.7) son sensibles a los detalles de la radiación partónica y al fenómeno de hadronización. La Figura 7.8 muestra estas distribuciones para jets con momento entre 20 y 60 GeV. Puede verse que, en la región dentro del cono ($r \leq R_C$=0.4), las predicciones de Monte Carlo describen los datos dentro de los errores estadísticos. Cabe destacar que las incertidumbres sistemáticas no se han estimado, ni tampoco se han corregido los datos por los efectos del detector, de modo que la comparación de los datos y las predicciones teóricas es a nivel de reconstrucción.

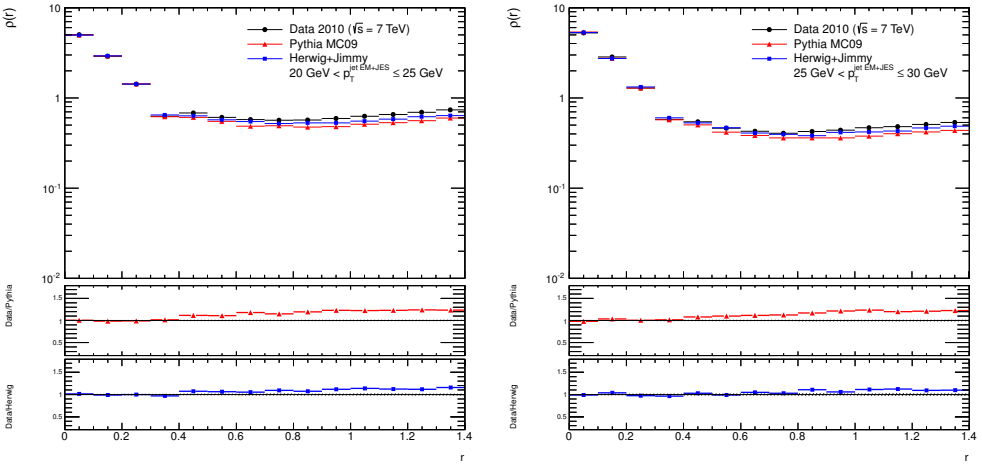

Figura 7.8: *Distribución de momento del jet reconstruido, $\rho(r)$, en sucesos con dos jets con $|\eta| < 2.5$ y 20 GeV < $p_T \leq$ 60 GeV. También se muestran las predicciones de* Pythia *y* Herwig.

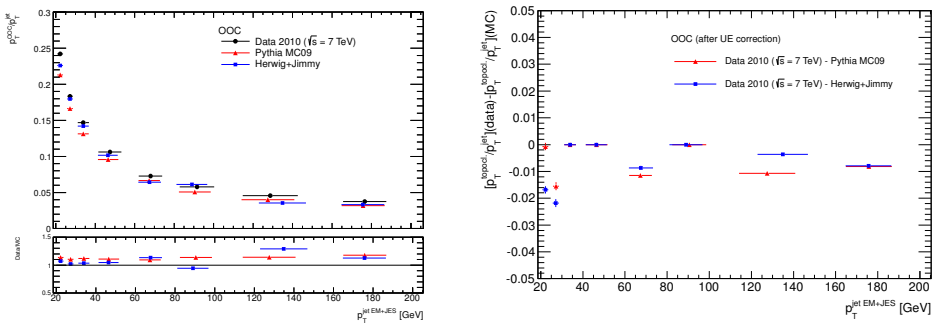

Figura 7.9: *Suma del momento transverso de los topoclusters en la región 'fuera del cono', de R_C=0.4 a R_0=0.8, normalizada al momento del jet reconstruido (R_C=0.4).*

A partir de estas distribuciones se ha obtenido la fracción de energía que queda fuera del cono y la contribución del 'underlying event'[5]. La parte izquierda de la Figura 7.9 muestra la suma del momento transverso de los topoclusters en la región 'fuera del cono', i.e. $0.4< r \leq 0.8$, normalizada al momento del jet reconstruido ($r \leq R_C$), es decir, la fracción de momento del jet que queda fuera del cono. Sin embargo, esta cantidad incluye contribuciones subyacentes del 'underlying event'. Para discernir entre los dos efectos, esta última ha sido estimada teniendo en cuenta que es independiente de la distancia al eje del jet y de su energía. Así, el 'underlying event' se estima a partir de la energía en la región transversa ($60° < \Delta\phi \leq 120°$) a la dirección del jet de mayor momento y se define como la suma del momento de los topoclusters normalizada a la unidad de área. Tras substraer esta cantidad se obtiene que la discrepancia entre la fracción de momento que queda realmente fuera del cono del jet en datos reales y las predicciones del Monte Carlo es de 1-2 %, como se muestra en Figura 7.9-derecha. En general ambos modelos reproducen los datos de forma similar dentro de las incertidumbres estadísticas asociadas.

7.5 Búsqueda de violación de CP en sucesos con quarks top

El quark top es la partícula elemental más masiva que se conoce ($m_{top} = 173{,}34 \pm 0{,}27(\text{stat.}) \pm 0{,}71(\text{syst.})$ GeV [18]) y pertenece a la tercera generación de quarks. Debido a su alta masa, este quark posee unas propiedades muy interesantes que no poseen los demás quarks: su vida media es tan corta ($5 \cdot 10^{-25}$ s) que se desintegra (con cambio de sabor) antes de formar hadrones con otros quarks. Esto permite estudiar las propiedades de un quark aislado, tras su reconstrucción a partir de sus productos de desintegración. El quark top se desintegra casi exclusivamente en un bosón W y en un quark b.

El quark top se descubrió en 1995 en los experimentos de Tevatron[6], CDF [42] y D0 [43], en el laboratorio de Fermilab. Previo al Tevatrón, ningún acelerador de partículas había alcanzado la energía necesaria. En los colisionadores de hadrones, la producción de quarks top es posible mediante dos mecanismos: producción dominante de pares $t\bar{t}$ vía interacción fuerte, y producción de un único quark top ('single top quark') vía interacción electrodébil. En el ME, los pares de quarks top son producidos vía fusión de gluones y aniquilación quark-antiquark. En el caso de single top quarks, existen tres modos: intercambio de bosones W a través de los canales t y s, y la producción asociada de un quark top junto con un bosón W. La sección eficaz de producción esperada para single top quarks es un factor 2-3 inferior a la de pares $t\bar{t}$ y además la señal es mucho menos nítida debido a los procesos de fondo. La observación de la producción electrodébil del quark top es un reto experimental y solo fue posible en 2009, también en el Tevatrón, con una luminosidad integrada de unos 3.2 fb^{-1}. En la actualidad el colisionador LHC es una fábrica de quarks top y permite realizar nuevas medidas y con mayor precision. La producción de single top quarks proporciona una oportunidad única para el estudio de la polarización de los quark top, ya que el ME predice que éstos deben estar casi 100 % polarizados cuando son producidos mediante interacción electrodébiles. La mayor contribución de este trabajo de tesis es precisa-

[5] 'Underlying event' son todos aquellos procesos de baja energía que acompañan a la interacción principal de interés, es decir, todas la partículas del suceso excepto las del propio 'hard scattering'.

[6] Tevatron fue el acelerador de partículas más potente del mundo hasta que se construyó el LHC. Estaba ubicado en el laboratorio de Fermilab en Batavia, Illinois (Estados Unidos). Era también circular y aceleraba protones y antiprotones hasta energías de casi 1 TeV. Hubo dos fases de toma de datos: 1992-1996 y 2001-2011.

mente la medida de la asimetría $A_{\mathrm{FB}}^{\mathrm{N}}$ sensible a nuevas fuentes de violación de $\mathcal{CP}$ y definida a partir de la dirección de polarización del quark top en el canal t. Este análisis constituyó en su momento la primera medida de una propiedad de single top quarks, proporcionando también por primera vez un límite de exclusión a la parte imaginaria de uno de los acoplamientos anomalos del vértice Wtb.

7.5.1 Introducción

El análisis presentado se basa en los datos registrados en ATLAS en el año 2011 en colisiones de protones a 7 TeV, y que corresponde a una luminosidad integrada de 4.66 fb^{-1}. La señal son sucesos de single top quarks producidos a través del canal t, que es el dominante con una sección eficaz de unos 65 pb [51]. Los diagramas de Feynman para este canal de producción de single top quarks se presentan en la Figura 7.10. Sólo los sucesos en los que el bosón W decae leptónicamente son seleccionados en este análisis ya que proporcionan una signatura mucho más limpia. Los leptones considerados en este caso son electrones y muones; la desintegración del tau se incluye cuando éste se desintegra a uno de los otros leptones. Por tanto, en el estado final se espera un leptón, una cantidad signicativa de energía transversa faltante $E_{\mathrm{T}}^{\mathrm{miss}}$ (debido a la presencia de un neutrino, que no es directamente detectable) y dos jets, uno de ellos procedente de la fragmentación de un quark b. La Figura 7.11 muestra un candidato a este tipo de proceso.

Son muchos y con una alta tasa de producción los procesos que presentan este mismo estado final, contribuyendo así a la composición de la muestra estudiada. Estos procesos se llaman fondos; los considerados en este análisis son: pares de quarks top (producción vía interacción fuerte) y otros canales con un único quark top, W+jets, Z+jets, dibosones (WZ, ZZ y WW) y QCD multijets. Estos procesos han sido simulados usando diferentes generadores: AcerMC+Pythia [127, 133] para la señal, Powheg+Pythia [142] para los procesos de fondo con quarks top, Alpgen+Herwig [145] para W/Z+jets, Herwig para dibosones y Pythia para QCD multijets. Además, para algunos de los fondos principales (W+jets y QCD), se han empleado métodos basados en datos para estimar su contribución, ya que la predicción dada por la simulación de Monte Carlo no es lo suficientemente precisa. Los objetos reconstruidos en el estado final así como los sucesos deben pasar una serie de criterios de calidad y selección, optimizados con el propósito de maximizar la eliminación de los fondos, a la vez que se consigue una alta eficiencia de selección para los sucesos de señal.

7.5.2 Reconstrucción de objetos en el estado final y preselección de sucesos

A continuación se describe brevemente la reconstrucción y selección de los objetos en el estado final:

- **Electrones:** Éstos dejan su trayectoria en el detector de trazas y toda su energía en el calorímetro electromagnético, siendo estas señales explotadas para su identificación y recontrucción. En este análisis se seleccionan sucesos con un único electrón aislado (cortes en la energía en los calorímetros y trazas en un cono alrededor del electrón de ΔR [7] 0.2 y 0.3, respectivamente), con $p_T > 25$ GeV y pseudo-rapidez $|\eta| < 2.47$, excluyendo la zona de transición entre el barril y los end-caps.

[7] $\Delta R = \sqrt{\Delta\eta^2 + \Delta\phi^2}$

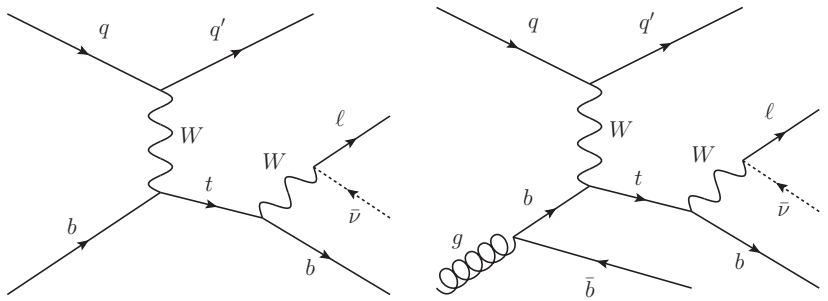

Figura 7.10: *Diagramas de Feynman para el proceso de producción de un único quark top en el canal t. El quark b inicial proviene del 'mar' de quarks y gluones del protón o de la fragmentación de un gluón.*

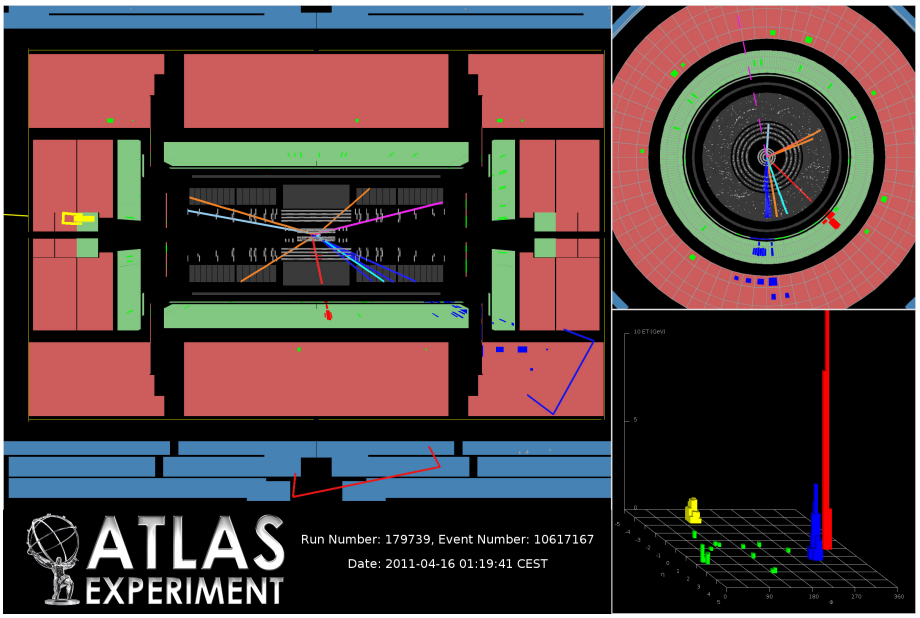

Figura 7.11: *Ilustración de un candidato a single top quark. El leptón (en este caso electrón) se muestra en rojo, el jet etiquetado como b-jet en azul, y el quark ligero de la zona 'forward' en amarillo. La energía transversa faltante $E_{\mathrm{T}}^{\mathrm{miss}}$ corresponde a la línea discontinúa en la proyección x-y transversal al eje de los haces (arriba derecha). El quark ligero se detecta en la zona 'forward' del calorímetro y por tanto no aparece en la proyección x-y.*

- **Muones:** Éstos se reconstruyen combinando las trazas reconstruidas en el detector interno con aquellas de las cámaras de muones y se requiere que tengan $p_T > 25$ GeV y $|\eta| < 2.5$. Además, los muones deben satisfacer una serie de cortes en el número de medidas ('hits')

presentes en cada uno de los subdetectores y deben estar aislados (criterio similar al aplicado a los electrones). Los muones que solapen con algún jet de $p_T > 25$ GeV y $\Delta R < 0.4$ son eliminados.

- **Jets:** Los jets se reconstruyen a partir de las celdas en los calorímetros usando el algoritmo anti-k_t con tamaño R_C=0.4. Posteriormente se les aplica todas las correcciones de energía necesarias con el fin de reducir los efectos del 'pile-up', ruido electrónico, variaciones relativas del momento según la región del detector, etc. En este análisis se seleccionan sucesos con exactamente dos jets con $p_T > 30$ GeV y $\eta < 4.5$. Si un jet se solapa con un electrón ($\Delta R(jet, e)$ <0.2) el jet se elimina y el objeto se clasifica como electrón.

  Además se exije que uno de los jets sea identificado como b-jet en la región $\eta < 2.5$. Existen diferentes técnicas de identificación de jets procedentes de la hadronización de quarks b. Éstas explotan las propiedades distintivas de la desintegración de los hadrones B: vida media relativamente larga (∼1.5 ps) de modo que el vértice del jet, conocido como vértice secundario, se encuentra desplazado con respecto al punto de desintegración. Además, habitualmente producen varias trazas con un parámetro de impacto no despreciable. Por último, si su desintegración es leptónica, una de las trazas resultante puede ser un leptón suave (de bajo p_T). El algoritmo de 'b-tagging' utilizado en en este trabajo es el 'JetFitterCOMBNNc' [114, 115, 117] que combina la información del parámetro de impacto y explota la topología de la desintegración de hadrones B y de hadrones con quarks c. De hecho, el sufijo del nombre indica que está optimizado para discriminar jets procedentes de quarks c (charm). Según la eficiencia de la reconstrucción de b-jets y el poder de rechazo frente a otro tipo de jets, se definen diferente puntos de trabajo para un cierto algoritmo. En este caso se corresponde a una eficiencia de un 55 % en sucesos $t\bar{t}$ y un factor de rechazo para quarks c o más ligeros de 20 y 200, respectivamente.

- $\boldsymbol{E_T^{miss}}$ **:** La energía transversa perdida es la suma vectorial del momento transverso de todos los objetos seleccionados, más cualquier otra actividad en el calorímetro cerca de éstos.

La selección de sucesos candidatos a single top quarks explota las características cinemáticas del canal t. El primer paso consiste en elegir los triggers pertinentes que seleccionen sucesos de acuerdo a sus características más distintivas, en este caso la presencia de leptones de alto momento. A continuación hay una preselección de sucesos: un único leptón (electrón o muón) en el estado final, exactamente dos jets siendo uno de ellos etiquetados como b-jets y que la energía transversa perdida sea $E_{\mathrm{T}}^{\mathrm{miss}} > 30$ GeV. Varios cortes adicionales son aplicados para rechazar fondos específicos. Muones procedentes de rayos cósmicos son drásticamente reducidos rechazando sucesos cuya topología e información temporal del detector de tiempo de vuelo sea consistente con la de un rayo cósmico. Por otra parte, para asegurarnos una buena reconstrucción del suceso, requerimos que el vértice del suceso tenga al menos cinco trazas. Además, para reducir el fondo de multijets (cuya sección eficaz es mucho mayor) que no contiene bosones W, se aplica un corte en la masa transversa del bosón W reconstruido, $m_{\mathrm{T}}(W) > 30$ GeV. Tras estos cortes, se obtiene una muestra de sucesos que se llama nivel 'preselección'.

7.5.3 Estimación de los fondos

Un modelado preciso tanto de la señal como de los fondos y una estimación apropiada de la composición de los mismos en la muestra de candidatos final es esencial para distinguir la producción de single top quarks. Como se ha anticipado, muchos de estos procesos ($t\bar{t}$, canal s y Wt con single top quarks, Z+jets y dibosones) se pueden modelar y estimar utilizando simplemente simulaciones de Monte Carlo, mientras que para otros (W+jets y QCD multijets) la simulación no proporciona un modelo suficientemente adecuado y se utilizan métodos basados en datos reales para la estimación de los mismos.

Uno de los fondos más importantes corresponde a interacciones entre quarks en las que se radia un bosón W en asociación con jets (W+jets), distinguiéndose los casos en que algún jet proviene realmente de quarks de sabor pesado $W + HF$ (charm o bottom), o en los que los jets son de sabor ligero $W + LF$ (up, down o strange) pero falsamente etiquetados como b-jets. Este último puede ser reducido mediante una selección más estricta en el etiquetado de b-jets, sin embargo, debido a su enorme sección eficaz, aún contribuye de forma sustancial al fondo total. El etiquetado de jets no es útil en los casos en los que el bosón W es producido junto con quarks de sabor pesado, por lo que los procesos W+bb, W+cc y W+c constituyen los fondos más importantes de este análisis. Las simulaciones de Monte Carlo reproducen adecuadamente la cinemática de W+jets, sin embargo, las incertidumbres teóricas en la sección eficaz de estos procesos y en la fracción de sucesos $W + HF$ es muy grande. Por ello, es necesaria una calibración de éstas en una región de control, que se obtiene seleccionando sucesos con un leptón aislado, cierta $E_{\mathrm{T}}^{\mathrm{miss}}$, 1 o 2 jets y exigiendo que la masa del quark top reconstruido esté fuera del rango esperado ($150 < m_{top} < 190$ GeV). Según el número de jets y si se aplica o no el etiquetado de los b-jets, se distinguen cuatro regiones: 1-jet/2-jets 'pretag'/'tag'. El método asume que la contribución real de W+jets, $N_{W+jets,data}$, es el número de sucesos en esta región de control tras substraer la contribución de procesos que no son W+jets, $N_{W+jets,data} = N_{data} - N_{EW} - N_{top} - N_{QCD}$. El factor de normalización global (en inglés scale factor SF) se obtiene para cada 'jet bin' y es el cociente del número de sucesos W+jets en datos y en las simulactiones Monte Carlo: $SF = \frac{N_{W+jets,data}}{N_{W+jets,MC}}$. Las fracciones de HF se obtienen resolviendo un sistema de cuatro ecuaciones con el número de sucesos en cada región tras sustraer los fondos que no son W+jets. Los factores de corrección $K_{bb,n}$, $K_{cc,n}$, $K_{c,n}$ y $K_{light,n}$ son los cocientes de las fracciones $F_{bb,n}$, $F_{cc,n}$, $F_{c,n}$ y $F_{light,n}$ derivadas de estas ecuaciones y los valores en las muestras de Monte Carlo: $K_{k,n} = \frac{F_{k,n}}{F_{k,n}^{MC}}$.

El fondo más difícil de modelar proviene de sucesos multijet de producción QCD, en los que uno de los jets se confunde con un leptón y en los que imperfecciones en las medidas dan lugar a energía faltante. Esto es altamente improbable pero dada la gran sección eficaz de producción de jets, este fondo puede contaminar la señal. Debido a la gran cantidad de procesos de multijets que pueden producir estas configuraciones, siendo además difíciles de estimar y modelar, es necesario un modelo basado en datos. Además, la probabilidad de que un jet sea falsamente identificado como un electrón o un muón es diferente de modo que se han desarrollado modelos diferentes para cada caso. Para sucesos con electrones, más sensibles a la presencia de este fondo, se crea una muestra de 'jet-electrons' a partir de un trigger genérico de jets y seleccionando jets que parezcan electrones, i.e. con $E_T > 25$ GeV, $|\eta| < 2.47$, una fracción alta de energía depositada en el calorímetro y que contengan al menos tres trazas. A estos "electrones" (llamados 'jet-electron') se les asigna una carga aleatoriamente, y después el resto de cortes de

preselección salvo el de $E_{\mathrm{T}}^{\mathrm{miss}}$. Precisamente a partir de un ajuste de esta distribución a los datos se infiere la contribución de este fondo en la región la señal. La zona de baja $E_{\mathrm{T}}^{\mathrm{miss}}$ está dominada por sucesos de fondo multijet mientras que a mayor $E_{\mathrm{T}}^{\mathrm{miss}}$ dominan otros procesos y es la zona en la que se encuentra la señal de single top quarks, $E_{\mathrm{T}}^{\mathrm{miss}} > 30$ GeV.

En el caso de muones, se utiliza un método basado en matrices (en inglés, 'matrix method') en el que se definen dos regiones según el criterio de aislamiento de los muones: 'loose' y 'tight', siendo el segundo un subset del primero pero con cortes más estrictos y el que se usa en el análisis. En cada una de estas muestras tenemos muones aislados 'real' (procedentes de procesos con quarks top, W+jets, Z+jets y dibosones) y muones no aislados 'fake' (multijets), lo cual permite escribir:

$$\begin{aligned} N^{loose} &= N_{real}^{loose} + N_{fake}^{loose} \\ N^{tight} &= N_{real}^{tight} + N_{fake}^{tight} = \epsilon_{real} N_{real}^{loose} + \epsilon_{fake} N_{fake}^{loose} , \end{aligned} \tag{7.11}$$

donde la eficiencia para pasar de 'loose' a 'tight', $\epsilon = N^{tight}/N^{loose}$, es diferente para muones 'real' y 'fake'. ϵ_{real} se mide en muestras con muones reales como $Z \to \mu\mu$. ϵ_{fake} se deriva en un región en la que domina la contribución de 'fakes'. A partir de estas medidas, se obtiene el número de sucesos de fondo de multijets N_{real}^{tight} así como el modelado del mismo ponderando (aplicando pesos a) la muestra de datos en función del criterio de calidad que el leptón seleccionado satisface:

$$\begin{aligned} N_{fake}^{tight} &= \frac{\epsilon_{fake}}{\epsilon_{real} - \epsilon_{fake}} (N^{loose}\epsilon_{real} - N^{tight}) \\ w_{tight} &= -(1 - \epsilon_{real})\epsilon_{fake}/(\epsilon_{real} - \epsilon_{fake}) \\ w_{loose} &= \epsilon_{real}\epsilon_{fake}/(\epsilon_{real} - \epsilon_{fake}) \end{aligned} \tag{7.12}$$

7.5.3.1 Distribuciones cinemáticas en la región de control 'preselección'

La Figura 7.12 muestra las distribuciones de $E_{\mathrm{T}}^{\mathrm{miss}}$ y $m_{\mathrm{T}}(W)$ tras los cortes de preselección, para sucesos con electrones y muones por separado. Puede verse que las predicciones reproducen los datos. A este nivel, la muestra está dominada por los fondos W+jets, pares de quarks top y QCD multijets, mientras que la contribución de sucesos de señal es sólo del 11 %.

7.5.4 Selección final de sucesos

Para purificar la muestra y alcanzar un cociente señal-fondo cercano a la unidad, se han aplicado cuatro cortes adicionales explotando la topología del proceso de interés y características del quark top. La selección se realiza por medio de una serie de cortes secuenciales en ciertos observables: pseudo-rapidez del jet ligero (llamado quark espectador en el canal t $|\eta_{light\,jet}| > 2$, la suma escalar del momento transverso de todos los objetos en el estado final H_{T} debe ser mayor que 210 GeV, la masa invariante del quark top reconstruido m_t debe estar entre 150 y 190 GeV, y la diferencia en η entre los dos jets del suceso $\Delta\eta$(light-jet, b-jet) debe ser superior a 1. En la Figura 7.13 se muestran algunas de estas variables tras aplicar todos los cortes de selección salvo el que afecta a la variable representada. En general el acuerdo entre los datos y las predicciones en estas variables discriminatorias es razonablemente bueno.

La masa invariante del quark top se estima a partir de sus productos de desintegración: el cuadrimomento del lepton, del jet etiquetado como b-jet y la $E_{\mathrm{T}}^{\mathrm{miss}}$. Para reconstruir el bosón W leptónico hace falta calcular el cuadrimomento del neutrino del estado final, que no se detecta. Éste se reconstruye asumiendo $m(\nu)$=0 y que toda la $E_{\mathrm{T}}^{\mathrm{miss}}$ del suceso es debida a dicho neutrino, de modo que $E_{\mathrm{T}}^{\mathrm{miss}}$ es la componente transversal del momento del neutrino $p_T(\nu) = E_{\mathrm{T}}^{\mathrm{miss}}$. La componente longitudinal $p_z(\nu)$ se calcula aplicando la restricción $m(l\nu) = m_T(W)$. Finalmente se asocia el b-jet obteniendo así la masa invariante del quark top reconstruido.

7.5.5 Medida de la asimetría $A_{\mathrm{FB}}^{\mathrm{N}}$

La asimetría $A_{\mathrm{FB}}^{\mathrm{N}}$ se calcula a partir de la distribución angular $\cos\theta^{\mathrm{N}}$ reconstruida, siendo θ^{N} el ángulo entre la dirección normal $\vec{N}$ al plano definido por $\vec{q}$ y $\vec{s_t}$ y el leptón en el sistema de referencia del bosón W en reposo, según se definió en la Section 7.2. La Figura 7.14 muestra este observable para los sucesos que pasan todos los cortes de selección. Esta distribución está distorsionada debido a limitaciones experimentales como la resolución del detector, la aceptancia geométrica del mismo y los cortes de selección. Como puede verse en la Figura 7.15, estos efectos afectan potencialmente a la forma y normalización de la misma, de modo que, antes de extraer el valor de la asimetría a partir de ellas hay que deconvolucionarlas a nivel de partones. La medida de la asimetría $A_{\mathrm{FB}}^{\mathrm{N}}$ en términos de los observables experimentales viene dada por:

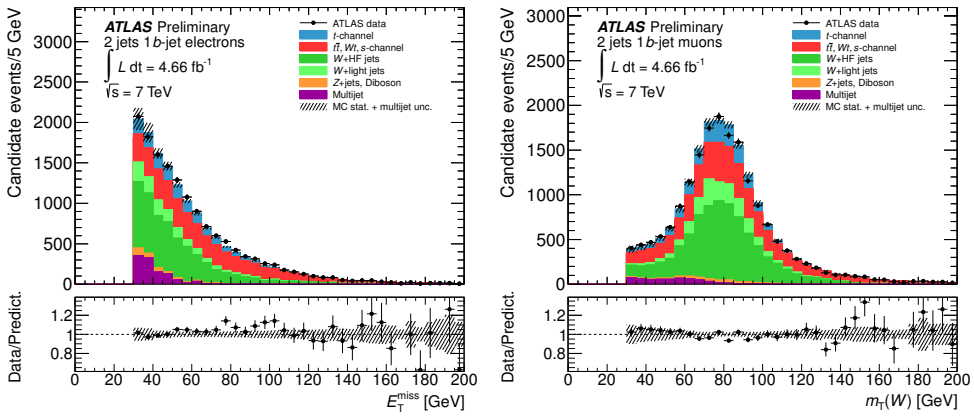

Figura 7.12: *Comparación entre los datos y las simulaciones de Monte Carlo de las distribuciones de $E_{\mathrm{T}}^{\mathrm{miss}}$ (canal de electrones) y $m_T(W)$ (canal de muones). En la parte inferior de cada distribución se muestra el cociente entre lo observado en datos y la predicción. La banda de incertidumbre incluye únicamente el error estadístico.*

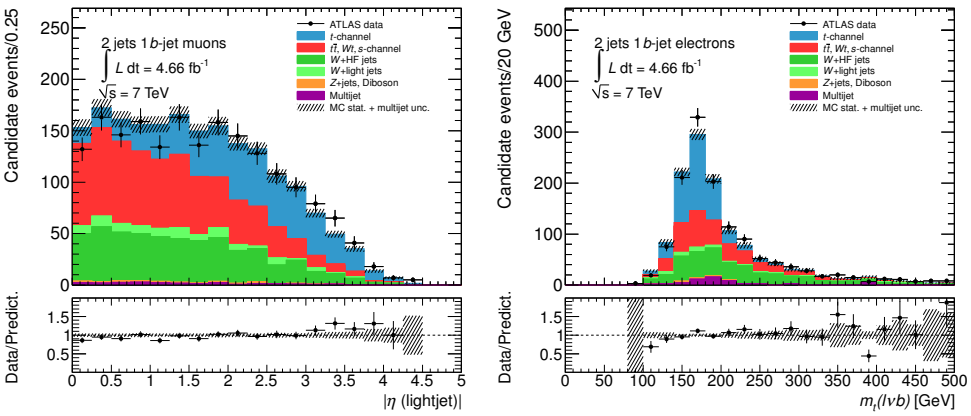

Figura 7.13: *Comparación entre los datos y las predicciones en dos variables discriminatorias, $\eta_{light\,jet}$ (canal de muones) y m_{top} (canal de electrones) tras aplicar todos los cortes de selección excepto el de la variable que se muestra. La banda de incertidumbre incluye únicamente el error estadístico.*

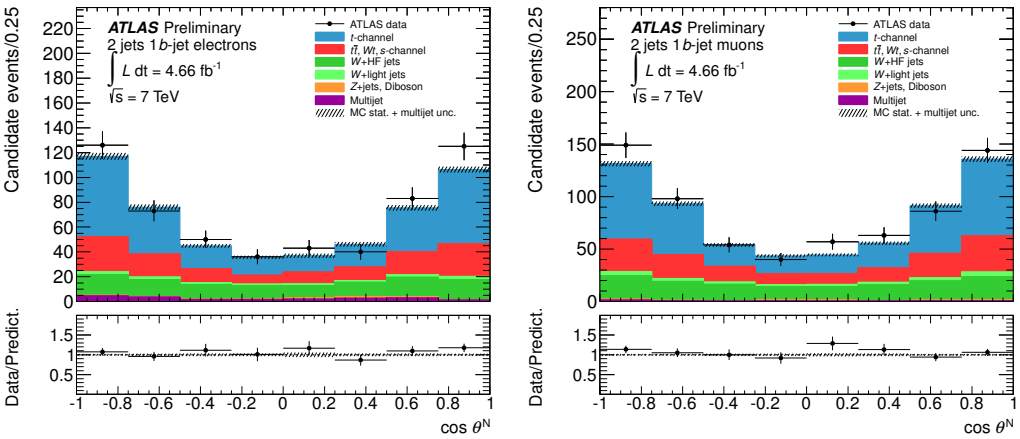

Figura 7.14: *Distribución angular $\cos\theta^N$ reconstruida a nivel de selección para el canal de electrones (izquierda) y de muones (derecha). La banda de incertidumbre incluye únicamente el error estadístico.*

$$N_i^{\text{datos}} = N_i^{\text{señal, reco.}} + N_i^{\text{fondo}} = M_{ji}\epsilon_j N_j^{\text{señal, partones}} + N_i^{\text{fondo}} \tag{7.13}$$

$$\Longrightarrow \quad N_j^{\text{señal, partones}} = \frac{M_{ji}^{-1}(N_i^{\text{datos}} - N_i^{\text{fondo}})}{\epsilon_j} \tag{7.14}$$

$$A_{FB}^N = \frac{N^{\text{señal, partones}}(\cos\theta^{\text{N}} > 0) - N^{\text{señal, partones}}(\cos\theta^{\text{N}} < 0)}{N^{\text{señal, partones}}(\cos\theta^{\text{N}} > 0) + N^{\text{señal, partones}}(\cos\theta^{\text{N}} < 0)} \tag{7.15}$$

donde ϵ_j es la eficiencia de selección de sucesos en cada bin de la distribución angular y M_{ji} (M_{ji}^{-1}) la (inversa de la) matriz de respuesta del detector, que pueden verse en la Figura 7.16. Los elementos de la matriz M_{ji} representan la probabilidad de que un suceso para el que $\cos\theta^{\mathrm{N}}{}_j$ a nivel de partones (bin j) se reconstruya, tras todos los criterios de selección, con un valor $\cos\theta^{\mathrm{N}}{}_i$ (bin i). Tanto la eficiencia de selección como la matriz de respuesta se derivan a partir de simulaciones Monte Carlo. En este análisis, las muestras de señal han sido generadas con AcerMC para la interacción a nivel partónico y Pythia para el proceso de fragmentación y hadronización. Con el objetivo de minimizar la dependencia con el modelo de Monte Carlo, se compararon muestras de señal simuladas con diferentes generadores (AcerMC y Protos) y las diferencias observadas se considera como una incertidumbre sistemática.

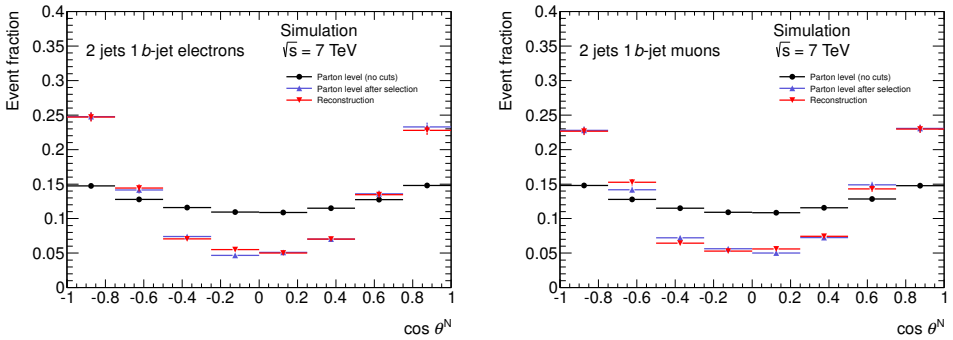

Figura 7.15: *Comparación de la distribución angular* $\cos\theta^N$ *para el canal de electrones (izquierda) y el de muones (derecha) a diferentes niveles: para todos los sucesos de señal simulados, tras la selección de cortes y tras la reconstrucción en el detector.*

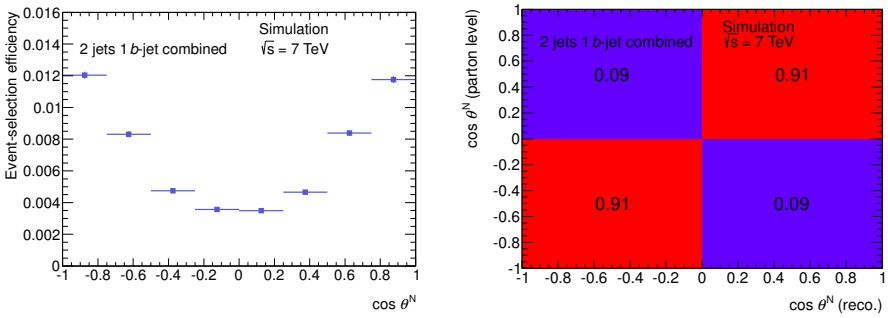

Figura 7.16: *Izquierda: Eficiencia de selección de sucesos en función de* $\cos\theta^N$*. Derecha: Matriz de respuesta del detector* M_{ji} *para la combinación del canal de electrones y muons.*

Existen diferentes métodos para corregir el número de sucesos observados por los efectos de resolución. Puesto que el objetivo es medir una asimetría en una distribución y es suficiente con dos bines, se ha optado por la forma más directa mediante la simple inversión de la matriz respuesta. Este método puede ser sensible a grandes fluctuaciones estadísticas, en especial, en los

elementos no diagonales de la matriz. Incluso puede ocurrir que, debido a la muestra finita de la simulación, sea singular, y por tanto no invertible. Por ello, se han diseñado otros métodos de deconvolución o 'unfolding', basados en la descomposición en valores singulares de la matriz y la regularización de la solución; pero en este caso no ha sido necesario recurrir a ellos.

A partir de la distribución ya corregida puede calcularse el valor de la asimetría. El error estadístico de la misma se ha evaluado mediante pseudo-experimentos teniendo en cuenta las incertidumbres asociadas a cada uno de los términos de la Ecuación 7.15. El método consiste en generar 1000 muestras de 'pseudo-datos' variando la distribución de datos que sigue un patrón Poissoniano y repitiendo la medida de la asimetría $A_{\mathrm{FB}}^{\mathrm{N}}$ cada vez. La incertidumbre asociada a la estadística limitada de las muestras de Monte Carlo se tiene en cuenta variando la distribución de los fondos, la eficiencia de seleción y la matriz de respuesta mediante fluctuaciones Gaussianas. Los 1000 valores de la asimetría obtenidos siguen una distribución Gaussiana cuya media proporciona el valor final de $A_{\mathrm{FB}}^{\mathrm{N}}$ y su varianza el error estadístico de la misma.

Por completitud, se ha calculado la sección eficaz para el canal t de producción de single top quarks obteniéndose un valor de σ_{t-ch}=74±9 (stat.) pb, en acuerdo, dentro de la incertidumbre estadística asociada, con otras medidas en ATLAS y CMS y con la predicción del ME.

Errores sistemáticos

Las distribuciones también están sujetas a efectos instrumentales y experimentales, así como incertidumbres teóricas (e.g. precisión de las secciones eficaces). Todas estas incertidumbres afectan potencialmente a su forma y normalización, tanto para las distribuciones de datos como para las de fondo y de senal. La cuantificación del impacto de estos efectos, llamados sistemáticos, en el resultado final es una parte importante del análisis. El error dominante está relacionado con el modelado de procesos con quarks top, tanto de la señal como sucesos $t\bar{t}$. Otras contribuciones importantes son incertidumbres en la estimación de los fondos, en la escala y resolución de la energía de los jets, y el conocimiento limitado de las funciones de distribución de los partones.

Resultado final

El resultado final de la medida de la asimetría $A_{\mathrm{FB}}^{\mathrm{N}}$ es:

$$A_{\mathrm{FB}}^{\mathrm{N}} = 0{,}031 \pm 0{,}065\,(\mathrm{stat.})\,^{+0{,}029}_{-0{,}031}\,(\mathrm{syst.})\,.$$

A partir de ésta y de su relación con $Im(g_{\mathrm{R}})$ ($A_{\mathrm{FB}}^{\mathrm{N}} \approx 0{,}64\ P\ Im(g_{\mathrm{R}})$), es posible establecer límites al valor de este acoplamiento anómalo del vértice Wtb. En la Figura 7.17 pueden verse las regiones permitidas para éste en función del grado de polarización del quark top. Este resultado constituye la primera cota experimental para la parte imaginaria de un acoplamiento anómalo del vértice Wtb. La incertidumbre asociada a esta medida está dominada por el error estadístico. Cabe recordar que es la suma de las asimetrías $A_{FB}^{CP} = A_{FB}^{N}(t) + A_{FB}^{N}(\bar{t})$ la que señala, sin ambiguedad, la presencia de violación de $\mathcal{CP}$. El análisis con la muestra de datos del 2012 (cuatro veces más estadística) permitirá obtener resultados más precisos, separar la medida para sucesos con quarks top y antitops, así como medir la polarización del quark top en este canal de producción (P ∼0.9 según el ME), y por tanto acotar más la región permitida.

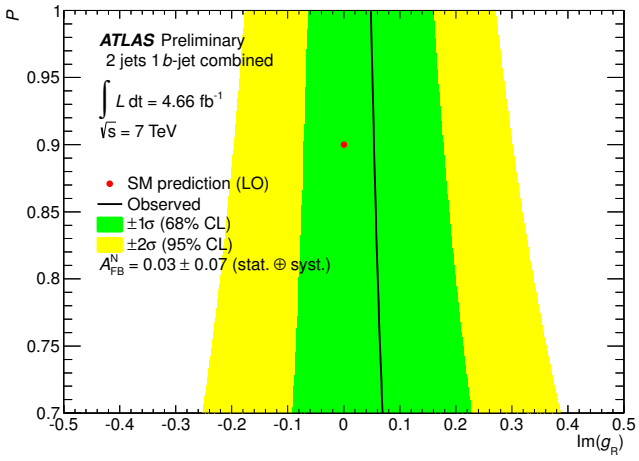

Figura 7.17: *Límites para $Im(g_R)$ en función del grado de polarización del quark top obtenido a partir de la medida de la asimetría A_{FB}^{N}.*

7.6 Conclusiones

Esta tesis doctoral se ha desarrollado en el marco del proyecto del LHC y presenta una serie de resultados obtenidos con los datos del detector ATLAS. Con los primeros datos registrados por el detector, durante la fase de puesta a punto (2008-2009) rayos cósmicos y luego las primeras colisiones de protones (2010), se llevaron a cabo estudios relacionados con la reconstrucción de muones y de jets respectivamente. Con la muestra de datos del 2011 se ha llevado a cabo el análisis principal de esta tesis que consiste en una búsqueda de nuevas fuentes de violación de la simetría $\mathcal{CP}$ en sucesos con un quark top en el estado final.

Durante la fase de puesta a punto, la mayoría de los estudios se centraron en entender por separado cada uno de los subdetectores de ATLAS. Sin embargo, la contribución de este trabajo fue estudiar la reconstrucción de muones cósmicos combinando la información de todos los subsistemas obteniendo los primeros resultados de la reconstrucción combinada de muones en el detector ATLAS con datos reales, que fueron incluidos en el artículo de la puesta a punto de ATLAS con rayos cósmicos [1]. Con la muestra de datos de colisiones de protones a 7 TeV del año 2010 (unos ~45 pb^{-1}) se realizó un estudio relacionado con la estructura de los jets, sensible a los detalles del proceso de radiación y fragmentación de gluones (perturbativo) y de hadronización (no perturbativo). La distribución de momento del jet y en particular la fracción de p_T que queda fuera del cono del jet reconstruido con el algoritmo anti-k_t R_C=0.4 fue estimada en sucesos con dos jets. Éstas medidas fueron comparadas con las predicciones de varios modelos, obteniéndose una diferencia de ~1-2 % [2].

La producción de quarks top polarizados (interacción electrodébil) proporciona una oportunidad única para el estudio del vértice Wtb. Explotando la dirección de polarización del quark top, es posible definir nuevas distribuciones angulares a partir de sus productos de desintegración. La

mayor contribución de este trabajo de tesis es precisamente la medida de la asimetría $A_{\mathrm{FB}}^{\mathrm{N}}$, cuyo valor esperado según el ME es cero y que es sensible a nuevas fuentes de violación de $\mathcal{CP}$ en el vértice Wtb. Este resultado, documentado también en Refs. [6, 7], constituyó en su momento la primera medida de una propiedad de single top quarks, proporcionando además por primera vez un límite de exclusión a la parte imaginaria de uno de los acoplamientos anómalos del vértice Wtb. La incertidumbre en el resultado obtenido está limitada por el error estadístico. Los datos registrados en 2012 y en la próxima fase de toma de datos de este acelerador permitirán alcanzar mayor precisión y además medir estas asimetrías para sucesos con quarks top y antitop por separado.

Acknowledgements

I want to take this opportunity to thank all the people that contributed directly and indirectly to the successful completion of this thesis. This work would not have been possible without the support of a large number of people both inside and outside the physics society- with regards to physics or not. To all, a big thank you!

First of all, I would like to thank my supervisors, María José Costa and José Bernabéu, for their professional supervision, and for the attention they dedicated to my formation as a scientist. María José thanks for your continuous support and guidance. We have covered a wide variety of topics over these historical years of the LHC operation. Along the way, I have developed a deep respect and admiration for the way you work. I am also extremely grateful to my other supervisor, Pepe, who first helped me to realize that my real interest is on the experimental side of high energy physics and proposed me to join the CERN summer students program. Thanks for sharing with me your extraordinary knowledge in the field of particle physics.

In addition, I would like to thank the IFIC for providing me with all the institutional support needed for my work, with an acknowledgement, in particular, to 'aTOPe' group and IT people. Thanks for allowing me to participate at a variety of conferences and for the opportunity I was given to work at CERN. Thanks to the ATLAS Collaboration, in particular the Single Top Group members. I feel fortunate to have been given an opportunity to own a LHC analysis. This would not have been possible without the support and help of many other single top quark fans. Special thanks to Dominic Hirschbuehl for many fruitful discussions, and also to Barbara, Kathrin and Nuno Castro. Thanks also to CERN laboratory, for its unique atmosphere where people from different cultures work together in harmony and with respect. It is a very special place for me.

Special thanks to Carlos Escobar, with whom I worked very close during the last years, for his help and time, as well as for his friendship. Thanks to all my friends, office mates and other colleagues at CERN and IFIC, for the lovely time we spent together. Uiji! In particular to 'Campa town', 'SAFA', 'La flaca' and 'ADN' teams. I would also like to express my gratitude to a very special person, Vicent Benedito, for his extraordinary tips and enthusiasm.

Last but not least, I would like to thank all my family. Your unconditional love and support mean more to me than you will ever know. I love you! My deepest gratefulness to my parents (José and Merche), my brother Albert and my sister Marta. I am extremely fortunate to have you. Daniel, my fiance, words cannot express my feelings. I could not have done this without your constant support and understanding. Thanks for sharing your life with me. We can do it!

Appendices

A

Jet shapes for dijets events

A.1 Differential jet shapes

$\rho(r)$	$20 < p_T \leq 25$ GeV		
r	Data	Pythia	Herwig
(0.0, 0.1)	5.016 ± 0.021	4.978 ± 0.030	4.953 ± 0.045
(0.1, 0.2)	2.889 ± 0.018	2.927 ± 0.025	2.931 ± 0.038
(0.2, 0.3)	1.425 ± 0.009	1.435 ± 0.014	1.424 ± 0.021
(0.3, 0.4)	0.628 ± 0.005	0.618 ± 0.007	0.648 ± 0.010
(0.4, 0.5)	0.679 ± 0.005	0.608 ± 0.007	0.634 ± 0.011
(0.5, 0.6)	0.609 ± 0.005	0.549 ± 0.007	0.573 ± 0.010
(0.6, 0.7)	0.575 ± 0.005	0.486 ± 0.006	0.548 ± 0.010
(0.7, 0.8)	0.566 ± 0.005	0.490 ± 0.006	0.519 ± 0.010
(0.8, 0.9)	0.567 ± 0.005	0.475 ± 0.006	0.528 ± 0.010
(0.9, 1.0)	0.591 ± 0.005	0.480 ± 0.006	0.530 ± 0.010
(1.0, 1.1)	0.627 ± 0.005	0.511 ± 0.007	0.552 ± 0.010
(1.1, 1.2)	0.654 ± 0.005	0.531 ± 0.007	0.583 ± 0.011
(1.2, 1.3)	0.693 ± 0.005	0.560 ± 0.007	0.619 ± 0.011
(1.3, 1.4)	0.739 ± 0.006	0.598 ± 0.007	0.638 ± 0.011

$\rho(r)$	$20 < p_T \leq 30$ GeV		
r	Data	Pythia	Herwig
(0.0, 0.1)	5.257 ± 0.028	5.360 ± 0.031	5.316 ± 0.053
(0.1, 0.2)	2.838 ± 0.024	2.743 ± 0.026	2.729 ± 0.044
(0.2, 0.3)	1.289 ± 0.012	1.284 ± 0.014	1.321 ± 0.024
(0.3, 0.4)	0.579 ± 0.006	0.570 ± 0.007	0.601 ± 0.011
(0.4, 0.5)	0.542 ± 0.006	0.502 ± 0.007	0.527 ± 0.011
(0.5, 0.6)	0.461 ± 0.005	0.418 ± 0.006	0.466 ± 0.010
(0.6, 0.7)	0.427 ± 0.005	0.383 ± 0.005	0.408 ± 0.009
(0.7, 0.8)	0.406 ± 0.005	0.360 ± 0.005	0.395 ± 0.009
(0.8, 0.9)	0.423 ± 0.005	0.361 ± 0.005	0.382 ± 0.009
(0.9, 1.0)	0.438 ± 0.005	0.361 ± 0.005	0.415 ± 0.009
(1.0, 1.1)	0.466 ± 0.005	0.378 ± 0.005	0.419 ± 0.009
(1.1, 1.2)	0.481 ± 0.005	0.401 ± 0.006	0.429 ± 0.010
(1.2, 1.3)	0.508 ± 0.006	0.421 ± 0.006	0.465 ± 0.010
(1.3, 1.4)	0.534 ± 0.006	0.436 ± 0.006	0.486 ± 0.011

$\rho(r)$	$30 < p_T \leq 40$ GeV		
r	Data	Pythia	Herwig
(0.0, 0.1)	5.692 ± 0.030	5.741 ± 0.023	5.789 ± 0.050
(0.1, 0.2)	2.604 ± 0.025	2.617 ± 0.019	2.539 ± 0.041
(0.2, 0.3)	1.132 ± 0.012	1.096 ± 0.009	1.121 ± 0.021
(0.3, 0.4)	0.542 ± 0.006	0.519 ± 0.005	0.532 ± 0.010
(0.4, 0.5)	0.436 ± 0.005	0.407 ± 0.004	0.428 ± 0.009
(0.5, 0.6)	0.375 ± 0.005	0.335 ± 0.003	0.359 ± 0.008
(0.6, 0.7)	0.339 ± 0.004	0.295 ± 0.003	0.329 ± 0.007
(0.7, 0.8)	0.319 ± 0.004	0.277 ± 0.003	0.303 ± 0.007
(0.8, 0.9)	0.327 ± 0.004	0.272 ± 0.003	0.309 ± 0.007
(0.9, 1.0)	0.340 ± 0.004	0.279 ± 0.003	0.317 ± 0.007
(1.0, 1.1)	0.355 ± 0.004	0.287 ± 0.003	0.322 ± 0.007
(1.1, 1.2)	0.369 ± 0.005	0.301 ± 0.003	0.342 ± 0.008
(1.2, 1.3)	0.389 ± 0.005	0.313 ± 0.003	0.358 ± 0.008
(1.3, 1.4)	0.413 ± 0.005	0.330 ± 0.003	0.383 ± 0.009

$\rho(r)$	$40 < p_T \leq 60$ GeV		
r	Data	Pythia	Herwig
(0.0, 0.1)	6.186 ± 0.041	6.336 ± 0.021	6.257 ± 0.067
(0.1, 0.2)	2.440 ± 0.035	2.347 ± 0.017	2.327 ± 0.055
(0.2, 0.3)	0.917 ± 0.016	0.869 ± 0.008	0.956 ± 0.026
(0.3, 0.4)	0.432 ± 0.007	0.428 ± 0.004	0.436 ± 0.012
(0.4, 0.5)	0.323 ± 0.006	0.302 ± 0.003	0.318 ± 0.009
(0.5, 0.6)	0.266 ± 0.005	0.243 ± 0.002	0.260 ± 0.008
(0.6, 0.7)	0.243 ± 0.005	0.213 ± 0.002	0.229 ± 0.007
(0.7, 0.8)	0.225 ± 0.004	0.199 ± 0.002	0.207 ± 0.007
(0.8, 0.9)	0.225 ± 0.004	0.191 ± 0.002	0.206 ± 0.007
(0.9, 1.0)	0.236 ± 0.005	0.195 ± 0.002	0.204 ± 0.007
(1.0, 1.1)	0.239 ± 0.005	0.201 ± 0.002	0.213 ± 0.007
(1.1, 1.2)	0.253 ± 0.005	0.204 ± 0.002	0.243 ± 0.008
(1.2, 1.3)	0.273 ± 0.005	0.219 ± 0.002	0.247 ± 0.008
(1.3, 1.4)	0.281 ± 0.005	0.232 ± 0.002	0.259 ± 0.009

$\rho(r)$	$60 < p_T \leq 80$ GeV		
r	Data	Pythia	Herwig
(0.0, 0.1)	6.733 ± 0.027	6.985 ± 0.023	6.963 ± 0.121
(0.1, 0.2)	2.181 ± 0.022	1.995 ± 0.018	1.947 ± 0.110
(0.2, 0.3)	0.730 ± 0.010	0.676 ± 0.008	0.676 ± 0.046
(0.3, 0.4)	0.344 ± 0.004	0.325 ± 0.004	0.314 ± 0.021
(0.4, 0.5)	0.229 ± 0.003	0.216 ± 0.002	0.218 ± 0.014
(0.5, 0.6)	0.187 ± 0.002	0.173 ± 0.002	0.162 ± 0.011
(0.6, 0.7)	0.161 ± 0.002	0.144 ± 0.002	0.141 ± 0.010
(0.7, 0.8)	0.151 ± 0.002	0.134 ± 0.002	0.125 ± 0.009
(0.8, 0.9)	0.148 ± 0.002	0.128 ± 0.002	0.126 ± 0.010
(0.9, 1.0)	0.151 ± 0.002	0.129 ± 0.002	0.120 ± 0.010
(1.0, 1.1)	0.157 ± 0.002	0.132 ± 0.002	0.117 ± 0.009
(1.1, 1.2)	0.163 ± 0.002	0.137 ± 0.002	0.132 ± 0.010
(1.2, 1.3)	0.176 ± 0.002	0.147 ± 0.002	0.143 ± 0.011
(1.3, 1.4)	0.184 ± 0.002	0.151 ± 0.002	0.152 ± 0.011

$\rho(r)$	$80 < p_T \leq 110$ GeV		
r	Data	Pythia	Herwig
(0.0, 0.1)	7.167 ± 0.022	7.436 ± 0.018	6.948 ± 0.349
(0.1, 0.2)	1.912 ± 0.018	1.728 ± 0.015	2.137 ± 0.301
(0.2, 0.3)	0.615 ± 0.008	0.551 ± 0.006	0.545 ± 0.103
(0.3, 0.4)	0.292 ± 0.003	0.269 ± 0.003	0.358 ± 0.048
(0.4, 0.5)	0.181 ± 0.002	0.169 ± 0.002	0.198 ± 0.027
(0.5, 0.6)	0.147 ± 0.002	0.130 ± 0.001	0.141 ± 0.020
(0.6, 0.7)	0.128 ± 0.001	0.109 ± 0.001	0.173 ± 0.031
(0.7, 0.8)	0.121 ± 0.001	0.100 ± 0.001	0.100 ± 0.016
(0.8, 0.9)	0.120 ± 0.001	0.094 ± 0.001	0.082 ± 0.017
(0.9, 1.0)	0.123 ± 0.001	0.095 ± 0.001	0.082 ± 0.017
(1.0, 1.1)	0.127 ± 0.001	0.097 ± 0.001	0.094 ± 0.018
(1.1, 1.2)	0.132 ± 0.002	0.099 ± 0.001	0.090 ± 0.017
(1.2, 1.3)	0.142 ± 0.002	0.104 ± 0.001	0.086 ± 0.018
(1.3, 1.4)	0.149 ± 0.002	0.109 ± 0.001	0.088 ± 0.020

Table A.1: *Differential jet shapes for data and two Monte Carlo predictions for different p_T ranges covering jets from 20 to 110 GeV.*

$\rho(r)$	$110 < p_T \leq 160$ GeV		
r	Data	Pythia	Herwig
(0.0, 0.1)	7.575 ± 0.019	7.802 ± 0.016	7.939 ± 0.534
(0.1, 0.2)	1.659 ± 0.015	1.518 ± 0.013	1.514 ± 0.427
(0.2, 0.3)	0.519 ± 0.006	0.454 ± 0.005	0.369 ± 0.171
(0.3, 0.4)	0.235 ± 0.003	0.218 ± 0.002	0.175 ± 0.075
(0.4, 0.5)	0.145 ± 0.001	0.133 ± 0.001	0.112 ± 0.036
(0.5, 0.6)	0.117 ± 0.001	0.104 ± 0.001	0.090 ± 0.034
(0.6, 0.7)	0.102 ± 0.001	0.086 ± 0.001	0.102 ± 0.030
(0.7, 0.8)	0.093 ± 0.001	0.077 ± 0.001	0.071 ± 0.026
(0.8, 0.9)	0.092 ± 0.001	0.072 ± 0.001	0.050 ± 0.024
(0.9, 1.0)	0.094 ± 0.001	0.072 ± 0.001	0.148 ± 0.035
(1.0, 1.1)	0.097 ± 0.001	0.073 ± 0.001	0.063 ± 0.025
(1.1, 1.2)	0.103 ± 0.001	0.076 ± 0.001	0.063 ± 0.025
(1.2, 1.3)	0.108 ± 0.001	0.077 ± 0.001	0.128 ± 0.047
(1.3, 1.4)	0.115 ± 0.001	0.082 ± 0.001	0.089 ± 0.025

$\rho(r)$	$160 < p_T \leq 210$ GeV		
r	Data	Pythia	Herwig
(0.0, 0.1)	7.882 ± 0.022	8.120 ± 0.013	7.980 ± 0.018
(0.1, 0.2)	1.461 ± 0.018	1.306 ± 0.010	1.395 ± 0.015
(0.2, 0.3)	0.452 ± 0.007	0.391 ± 0.004	0.433 ± 0.006
(0.3, 0.4)	0.197 ± 0.003	0.177 ± 0.002	0.188 ± 0.002
(0.4, 0.5)	0.121 ± 0.001	0.108 ± 0.001	0.112 ± 0.001
(0.5, 0.6)	0.095 ± 0.001	0.083 ± 0.001	0.085 ± 0.001
(0.6, 0.7)	0.082 ± 0.001	0.068 ± 0.001	0.072 ± 0.001
(0.7, 0.8)	0.076 ± 0.001	0.060 ± 0.001	0.064 ± 0.001
(0.8, 0.9)	0.076 ± 0.001	0.057 ± 0.001	0.060 ± 0.001
(0.9, 1.0)	0.076 ± 0.001	0.055 ± 0.001	0.059 ± 0.001
(1.0, 1.1)	0.078 ± 0.001	0.056 ± 0.001	0.060 ± 0.001
(1.1, 1.2)	0.082 ± 0.001	0.058 ± 0.001	0.062 ± 0.001
(1.2, 1.3)	0.087 ± 0.001	0.060 ± 0.001	0.064 ± 0.001
(1.3, 1.4)	0.091 ± 0.001	0.062 ± 0.001	0.067 ± 0.001

$\rho(r)$	$210 < p_T \leq 260$ GeV		
r	Data	Pythia	Herwig
(0.0, 0.1)	8.163 ± 0.030	8.363 ± 0.014	8.186 ± 0.021
(0.1, 0.2)	1.275 ± 0.023	1.145 ± 0.011	1.260 ± 0.017
(0.2, 0.3)	0.385 ± 0.009	0.334 ± 0.004	0.381 ± 0.007
(0.3, 0.4)	0.172 ± 0.004	0.150 ± 0.002	0.167 ± 0.003
(0.4, 0.5)	0.103 ± 0.002	0.090 ± 0.001	0.095 ± 0.001
(0.5, 0.6)	0.084 ± 0.002	0.070 ± 0.001	0.073 ± 0.001
(0.6, 0.7)	0.070 ± 0.001	0.057 ± 0.001	0.060 ± 0.001
(0.7, 0.8)	0.066 ± 0.001	0.051 ± 0.001	0.053 ± 0.001
(0.8, 0.9)	0.065 ± 0.001	0.047 ± 0.001	0.050 ± 0.001
(0.9, 1.0)	0.065 ± 0.001	0.046 ± 0.001	0.049 ± 0.001
(1.0, 1.1)	0.066 ± 0.001	0.047 ± 0.001	0.050 ± 0.001
(1.1, 1.2)	0.068 ± 0.001	0.047 ± 0.001	0.051 ± 0.001
(1.2, 1.3)	0.074 ± 0.001	0.049 ± 0.001	0.054 ± 0.001
(1.3, 1.4)	0.076 ± 0.001	0.052 ± 0.001	0.054 ± 0.001

$\rho(r)$	$260 < p_T \leq 310$ GeV		
r	Data	Pythia	Herwig
(0.0, 0.1)	8.255 ± 0.051	8.496 ± 0.017	8.302 ± 0.025
(0.1, 0.2)	1.225 ± 0.040	1.055 ± 0.014	1.205 ± 0.020
(0.2, 0.3)	0.359 ± 0.016	0.307 ± 0.005	0.339 ± 0.007
(0.3, 0.4)	0.153 ± 0.006	0.135 ± 0.002	0.152 ± 0.003
(0.4, 0.5)	0.092 ± 0.003	0.081 ± 0.001	0.084 ± 0.001
(0.5, 0.6)	0.072 ± 0.002	0.061 ± 0.001	0.064 ± 0.001
(0.6, 0.7)	0.063 ± 0.002	0.048 ± 0.001	0.052 ± 0.001
(0.7, 0.8)	0.054 ± 0.002	0.042 ± 0.001	0.048 ± 0.001
(0.8, 0.9)	0.053 ± 0.002	0.040 ± 0.001	0.043 ± 0.001
(0.9, 1.0)	0.055 ± 0.002	0.039 ± 0.001	0.042 ± 0.001
(1.0, 1.1)	0.056 ± 0.002	0.039 ± 0.001	0.043 ± 0.001
(1.1, 1.2)	0.055 ± 0.002	0.040 ± 0.001	0.044 ± 0.001
(1.2, 1.3)	0.060 ± 0.002	0.041 ± 0.001	0.046 ± 0.001
(1.3, 1.4)	0.063 ± 0.002	0.043 ± 0.001	0.048 ± 0.001

$\rho(r)$	$310 < p_T \leq 400$ GeV		
r	Data	Pythia	Herwig
(0.0, 0.1)	8.408 ± 0.076	8.640 ± 0.009	8.494 ± 0.014
(0.1, 0.2)	1.113 ± 0.057	0.961 ± 0.007	1.060 ± 0.012
(0.2, 0.3)	0.325 ± 0.023	0.271 ± 0.003	0.310 ± 0.004
(0.3, 0.4)	0.149 ± 0.010	0.118 ± 0.001	0.130 ± 0.002
(0.4, 0.5)	0.079 ± 0.004	0.069 ± 0.001	0.073 ± 0.001
(0.5, 0.6)	0.059 ± 0.003	0.053 ± 0.000	0.055 ± 0.001
(0.6, 0.7)	0.050 ± 0.003	0.043 ± 0.000	0.045 ± 0.000
(0.7, 0.8)	0.045 ± 0.002	0.037 ± 0.000	0.040 ± 0.000
(0.8, 0.9)	0.043 ± 0.002	0.035 ± 0.000	0.037 ± 0.000
(0.9, 1.0)	0.041 ± 0.002	0.033 ± 0.000	0.037 ± 0.000
(1.0, 1.1)	0.045 ± 0.002	0.033 ± 0.000	0.036 ± 0.000
(1.1, 1.2)	0.043 ± 0.002	0.035 ± 0.000	0.037 ± 0.000
(1.2, 1.3)	0.049 ± 0.003	0.036 ± 0.000	0.039 ± 0.000
(1.3, 1.4)	0.051 ± 0.002	0.038 ± 0.000	0.041 ± 0.000

$\rho(r)$	$400 < p_T \leq 500$ GeV		
r	Data	Pythia	Herwig
(0.0, 0.1)	8.505 ± 0.156	8.784 ± 0.008	8.639 ± 0.015
(0.1, 0.2)	0.959 ± 0.109	0.871 ± 0.007	0.957 ± 0.012
(0.2, 0.3)	0.343 ± 0.048	0.237 ± 0.002	0.277 ± 0.004
(0.3, 0.4)	0.118 ± 0.017	0.101 ± 0.001	0.120 ± 0.002
(0.4, 0.5)	0.075 ± 0.008	0.059 ± 0.000	0.064 ± 0.001
(0.5, 0.6)	0.055 ± 0.005	0.044 ± 0.000	0.047 ± 0.001
(0.6, 0.7)	0.039 ± 0.004	0.035 ± 0.000	0.039 ± 0.000
(0.7, 0.8)	0.033 ± 0.003	0.030 ± 0.000	0.034 ± 0.000
(0.8, 0.9)	0.033 ± 0.003	0.028 ± 0.000	0.032 ± 0.000
(0.9, 1.0)	0.039 ± 0.005	0.028 ± 0.000	0.031 ± 0.000
(1.0, 1.1)	0.045 ± 0.004	0.027 ± 0.000	0.031 ± 0.000
(1.1, 1.2)	0.039 ± 0.005	0.028 ± 0.000	0.032 ± 0.000
(1.2, 1.3)	0.037 ± 0.003	0.029 ± 0.000	0.033 ± 0.000
(1.3, 1.4)	0.038 ± 0.003	0.030 ± 0.000	0.034 ± 0.000

Table A.2: *Differential jet shapes for data and two Monte Carlo predictions for different p_T ranges covering jets from 110 to 500 GeV.*

A.2 Integrated jet shapes

$\rho(r)$	$20 < p_T \leq 25$ GeV		
r	Data	Pythia	Herwig
(0.0, 0.1)	0.5054 ± 0.0021	0.5009 ± 0.0031	0.4995 ± 0.0045
(0.1, 0.2)	0.7948 ± 0.0011	0.7948 ± 0.0016	0.7928 ± 0.0023
(0.2, 0.3)	0.9372 ± 0.0005	0.9382 ± 0.0007	0.9352 ± 0.0010
(0.3, 0.4)	1.0000 ± 0.0000	1.0000 ± 0.0000	1.0000 ± 0.0000

$\rho(r)$	$20 < p_T \leq 30$ GeV		
r	Data	Pythia	Herwig
(0.0, 0.1)	0.5292 ± 0.0028	0.5392 ± 0.0031	0.5339 ± 0.0053
(0.1, 0.2)	0.8132 ± 0.0014	0.8146 ± 0.0016	0.8078 ± 0.0027
(0.2, 0.3)	0.9421 ± 0.0006	0.9430 ± 0.0007	0.9399 ± 0.0011
(0.3, 0.4)	1.0000 ± 0.0000	1.0000 ± 0.0000	1.0000 ± 0.0000

$\rho(r)$	$30 < p_T \leq 40$ GeV		
r	Data	Pythia	Herwig
(0.0, 0.1)	0.5721 ± 0.0030	0.5767 ± 0.0023	0.5807 ± 0.0050
(0.1, 0.2)	0.8326 ± 0.0014	0.8385 ± 0.0011	0.8347 ± 0.0024
(0.2, 0.3)	0.9458 ± 0.0006	0.9481 ± 0.0005	0.9468 ± 0.0010
(0.3, 0.4)	1.0000 ± 0.0000	1.0000 ± 0.0000	1.0000 ± 0.0000

$\rho(r)$	$40 < p_T \leq 60$ GeV		
r	Data	Pythia	Herwig
(0.0, 0.1)	0.6211 ± 0.0041	0.6354 ± 0.0021	0.6281 ± 0.0067
(0.1, 0.2)	0.8651 ± 0.0018	0.8702 ± 0.0009	0.8608 ± 0.0030
(0.2, 0.3)	0.9568 ± 0.0007	0.9572 ± 0.0004	0.9564 ± 0.0012
(0.3, 0.4)	1.0000 ± 0.0000	1.0000 ± 0.0000	1.0000 ± 0.0000

$\rho(r)$	$60 < p_T \leq 80$ GeV		
r	Data	Pythia	Herwig
(0.0, 0.1)	0.6745 ± 0.0027	0.7005 ± 0.0023	0.7062 ± 0.0136
(0.1, 0.2)	0.8926 ± 0.0011	0.8999 ± 0.0009	0.9011 ± 0.0054
(0.2, 0.3)	0.9656 ± 0.0004	0.9675 ± 0.0004	0.9686 ± 0.0021
(0.3, 0.4)	1.0000 ± 0.0000	1.0000 ± 0.0000	1.0000 ± 0.0000

$\rho(r)$	$80 < p_T \leq 110$ GeV		
r	Data	Pythia	Herwig
(0.0, 0.1)	0.7181 ± 0.0022	0.7451 ± 0.0018	0.6959 ± 0.0348
(0.1, 0.2)	0.9092 ± 0.0009	0.9179 ± 0.0007	0.9096 ± 0.0117
(0.2, 0.3)	0.9708 ± 0.0003	0.9731 ± 0.0003	0.9642 ± 0.0048
(0.3, 0.4)	1.0000 ± 0.0000	1.0000 ± 0.0000	1.0000 ± 0.0000

$\rho(r)$	$110 < p_T \leq 160$ GeV		
r	Data	Pythia	Herwig
(0.0, 0.1)	0.7587 ± 0.0019	0.7810 ± 0.0016	0.7942 ± 0.0533
(0.1, 0.2)	0.9246 ± 0.0007	0.9328 ± 0.0006	0.9456 ± 0.0202
(0.2, 0.3)	0.9765 ± 0.0003	0.9782 ± 0.0002	0.9825 ± 0.0075
(0.3, 0.4)	1.0000 ± 0.0000	1.0000 ± 0.0000	1.0000 ± 0.0000

$\rho(r)$	$160 < p_T \leq 210$ GeV		
r	Data	Pythia	Herwig
(0.0, 0.1)	0.7890 ± 0.0022	0.8127 ± 0.0013	0.7983 ± 0.0018
(0.1, 0.2)	0.9351 ± 0.0008	0.9432 ± 0.0005	0.9378 ± 0.0007
(0.2, 0.3)	0.9803 ± 0.0003	0.9823 ± 0.0002	0.9812 ± 0.0002
(0.3, 0.4)	1.0000 ± 0.0000	1.0000 ± 0.0000	1.0000 ± 0.0000

$\rho(r)$	$210 < p_T \leq 260$ GeV		
r	Data	Pythia	Herwig
(0.0, 0.1)	0.8168 ± 0.0030	0.8371 ± 0.0014	0.8192 ± 0.0021
(0.1, 0.2)	0.9443 ± 0.0011	0.9516 ± 0.0005	0.9452 ± 0.0008
(0.2, 0.3)	0.9828 ± 0.0004	0.9850 ± 0.0002	0.9833 ± 0.0003
(0.3, 0.4)	1.0000 ± 0.0000	1.0000 ± 0.0000	1.0000 ± 0.0000

$\rho(r)$	$260 < p_T \leq 310$ GeV		
r	Data	Pythia	Herwig
(0.0, 0.1)	0.8263 ± 0.0050	0.8502 ± 0.0017	0.8305 ± 0.0025
(0.1, 0.2)	0.9488 ± 0.0019	0.9557 ± 0.0006	0.9510 ± 0.0008
(0.2, 0.3)	0.9847 ± 0.0006	0.9865 ± 0.0002	0.9848 ± 0.0003
(0.3, 0.4)	1.0000 ± 0.0000	1.0000 ± 0.0000	1.0000 ± 0.0000

$\rho(r)$	$310 < p_T \leq 400$ GeV		
r	Data	Pythia	Herwig
(0.0, 0.1)	0.8414 ± 0.0076	0.8649 ± 0.0009	0.8500 ± 0.0014
(0.1, 0.2)	0.9527 ± 0.0028	0.9611 ± 0.0003	0.9560 ± 0.0005
(0.2, 0.3)	0.9851 ± 0.0010	0.9882 ± 0.0001	0.9870 ± 0.0002
(0.3, 0.4)	1.0000 ± 0.0000	1.0000 ± 0.0000	1.0000 ± 0.0000

$\rho(r)$	$400 < p_T \leq 500$ GeV		
r	Data	Pythia	Herwig
(0.0, 0.1)	0.8580 ± 0.0145	0.8791 ± 0.0008	0.8645 ± 0.0015
(0.1, 0.2)	0.9539 ± 0.0054	0.9662 ± 0.0003	0.9603 ± 0.0005
(0.2, 0.3)	0.9882 ± 0.0017	0.9899 ± 0.0001	0.9880 ± 0.0002
(0.3, 0.4)	1.0000 ± 0.0000	1.0000 ± 0.0000	1.0000 ± 0.0000

Table A.3: *Integrated jet shapes for data and two Monte Carlo predictions for different p_T ranges covering jets from 20 to 500 GeV.*

B

Performance of *b*-tagging algorithms in single top quark events

To distinguish between *b*-jets and light-jets the so-called *b*-tagging algorithms are used. These *b*-taggers analyse a jet and derive a weight of the probability that the jet is originating from a *b* quark. The higher the weight, the higher is the probability that the jet is a *b*-jet. A certain minimum weight (weight cut w_{cut}) can be chosen, and jets with weights exceeding the weight cut are tagged as *b*-jet. The performance of two different algorithms used in ATLAS, the $MV1$ and the $JetFitterCombNNc$ (the one used in the main analysis of this thesis), is studied using *t*-channel single top quark simulated events. The weight distributions for *t*-channel Monte Carlo events are shown in Figure B.1.

To find the optimal cut value for a given algorithm, the *b*-tagging efficiency and purity and the *c*- and light-rejection factors are studied as a function of the *b*-weight. These properties are defined as follows:

$$\epsilon_{c-tagged} = b\text{-tagging efficiency} = \frac{N^{tagged}_{b-quarks}}{N_{b-quarks}}$$

$$P_{c-tagged} = b\text{-tagging purity} = \frac{N^{tagged}_{b-quarks}}{N^{tagged}}$$

$$c\text{ -mistag rate} = \frac{N^{tagged}_{c-quarks}}{N_{c-quarks}}$$

$$\text{light-mistag rate} = \frac{N^{tagged}_{light-quarks}}{N_{light-quarks}}$$

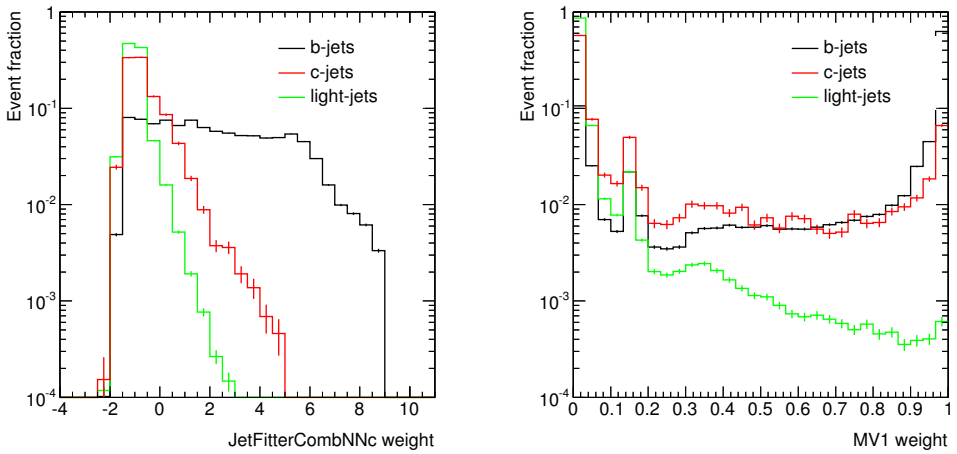

Figure B.1: *Weight distributions for b, c and light quarks for simulated t-channel single top quark events (jets with p_T >30 GeV and $|\eta|$ <4.5) for JetFitterCOMBNNc (left) and MV1 (right) taggers. The weight distribution is different for b-, c- and light-jets, which allows to separate jets of various flavours.*

Based on the c- and light-mistag rate, one can define the c-jet and light-jet rejection factor can be calculated.

$$c\text{ -tag rejection factor } = \frac{1}{c\text{ -mistag rate}}$$

$$\text{light-tag rejection factor } = \frac{1}{\text{light-mistag rate}}$$

Figure B.2 shows the b-tagging efficiency, c- and light-mistag rate as a function of the b-weight cut in t-channel Monte Carlo events. Figure B.3 shows the b-tagging efficiency as a function of the jet p_T and η. Figures B.4-B.5 show the b-tagging efficiency compared to the purity of the sample and to the c- and light-rejection factors.

An important criterion for the choice of a tagger are the rejection factors for light and c-jets. Table B.1 shows these values for both taggers and it can be seen that the light rejection is similar while c-jet rejection is higher for $JetFitterCombNNc$ than for $MV1$. In single top quark analysis a good c-jet rejection is desired in order to reject W+jets background.

Tagger	b**-tagging efficiency**	**light-jet rejection**	c**-jet rejection**
$MV1$	50%	80%	88%
$JetFitterCombNNc$	50%	80%	92%

Table B.1: *Performance of MV1 and JetFitterCOMBNNc b-tagging algorithms.*

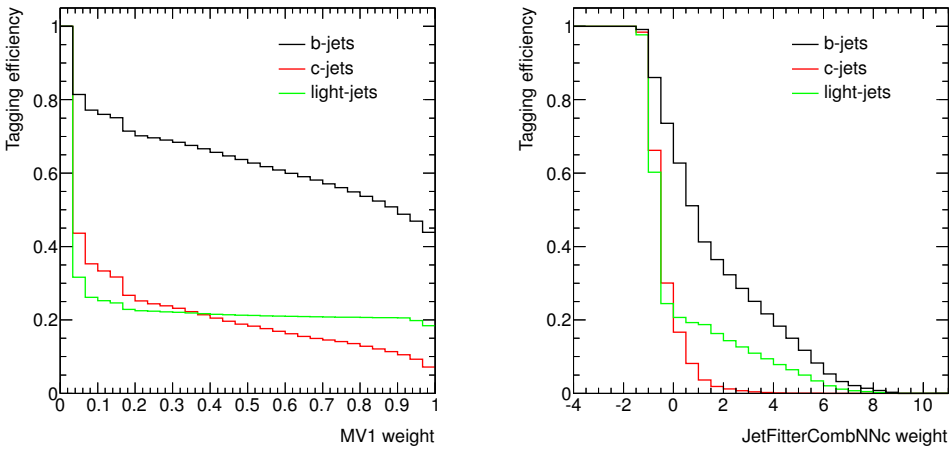

Figure B.2: *b-tagging efficiency for MV*1 *(left) and JetFitterCOMBNNc (right) taggers.*

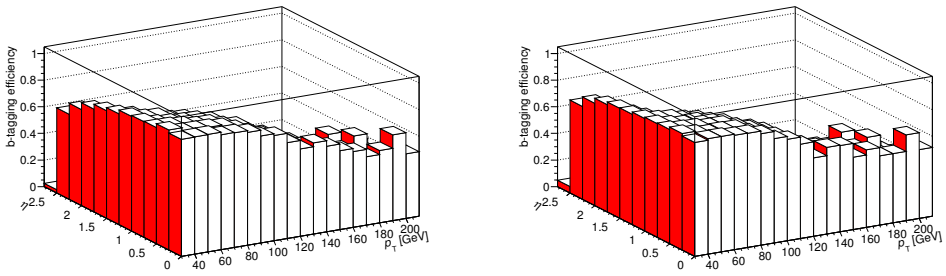

Figure B.3: *b-tagging efficiency vs. jet* p_T *and* η *for MV*1 *(left) and JetFitterCOMBNNc (right) taggers.*

In this context, the behaviour of the $MV1$ b-tagger (a working point of 60% b-tagging efficiency in $t\bar{t}$ events) has been compared with the so-called $JetFitterCombNNc$ tagger (a working point of 55% b-tagging efficiency in $t\bar{t}$ events) in terms of the signal-to-background ratio as can be seen in Table B.2. The signal-to-background ratio is around one half higher using $JetFitterCombNNc$ tagger. The signal efficiency is quite similar while the W+heavy flavour jets ($W + HF$) background is drastically reduced. For this reason, in most of the single top analysis and in the one presented in this thesis, the $JetFitterCombNNc$ is used.

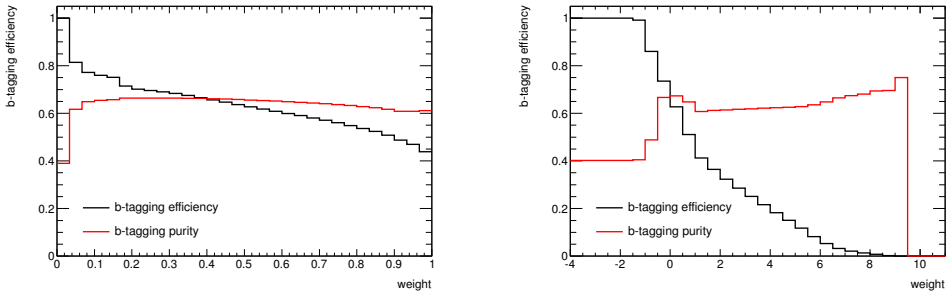

Figure B.4: *b-tagging efficiency and purity for MV1 (left) and JetFitterCOMBNNc (right) taggers.*

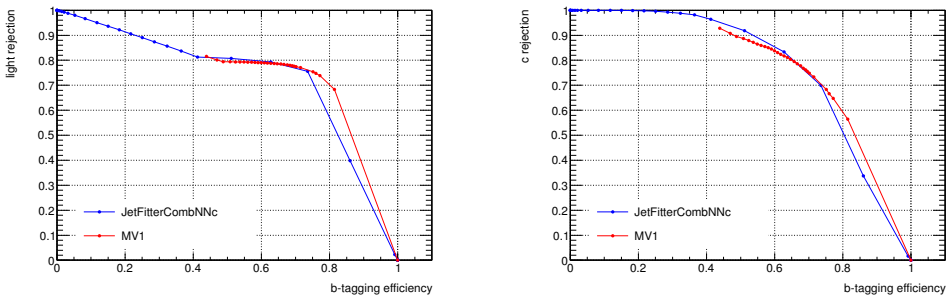

Figure B.5: *Light- (left) and c-jet (right) rejection Vs. b-tagging efficiency for JetFitterCOMBNNc and MV1 taggers.*

Tagger	**S/B preselection**	**S/B selection**
MV1	0.09	0.63
JetFitterCombNNc	0.13	0.95

Table B.2: *Signal-to-background ratio in t-channel single top quark events for the MV1 and JetFitterCombNNc taggers (with working points of 60% and 55% b-tagging efficiency in $t\bar{t}$ events, respectively).*

C
Monte Carlo samples

Table C.1 and Table C.2 contain the list of the Monte Carlo samples used in single top quark analyses and summarize the relevant information about them: the generator and shower models used, the total number of events in each sample, the cross sections of each process and the corresponding K-factors.

Process	Generator	$\sigma \times BR$ [pb]	K-factors	N_{evt}^{MC}
t-channel (exclusive e decay)	AcerMC+Pythia	8.06	0.87	999295
t-channel (exclusive μ decay)	AcerMC+Pythia	8.06	0.87	999948
t-channel (exclusive τ decay)	AcerMC+Pythia	8.05	0.87	998995
s-channel (inclusive lepton decay)	Powheg+Pythia	1.39	1.079	199998
Wt-channel (all inclusive)	Powheg+Pythia	14.79	1.083	194945
$t\bar{t}$ (no fully had)	Powheg+Pythia	80.07	1.131	9994443

Table C.1: *Simulated samples for top quark processes. The samples are normalised to the predicted approximate NNLO theoretical cross sections [51–53, 138].*

Process	Generator	$\sigma \times$ *BR* [pb]	*K*-factors	N_{evt}^{MC}
$Z \to ll$ + 0 parton	Alpgen+Jimmy	668.32	1.25	6618284
$Z \to ll$ + 1 parton		134.36	1.25	1334897
$Z \to ll$ + 2 partons		40.54	1.25	2004195
$Z \to ll$ + 3 partons		11.16	1.25	549949
$Z \to ll$ + 4 partons		2.88	1.25	149948
$Z \to ll$ + 5 partons		0.83	1.25	50000
$W \to l\nu$ + 0 parton	Alpgen+Jimmy	6930.50	1.20	6952874
$W \to l\nu$ + 1 parton		1305.30	1.20	4998487
$W \to l\nu$ + 2 partons		378.13	1.20	3768632
$W \to l\nu$ + 3 partons		101.86	1.20	1008947
$W \to l\nu$ + 4 partons		25.68	1.20	250000
$W \to l\nu$ + 5 partons		6.99	1.20	69999
$W \to l\nu + b\bar{b}$ + 0 parton	Alpgen+Jimmy	47.35	1.20	474997
$W \to l\nu + b\bar{b}$ + 1 parton		35.76	1.20	205000
$W \to l\nu + b\bar{b}$ + 2 partons		17.33	1.20	174499
$W \to l\nu + b\bar{b}$ + 3 partons		7.61	1.20	69999
$W \to l\nu + c\bar{c}$ + 0 parton	Alpgen	127.53	1.20	1274846
$W \to l\nu + c\bar{c}$ + 1 parton		104.68	1.20	1049847
$W \to l\nu + c\bar{c}$ + 2 partons		52.08	1.20	524947
$W \to l\nu + c\bar{c}$ + 3 partons		16.96	1.20	170000
$W \to l\nu + c$ + 0 parton	Alpgen	644.40	1.52	6427837
$W \to l\nu + c$ + 1 parton		205.00	1.52	2069646
$W \to l\nu + c$ + 2 partons		50.80	1.52	519974
$W \to l\nu + c$ + 3 partons		11.40	1.52	115000
$W \to l\nu + c$ + 4 partons		2.80	1.52	30000
WW	Herwig	11.50	1.48	2489242
WZ		3.46	1.60	999896
ZZ		0.97	1.30	249999
Multijet	Pythia	-	-	9999419

Table C.2: *Simulated samples for W+jets, Z+jets, diboson and multijet background processes. For W+jets and multijet processes, their normalisation is determined in-situ using control regions (see Section 5.4.2 and Section 5.4.1). For Z+jets background the inclusive cross sections are calculated to NNLO with FEWZ [140]. The diboson cross sections are normalised to NLO theoretical calculations [141].*

D

W+jets background normalisation

As discussed in Section 5.4.2, in-situ data driven techniques are used to estimate the different flavour composition and the overall normalisation of W+jets background. This is done in a control region dominated by W+jets events, by selecting events that pass all the preselection cuts except the requirement in the number of jets and in which the mass of the reconstructed top quark is m_t <150 GeV or m_t >190 GeV. The method assumes that W+jets contribution is the result of subtracting electroweak (WW, WZ, ZZ and Z+jets), top quark and QCD multijet background processes from the data events. An overall normalisation scale factor (denoted by SF) for the W+jets sample is obtained for each jet bin using:

$$\frac{N_{W+jets,Data}}{N_{W+jets,MC}} = \frac{N_{data} - N_{EWK} - N_{top} - N_{QCD}}{N_{W+jets,MC}} \,. \tag{D.1}$$

In addition, a single scale factor is derived for each flavour of W+jets events. Both $W+b\bar{b}$ and $W+c\bar{c}$ scale factors are considered the same. These flavour scale factors are extracted using the '1-jet' and '2-jets' bins of the 'pretag' and 'tag' data sample. A series of equations can be written using these control regions which can then be solved to derive scale factors. The number of data events after background subtraction ($N_{data\text{-}bkg}$) is a function of the jet flavour fractions (F_{bb}, F_{cc}, F_c and F_{light}) for the '1-jet pretag' and '2-jets pretag' regions is given by:

$$N^{pretag}_{data\text{-}bkg,1} = N^{pretag}_{data\text{-}bkg,1}\left(F^{pretag}_{bb,1} + F^{pretag}_{cc,1} + F^{pretag}_{c,1} + F^{pretag}_{light,1}\right) \,, \tag{D.2}$$

$$N^{pretag}_{data\text{-}bkg,2} = N^{pretag}_{data\text{-}bkg,2}\left(F^{pretag}_{bb,2} + F^{pretag}_{cc,2} + F^{pretag}_{c,2} + F^{pretag}_{light,2}\right) \,. \tag{D.3}$$

The expected number of 'tag' events with n jets in flavour sample Φ, ($N^{tag}_{\Phi,n}$), is a function of the number of 'pretag' events (N^{pretag}_{n}), the fraction of events of flavour Φ ($F^{pretag}_{\Phi,n}$) and the average event tagging probability ($P^{tag}_{\Phi,n}$) for each configuration:

$$N^{tag}_{\Phi,n} = N^{pretag}_{n} \cdot F^{pretag}_{\Phi,n} \cdot P^{tag}_{\Phi,n} \,. \tag{D.4}$$

The event tagging probability ($P^{tag}_{\Phi,n}$) is the fraction of all Monte Carlo events in the 'pretag' sample with configuration (Φ, n) that survive the tagging requirement (exactly 1 tag) and is determined using the full Alpgen W+jets Monte Carlo sample. With this, the number of 'tag' data events after background subtraction in the '1-jet' and '2-jets' bin can be written as:

$$N^{tag}_{data\text{-}bkg,1} = N^{pretag}_{data\text{-}bkg,1}\left(F^{pretag}_{bb,1}\cdot P^{tag}_{bb,1} + F^{pretag}_{cc,1}\cdot P^{tag}_{cc,1} + F^{pretag}_{c,1}\cdot P^{tag}_{c,1} + F^{pretag}_{light,1}\cdot P^{tag}_{light,1}\right), \quad \text{(D.5)}$$

$$N^{tag}_{data\text{-}bkg,2} = N^{pretag}_{data\text{-}bkg,2}\left(F^{pretag}_{bb,2}\cdot P^{tag}_{bb,2} + F^{pretag}_{cc,2}\cdot P^{tag}_{cc,2} + F^{pretag}_{c,2}\cdot P^{tag}_{c,2} + F^{pretag}_{light,2}\cdot P^{tag}_{light,2}\right). \quad \text{(D.6)}$$

In writing the full set of equations, certain assumptions must be made to combine the $c\bar{c}$ and $b\bar{b}$ fractions and extract the $b\bar{b}/c\bar{c}$, c, and light samples in the 1-jet bin:

- F^{pretag}_{cc} is replaced by $k^{pretag}_{cctobb}\cdot F^{pretag}_{bb}$, where k^{pretag}_{cctobb} is the ratio between the $c\bar{c}$ fraction and the $b\bar{b}$ fraction.
- $F^{pretag}_{bb,1}$ is replaced by $k^{pretag}_{bb2to1}\cdot F^{pretag}_{bb,2}$, where k_{bb2to1} is the ratio of $b\bar{b}$ events in the '1-jet' bin over the 2 jet bin.

With all this, one can write the following equations for 'pretag' events with '1-jet':

$$\begin{aligned} N^{pretag}_{data\text{-}bkg,1} &= N^{pretag}_{data\text{-}bkg,1}\left(F^{pretag}_{bb,1} + k^{pretag}_{cctobb}\cdot F^{pretag}_{bb,1} + F^{pretag}_{c,1} + F^{pretag}_{light,1}\right) \\ &= N^{pretag}_{data\text{-}bkg,1}\left(k^{pretag}_{bb2to1}\cdot F^{pretag}_{bb,2} + k^{pretag}_{cctobb}\cdot k^{pretag}_{bb2to1}\cdot F^{pretag}_{bb,2} + k^{pretag}_{c2to1}\cdot F^{pretag}_{c,2} + k^{pretag}_{l2to1}\cdot F^{pretag}_{light,2}\right), \end{aligned} \quad \text{(D.7)}$$

for 'tag' events with '1-jet' in the final state:

$$\begin{aligned} N^{tag}_{data\text{-}bkg,1} &= N^{pretag}_{data\text{-}bkg,1}\left(F^{pretag}_{bb,1}\cdot P^{tag}_{bb,1} + k^{pretag}_{cctobb}\cdot F^{pretag}_{bb,1}\cdot P^{tag}_{cc,1} + F^{pretag}_{c,1}\cdot P^{tag}_{c,1} + F^{pretag}_{light,1}\cdot P^{tag}_{light,1}\right) \\ &= N^{pretag}_{data\text{-}bkg,1}\left(k^{pretag}_{bb2to1}\cdot F^{pretag}_{bb,2}\cdot P^{tag}_{bb,1} + k^{pretag}_{cctobb}\cdot k^{pretag}_{bb2to1}\cdot F^{pretag}_{bb,2}\cdot P^{tag}_{cc,1}\right. \\ &\quad \left. + k^{pretag}_{c2to1}\cdot F^{pretag}_{c,2}\cdot P^{tag}_{c,1} + k^{pretag}_{l2to1}\cdot F^{pretag}_{light,2}\cdot P^{tag}_{light,1}\right), \end{aligned} \quad \text{(D.8)}$$

for 'pretag' events with '2-jets' in the final state:

$$N^{pretag}_{data\text{-}bkg,2} = N^{pretag}_{data\text{-}bkg,2}\left(F^{pretag}_{bb,2} + k^{pretag}_{cctobb}\cdot F^{pretag}_{bb,2} + F^{pretag}_{c,2} + F^{pretag}_{light,2}\right), \quad \text{(D.9)}$$

and for 'tag' events with '2-jets' in the final state:

$$N^{tag}_{data\text{-}bkg,2} = N^{pretag}_{data\text{-}bkg,2}\left(F^{pretag}_{bb,2}\cdot P^{tag}_{bb,2} + k^{pretag}_{cctobb}\cdot F^{pretag}_{bb,2}\cdot P^{tag}_{cc,2} + F^{pretag}_{c,2}\cdot P^{tag}_{c,2} + F^{pretag}_{light,2}\cdot P^{tag}_{light,2}\right). \quad \text{(D.10)}$$

This system of four equations can be solved algebraically for the three unknown flavour fractions: F^{pretag}_{bb}, F^{pretag}_{c} and F^{pretag}_{light}. The correction factors, K_{bb}, K_c and K_{light}, for each W+jets flavour sample are then derived from these fractions. For example, the $b\bar{b}$ correction factor is defined as the number of $W + b\bar{b}$ events in data over the number of events in Monte Carlo:

$$K_{bb} = \frac{N^{pretag,data}_{Wbb}}{N^{pretag,MC}_{Wbb}}, \quad \text{(D.11)}$$

and similarly for c and light. For '2-jets' events this is:

$$K_{bb,2} = \frac{N^{pretag,data}_{Wbb,2}}{N^{pretag,MC}_{Wbb,2}} = \frac{F^{pretag,data}_{bb,2} \cdot N^{pretag,data}_{Wjets,2}}{F^{pretag,MC}_{bb,2} \cdot N^{pretag,MC}_{Wjets,2}} \,. \tag{D.12}$$

The correction factors for 1, 3 and 4 jets normalisations are derived from the '2-jets' correction factors and the W+jets data and Monte Carlo contributions:

$$K_{bb,i\text{-}jet} = \frac{F^{pretag,data}_{bb,2} \cdot N^{pretag,data}_{Wjets,i\text{-}jet}}{F^{pretag,MC}_{bb,2} \cdot (N^{pretag,MC}_{Wbb,i\text{-}jet} \cdot K_{bb,2} + N^{pretag,MC}_{Wcc,i\text{-}jet} + N^{pretag,MC}_{Wc,i\text{-}jet} + N^{pretag,MC}_{Wlight,i\text{-}jet})} \,. \tag{D.13}$$

Different set of values for the overall normalisation and flavour fraction scale factors are obtained for each systematic uncertainty. The values obtained are presented in Table D.1 for the electron channel and in Table D.2 for the muon channel.

Systematic	SF	Rel. Diff. (%)	$K_{bb} = K_{cc}$	Rel. Diff. (%)	K_c	Rel. Diff. (%)	K_{light}	Rel. Diff. (%)
Nominal	0.992	0.000	1.135	0.000	1.423	0.000	0.887	0.000
Lepton reco. eff. up	0.964	-2.812	1.071	-5.677	1.466	3.045	0.887	0.029
Lepton reco. eff. down	1.022	2.959	1.195	5.279	1.386	-2.597	0.886	-0.109
Lepton energy reso. up	0.992	-0.014	1.131	-0.362	1.428	0.354	0.887	-0.056
Lepton energy reso. down	0.992	-0.006	1.149	1.189	1.403	-1.404	0.889	0.271
Lepton energy scale up	0.984	-0.797	1.139	0.308	1.415	-0.576	0.888	0.138
Lepton energy scale down	0.998	0.585	1.152	1.439	1.410	-0.898	0.887	0.046
Jet energy scale up	0.868	-12.533	1.427	25.703	1.349	-5.153	0.864	-2.570
Jet energy scale down	1.076	8.424	0.984	-13.342	1.446	1.651	0.904	1.949
$E_{\mathrm{T}}^{\mathrm{miss}}$: (cellout) up	0.988	-0.418	1.139	0.360	1.417	-0.389	0.888	0.059
$E_{\mathrm{T}}^{\mathrm{miss}}$: (cellout) down	0.993	0.061	1.135	-0.046	1.426	0.206	0.886	-0.074
$E_{\mathrm{T}}^{\mathrm{miss}}$: (pileup) up	0.991	-0.182	1.144	0.777	1.414	-0.621	0.888	0.081
$E_{\mathrm{T}}^{\mathrm{miss}}$: (pileup) down	0.993	0.052	1.152	1.508	1.401	-1.515	0.889	0.232
SF b-tag up	0.992	0.000	0.974	-14.175	1.492	4.857	0.896	1.029
SF b-tag down	0.992	0.000	1.321	16.362	1.343	-5.594	0.876	-1.192
SF c-tag up	0.992	0.000	1.085	-4.413	1.343	-5.600	0.912	2.818
SF c-tag down	0.992	0.000	1.188	4.647	1.516	6.519	0.859	-3.186
SF mistag up	0.992	0.000	1.122	-1.155	1.411	-0.795	0.891	0.502
SF mistag down	0.992	0.000	1.156	1.798	1.428	0.401	0.883	-0.487
JVF SF up	0.985	-0.783	1.108	-2.405	1.436	0.902	0.888	0.151
JVF SF down	1.001	0.826	1.158	1.992	1.412	-0.746	0.886	-0.122
Jet reco. efficiency	0.992	-0.008	1.140	0.435	1.421	-0.128	0.887	-0.043
Jet energy resolution	0.956	-3.678	1.178	3.785	1.401	-1.530	0.886	-0.126
Z+jets norm. up	0.949	-4.414	1.204	6.044	1.432	0.629	0.875	-1.387
Z+jets norm. down	1.036	4.413	1.074	-5.378	1.411	-0.851	0.899	1.336
$t\bar{t}$ norm. up	0.989	-0.301	0.995	-12.377	1.516	6.563	0.888	0.083
$t\bar{t}$ norm. down	0.995	0.302	1.274	12.222	1.331	-6.464	0.886	-0.087
dibosons norm. up	0.992	-0.070	1.134	-0.075	1.423	0.004	0.887	0.013
dibosons norm. down	0.993	0.071	1.135	-0.001	1.423	0.044	0.887	-0.015
W+jets shape (iqopt3)	0.988	-0.431	1.133	-0.198	1.426	0.252	0.887	-0.043
W+jets shape: (ptjmin10)	0.984	-0.813	1.136	0.074	1.422	-0.046	0.887	0.001
QCD norm. up	0.946	-4.691	1.022	-9.963	1.466	3.066	0.895	0.845
QCD norm. down	1.039	4.691	1.237	8.987	1.385	-2.646	0.880	-0.804
Syst. Uncertainty	-	18.425	-	50.667	-	24.107	-	5.380
Stat. Uncertainty	-	0.394	-	9.828	-	6.104	-	0.248
Total Uncertainty	-	18.429	-	51.612	-	24.868	-	5.385

Table D.1: *Overall W+jets normalisation scale factors (SF) and flavour fraction scale factors (K_i) for each systematic source of uncertainty for events with '2-jets' in the electron channel.*

Systematic	SF	Rel. Diff. (%)	$K_{bb} = K_{cc}$	Rel. Diff. (%)	K_c	Rel. Diff. (%)	K_{light}	Rel. Diff. (%)
Nominal	1.031	0.000	1.413	0.000	1.236	0.000	0.890	0.000
Lepton reco. eff. up	1.014	-1.622	1.385	-1.971	1.253	1.342	0.891	0.082
Lepton reco. eff. down	1.049	1.679	1.448	2.471	1.214	-1.796	0.889	-0.069
Lepton reso. eff: no scale	1.026	-0.477	1.399	-0.964	1.246	0.803	0.890	-0.004
Lepton reso. eff: ID up	1.031	-0.015	1.412	-0.093	1.237	0.070	0.890	-0.000
Lepton reso. eff: ID down	1.031	0.003	1.412	-0.054	1.235	-0.092	0.890	0.041
Lepton reso. eff: MS up	1.031	-0.019	1.413	0.021	1.235	-0.074	0.890	0.014
Lepton reso. eff: MS down	1.031	0.015	1.413	0.001	1.237	0.018	0.890	-0.005
Jet energy scale up	0.912	-11.541	1.741	23.215	1.137	-8.049	0.868	-2.442
Jet energy scale down	1.110	7.615	1.288	-8.820	1.253	1.307	0.903	1.521
$E_{\mathrm{T}}^{\mathrm{miss}}$: (cellout) up	1.027	-0.412	1.404	-0.662	1.249	1.018	0.889	-0.146
$E_{\mathrm{T}}^{\mathrm{miss}}$: (cellout) down	1.034	0.292	1.418	0.372	1.235	-0.107	0.889	-0.045
$E_{\mathrm{T}}^{\mathrm{miss}}$: (pileup) up	1.029	-0.236	1.421	0.556	1.227	-0.782	0.891	0.091
$E_{\mathrm{T}}^{\mathrm{miss}}$: (pileup) down	1.033	0.164	1.416	0.198	1.233	-0.312	0.890	0.061
SF b-tag up	1.031	0.000	1.260	-10.810	1.295	4.776	0.900	1.193
SF b-tag down	1.031	0.000	1.599	13.159	1.159	-6.242	0.878	-1.331
SF c-tag up	1.031	0.000	1.371	-2.997	1.160	-6.155	0.912	2.466
SF c-tag down	1.031	0.000	1.467	3.848	1.316	6.416	0.865	-2.743
SF mistag up	1.031	0.000	1.402	-0.812	1.223	-1.089	0.894	0.503
SF mistag down	1.031	0.000	1.429	1.124	1.245	0.721	0.886	-0.472
JVF SF up	1.023	-0.772	1.387	-1.855	1.247	0.836	0.892	0.204
JVF SF down	1.039	0.798	1.442	2.028	1.220	-1.331	0.889	-0.098
Jet reco. efficiency	1.031	0.012	1.413	0.013	1.235	-0.107	0.890	0.022
Jet energy resolution	1.005	-2.574	1.385	-1.958	1.287	4.134	0.885	-0.597
Z+jets norm. up	1.008	-2.253	1.440	1.892	1.243	0.551	0.884	-0.605
Z+jets norm. down	1.054	2.254	1.388	-1.762	1.229	-0.591	0.895	0.586
$t\bar{t}$ norm. up	1.029	-0.255	1.302	-7.873	1.313	6.208	0.891	0.090
$t\bar{t}$ norm. down	1.034	0.255	1.523	7.786	1.161	-6.124	0.889	-0.093
dibosons norm. up	1.031	-0.064	1.413	0.012	1.235	-0.071	0.890	0.017
dibosons norm. down	1.032	0.064	1.413	-0.012	1.237	0.070	0.890	-0.017
W+jets shape (iqopt3)	1.030	-0.084	1.403	-0.681	1.253	1.347	0.888	-0.266
W+jets shape: (ptjmin10)	1.030	-0.166	1.402	-0.755	1.244	0.607	0.889	-0.077
QCD norm. up	1.024	-0.731	1.356	-4.028	1.233	-0.309	0.899	1.041
QCD norm. down	1.039	0.731	1.469	3.978	1.240	0.281	0.881	-1.021
Syst. Uncertainty	-	15.171	-	47.250	-	21.948	-	4.787
Stat. Uncertainty	-	0.333	-	6.085	-	5.743	-	0.200
Total Uncertainty	-	15.175	-	47.641	-	22.687	-	4.791

Table D.2: *Overall W+jets normalisation scale factors (SF) and flavour fraction scale factors (K_i) for each systematic source of uncertainty for events with '2-jets' in the muon channel.*

E

Distributions in control regions: data and expectation comparisons

The kinematic distributions of t-channel final state objects are presented in Figures E.1-E.2 for the preselection control region. In general, a good agreement between data and prediction is observed.

Figures E.3-E.4 show the distributions of the discriminant variables used in the selection cuts, η of the light jet (i.e. spectator quark), H_{T}, reconstructed top quark mass and $\Delta\eta$(light-jet, b-jet), for the three control regions defined in this analysis (see Section 5.5).

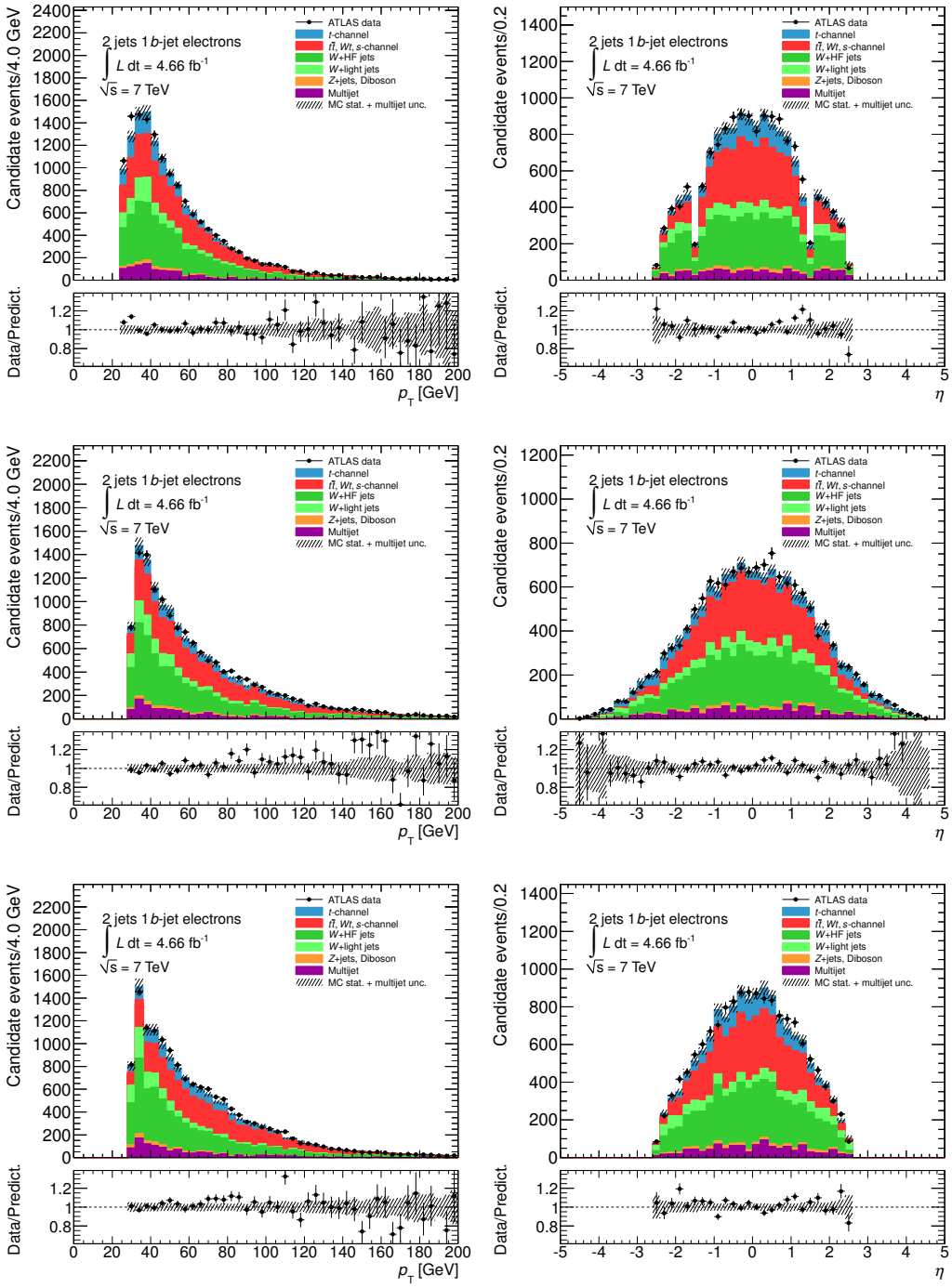

Figure E.1: *Kinematic distributions of p_T (left) and η (right) of the final state objects: lepton (top), light jet (middle) and b-jet (bottom) for the electron channel at preselection level.*

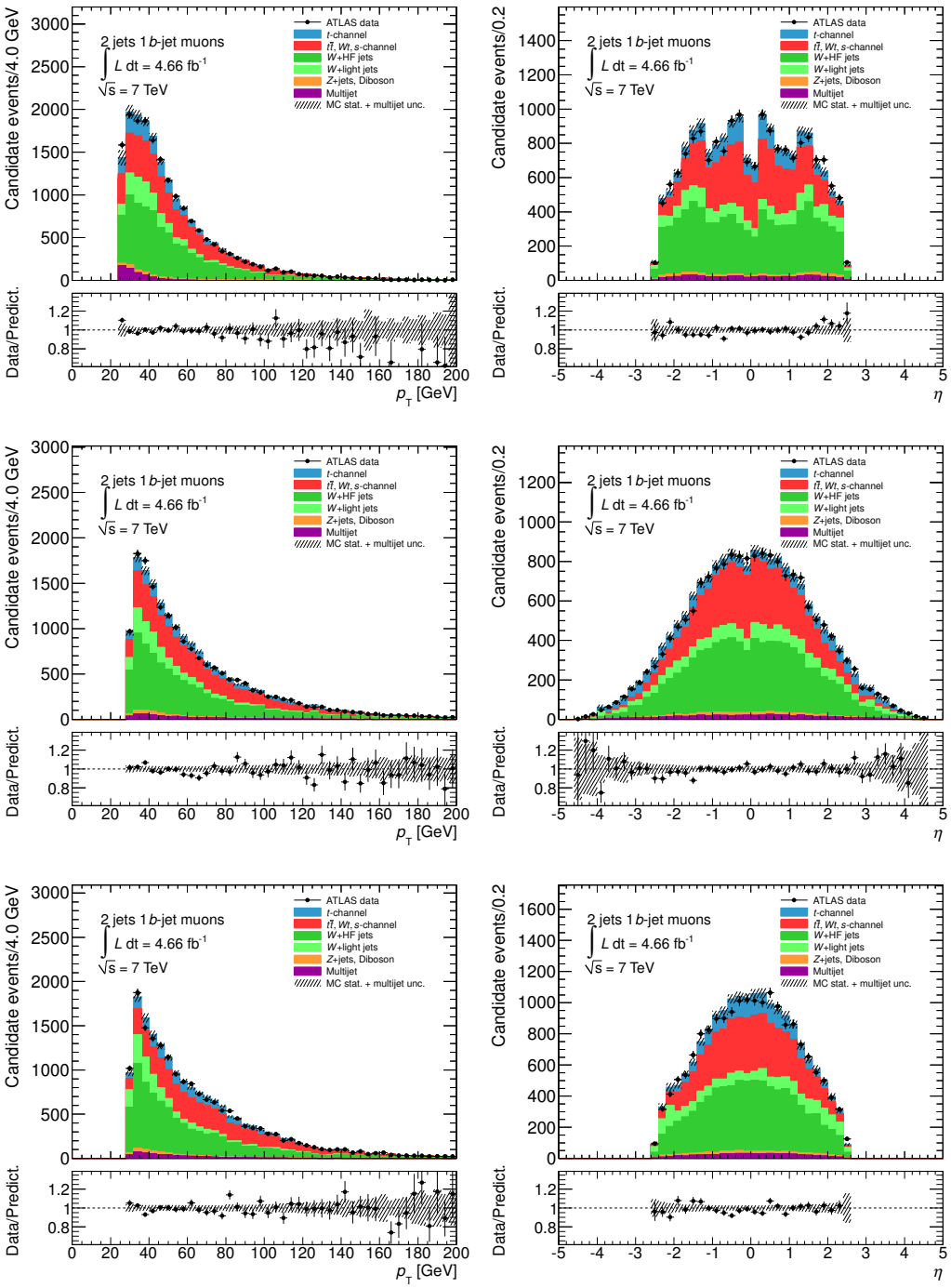

Figure E.2: *Kinematic distributions of p_T (left) and η (right) of the final state objects: lepton (top), light jet (middle) and b-jet (bottom) for the muon channel at preselection level.*

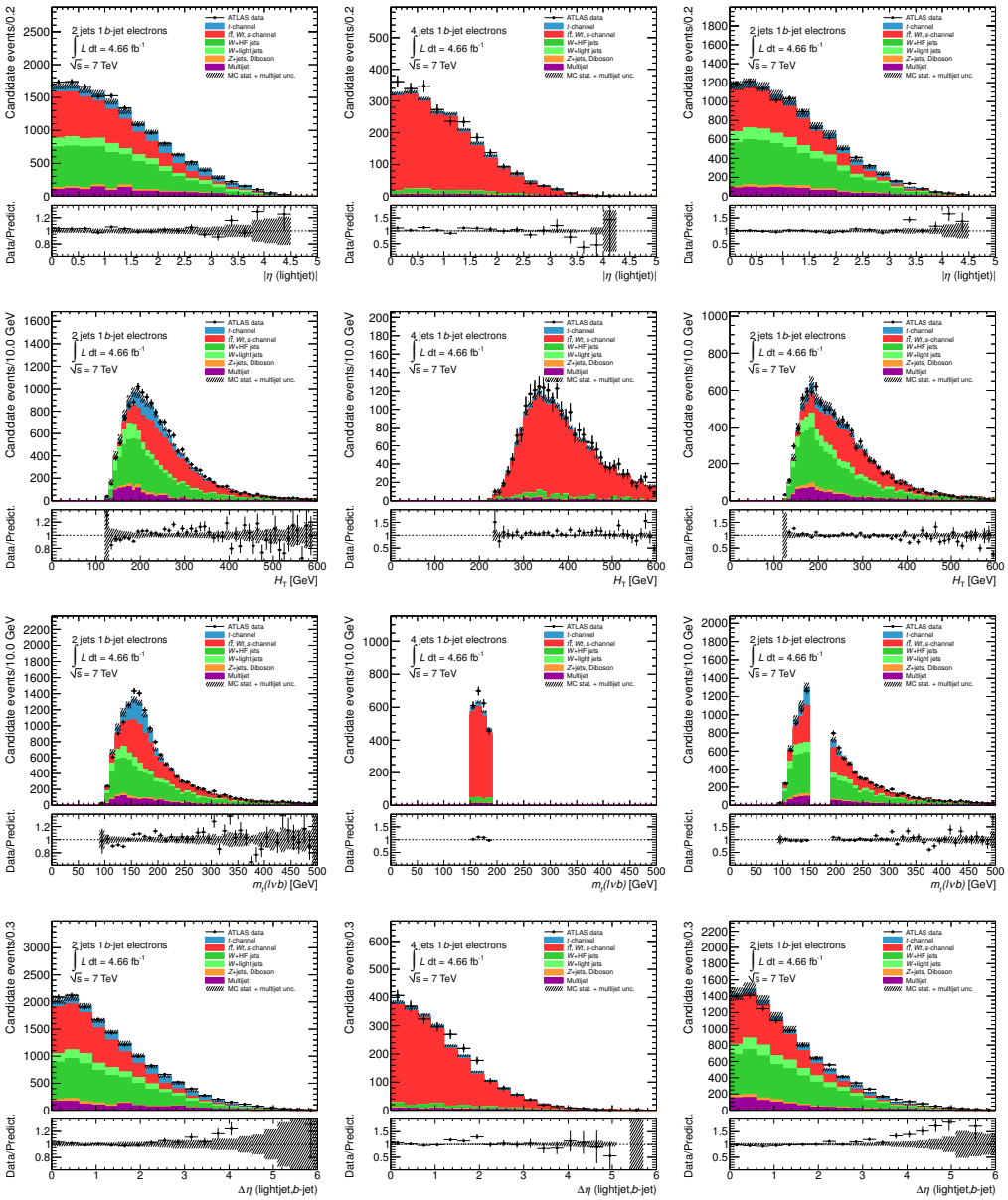

Figure E.3: *Discriminant variables (η of the light jet, H_{T}, reconstructed top quark mass and $\Delta\eta$(light-jet, b-jet) for the different control regions for the electron channel: preselection (left), top quark pair (middle) and W+jets (right) enriched regions.*

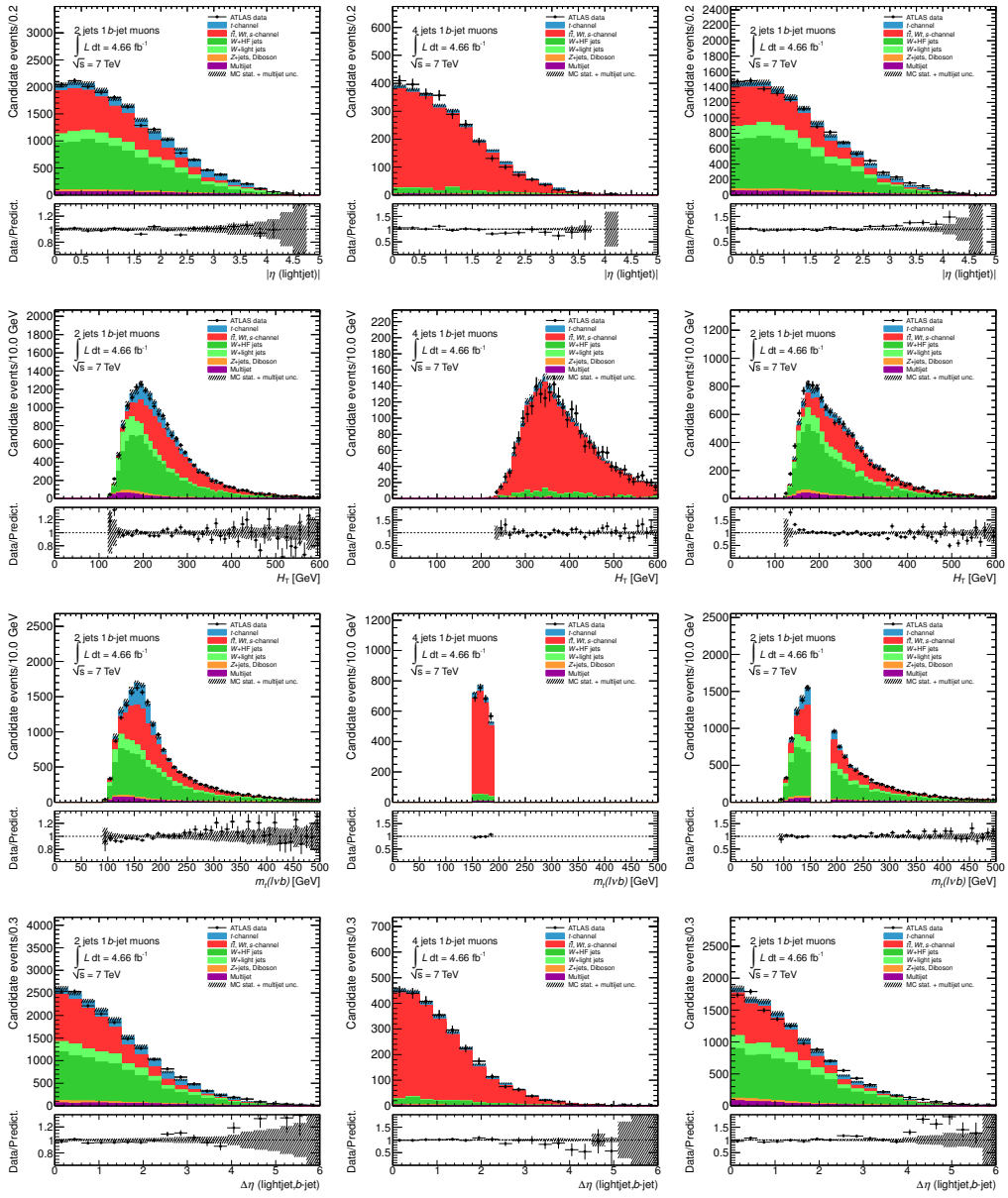

Figure E.4: *Discriminant variables (η of the light jet, H_{T}, reconstructed top quark mass and $\Delta\eta$(light-jet, b-jet) for the different control regions for the muon channel: preselection (left), top quark pair (middle) and W+jets (right) enriched regions.*

F

Measurement of $A_{\mathrm{FB}}^{\mathrm{N}}$ for each lepton channel

This appendix shows results obtained in the $A_{\mathrm{FB}}^{\mathrm{N}}$ measurement for the electron and muon channel separately. These allow to understand and cross check the results obtained for the combined channel. Before presenting the different results, the data/expectation ratio of the $\cos\theta^{\mathrm{N}}$ distribution for both channels is compared by computing a double ratio, as can be seen in Figure F.1. One can see that both channels agree quite well.

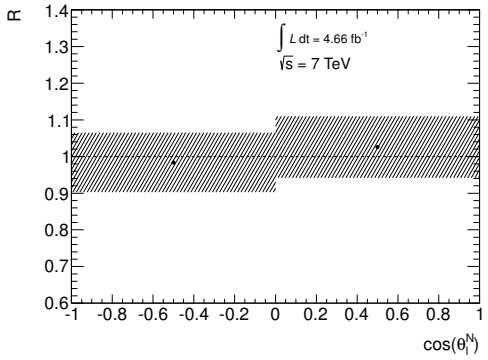

Figure F.1: *Comparison of the* $\cos\theta^N$ *data/expectation ratio for the electron and muon channel by computing the 'double ratio'. The hatched band indicates the statistical uncertainty.*

F.1 Distortions of the angular distribution $\cos\theta^{N}$

Figure F.2 shows the event selection efficiency as a function of $\cos\theta^{N}$ for electrons and muons independently. As in the combined case and explained in Section 5.7.1, a strong suppression of events with $\cos\theta^{N}$ values in the central region. Figure F.3 shows the transfer and migration matrices for both channels.

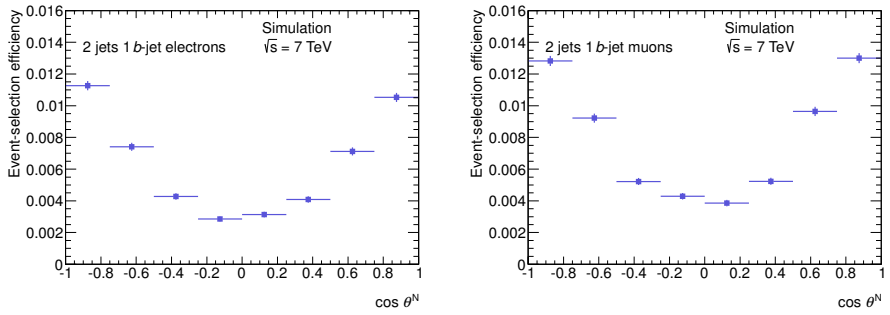

Figure F.2: *Event selection efficiency for the electron (left) and muon (right) channels.*

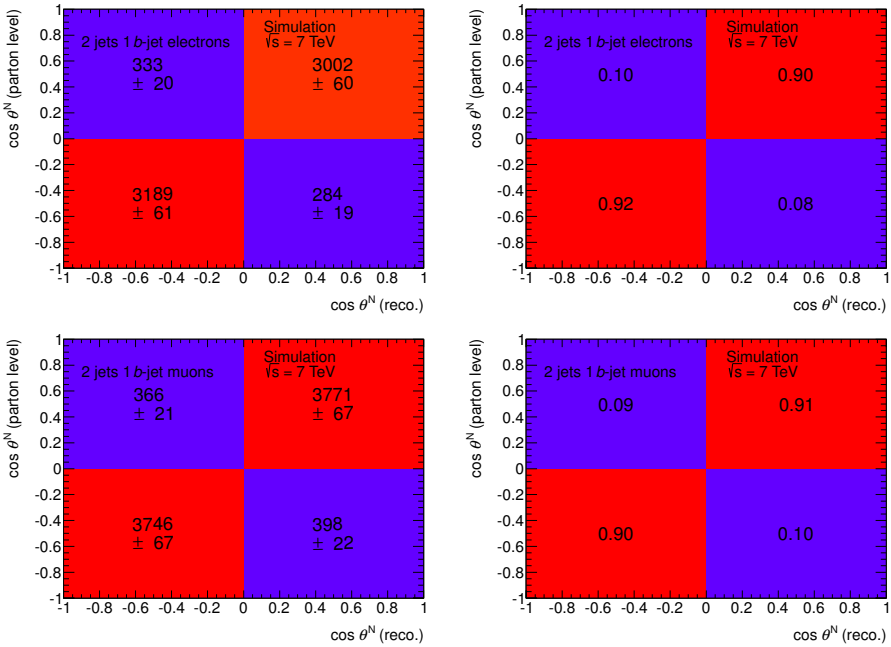

Figure F.3: *Transfer matrix T_{ji} (left) and migration matrix M_{ji} (right) for electrons (top) and muons (bottom).*

F.2 Unfolded data distribution

Tables F.1-F.2 show the A_{FB}^{N} values obtained before and after background subtraction and after the unfolding for electron and muon channels separately. The unfolded value for the A_{FB}^{N} is compared with the SM prediction for both channels.

el	$A_{\mathrm{FB}}^{\mathrm{N}}$
Data (raw)	0.010 ± 0.042 (data stat.)
Data (raw, bkg. subtracted)	0.018 ± 0.080 (data st.) ± 0.013 (bkg. st.) = 0.018 ± 0.081 (total stat.)
Data unfolded	0.065 ± 0.098 (data st.) ± 0.019 (bkg. st.) ± 0.009 (signal st.) = 0.065 ± 0.102 (total stat.)

Table F.1: *Measurement of A_{FB}^{N} for the electron channel. Only the statistical uncertainties are shown.*

mu	$A_{\mathrm{FB}}^{\mathrm{N}}$
Data (raw)	0.013 ± 0.038 (data stat.)
Data (raw, bkg. subtracted)	0.017 ± 0.073 (data st.) ± 0.011 (bkg. st.) = 0.017 ± 0.074 (total stat.)
Data unfolded	0.004 ± 0.089 (data st.) ± 0.015 (bkg. st.) ± 0.008 (signal st.) = 0.004 ± 0.091 (total stat.)

Table F.2: *Measurement of A_{FB}^{N} for the muon channel. Only the statistical uncertainties are shown.*

F.3 Systematic uncertainties

Table F.3 shows a breakdown of the systematic uncertainties and their contribution to the A_{FB}^{N} measurement for the electron and muon respectively.

F.4 Results

The final value of A_{FB}^{N} and its statistic and systematic uncertainties are quoted in Table F.4 for the different lepton channels individually.

Source	Electron	Muon
Lepton reco. eff.	0.004 / -0.002	0.002 / 0.001
Lepton energy scale	0.006 / 0.007	0.002 / <0.001
Lepton energy reso.	-0.003 / <0.001	0.002 / <0.001
Lepton energy reso.	-0.003 / <0.001	<0.001 / -0.001
Jet energy scale	0.004 / 0.018	-0.011 / 0.001
E_T^{miss} (cellout)	-0.007 / -0.004	0.005 / <0.001
E_T^{miss} (pileup)	0.002 / -0.007	0.003 / -0.001
SF b-tag	0.003 / 0.007	0.002 / <0.001
SF c-tag	0.001 / <0.001	0.002 / -0.002
SF mistag	0.002 / -0.002	0.003 / -0.001
JVF SF	0.003 / <0.001	0.001 / -0.001
Jet reconstruction efficiency	0.004 / -0.004	0.003 / -0.003
Jet energy resolution	0.014 / -0.014	0.005 / -0.005
Luminosity	0.003 / 0.001	0.002 / -0.001
Z+jets norm.	0.009 / 0.006	0.002 / -0.002
$t\bar{t}$ norm.	<0.001 / -0.001	0.002 / 0.001
s-ch. norm.	0.002 / -0.002	0.001 / -0.003
Wt-ch. norm.	0.002 / 0.001	<0.001 / <0.001
Diboson norm.	<0.001 / -0.001	0.002 / <0.001
W+jets shape (iqopt3)	0.003 / -0.003	0.003 / -0.003
W+jets shape (ptjmin10)	0.003 / -0.003	<0.001 / <0.001
QCD shape and norm.	0.010 / -0.010	0.004 / -0.004
ISR/FSR	0.002 / -0.002	0.005 / -0.005
t-ch. MC generator	0.055 / -0.055	0.001 / -0.001
$t\bar{t}$ MC gen. and PS	0.007 / -0.007	0.007 / -0.007
PDF	0.001 / -0.001	0.007 / -0.007
Unfolding	0.001 / -0.001	0.005 / -0.005
Total	+0.061 / -0.064	+0.020 / -0.015

Table F.3: *Detailed breakdown of the contribution of each source of systematic uncertainty for the electron and muon channel separately.*

$A_{\mathrm{FB}}^{\mathrm{N}}$	Electron	Muon
Data (raw)	0.010 ± 0.042 (stat.)	0.013 ± 0.038 (stat.)
Data (raw, bkg. subtracted)	0.018 ± 0.081 (stat.)	0.017 ± 0.074 (stat.)
Data unfolded	0.065 ± 0.102 (stat.) $^{+0.061}_{-0.064}$ (syst.)	0.004 ± 0.091 (stat.) $^{+0.020}_{-0.015}$ (syst.)

Table F.4: *A_{FB}^{N} measurement for the combined electron and muon channel. Both the statistic and systematic uncertainties are shown.*

List of Acronyms

ALICE: A Large Ion Collider Experiment

ATLAS: A Toroidal LHC Apparatus

CERN: Conseil Européen pour la Reserche Nucléaire

CKM: Cabibbo-Kobayashi-Maskawa

CMS: Compact Muon Solenoid

CP: Charge conjugation-Parity symmetry

CSC: Cathode Strip Chamber

ECAL: Electromagnetic Calorimeter

EM scale: ElectroMagnetic scale

FCal: Forward Calorimeter

FSR: Final State Radiation

HCAL: Hadronic Calorimeter

HEC: Hadronic End-cap Calorimeters

ID: Inner Detector

ISR: Initial State Radiation

JER: Jet Enery Resolution

JES: Jet Enery Scale

JVF: Jet Vertex Fraction

LCG: LHC Computing Grid

LCW scale: Local Cluster Weighting scale

LEP: Large Electron-Positron collider

LHC: Large Hadron Collider

LHCb: Large Hadron Collider beauty

LHCf: Large Hadron Collider forward

LINAC: LINear ACcelerators

LO: Leading Order

MBTS: Minimum-Bias Trigger Scintillators

MC: Monte Carlo

MDT: Monitored Drift Tubes

NNLL: Next-to-next-to-Leading Logarithm Order

NLO: Next-to-Leading Order

NNLO: Next-to-next-to-Leading Order

PS: Proton Synchrotron

QCD: Quantum Chromo-Dynamics theory

QED: Quantum Electro-Dynamics theory

RPC: Resistive Plate Chamber

SC: SynchroCyclotron

SCT: SemiConductor Tracker

SM: Standard Model

SPS: Super Proton Synchrotron

TGC: Thin Gap Chamber

TileCal: Tile Calorimeter

TOTEM: TOTal Elastic and diffractive cross section Measurement experiment

TRT: Transition Radiation Tracker

Bibliography

[1] The ATLAS Collaboration, "*Studies of the performance of the ATLAS detector using cosmic-ray muons*", The European Physical Journal C **71**, 1 (2011).

[2] S. Adomeit, J. F. Arguin *et al.*, "*Jets, Missing Transverse Energ and Taus for Top Physics Analysis in Release 16 with the 2010 Dataset*", ATL-PHYS-INT-2011-079, suporting note II for top quark analysis (2011).

[3] J. A. Aguilar-Saavedra and J. Bernabéu, "*W polarisation beyond helicity fractions in top quark decays*", Nucl. Phys. **B840**, 349 (2010),

[4] G. Mahlon and S. Parke, "*Single Top Quark Production at the LHC: Understanding Spin*", Phys.Lett. **B476**, 323 (2000),

[5] R. Schwienhorst, Q-H. Cao, C.-P. Yuan and C. Mueller, "*Single top quark production and decay in the t-channel at next-to-leading order at the LHC*", Phys. Rev. **D83**, 034019 (2011),

[6] The ATLAS Collaboration, "*Search for $\mathcal{CP}$ violation in single top quark events in pp collisions at $\sqrt{s}$ = 7 TeVwith the ATLAS detector*", ATLAS-CONF-2013-032 (2013).

[7] C. Escobar, M. Moreno Llácer *et al.*, "*Search for $\mathcal{CP}$ violation in single top quark events in pp collisions at $\sqrt{s}$ = 7 TeVwith the ATLAS detector*", ATL-COM-PHYS-2012-001 (2013).

[8] The ATLAS Collaboration, "*The ATLAS Experiment at the CERN Large Hadron Collider*", (2008), JINST 3 S08003.

[9] The CMS Collaboration, "*The CMS experiment at the CERN Large Hadron Collider*", (2008), JINST 3 S08004.

[10] L. Evans and P. Bryant (editors), "*LHC Machine*", (2008), JINST 3 S08001.

[11] CERN website, http://www.cern.ch.

[12] M. C. Gonzalez-Garcia, M. Maltoni, J. Salvado and T. Schwetz, "*Global fit to three neutrino mixing: critical look at present precision*", JHEP **1212**, 123 (2012),

[13] The Super-Kamiokande Collaboration, "*Evidence for Oscillation of Atmospheric Neutrinos*", Phys. Rev. Lett. **81**, 1562 (1998).

[14] The KamLAND Collaboration, "*First results from KamLAND: Evidence for reactor anti-neutrino disappearance*", Phys.Rev.Lett. **90**, 021802 (2003),

[15] B. Pontecorvo, "*Mesonium and anti-mesonium*", Sov.Phys.JETP **6**, 429 (1957).

[16] B. Pontecorvo, "*Inverse beta processes and non conservation of lepton charge*", Sov.Phys.JETP **7**, 172 (1958).

[17] J. Beringer et al. (Particle Data Group), "*Review of Particle Physics*", Phys. Rev. **D86**, 010001 (2012).

[18] The ATLAS, CDF, CMS and D0 Collaborations, "*First combination of Tevatron and LHC measurements of the top-quark mass*", (2014), arXiv:1403.4427.

[19] The ALEPH Collaboration, The DELPHI Collaboration, The L3 Collaboration, The OPAL Collaboration and The SLD Collaboration, "*Precision electroweak measurements on the Z resonance*", Phys.Rept. **427**, 257 (2006),

[20] A. Pich, "*The Standard model of electroweak interactions*", (2007), arXiv:0705.4264.

[21] A. Pich, "*Aspects of quantum chromodynamics*", p. 53 (1999), arXiv:hep-ph/0001118.

[22] A. S. J. Goldstone and S. Weinberg, "*Broken Symmetries*", Phys. Rev. **127**, 965 (1962).

[23] P. W. Higgs, "*Broken Symmetries, Massless Particles and Gauge Fields*", Phys.Lett. **12**, 132 (1964).

[24] F. Englert and R. Brout, "*Broken Symmetry and the Mass of Gauge Vector Mesons*", Phys. Rev. Lett. **13**, 321 (1964).

[25] P. W. Higgs, "*Broken Symmetries and the Masses of Gauge Bosons*", Phys. Rev. Lett. **13**, 508 (1964).

[26] P. W. Higgs, "*Spontaneous Symmetry Breakdown without Massless Bosons*", Phys. Rev. **145**, 1156 (1966).

[27] The ATLAS Collaboration, "*Observation of a new particle in the search for the Standard Model Higgs boson with the ATLAS detector at the LHC*", Physics Letters B **716**, 1 (2012).

[28] The CMS Collaboration, "*Observation of a new boson at a mass of 125 GeVwith the CMS experiment at the LHC*", Physics Letters B **716**, 30 (2012).

[29] T. D. Lee and C. N. Yang, "*Question of Parity Conservation in Weak Interactions*", Phys.Rev. **104**, 254 (1956).

[30] C. S. Wu *et al.*, "*Experimental Test of Parity Conservation in Beta Decay*", Phys.Rev. **105**, 1413 (1957).

[31] R. P. Feynman and M. Gell-Mann, "*Theory of the Fermi Interaction*", Phys. Rev. **109**, 193 (1958).

[32] N. Cabibbo, "*Unitary Symmetry and Leptonic Decays*", Phys. Rev. Lett. **10**, 531 (1963).

[33] J. H. Christenson, J. W. Cronin, V. L. Fitch and R. Turlay, "*Evidence for the 2π decay of the K_2^0 meson*", Phys. Rev. Lett. **13**, 138 (1964).

[34] The BaBar Collaboration, "*Observation of CP Violation in the B^0 Meson System*", Phys. Rev. Lett. **87**, 091801 (2001).

[35] The Belle Collaboration, "*Observation of Large CP Violation in the Neutral B Meson System*", Phys. Rev. Lett. **87**, 091802 (2001).

[36] The BaBar Collaboration, "*Observation of Time Reversal Violation in the B^0 Meson System*", Phys.Rev.Lett. **109**, 211801 (2012),

[37] J. Bernabéu, F. Martinez-Vidal and P. Villanueva-Perez, "*Time Reversal Violation from the entangled $B^0\overline{B^0}$ system*", JHEP **1208**, 064 (2012),

[38] S. L. Glashow, J. Iliopoulos and L. Maiani, "*Weak Interactions with Lepton-Hadron Symmetry*", Phys. Rev. D **2**, 1285 (1970).

[39] M. Kobayashi and T. Maskawa, "*CP-Violation in the Renormalizable Theory of Weak Interaction*", Progress of Theoretical Physics **49**, 652 (1973).

[40] S. Herb *et al.*, "*Observation of a Dimuon Resonance at 9.5 GeV in 400 GeV Proton-Nucleus Collisions*", Phys. Rev. Lett. **39**, 252 (1977).

[41] W. R. Innes *et al.*, "*Observation of Structure in the Υ Region*", Phys. Rev. Lett. **39**, 1240 (1977).

[42] The CDF Collaboration, "*Observation of Top Quark Production in proton-proton Collisions with the Collider Detector at Fermilab*", Phys. Rev. Lett. **74**, 2626 (1995).

[43] The D0 Collaboration, "*Observation of the Top Quark*", Phys. Rev. Lett. **74**, 2632 (1995).

[44] The BaBar Collaboration, "*BaBar technical design report*", (1995).

[45] The Belle Collaboration, "*The Belle detector: Detectors for Asymmetric B-factories*", NIM-A **479**, 117 (2002).

[46] J. A. Aguilar-Saavedra, J. Carvalho, N. Castro, A.Onofre and F. Veloso, "*Probing anomalous Wtb couplings in top pair decays*", Eur.Phys.J. **C50**, 519 (2007),

[47] G. A. González-Sprinberg, R. Martínez and J. Vidal, "*Top quark tensor couplings*", JHEP **1107**, 094 (2011),

[48] W. Bernreuther, O. Nachtmann, P. Overmann and T. Schroder, "*Angular correlations and distributions for searches of CP violation in top quark production and decay*", Nucl.Phys. **B388**, 53 (1992).

[49] W. Bernreuther, P. Gonzalez and M. Wiebusch, "*The Top Quark Decay Vertex in Standard Model Extensions*", Eur.Phys.J. **C60**, 197 (2009),

[50] M. Czakon, P. Fiedler and A. Mitov, "*The total top quark pair production cross section at hadron colliders through $O(\alpha_S^4)$*", Phys.Rev.Lett. **110**, 252004 (2013),

[51] N. Kidonakis, "*Next-to-next-to-leading-order collinear and soft gluon corrections for t-channel single top quark production*", Phys. Rev. **D83**, 091503 (2011),

[52] N. Kidonakis, "*Two-loop soft anomalous dimensions for single top quark associated production with a W^- or H^-*", Phys. Rev. **D82**, 054018 (2010),

[53] N. Kidonakis, "*NNLL resummation for s-channel single top quark production*", Phys. Rev. **D81**, 054028 (2010),

[54] The ATLAS Collaboration, "*Statistical combination of top quark pair production cross-section measurements using dilepton, single-lepton, and all-hadronic final states at $\sqrt{s}$ = 7 TeVwith the ATLAS detector*", (2012), ATLAS-CONF-2012-024.

[55] The ATLAS Collaboration, "*Measurement of the top quark pair production cross section in the single-lepton channel with ATLAS in proton-proton collisions at 8 TeV using kinematic fits with b-tagging*", (2012), ATLAS-CONF-2012-149.

[56] The ATLAS Collaboration, "*Measurement of the t-channel single top-quark production cross section in pp collisions at with the ATLAS detector*", Physics Letters B **717**, 330 (2012).

[57] The ATLAS Collaboration, "*Measurement of the single top production cross section in the t channel in proton proton collisions at 8 TeV* ", (2014), ATLAS-CONF-2014-007.

[58] The ATLAS Collaboration, "*Evidence for the associated production of a W boson and a top quark in ATLAS at $\sqrt{s}$ = 7 TeV*", Physics Letters B **716**, 142 (2012).

[59] The ATLAS Collaboration, "*Measurement of the cross-section for associated production of a top quark and a W boson at $\sqrt{s}$ = 8 TeV with the ATLAS detector*", (2013), ATLAS-CONF-2013-100.

[60] The ATLAS Collaboration, "*Search for s-channel Single Top-Quark Production in pp Collisions at $\sqrt{s}$ = 7 TeV*", (2011), ATLAS-CONF-2011-118.

[61] D. Collaboration, "*Improved determination of the width of the top quark*", Phys. Rev. D **85**, 091104 (2012).

[62] A. Czarnecki, J. G. Korner and J. H. Piclum, "*Helicity fractions of W bosons from top quark decays at NNLO in QCD*", Phys.Rev. **D81**, 111503 (2010),

[63] The ATLAS Collaboration and The CMS Collaboration, "*Combination of the ATLAS and CMS measurements of the W boson polarization in top quark decays*", (2013), ATLAS-CONF-2013-033, CMS PAS TOP-12-025.

[64] J. A. Aguilar-Saavedra and R. V. Herrero-Hahn, "*Model-independent measurement of the top quark polarisation*", Phys.Lett. **B718**, 983 (2013),

[65] R. R. Wilson, "*The Tevatron*", Phys.Today **30N10**, 23 (1977).

[66] The ALICE Collaboration, "*The ALICE experiment at the CERN Large Hadron Collider*", (2008), JINST 3 S08002.

[67] The LHCb Collaboration, "*The LHCb Detector at the Large Hadron Collider*", (2008), JINST 3 S08005.

[68] The TOTEM Collaboration, "*The TOTEM Experiment at the CERN Large Hadron Collider*", (2008), JINST 3 S08007.

[69] The LHCf Collaboration, "*The LHCf detector at the CERN Large Hadron Collider*", (2008), JINST 3 S08006.

[70] The ATLAS Collaboration, "*The ATLAS Computing Model*", (2005), CERN-LHCC-2004-037/G-085.

[71] LHC Computing Grid project website, http://lcg.web.cern.ch.

[72] S .D .Drell and T-M. Yan, "*Partons and their applications at high energies*", Annals of Physics **66**, 578 (1971).

[73] J. M.Campbell, J . W. Huston and W. J. Stirling, "*Hard Interactions of Quarks and Gluons: A Primer for LHC Physics*", Rept.Prog.Phys. **70**, 89 (2007),

[74] S. Alekhin *et al.*, "*HERA and the LHC A workshop on the implications of HERA for LHC physics*", (2006), arXiv:0601012 and arXiv:0601013.

[75] P. Nadolsky *et al.*, "*Implications of CTEQ global analysis for collider observables*", Phys. Rev. **D78**, 013004 (2008),

[76] A. D. Martin, W. J. Stirling *et al.*, "*Parton distributions for the LHC*", Eur.Phys.J. **C63**, 189 (2009),

[77] The ATLAS Collaboration, "*ATLAS high-level trigger, data-acquisition and controls : Technical Design Report*", (2003), CERN/LHCC/2003-22.

[78] The CDF Collaboration, "*The Underlying event in hard scattering processes*", eConf **C010630**, P501 (2001),

[79] T. Sjöstrand and M. van Zijl, "*A multiple-interaction model for the event structure in hadron collisions*", Phys.Rev. **D36**, 2019 (1987).

[80] J. M. Butterworth, J. R. Forshaw and M. H. Seymour, "*Multiparton interactions in photoproduction at HERA*", Z.Phys. **C72**, 637 (1996),

[81] M. Ferro-Luzzi, "*Determination of the luminosity at the LHC experiments*", PoS(ICHEP 2010)010 (2010), Proceedings of ICHEP 2010.

[82] M. Lamont, "*The First Years of LHC Operation for Luminosity Production*", Proceedings IPAC2013, Session: MOYAB1 - 13 May 2013 .

[83] The ATLAS Collaboration, "*ATLAS Technical Proposal for a General-Purpose pp Experiment at the Large Hadron Collider at CERN*", (1994), CERN-LHCC-94-43.

[84] The ATLAS Collaboration, "*ATLAS Detector and Physics Technical Design Report*", (1999), CERN/LHCC/99-14. CERN/LHCC/99-15.

[85] The ATLAS Collaboration, "*The ATLAS Experiment at the CERN Large Hadron Collider*", JINST **3**, S08003 (2008).

[86] The ATLAS Collaboration, "*ATLAS Inner Detector: Technical Design Report, volume 1*", (1997), CERN-LHCC-97-016.

[87] The ATLAS Collaboration, "*ATLAS Magnet System: Technical Design Report*", (1997), CERN-LHCC-97-018.

[88] G. Aad *et al.*, "*ATLAS pixel detector electronics and sensors*", JINST **3**, P07007 (2008).

[89] A. Abdesselam *et al.*, "*The barrel modules of the ATLAS semiconductor tracker*", NIM-A **568**, 642 (2006).

[90] A. Abdesselam *et al.*, "*The ATLAS semiconductor tracker end-cap module*", NIM-A **575**, 353 (2007).

[91] T. Akesson *et al.*, "*Status of design and construction of the Transition Radiation Tracker (TRT) for the ATLAS experiment at the LHC*", NIM-A **522**, 131 (2004), Proceedings of the 2nd Workshop on Advanced Transition Radiation Detectors for Accelerator and Space Applications.

[92] The ATLAS Collaboration, "*Alignment of the ATLAS Inner Detector Tracking System with 2010 LHC pp collisions at* $\sqrt{s}$ *= 7 TeV*", ATLAS-CONF-2011-012 (2011).

[93] The ATLAS Collaboration, "*ATLAS Liquid Argon Calorimeter: Technical Design Report*", (1996), CERN-LHCC-96-041.

[94] The ATLAS Collaboration, "*ATLAS Tile Calorimeter: Technical Design Repor*", (1996), CERN-LHCC-96-042.

[95] The ATLAS Collaboration, "*ATLAS Muon Spectrometer: Technical Design Report*", (1997), CERN-LHCC-97-022.

[96] The ATLAS Collaboration, "*ATLAS Level-1 Trigger: Technical Design Report*", (1998), CERN-LHCC-98-014.

[97] The ATLAS Collaboration, "*ATLAS high-level trigger, data-acquisition and controls : Technical Design Report*", (2003), CERN-LHCC-2003-022.

[98] The ATLAS Collaboration, "*Electron performance measurements with the ATLAS detector using the 2010 LHC pp collision data*", Eur.Phys.J. **C72**, 1909 (2012),

[99] J. Hartert and I. Ludwig, "*Electron isolation in the ATLAS experiment*", (2010), ATL-PHYS-INT-2010-052.

[100] B. Acharya *et al.*, "*Object selection and calibration, background estimations and MC samples for the Autumn 2012 Top Quark analyses with 2011 data*", (2012).

[101] Top quark working group recommendations - TopCommonObjects2011, https://twiki.cern.ch/twiki/bin/viewauth/AtlasProtected/TopCommonObjects2011.

[102] The ATLAS Collaboration, "*Expected Performance of the ATLAS Experiment - Detector, Trigger and Physics*", (2009), arXiv:0901.0512.

[103] N. Benekos *et al.*, "*Lepton trigger and identification for the Winter 2011 top quark analyses*", ATL-COM-PHYS-2011-123.

[104] M. Cacciari, G.P. Salam, and G. Soyez, "*The anti-k_t jet clustering algorithm*", JHEP **0804**, 063 (2008),

[105] The ATLAS Collaboration, "*Jet energy scale and its systematic uncertainty in pp collisions at $\sqrt{s}$ = 7 TeVwith ATLAS 2011 data*", (2013), ATLAS-CONF-2013-004.

[106] The ATLAS Collaboration, "*Pile-up corrections for jets from pp collisions at $\sqrt{s}$ = 7 TeVin ATLAS in 2011*", (2012).

[107] The ATLAS Collaboration, "*Jet energy measurement with the ATLAS detector in pp collisions at $\sqrt{s}$ = 7 TeV*", (2011), arXiv:1112.6426.

[108] The ATLAS Collaboration, "*Jet energy measurement and systematic uncertainties using tracks for jets and for b-quark jets produced in pp collisions at $\sqrt{s}$ = 7 TeVin the ATLAS detector*", (2013).

[109] D. Miller, A. Schwartzman and D. Su, "*Pile-up jet energy scale corrections using the jet-vertex fraction method*", (2009).

[110] B. Butler and A. Schwartzman, "*Track-Jet Reconstruction and Performance*", (2010).

[111] The ATLAS Collaboration, "*Jet Energy Resolution and Selection Efficiency Relative to Track Jets From In-Situ Techniques With the ATLAS Detector Using pp Collisions at a Center of Mass Energy $\sqrt{s}$ = 7 TeV*", (2010), ATLAS-CONF-2010-054.

[112] The ATLAS Collaboration, "*Jet energy resolution in pp collisions at $\sqrt{s}$ = 7 TeVrecorded in 2010 with the ATLAS detector*", Eur.Phys.J. **C73**, 2306 (2013),

[113] T. Carli, R. Piegaia, G. Romeo *et al.*, "*Jet Energy Resolution from In-situ Techniques with the ATLAS Detector Using pp Collisions at a Center of Mass Energy $\sqrt{s}$ = 7 TeV*", (2011).

[114] The ATLAS Collaboration, "*Commissioning of the ATLAS high-performance b-tagging algorithms in the 7 TeVcollision data*", (2011), ATLAS-CONF-2011-102.

[115] The ATLAS Collaboration, "*Measurement of the b-tag Efficiency in a Sample of Jets Containing Muons with 5 fb^{-1} of Data from the ATLAS Detector*", (2012), ATLAS-CONF-2012-043.

[116] R. E. Kalman, "*A New Approach to Linear Filtering and Prediction Problems*", **82**, 35 (1960).

[117] The ATLAS Collaboration, "*Measurement of the Mistag Rate of b-tagging algorithms with 5 fb^{-1} of Data Collected by the ATLAS Detector*", (2012), ATLAS-CONF-2012-040.

[118] The ATLAS Collaboration, "*Reconstruction and Calibration of Missing Transverse Energy and Performance in Z and W events in ATLAS pp Collisions at $\sqrt{s}$ = 7 TeV*", (2012), ATLAS-CONF-2012-101.

[119] The ATLAS Collaboration, "*Performance of Missing Transverse Momentum Reconstruction in Proton-Proton Collisions at 7 TeV with ATLAS*", Eur.Phys.J. **C72**, 1844 (2012),

[120] The ATLAS Collaboration, "*Measurement of the $W \to lv$ and $Z/\gamma^* \to ll$ production cross sections in proton-proton collisions at $\sqrt{s}$ = 7 TeVwith the ATLAS detector*", Journal of High Energy Physics **2010**, 1 (2010).

[121] The ATLAS Collaboration, "*The ATLAS Inner Detector commissioning and calibration*", The European Physical Journal C **70**, 787 (2010).

[122] The ATLAS Collaboration, "*Commissioning of the ATLAS Muon Spectrometer with cosmic rays*", The European Physical Journal C **70**, 875 (2010).

[123] T. G. Cornelissen *et al.*, "*The global χ^2 track fitter in ATLAS*", Journal of Physics: Conference Series **119**, 032013 (2008).

[124] P. Brckman, A. Hicheur and S. J. Haywood, "*Global χ^2 approach to the Alignment of the ATLAS Silicon Tracking Detectors*", ATL-INDET-PUB-2005-002, ATL-COM-INDET-2005-004 (2005).

[125] A. Bhatti, F. Canelli and B. Heinemann (The CDF collaboration), "*Determination of the jet energy scale at the Collider Detector at Fermilab*", NIM-A **566**, 375 (2006).

[126] Data and Monte Carlo datasets for 2010 analysis, https://twiki.cern.ch/twiki/bin/viewauth/AtlasProtected/DataMCForAnalysis#2010_data_set.

[127] T. Sjostrand, S. Mrenna and P. Skands, "*PYTHIA Generator version 6.418*", JHEP **05**, 026 (2006).

[128] The ATLAS Collaboration, CERN Report No. ATL-PHYS-PUB-2010-002, 2010 (unpublished).

[129] G. Corcella *et al.*, "*HERWIG 6.5: an event generator for Hadron Emission Reactions With Interfering Gluons (including supersymmetric processes)*", JHEP **01**, 010 (2001).

[130] J. M. Butterworth, J. R. Forshaw and M. H. Seymour, "*Multiparton interactions in photoproduction at HERA*", Z. Phys. **C72**, 637 (1996).

[131] The ATLAS Collaboration, "*Measurement of underlying event characteristics using charged particles in pp collisions at $\sqrt{s}$ = 900 GeVand 7 TeVwith the ATLAS detector*", Phys.Rev. **D83**, 112001 (2011),

[132] The ATLAS Collaboration, "*Improved luminosity determination in pp collisions at $\sqrt{s}$ = 7 TeVusing the ATLAS detector at the LHC*", (2013), arXiv:1302.4393.

[133] B. P. Kersevan and E. Richter-Was, "*The Monte Carlo Event Generator AcerMC versions 2.0 to 3.8 with interfaces to PYTHIA 6.4, HERWIG 6.5 and ARIADNE 4.1*", Comput. Phys. Commun. **184**, 919 (2013),

[134] A. Sherstnev and R. Thorne, "*Different PDF approximations useful for LO Monte Carlo generators*", arXiv:0807.2132.

[135] The ATLAS Collaboration, "*New ATLAS event generator tunes to 2010 data*", (2011), ATL-PHYS-PUB-2011-008.

[136] B. P. Kersevan and I. Hinchliffe, "*A Consistent Prescription for the Production Involving Massive Quarks in Hadron Collisions*", JHEP **0609**, 033 (2006),

[137] Protos - PROgram for TOp Simulations, http://jaguilar.web.cern.ch/jaguilar/protos/.

[138] M. Aliev, H. Lacker *et al.*, "*HATHOR: HAdronic Top and Heavy quarks cross section calculatoR*", Comput. Phys. Commun. **182**, 1034 (2011),

[139] M. J. J. M. Campbell and R. K. Ellis, "*MCFM for the Tevatron and the LHC*", Nucl.Phys.Proc.Suppl. **205-206**, 10 (2010),

[140] C. Anastasiou, L. Dixon, K. Melnikov and F. Petriello, "*High-precision QCD at hadron colliders: electroweak gauge boson rapidity distributions at NNLO*", Phys.Rev. **D69**, 094008 (2004),

[141] J.M. Campbell, R.K. Ellis and C. Williams, "*Vector boson pair production at the LHC*", JHEP **1107**, 018 (2011),

[142] P. Nason, "*A new method for combining NLO QCD computations with parton shower simulations*", JHEP **11**, 040 (2004),

[143] H. Lai *et al.*, "*New parton distributions for collider physics*", Phys.Rev. **D82**, 074024 (2010),

[144] P. Z. Skands, "*Tuning Monte Carlo generators: The Perugia tunes*", Phys. Rev. **D82**, 074018 (2010),

[145] M. L. Mangano, M. Moretti, F. Piccinini, R. Pittau and A. D. Polosa, "*ALPGEN, a generator for hard multiparton processes in hadronic collisions*", JHEP **0307** (2003),

[146] The ATLAS Collaboration, "*The ATLAS Simulation Infrastructure*", Eur. Phys. J. **C70**, 823 (2010),

[147] The GEANT4 Collaboration, "*GEANT4: A simulation toolkit*", Nucl. Instrum. Meth. **A506**, 205 (2003).

[148] The common parameters used for ATLAS MC production 2011, https://twiki.cern.ch/twiki/bin/viewauth/AtlasProtected/McProductionCommonParametersMC1.

[149] The ATLAS Collaboration, "*Misidentified lepton backgrounds in top quark pair production studies for EPS 2011 analyses*", (2011).

[150] B. Acharya *et al.*, "*Object selection and calibration, background estimations and MC samples for the Winter 2012 Top Quark analyses with 2011 data*", (2012).

[151] G. Cowan, "*A survey of unfolding methods for particle physics*", Conf.Proc. **C0203181**, 248 (2002).

[152] The ATLAS Collaboration, "*Measurement of the t-channel single top quark production cross section in pp collisions at* $\sqrt{s}$ *= 7 TeVwith the ATLAS detector*", Phys. Lett. **B717**, 330 (2012),

[153] The CMS Collaboration, "*Measurement of the single-top-quark t-channel cross section in pp collisions at* $\sqrt{s}$ *= 7 TeV*", JHEP **2012**, 1 (2012).

[154] Top Systematic Uncertainties for Winter 2012 (rel17) 5 fb^{-1} analyses, https://twiki.cern.ch/twiki/bin/viewauth/AtlasProtected/TopSystematicUncertainties2011.

[155] The ATLAS Collaboration, "*b-jet tagging calibration on c-jets containing* D^{*+} *mesons*", (2012), ATLAS-CONF-2012-039.

[156] The ATLAS Collaboration, "*Measurement of* $t\bar{t}$ *production with a veto on additional central jet activity in pp collisions at* $\sqrt{s}$ *= 7 TeVusing the ATLAS detector*", Eur.Phys.J. **C72**, 2043 (2012),

[157] M. Botje, J. Butterworth *et al.*, "*The PDF4LHC Working Group Interim Recommendations*", (2011), arXiv:1101.0538.

[158] TopFit - a program to fit the Wtb vertex, http://jaguilar.web.cern.ch/jaguilar/topfit/.